MODELING OF THE SIZE EFFECT IN THE PLASTIC BEHAVIOR

OF POLYCRYSTALLINE MATERIALS

A Thesis
Presented to
The Academic Faculty

by

Laurent Capolungo

In Partial Fulfillment
of the Requirements for the Degree
Doctor of Philosophy in the
School of Mechanical Engineering

Georgia Institute of Technology
AUGUST 2007

MODELING OF THE SIZE EFFECT IN THE PLASTIC BEHAVIOR

OF POLYCRYSTALLINE MATERIALS

Approved by:

Dr. Jianmin Qu, Co-Advisor
School of Mechanical Engineering
Georgia Institute of Technology

Dr. Mohammed Cherkaoui, Co-Advisor
School of Mechanical Engineering
Georgia Institute of Technology

Dr. David L. McDowell
School of Mechanical Engineering
Georgia Institute of Technology

Dr. Hamid Garmestani
School of Materials Science and
Engineering
Georgia Institute of Technology

Dr. Steven Johnson
School of Materials Science and
Engineering
Georgia Institute of Technology

Date Approved: June 8th, 2007

ACKNOWLEDGEMENTS

First and foremost, I would like to thank my co-advisors, Dr. Mohammed Cherkoaui and Dr. Jianmin Qu. They have given me an outstanding chance to pursue my education and have always been a great source of motivation and inspiration. I would like to express my deepest gratitude for their guidance and for their passion for research, and science in general, which they have kindly shared with me. Second, I would like to thank Dr. David L. McDowell and Dr. Esteban P. Busso for the numerous discussions we have had over the past years. Their advices, support and trust have undoubtly added to the quality of this research and to my personnal experience.

This thesis has been the chance for me to initiate a superb collaboration with Dr. Douglas Spearot who has kindly accepted to contribute to this research by perfoming molecular simulations and by sharing his experience knowledge and passion with me.

I express my deepest gratitude to Dr. Hamid Garmestani and Dr. Steven Johnson who have kindly accepted to be part of this thesis committee. I perceive their presence as a great honor.

My experience in graduate school would not have been so pleasant without my colleagues and friends at Georgia Tech Atlanta and Georgia Tech Lorraine. In particular, I would like to thank Ryan Austin for letting me discover the American way of life.

Finally, I would like to thank my parents Carlo and Rosinne Capolungo, and my brother David Capolungo who have been there to support me and to encourage me to perform the best that I could. I hope one day to merit the sacrifices they have made for me. This thesis is dedicated to them.

TABLE OF CONTENTS

LIST OF TABLES

LIST OF FIGURES

angle.

excess interface energy as a function of applied tensile stress. Boundaries which contain B' and C structural units show a decrease in excess interface energy, while Σ13 and Σ17 boundaries show an increase in excess energy.

SUMMARY

This thesis focuses on the study of the size effect in the elastic-viscoplastic response of pure face centered cubic polycrystalline materials.

First, the effect of vacancy diffusion is studied via the use of a two-phase self-consistent scheme in which the inclusion phase represents grain interiors and the matrix phase represents grain boundaries. The behavior of the inclusion phase is driven by the activity of dislocations, described with typical strain hardening laws, and by the activity of Coble creep. The behavior of the matrix phase is modeled as elastic-perfect plastic. This model is then extended to account for the possible activity of Lifschitz sliding.

Second, grain boundary assisted deformation is studied. Detailed atomic motions within pure tilt bicrystal interfaces are predicted via molecular simulations. It is revealed that grain boundaries containing C structural units exhibit particular atomic motions in the elastic regime characterized by "bifurcation" events.

The active role of grain boundaries to the viscoplastic deformation is studied with the introduction of a novel method allowing the scale transition from the atomistic scale to the macroscopic scale. A model describing the mechanism of grain boundary dislocation emission and penetration is informed with molecular simulations and finite element simulations. The macroscopic response of the material is then predicted with use of several self-consistent schemes, among which two novel three-phases schemes are introduced. The most refined micromechanical scheme proposed is based on a two-phase representation of the material and is valid in the elastic-viscoplastic regime and accounts for the effect of slightly weakened interfaces.

CHAPTER 1

INTRODUCTION

Over the past two decades, nanoscience in general and nanotechnologies (NT) in particular, have been source of strong interest in the scientific community as well as in the industry. Indeed, nanotechnologies can be implemented in areas as diverse as transportation, construction, electronic packaging, bio-engineering etc., and could result in substantial improvement of complex systems in terms of dimensions, mass and consequently in terms of energy consumption. This is obviously of great economical impact. Therefore, NT are already considered by many as possible precursors to a new technological revolution.

Let us note that NT have yet led to relatively few applications. However, numerous encouraging advances have already been developed. For example, atomistic scale studies on bio-nanomotors, corresponding to proteins or protein complexes ensuring vital functions in living cells such as reproduction, have lead to a better understanding of their detailed functioning. A schematic of three types of nanomotors is presented in Figure 1.1.(a) in which one can observe, from top to bottom, a kinesin, a dinein and a myosin V nanomotor, respectively (Vogel 2005). In a different domain, King et al. (2002) developed a thermal writing process on a polymer substrate based on the use of a heated atomic force microscope cantilever. An image of the surface of the polymer substrate during cyclic write/ erase steps is shown in Figure 1.1.b. Among others, it is shown that this thermal writing process combined with nanoimaging could be used to

fabricate data storage devices with data density as high as 400 Gb/in^2 which is four times larger than the maximum achievable data density in magnetic data storage devices (King et al., 2001). Finally, carbon nanotubes, owing to their exceptional mechanical and electronic properties, have been one of the most studied novel nanomaterials. Indeed, reported values of the critical stress at which multiwalled carbon nanotubes collapse in compression range from ~115GPa. to ~ 150 GPa (Lu and Zhang, 2006). Also, while first fabricated carbon nanotubes rarely exhibited lengths longer than a few micrometers (Li et al. 2005), novel methods were recently introduced allowing the fabrication of up to ~20cm-long-single-walled carbon nanotubes (Gu et al., 2006). With this non exhaustive list of examples, one can easily comprehend the rational behind the excitement NT have been source of.

(a)   (b)
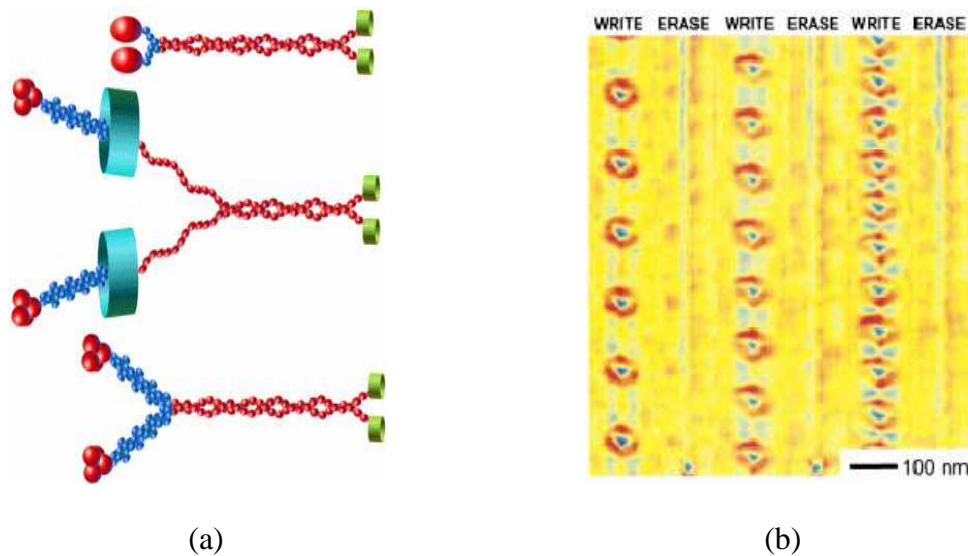
Figure 1.1: (a) Bio-nanomotors,   (b) Nanoindentation on a polymer substrat.

Although, the word "nanotechnology" has already become a common term in our language, let us clearly define its significance. All systems (e.g., device, cell, material)

with characteristic length scale in the order of a few nanometers (e.g. 1^E-9m) can be referred to as belonging to the generic term nanotechnology. While NT are recent, the concept and premises of NT were introduced more than 40 years ago. Indeed, Dr.Richard Feynman already discussed, in his now famous talk "There is plenty of room at the bottom" (1959), of the feasibility of printing and reading the 24 volumes of the Encyclopedia Britannica on the head of a pin. In recent article, Uyeda (1991) described the nanoparticule synthesis processes developed and used in Japan during World War II. Surprisingly, 3nm-size metal particle could already be fabricated in the early 1950s (Uyeda, 1991).

The emergence of NT, which concept relies on the reduction of the critical length of a device or material, has shed light on numerous issues both fundamental and technological. This is the case of the experimentally measured "abnormal grain growth" occurring in polycrystalline metals with nano-sized grains (Moelle et al. 1995).

The present research is dedicated to the study of the size effect in the quasi-static response of pure polycrystalline materials with a face centered cubic structure (F.C.C.). Indeed, as will be discussed in more details in next chapter, these materials exhibit unexpected responses characterized, among others, by the breakdown of the hall Petch law and the abnormal strain rate sensitivity. The models to be presented, aim at describing the response of both conventional materials and nanocrystalline (NC) materials. Let us recall that as discussed in Gleiter's pioneering work (2000), nanostructured materials can be sorted in twelve different categories depending on their

chemical composition and crystal shapes. The term nanocrystalline material refers to pure materials with equiaxed grains. Let us note that, as discussed in recent review by Koch (2007) these materials could have applications in several domains. For example, electrodeposited NC materials can be used in the cutting tools industry. Also, Palumbo et al. (1997) suggested the use of electrodeposited Ni microalloys to conduct the repair of nuclear steam generators tubing. Finally, in the military field, the possibility of fabricating NC kinetic penetrators was investigated (Wei et al. 2004).

Although, the structure of NC materials will be presented in details in next chapter, let us briefly introduce the microstructural features of NC materials. Three constituents compose NC materials: (1) grain interiors which exhibit a crystalline structure, (2) grain boundaries which correspond to the interphase between two adjacent grains and (3) triple junctions corresponding to regions of the material where three grains meet. The structure of grain boundaries and triple junctions is still subject to debate for there is currently no general agreement on the degree of atomic order exhibited by these constituents. Let us now enunciate the motivations and resulting challenges of this research.

Motivations

As mentioned in the above, abnormal size effects have been revealed in NC materials. The most striking example is that of the breakdown of the Hall-Petch law presented here below. The yield strength of conventional polycrystalline materials (with grain size larger than a micrometer) is known to be grain-size-dependent and is given by the phenomenological Hall-Petch law (Hall, 1951; Petch, 1953):

$$\sigma_y = \sigma_0 + \frac{K^{HP}}{\sqrt{d}} \qquad\qquad (1.1)$$

Here σ_y, σ_0, d, K^{HP} represent the yield stress, the friction stress, the grain size and the Hall Petch slope, respectively. The Hall-Petch slope depends on the sessile dislocation interaction. As exhibited by equation (1.1), a decrease in the grain size leads to an increase in the yield stress proportional to the inverse of the square root of the grain size. From this simple empirical law it is shown that material enhancement can be successfully performed via structural refinement. The other improvement method generally consists of adding extraneous constituents to the material. Let us consider the case of pure copper which typically exhibits a Hall-Petch slope of $0.11 MPa \cdot \sqrt{m}$. Starting from a 1 micron grain size material with 180 MPa. yield stress, and decreasing the grain size to 50 nm, according to the Hall-Petch law the yield stress of the fine grained copper sample will be 561MPa. In other words, the yield strength is multiplied by a factor 3.

Four types of models were developed to describe the Hall-Petch law. All of these account for the interactions between sessile dislocations and grain boundaries. The first approach was introduced by Petch and is based on the propagation of stresses localized near boundaries (which do not actively contribute to the plastic deformation) and due to dislocation pile-ups (Petch, 1953). However, this first model avers inappropriate since body centered cubic materials, in which dislocation pile-up does not occur, also exhibit a grain size dependent yield stress given by the Hall-Petch law.

In 1963, J.C.M. Li developed a model based on dislocation emission by grain boundary ledges (which will be discussed in Chapter 2). Grain boundary ledges can be assimilated as extraneous atomic layers located at the grain boundary grain core interface. This model is based on the stress fields localized near grain boundaries and engendered by the presence of Taylor-types dislocation forests near the boundaries. The dislocations forests are assumed to result from dislocations emitted by grain boundary ledges (Li 1963). In this model the initial ledge density is assumed to be size independent and is related to the grain boundary misorientation angle. Then, the misorientation angle is related to the density of dislocations stored in the Taylor type forests. Murr and Venkatesh investigated the validity of Li's model (Murr and Venkatesh, 1978). The yield strength was revealed to be strongly dependent on the initial ledge density (measured via TEM observations) (Venkatesh and Murr, 1978). However, contrary to Li's hypothesis, the ledge density exhibited size dependence. Let us note that Murr and Venkatesh's work has also shown that as predicted by Li, grain boundary ledges can emit dislocations (Murr, 1981).

The Hall Petch law can also be derived from Ashby's reasoning (1970) in which the yield stress is directly dependent on the dislocation density through Taylor's model (1934). The dislocation density is related to the grain size with use of the principle of similitude introduced by Kuhlman-Wisdorf (1962). Let us recall that the principle of similitude gives proportionality relations between several characteristic lengths of the material, such as the dislocation mean free path and the cell wall thickness for example.

Finally, the most up-to-date models are based on strain gradients engendered by the presence of geometrically necessary dislocations within the grain boundaries. Geometrically necessary dislocations, as opposed to statistically stored dislocations, are present in regions of the materials presenting curvature in their lattice. For example, this is the case of grain boundaries. Nye (1953) introduced a dislocation tensor relating the density of geometrically necessary dislocations. Several models based on strain gradient plasticity were successful in modeling the size dependent yield strength in conventional materials (Gao et al. 1999; Huang et al. 2000). For example, Cheong et al. (2005) modeled the size effect in F.C.C. polycrystals with a non-local strain gradient model implemented in finite element simulations. While the model was successful in predicting the size effect in conventional materials (with grain size ranging form 150 microns to 7.5 microns), the authors reported convergence problems when the grain size was reduced.

While substantial effort was being dedicated to the understanding of the fundamentals resulting in the observed size-dependent response of metals, novel techniques motivated by the appeal of the Hall-Petch law were developed allowing the fabrication of sub-micron size polycrystalline materials. Inert gas condensation and crystallization from an amorphous glass were the first two techniques introduced (Birringer et al. 1984; Gleiter et al. 1984).

Early experiments on nanocrystalline materials exhibited interesting phenomena and microstructures. First, X-ray diffraction and Mossbauer microscopy suggested that grain boundaries exhibit neither short range nor long distance atomic order (Schumacher

et al. 1989). Also, the self-diffusion coefficients of the NC samples were reported to be as high as four times that of grain boundaries (Birringer 1988). Let us note that these measures were obtained on NC materials with grain size smaller than~10nm. More recent experiments on high purity Cu samples report limited hardening of the material (Youssef et al., 2004; Cheng et al., 2005). The response of NC materials will be presented in details in next Chapter.

In the case of the size-dependent yield strength, it was shown that the Hall Petch law is not valid when the grain size is smaller than a critical grain size in the neighborhood of ~20-30nm (Gleiter 1991; Weertman 1993; Conrad et al. 2000). Indeed, it was observed that below this critical grain size, the Hall-Petch slope decreases and could take negative values (Schuh et al. 2002). This phenomenon is referred to as the "breakdown" of the Hall-Petch law and is presented schematically in Figure1.2. Since the yield strength is not an intrinsic material property, it depends for example of the loading history of the material, the breakdown of the Hall Petch law naturally leads to the following two hypothesis: (1) a change in the nature of the deformation mechanism governing the materials response occurs in NC materials and, (2) there is a size effect in the microstructure of NC materials.
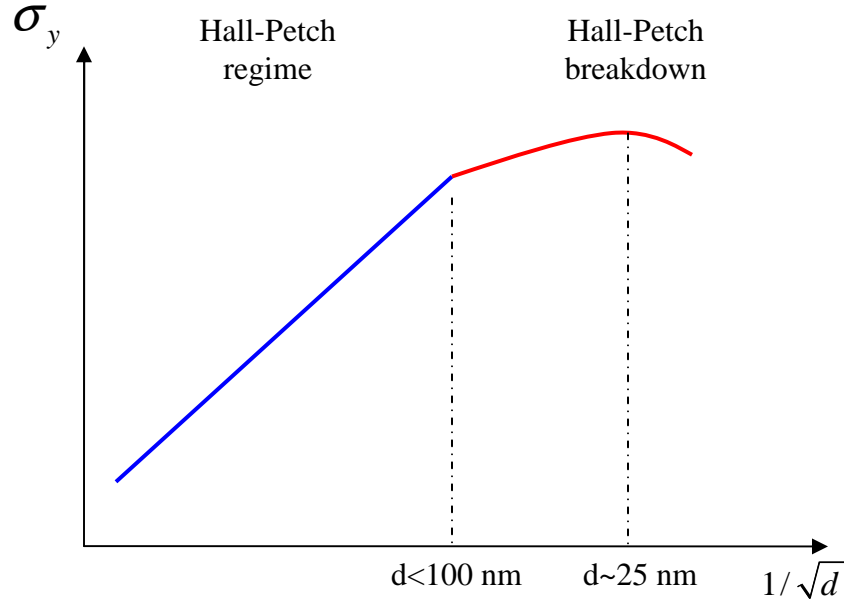
Figure 1.2: Schematic of the evolution of yield stress with grain size

Let us first discuss one of the early hypotheses suggesting that the size effect is due to the structure of grain boundaries which would differ in conventional polycrystalline materials and in NC materials. Since grain boundary thickness is not affected by grain size and typically ranges in the neighborhood of ~1nm (Kim et al. 2000), a decrease in the grain size leads to an increase in the relative volume fraction of interphase (e.g., grain boundaries and triple junctions). Birringer et al. in their early work reported grain boundary volume fraction as high as 50% (1984). Therefore, the role of grain boundaries shall be increasing with decreasing grain sizes. It was suggested that grain boundaries exhibited an amorphous structure which resulted in the softening in the response of NC materials (Birringer 1988). However, recent observations and molecular simulations (in dynamics and in statics) reported higher degrees of atomic order in grain

boundaries and triple junctions (Van Swygenhoven et al. 2001; Kumar et al. 2003).

Indeed, it was shown that while triple junctions did not exhibit any particular atomic

order, grain boundaries cannot be considered amorphous for some grain boundary regions

may exhibit well organized structure (e.g., structural units) and some other regions may

not show any particular organization. Hence, the size effects in polycrystalline materials

may not be entirely attributed to the structure of grain boundaries.

This leads us to the problematic of the present research which aims at identifying

and modeling the deformation mechanisms which may be active in NC materials in order

to predict the size effects in pure F.C.C. polycrystalline materials. The major difficulty

stands in the fact that the study of NC materials is relatively new. Consequently, there is a

relatively large number of issues which are still subject to debate. Scientifically the major

challenge is to extract data at the atomistic level, from molecular dynamics simulations or

transmission electron microscopies, and use this knowledge to predict the macroscopic

response of the material. In other words, this corresponds to the scale transition from the

atomistic to the macroscopic scales. In order to perform this scale transition, one must be

familiar with the limitations and outcomes of the different techniques used to study NC

materials.

Studying tools

First, let us note that the investigation tools will be discussed in details later

throughout this dissertation. The objective here is solely to concisely describe the

advantages, limitations and domain of applications of the most commonly used

techniques.

Three complimentary approaches are necessary to investigate the size effect in NC materials: (1) experimental studies, (2) numerical simulations, especially molecular dynamics and statics which are of primary use due to localized nature of the observed phenomena and, (3) analytical models.

Obviously, numerical and analytical models will be based on, or suggested by, experiments. However, it is important to be aware of the several difficulties in fabricating and testing NC samples.

In the case of the synthesis of samples, the five most often used processes generally lead to materials with defects (which type and amount is dependent on the fabrication process). These artifacts clearly affect the quality of the experimental measures and will penalize the reproducibility of the results. For example, two samples with similar grain sizes and chemical composition but synthesized via two different routes can exhibit a 200% difference in their yield strength. Hence, models cannot currently be confronted with rigorous statistical analysis.

Moreover, as-produced samples typically exhibit small dimensions. For example Khan et al. (2000) produced cylindrical samples with height 10 mm and diameter 15 mm which requires the fabrication of adapted experimental apparatus.

Finally, microstructural observation, performed mostly via transmission electron microscopy (TEM), has limitation inherent to the microscope itself. Indeed, the principle of the TEM relies on the diffraction of electrons bombarded on the sample. This leads to a diffraction figure corresponding to the Fourier transform of the interactions between

atoms given by an assumed potential. Hence, the high resolution image is obtained via an

inverse Fourier transform of the diffraction figure. Although, TEM is an extremely useful

apparatus since it allows material observation at the atomistic scale, it also suffers from

several limitations. Indeed, as mentioned in the above, the high resolution image is

conditional on the fact that a diffraction figure can be obtained. Hence, the sample

thickness is limited by the energy required by the electrons to go through the sample.

Typically samples have a thickness inferior to ~30nm which can potentially lead to

relaxation phenomena (e.g., decrease in the dislocation density due to the free surface).

Therefore, considering the few arguments presented in the above, a great care

must be taken when analyzing experimental data.

In the case of numerical simulations, with the increase in the frequency of the

processors and in the data storage capability, it is now possible to simulate the response

of a large number of atoms via molecular dynamics (MD) and statics (MS). Hence,

atomic motion within a crystal can now be modeled dynamically which allows for

example the observation of dislocation slip. MD and MS are ineluctably limited by their

large consumption of computer resources. Among others, MD and MS simulations rarely

allow the simulation of more than ~600000 atoms. Let us note that periodicity conditions

can be applied to the system studied. Hence, it is capital to acknowledge the fact that so

far molecular simulations are not representative of the geometry of the material.

Also, in the case of MD simulations, unrealistic boundary conditions, such as

strain rates in the order of 1.E7/s, or stresses in the order of several GPa, must be applied

in order to simulate plastic deformation and the simulations can generally not exceed

several hundred picoseconds of real time. These limitations result from the fact that the time step used in calculations must be inferior to the period of vibration of atoms (in the order of the femtosecond) in order not to introduce atomic collision.

The evaluation of the stress field via Virial's theorem is a fundamental issue being debated. Indeed, Zhou (2002, 2003) discussed of the validity of the use of Virial's stress to represent Cauchy stress. The author shows that while Virial's stress accounts for both a kinetic and an interatomic force term, solely the second term shall be used in order to respect the momentum balance equation.

Finally, owing to the complex microstructure of NC materials (e.g., grain shape, grain size distribution, grain boundary misorientation, triple lines...), numerical modeling of realistic structures avers to be very challenging.

Hence, while MD and MS are necessary and powerful tools to model NC materials, one must keep their limitations in mind for they could predict the activity of mechanism that are not representative of the material's response in the quasi-static regime.
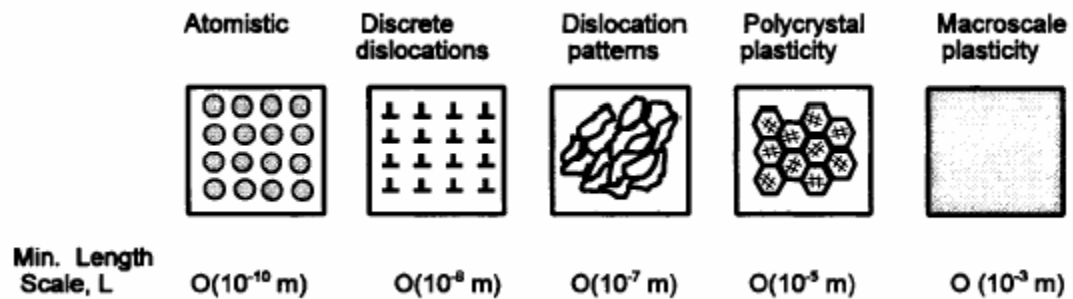
Extracted from(McDowell 2000)

Figure1.3: Schematic of the different scales of resolution of plasticity.

13

Experiments and numerical simulations provide information at the atomistic scale. However, as recalled by MC Dowell (2000), another difficulty resides in the scale transition that is to be performed to allow the quantification, at the macroscopic scale, of the effects of mechanisms exhibited by studies at the atomistic scale. The different scales of resolution of dislocation plasticity are presented in Figure 1.3. The scale transition from the microscopic scale to the macroscopic scale can so far be performed via two different routes; (1) analytical models such as continuum micromechanics and, (2) finite elements simulations. These two techniques have their limitations which are well known and will be discussed in following chapters. However, there is currently no consistent method to perform the transition from the atomistic scale to the microscopic scale.

Goals and Strategy

The size effect in the elastic-viscoplastic response of pure F.C.C. polycrystalline materials is investigated in this dissertation. The present research is limited to the quasistatic regime; the effect of temperature will be briefly studied as well as the creep response.

The presented study has two main objectives and has applications both in the short term and in the long term. The first objective is to identify and model the different mechanisms that may contribute to the so-called abnormal behavior of NC materials. The identification of these mechanisms will be entirely based on an extensive literature

14

review with focuses on experiments and numerical simulations. From the literature review, a first map of deformation, similar in essence to Ashby's map, will be established.

The second objective is to introduce novel modeling techniques allowing the bridging of different scales. Moreover, these techniques shall be highly adaptable to future research in the field and in other fields involving multi-physics.

Considering the fact that most phenomena in the field of NC materials are still subject to debate, we propose a careful approach consisting of studying independently the effect of each mechanism and of gradually increasing the complexity of the models. This dissertation is organized as follows:

The state of the art presented in Chapter 2, is primarily dedicated to the detailed presentation of the mechanical response, properties, fabrication process and models related to NC materials. Also, this chapter will briefly present some active deformation mechanisms of interest occurring in conventional F.C.C. materials. This chapter will be concluded with a discussion on the potentially active plastic deformation mechanisms (e.g., Coble creep, Nabarro Herring creep, grain boundary sliding, grain boundary dislocation emission…)

The following chapter is dedicated to continuum micromechanics. The aim of this chapter is to briefly recall the fundamentals of continuum micromechanics, which is traditionally used to perform the micro-macro-scale transition. Moreover two novel self-

consistent micromechanical schemes will be presented. The first scheme is a three-phase model where the material is equivalently represented by a coated inclusion embedded in an infinite matrix. The inclusion phase represents grain cores, the coating represents both grain boundaries and triple junctions, and the matrix phase represents the effective material. Interfaces are assumed perfect (no relative motion of grain is permitted). Inclusions are also assumed spherical. The second micromechanical scheme is based on on the consecutive use of two biphased topologies. This scheme is valid in the case of elastic-viscoplastic behaviors and allows the description of slightly weakened interfaces. Therefore, this scheme is particularly suited to quantify the effects of relative motions of grains (e.g., grain boundary sliding, grain rotation).

Chapter 4 is dedicated to the study of the effect of diffusion mechanism on the macroscopic response of NC materials. In a first part solely the mechanism of Coble creep is accounted for. Let us recall that Coble creep (1963) describes the steady state vacancy diffusion along grain boundaries. This study was motivated by the fact that early experiments reported that NC materials could creep at room temperature. In this first attempt, the material is represented as a two-phase composite and the scale transition from the microscopic scale to the macroscopic scale is performed via the use of an extension to Eshelby's solution to the case of elasto-viscoplasticity (Cherkaoui et al. 2000). The inclusion phase represents grain cores while the matrix phase represents grain boundaries. The viscoplastic response of the inclusion phase is governed by the activity of dislocations and described with the formalism developed by Kim et al. (2000), and by the mechanism of Coble creep. The response of grain boundaries is approximated as

16

elastic perfect- plastic. This hypothesis is based on the limited data available at the time

regarding the response of grain boundaries.

The model is later extended to account for the diffusion assisted grain boundary

sliding, also referred to as Lifschitz sliding .Indeed, as in the case of vacancy diffusion,

grain boundary sliding has been subject to in depth investigations and to debate regarding

its possible accommodation by vacancy diffusion.

The effect of grain boundary assisted deformation is presented in Chapter 5. This

chapter is subdivided into two sections. The first section treats of the elastic behavior of

grain boundaries which is investigated via molecular dynamics simulations (performed

by Dr. Spearot) and aims at revealing the peculiarities of atomic motion in interfaces in

the elastic regime. The second section of this chapter is dedicated to the modeling of the

grain boundary dislocation emission mechanism. Although this mechanism was first

discussed some 40 years ago, there is no model allowing the quantitative prediction of its

effect on the macroscopic response. The proposed model results from in depth discussion

on the activity of intra-granular dislocation sources in NC materials and is based on a

statistical description of the grain boundary dislocation emission mechanism. As will be

discussed, with this description a scale transition from the atomistic scale to the

mesoscopic scale can be performed. The parameters constants are obtained via molecular

dynamics simulations on bicrystal interfaces. These simulations reveal the importance of

grain boundary ledges to the emission process. Among other, it is shown that contrary to

Li's hypothesis, grain boundary ledges can act as dislocation sources and not solely as

dislocation donors. The effect of grain boundary dislocation emission is estimated via the

use of three different micromechanical schemes (2 phase elasto-viscoplastic, 3-phase viscoplastic) informed by a set of finite element simulations evaluating stress heterogeneities that cannot be accounted for with traditional Eshelbian schemes. The behavior of grain interiors is driven via dislocation motion and the typical formalism describing strain hardening (Kocks et al. 1975; Kocks et al. 2003) is enhanced to account for the long distance stress engendered by the presence of grain boundaries and triple junctions. The effect of temperature, strain rate and the creep response of the material is then simulated. It is shown , among other, that grain boundary dislocation emission can contribute to the softening in the plastic response of NC materials.

Chapter 6 introduces a numerical scheme based on a modified strain gradient crystal plasticity theory to be implemented into a non-conventional finite element scheme. This Chapter presents a possible route allowing the quantification of the activity of dislocations (e.g., creation and emission from grain boundaries, transport through grains and absorption into grain boundaries). In order to account for dislocation emission, a finite element method accounting for dislocations as degrees of freedom (as opposed to internal state variables) is introduced. The numerical scheme composed of a global and of a local integration procedure at the element level and at the material level, respectively, is described in details.

Future work is presented in Chapter 7. A procedure discussing the several steps envisaged to numerically model volume elements representative of real samples is introduced.

References

Ashby, M. F. (1970). "The deformation of plastically non homogeneous materials". Philosophical magazine 21: 399-424

Birringer, R., Gleiter, H., Klein, H.-P., Marquardt, P. (1984). "Nanocrystalline materials-an approach to a novel solid structure with gas-like disorder?" Physics Letters A 102A: 365.

Birringer, R., Hahn, H., Hofler, H., Karch, J.; Gleiter, H..(1988), Diffusion and low temperature deformation by diffusional creep of nanocrystalline materials. Diffusion and Defect Data - Solid State Data, Part A (Defect and Diffusion Forum), 1988. A59: 17

Coble, R. L. (1963). "A Model for Boundary Diffusion Controlled Creep in Polycrystalline Materials." Journal of Applied Physics 34(6): 1679-1682.

Conrad, H. and J. Narayan (2000). "On the grain size softening in nanocrystalline materials." Scripta materialia 42: 1025-1030.

Cheng, S., Ma, E., Wang, Y.M., Kecskes, L.J., Youssef, K.M., Koch, C.C., Trociewitz, U.P., Han, K. (2005). " Tensile properties of in situ consolidated nanocrystalline Cu". Acta Materialia 53: 1521-1533.

Cheong, K.S., Busso, E.P., Arsenlis, A. (2005). "A study of microstructural length scale effects on the behaviour of FCC polycrystals using strain gradient concepts." International Journal of Plasticity 21: 1797-1814.

Cherkaoui, M., Sun, Q., Song, G.Q. (2000). "Micromechanics modeling of composite with ductile matrix and shape memory alloy reinforcement." International journal of solids and structures 37: 1577-1594.

Gao, H., Y. Huang, Nix, W.D, Hutchinson, J.W. (1999). "Mechanism based strain gradient plasticity II Analysis." Journal of the Mechanics and Physics of Solids 47: 1239-1263.

Huang, Y. Gao, H.,Nix, W.D, Hutchinson, J.W. (2000). "Mechanism based strain gradient plasticity II Analysis." Journal of the Mechanics and Physics of Solids 48: 99-128.

Gleiter, H. and P. Marquardt (1984), Nanocrystalline structures-an approach to new materials? Zeitschrift fur Metallkunde, 75: 263.

Gleiter, H. (1991). "Nanocrystalline solids". Journal of Applied Crystallography 24: 79-90.

Gleiter, H. (2000). "Nanostructured materials: Basic concepts and microstructure." Acta materialia 48: 1-29.

Gu, Z., Wang, K., Wei, J., Li, C. Jia, Y., Wang, Z., Luo, J., Wu, D. (2006). "Tensile properties of ultrathin double-walled carbon nanotube membranes". Carbon 44: 3315-3319.

Hall, E. O. (1951). "The deformation and aging of mild steel." Proceedings of the Physical society of London B64: 747-753.

Khan, A. S., H. Zhang, et al. (2000). "Mechanical response and modeling of fully compacted nanocrystalline iron and copper." International journal of plasticity 16: 1459-1476.

Kim, H. S., Y. Estrin, Bush, M.B. (2000). "Plastic deformation behaviour of fine grained materials." Acta materialia 48: 493-504.

King, W. P., Kenny, T. W., Goodson, K. E., Cross, G., Despont, M., Durig, U., Rothuizen, H.,Binnig, G. K.Vettiger, P. (2001). "Atomic force microscope cantilevers for combined thermomechanical data writing and reading". Applied Physics Letters 78: 3000-2.

King, W. P. and K. E. Goodson (2002). "Thermal Writing and Nanoimaging With a Heated Atomic Force Microscope Cantilever." Journal of Heat Transfer 124(4): 597.

Koch, C.C. (2007). "Structural nanocrystalline materials: an overview". Journal of Materials Science 42:1403–1414.

Kocks, U. F., U. F. Argon, et al. (1975). Progress in materials science 19: 110-170.

Kocks, U. F. and H. Mecking (2003). "Physics and phenomenology of strain hardening." Progress in materials science 48: 171-273.

Kuhlman-Wilsdorf, D. (1962). "A new theory of work hardening". Transactions of the Metallurgical Society of AIME 224: 1047.

Kumar, K.S.,Suresh, S., Chisolm, M.F., Horton, J.A., Wang, P. (2003). "Deformation of electrodeposited nanocrystalline nickel". Acta materialia 51: 387-405.

Li, J. C. M. (1963). "Petch relation and grain boundary sources". Transactions of the metallurgical society of AIME 227: 239-247.

Lu, J., Zhang, L. (2006). "Analysis of localized failure of single-wall carbon nanotubes". Computational Materials Science 35:432-441.

McDowell, D. L. (2000). "Modeling and experiments in plasticity". International Journal of Solids and Structures 37: 293-309.

Moelle, C. H. and H. J. Fecht (1995). "Thermal stability of nanocrystalline iron prepared by mechanical attrition." Nanostructured Materials 6: 421-424.

Murr, L.E., Venkatesh, E. (1978). "Contrast phenomena and indentification of grain boundary ledges". Metallography 11:61-79.

Murr, L. E. (1981). "Strain induced dislocation emission from grain boundaries in stainless steel." Materials science and engineering 51: 71-79.

Nye, J.F. (1953). "Some geometric relations in dislocated crystals". Acta metallurgica 1: 153-162.

Palumbo G, Gonzalez G, Brennenstuhl AM, Erb U, Shmayda W, Lichtenberger PC (1997). "In-situ nuclear steam generator repair using electrodeposited nanocrystalline nickel". NanoStructured Materials 9:737-746.

Petch, N. J. (1953). "The cleavage strength of polycrystals". Journal of iron steel Inst. 174: 25-28.

Schuh, C. A., T. G. Nieh, et al. (2002). "Hall Petch Breakdown manifested in abrasive wear resistance of nanocrystalline nickel". Scripta materialia 46: 735-740.

Schumacher, S., et al. (1989), Diffusion of silver nanocrystalline copper between 303 and 373 K. Acta Metallurgica 37: 2485.

Taylor, G. I. (1934). "The mechanism of plastic deformation of crystals: Part 1 theoretical." Proceedings of the Royal Society A CXLV: 362-387.

Uyeda, R. (1991)." Studies of ultrafine particles in Japan: crystallography. Methods of preparation and technological applications". Progress in Materials Science 35:1-96.

Van Swygenhoven, H., A. Caro, et al. (2001). "Grain boundary structure and its influence on plastic deformation of polycrystalline FCC metals at the nanoscale: a molecular dynamics study." Scripta materialia 44: 1513-1516.

Venkatesh, E.S., Murr, L.E. (1978). "The influence of grain boundary ledge density on the flow stress in Nickel". Materials science and engineering 33: 69-80.

Vogel, P. D. (2005). "Nature's design of nanomotors." European Journal of Pharmaceutics and Biopharmaceutics 60(2): 267-277.

Weertman, J. R. (1993). "Hall-Petch strengthening in nanocrystalline metals". Materials Science and Engineering A 166: 161-167.

Wei Q, Ramesh KT, Ma E, Kesckes LJ, Dowding RJ, Kazykanov VU, Valiev RZ (2005)." Plastic flow localization in bulk tungsten with ultrafine microstructure". Applied Physics Letters 86:101907 1-3.

Youssef, K. M.,Scattergood, R. O., Murty, K. L., Koch, C. C. (2004). "Ultratough nanocrystalline copper with a narrow grain size distribution". Applied Physics Letters 6: 929-931.

Zhou, M. (2002). "The virial stress is not a measure of mechanical stress". Materials Research Society Symposium – Proceedings, San Francisco, CA, United States 731: 59-70

Zhou, M. (2003). "Theoretical interpretation of the virial stress". Collection of Technical Papers - AIAA/ASME/ASCE/AHS/ASC Structures, Structural Dynamics and Materials Conference, Norfolk, VA, United States 5: 3368-3383.

CHAPTER 2

STATE OF THE ART

This literature review chapter is divided in two sections. The first part of this chapter is dedicated to conventional materials. The fundamentals of thermal activation, dislocation storage and annihilation will be recalled. The second part of this chapter is dedicated to NC materials. First, a description of the fabrication processes and resulting materials will be presented (e.g., inert gas condensation, ball milling, severe plastic deformation and electrodeposition). Second, the microstructure of NC materials composed of grain interiors, grain boundaries and triple junctions will be discussed. Third, the mechanical response and properties of NC materials will be presented from an experimental standpoint. Considering the importance of grain boundaries, a subsection will be dedicated to the presentation of existing grain boundary models based on dislocation and disclination unit models. This subsection is followed by a detailed presentation of the several mechanisms, such as (e.g., Nabarro Herrin creep, grain boundary dislocation emission and so forth) that have been suggested to actively contribute to the viscoplastic deformation of NC. This chapter is concluded with a discussion resulting in a proposed deformation mechanisms map.

Conventional materials

The elasto-viscoplastic response of conventional materials has been subject to in depth investigations since the early 1900s (W. 1898; Loss 1901; Nishikawa et al. 1920). Substantial advances were made in the field, (e.g., dislocation dynamics and phase field

23

theories) and contemporaneous models can now predict texture evolution and local dislocation activity on active slip systems.

Therefore, this section does not intend to establish a detailed review on conventional materials, but solely to briefly recall the plastic deformation mechanisms active at room temperature and in the quasistatic regime.

During elastic deformation, conventional materials do not sustain any irreversible motion of atoms. This results from the fact that inter-atomic bonds are not broken in the elastic regime. Hence, the system (e.g., sample) can be restored to its initially stable configuration. On the contrary, plastic deformation engenders irreversible microstructural changes within the material. These irreversibilities are engendered by the simultaneous contribution of several mechanisms which contributions can depend on temperature, strain rate etc. Typically the plastic regime is graphically represented as the succession of four stages. While stage I is typically observed in single crystals, stage II and III are associated with athermal hardening and dynamic recovery, respectively. Stage IV is typically observed after large strains are imposed to the material. As discussed in review by Kocks and Mecking (2003), the activity of each mechanism dominating work hardening evolves during deformation.

Locally, in the quasi-static regime and at room temperature, plastic deformation results from the motion of dislocations on active slip systems. The interaction between mobile dislocations and other mobile and sessile dislocations drives the local state of stress and influences the resulting microstructure. For example, in F.C.C. materials,

mobile dislocations are typically stopped at grain boundaries which are regions of high

density of geometrically necessary dislocations (Zhonghao et al. 1995). This leads to a

pile-up of dislocations leading to an increase in the stress required to activate the glide of

dislocations. Prior to presenting the mechanisms involved in work hardening theories, let

us discuss the fundamentals of the modeling of thermally activated mechanisms such as

dislocation glide.

Thermal activation

Mathematically, thermally activated mechanisms are described as the product of a

fluctuation term and of a term describing the average effect of the mechanism studied at

the microscopic scale (Kocks et al. 1975). Hence, one can write:

$$\dot{\gamma} = \gamma_0 P_t \tag{2.1}$$

Here $\dot{\gamma}$, γ_0 and P_t represent the strain rate engendered by the event considered (dislocation

glide for example), the average strain engendered by the event and its activation rate,

respectively. Let us note that the inverse event (dislocation motion in the opposite

direction in this case) is not taken into account in equation (2.1).

The activation rate P_t depends on the frequency of thermal fluctuation. In the case

of dislocation glide, it can be considered as the product of the frequency at which a

dislocation attempts to go through obstacles (here lattice atoms) by the probability that a

fluctuation in the dislocation energy is greater than a critical value for a glide event to be

successful.

Two different approaches can be used to evaluate the frequency factor: (1) the

kinematic approach and, (2) the statistical approach (Kocks et al. 1975). In the kinematic

approach the reaction paths, that is the different positions of a dislocation during its

motion, is supposed known and the frequency in the direction of the reaction coordinate

is evaluated, while in the statistical approach all reactions paths are considered.

The probability of success, p, is given by a Boltzmann distribution.

Fundamentally, it represents the probability that the energy fluctuation in the system

considered (e.g. the dislocation) is superior to a given value ΔG, representing the

activation enthalpy. Hence, one obtains the following Arrhenius law:

$$p = \exp\left(-\frac{\Delta G}{kT}\right) \tag{2.2}$$

'p', 'ΔG', 'k''T' represent the probability of success of the event, the activation

enthalpy, Boltzmann's constant and the temperature, respectively. It can be noted that at a

given value of the activation enthalpy an increase in the temperature leads to an increase

in the probability of success.

Let us take the example of a dislocation glide event. A schematic of a dislocation

glide resistance diagram is presented in Figure 2.1. It presents the product of the shear

stress by the Burger's vector as a function of the distance traveled by a dislocation. In

other words Figure 2.1 represents the evolution of the state of stress perceived by the

dislocation during its motion. The state of stress is due, among other, to the Nabarro

Peierls forces imposed by the atoms surrounding the dislocation. Dislocation glide is successful if a dislocation moves from a stable configuration, denoted 'a', to an unstable configuration with positive driving force. This configuration is noted 'b' in Figure 2.1. When configuration 'b' is reached, the dislocation can continue its motion without external energy input. Finally let us note that Figure 2.1, represents a one-dimensional dislocation glide resistance diagram with know reaction coordinate.

Let us now discuss the signification of the free enthalpy of activation. A work input, denoted ΔW, is required to move a dislocation from state 'a' to state 'b'. If the stress applied on the dislocation is smaller than the maximum stress on the dislocation glide resistance diagram, dislocation glide cannot occur without additional energy input. This required energy input, defining the activation enthalpy, is engendered by thermal fluctuation. As recalled by Kocks and Ashby (1975), the definition of the activation enthalpy in mechanics is equivalent to the one in thermodynamics solely when no other work terms are present.
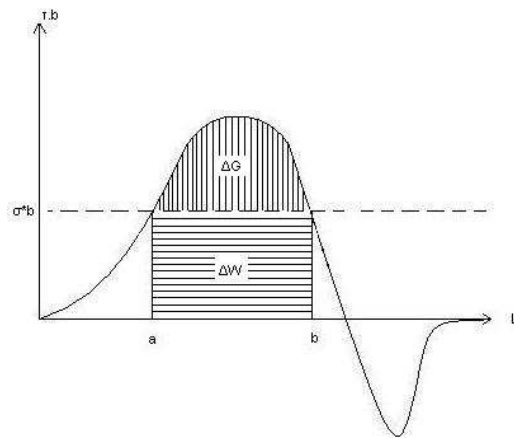
Figure 2.1: Schematic of a dislocation glide resistance diagram.

Since the evaluation of the activation enthalpy is rather complex, empirical laws of the
following form are typically used:

$$\Delta G \approx F_0 \left(1 - \left(\frac{\sigma}{\hat{\sigma}} \right)^r \right)^l$$

(2.3)

Here F_0 represents Helmholtz free energy. Consequently, it represents the energy

necessary for a dislocation to glide at zero Kelvin. In the case of dislocation glide,

$\hat{\sigma}$ corresponds to the maximum stress reached in the dislocation glide resistance diagram

and the parameters r an l describe its shapes. Also, these two parameters are bounded as

follows:

$$0 < r < 1 \quad \text{and} \quad 1 < l < 2$$

(2.4)

In the case of dislocation glide, a power law form is often preferred to the exponential

expression of the probability of successful glide (Kocks 1976; Estrin et al. 1984; Estrin

1998; Kocks et al. 2003). $\hat{\sigma}$ depends on the store dislocation density. This stress

corresponds to the yield stress at zero Kelvin and is typically given by Taylor's relation

(1934) and written as follows:

$$\hat{\sigma} = \alpha b M G \sqrt{\rho}$$

(2.5)

Here b, M, G, α and ρ represent Burger's vector, the Taylor's factor, the shear modulus,

a numerical constant and the stored (immobile) dislocation density. Let us note that

equation (2.5) holds in the case where only dislocations-dislocations interactions are

considered.

More refined models make the distinction between geometrically necessary

dislocations and statistically stored dislocations (Ashby 1970) and their edge and screw

components (Cheong et al. 2004; Cermelli and Gurtin 2002). However, independently of

the approach selected (e.g., crystal plasticity, work hardening models, strain gradient

plasticity), the stress-strain relation depends on the evolution of the dislocation density. A

modeling approach based on strain gradient crystal plasticity will be presented in Chapter

6.

The evolution of the dislocation density with strain results from the evolution of

the contribution of two antagonists phenomena: (1) dislocation storage and (2)

dislocation annihilation. These two mechanisms are briefly presented in the next two

subsections.

Dislocation storage

Dislocation storage is described in a strictly statistical manner. Also, experiments

have shown that except for the temperature dependence of the elastic constants,

dislocation storage is an athermal process. This was extensively discussed in review by

Nes (1997).

The increase in the material's strength with increasing strain is thus explained by the fact that dislocation storage results in a decrease in the mean free path of dislocations. Precisely, mobile dislocation can become sessile when they meet obstacles such as other stored dislocations and grain boundaries, which in the case of conventional materials have a passive role of barrier to the dislocation motion. Considering equation (2.1.5), one can conclude that an increase in the stored dislocation density leads to an increase in the stress required to engender plastic flow. The link between the dislocation density and their mean free path is obtained via the use of the principle of similitude introduced by Kuhlman-Wilsdorf (Kuhlman-Wilsdorf 1962).

Let us note that the less refined approach, in terms of description of the type of 1-dimensional defects, do not make the distinction between the type of dislocations (e.g., statistically stored dislocations, geometrically necessary dislocations…). This is the case of the first approach developed by Kocks and Mecking (Kocks 1976; Mecking et al. 1981) and their subsequent evolutions (Estrin et al. 1984; Estrin 1998; Kim et al. 2001; Kocks et al. 2003). Moreover, these approaches cannot successfully predict the Hall Petch law while models based on strain gradient can. Finally, the predicted mean free path is usually 10 to 30 times larger than that experimentally measured.

Dislocation annihilation

Although the mechanism of dislocation annihilation was discovered some 50 years ago with the work of Stokes and Cottrel (Stokes et al. 1954), a consensus has not yet been reached regarding its expression (Nes 1997; Kocks and Mecking 2003; Cheong et al. 2004). The annihilation of stored dislocations is a thermally activated mechanism

occurring at recovery sites when edge or screw dislocations of opposite signs meet. A

schematic presenting the process of annihilation of edge and screw dislocations is

presented in Figure 2.2 (a) and (b), respectively (Nes 1997). In Figure 2.2 (a) dislocation

annihilations occurs when two edge dislocations, denoted E_1 and E_2, of opposite signs

meet. The average distance between these dislocations is proportional to the inverse of

the square root of the dislocation density, denoted ρ. Figure 2.2 (b) shows the

annihilation of screw dislocations via cross slip. Note here that the recovery mechanisms

discussed in the above represent the simplest "picture" of dynamic recovery.
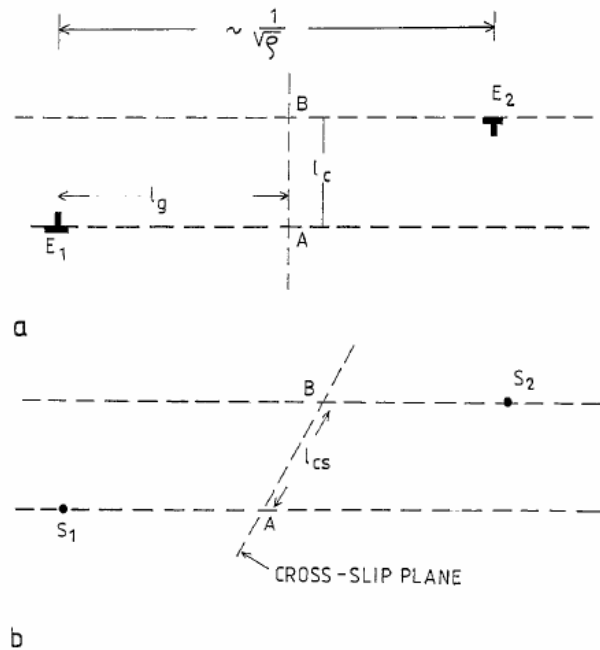
Extracted from Nes (1997)

Figure 2.2: Schematic of the dislocation annihilation mechanism (a) glide and slip of an

edge dislocation and (b) cross-slip of a screw dislocation.

31

Several different models describing dynamic recovery were proposed. The type of mechanism controlling the annihilation process (e.g. slip, cross slip, double cross slip) is still subject to debate. For example, Nes (1997) describes dislocation annihilation via the thermally activated jump of screw dislocations while Kock and Mecking (2003) proposed a model based on the rearrangement of mobile dislocations. Let us note that the previously mentioned authors have proposed several other models for dynamic recovery in the past (Kocks 1976).

Nanocrystalline materials

In what follows the nomenclature developed by Kumar et al. (2003) will be used. Hence, polycrystalline materials with an average grain size ranging from 1 micron down to 100 nm will be referred to as ultrafine (UF) grained materials while the terminology NC materials will apply to polycrystalline materials with grain size smaller than ~100nm.

As will be shown later throughout this chapter, in both the UF and NC regime, a decrease in the grain size leads to substantial increase in the volume fraction of grain boundaries and triple junctions. Recall that, as mentioned in Chapter 1, the abnormal response of NC materials (e.g., Hall-Petch breakdown, strain rate sensitivity, plastic response) cannot be considered to result entirely from a change in the microstructure of grain boundaries. Hence, it is reasonable to suppose that in the NC regime, the relative contribution of dislocation glide, which dominates the response of conventional materials, will decrease to the benefit of one, or more, other mechanisms.

Several mechanisms have been suggested to actively contribute to the viscoplastic deformation of NC materials. First, the activity of diffusion based mechanisms, typically active at high temperatures in the case of conventional materials, was suggested. Second, solid motion of grains via rotation and sliding (accommodated or not by vacancy diffusion) has also been investigated. Third, it was also suggested that a change in the role of grain boundaries, which play a passive role of barrier to dislocation motion in the case of conventional materials, could occur in the NC range. Indeed in the UF and NC regime, grain boundaries may act as dislocation sources and sinks.

This section focuses on the different fabrication processes and resulting microstructures of UF and NC materials. A subsection will be dedicated to grain boundary modeling. Then, this chapter will be ended with a literature review on experimental studies, numerical and theoretical models and on the different mechanisms sited in the above.

Fabrication processes

One of the main difficulties in confronting model predictions to experimental data stands from the lack of reproducibility of experiments which prevents the validation of models via rigorous statistical analysis (e.g., goodness of fit, hypothesis testing etc.). This limitation results partially from the complexity of the fabrications processes available to synthesize bulk NC samples. Moreover, the microstructure of the as-processed material (e.g., grain size distribution, texture, average grain boundary misorientation, amount of vacancies, voids, cracks, twins and so forth) is highly dependent on the fabrication process and on the experimental set-up. For example,

studies by Ebrahimi et al. (2006) on NC Ni fabricated via electrodeposition revealed that the grain size distribution of electrodeposited samples is generally wider than that of samples prepared via inert gas condensation.

Obviously the difference in microstructures, resulting from the use of a particular fabrication process, will result in differences in the mechanical response of the samples. In the case of NC materials, these differences can be very large. Also, so far samples are mostly fabricated in academic laboratories which all have their own "recipe". Consequently, two samples fabricated with the same procedure but in different laboratories can have different microstructures and inevitably different responses. Let us provide a couple examples to demonstrate the large variations in the responses of samples that can result from the use of different processes. Sanders et al. (1997a) report a yield stress of 365 MPa. and a 3% maximum elongation on Cu samples produced by inert gas condensation with nominal grain size of 26 nm while tests on 30 nm grained Cu samples produced by surface mechanical attrition treatment (similar to the ball milling process) exhibit the same limited ductility but a yield stress in the order of 760MPa (Wang et al. 2003). Moreover, samples with similar grain size but produced by cryomilling (ball milling in a liquid nitrogen environment) exhibit a high yield stress of 688 MPa. and a much higher maximum elongation in the order of 12% (Cheng et al. 2005).

From the large differences in the experimentally measured responses, the reader can assess of the difficulty in validating theoretical models. Let us note that over the past decade substantial progress was made in the fabrication of NC materials. This will be discussed later throughout this chapter. The quality of samples has greatly improved and

the variation in measured data has significantly decreased (for a similar fabrication process). With the above discussion, it appears critical to have a solid understanding of the various fabrication processes and of the resulting microstructures.

In general, the processing routes for NC materials, presented in Figure 2.3, can be sorted in two categories (Koch 2007; Meyers et al. 2006): (1) one-step approaches and, (2) two-steps approaches. One-step approach directly lead to a NC sample and does not require any compaction step while the two-step approach consists first of synthesizing nanoparticules and then compacting the resulting powder in order to obtain a bulk NC sample. The most frequently used one-step processes are severe plastic deformation, which encompasses a large family of processes, and electrodeposition. Within the family of severe plastic, the most often used techniques are equal channel angular pressing (ECAP) and high pressure torsion (HPT). As mentioned in the above, the first step composing 2-steps processing routes is the synthesis of nanoparticules which can be achieved via solid, vapor, liquid or mixed routes. Several different techniques, presented in Figure 2.3 can be used for each synthesis route. The most used techniques, to be presented in this chapter are ball milling, which is a solid processing route and physical vapor deposition.

Let us first present Physical vapor deposition and mechanical alloying (two-step processes). Nanoparticules synthesis will be presented first. Then a general presentation on compaction will be given.
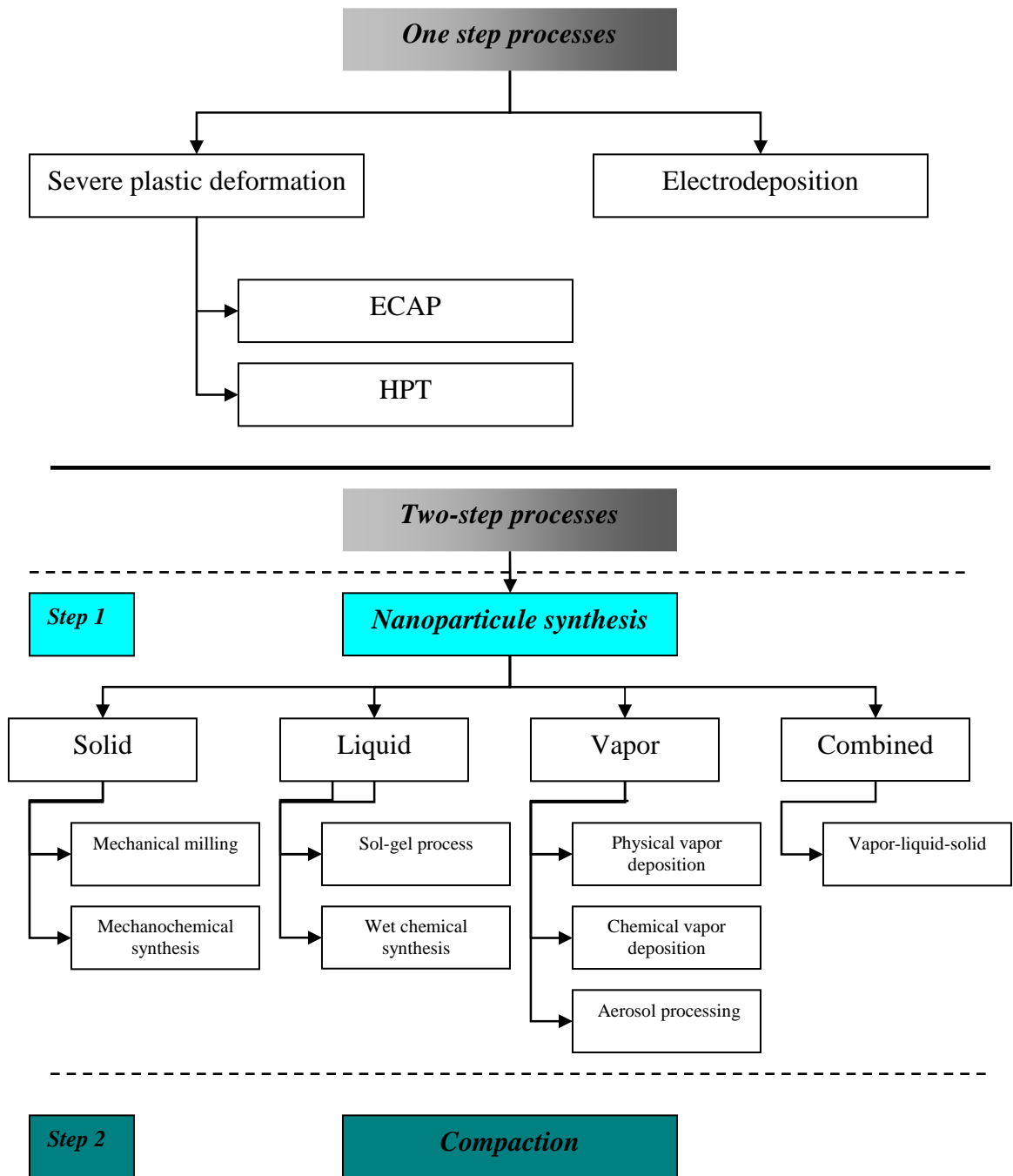
Figure 2.3: NC materials processing routes.

<u>Physical vapor deposition</u>

Inert gas condensation (IGC) is the most widely used physical vapor deposition process. It was one of the first methods which were developed, or more precisely adapted to the fabrication of bulk NC samples, in pioneering work by Gleiter. Indeed as discussed in extensive review by Uyeda (1991), the evaporation of a metallic source was already mastered in the early 1960s. For example, Morimoto and Sakata (1962) synthesized F.C.C. metals nanoparticules (~3 nm in diameter) via evaporation on a carbon thin film. IGC, which is a bottom up approach (the sample is created from the assembly of particles), is a rather complex process which fundamentals are recalled in what follows. A schematic of an IGC apparatus is presented in Figure 2.4, extracted from Morris (1998). The process of condensation of vaporized metals in contact with an inert gas can be divided in three steps. First, a metallic gas is formed in a vacuum chamber via the evaporation of a metallic source. Second, the metallic gas particles will condense in contact with a cold inert gas, such as Ar or He, and form atom clusters. These clusters are then transported on a cold finger via convection. Third, the clusters will grow on the cold finger and will then be collected simply by scrapping the cold finger. The following step, discussed later in this section, is obviously the compaction step.
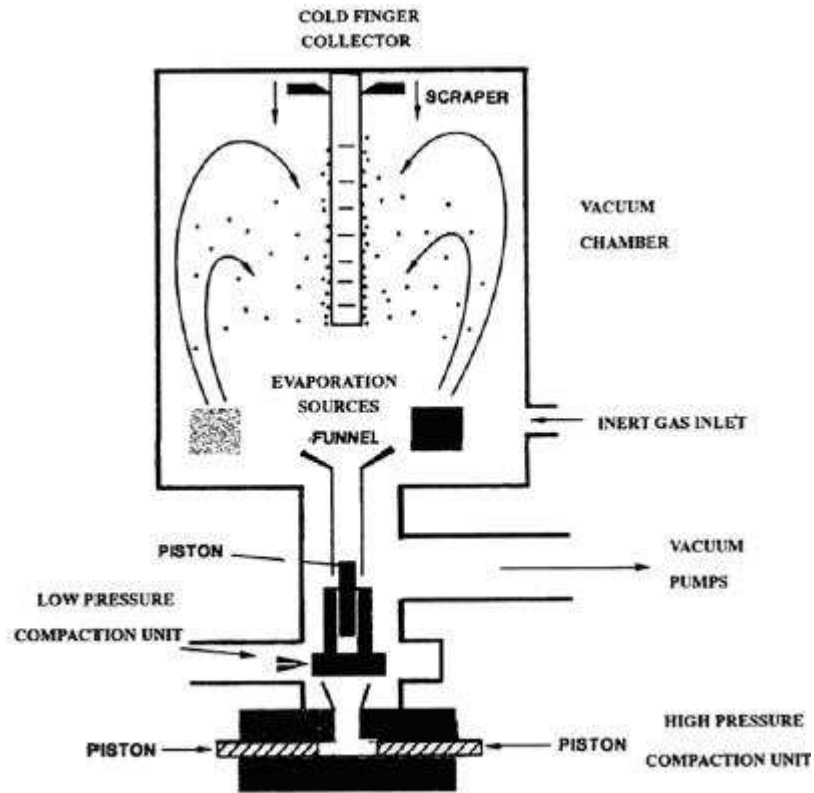
Figure 2.4: Schematic of an IGC device.

Let us now discuss the three steps involved in IGC (e.g. 1: Evaporation of the metal source, 2: condensation and, 3: growth and collection). The evaporation of a metallic source can be understood with simple thermodynamics. Indeed, increasing the temperature of a metal at a given pressure will result in the evaporation of the source. Several techniques can be used to perform this operation (e.g., resistive heating, ion sputtering, plasma/laser heating, radio-frequency heating, and ion beam heating). The simplest technique is resistive heating; an electrical current is used to heat a resistive coil in which the source is placed (see Figure 2.5, extracted from Uyeda 1991). Resistive

38

heating is usually limited by the number of evaporation cycle which can be performed (5 to 10 cycles at most). This operation is performed in an inert gas atmosphere and pressure and temperature control the particle size.
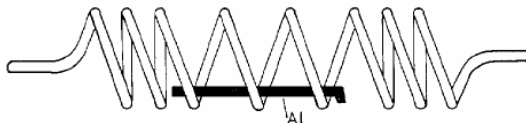
Figure 2.5: Resistive heating evaporation source.

Evaporation can also be performed via the method of Grandvquist and Buhram (1976) which original apparatus is shown in Figure 2.6. This method was used to synthesize Fe, Al, Cr, Co, Zn, Ga, Mg and Sn particles. As can be observed in Figure 2.6, the apparatus contains a crucible, in which the metallic source is placed. The crucible is placed near a graphite element which is heated with optical pyrometer. The system is placed in a glass cylinder fitted with water tubes used to cool a Cu plate (used for particle collection). The process is performed at low pressure in the order of 50 Pa, usually in an Ar atmosphere and the resulting particle size distribution is log-normal.
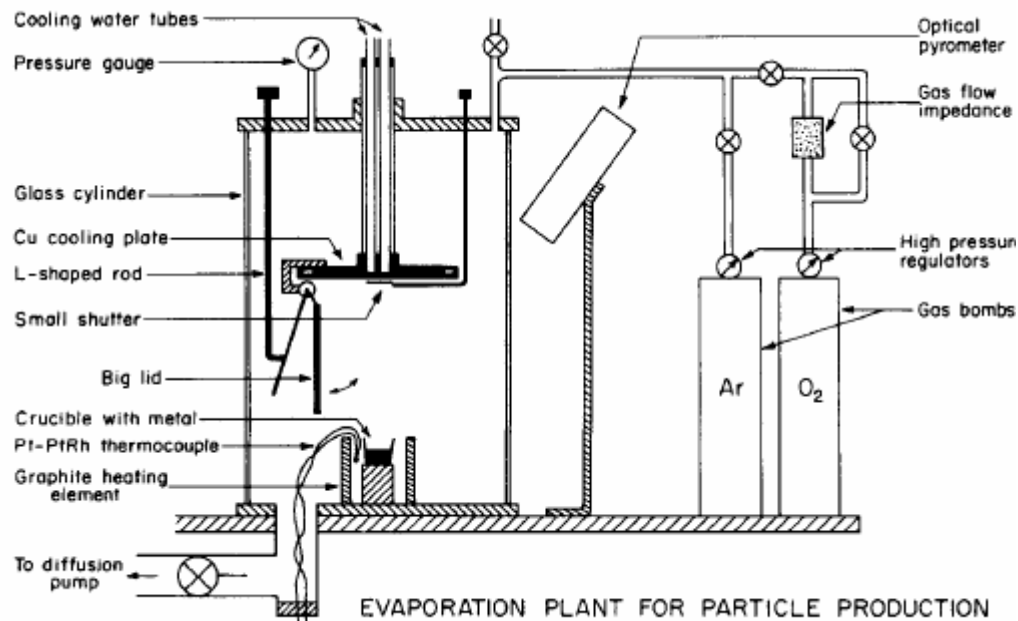
Figure 2.6: Schematic of the apparatus used for evaporation from a crucible.

Second, the vaporized metal will condense in contact with an inert gas. Condensation occurs near the metallic source and results in a supersaturated vapor refered to as "smoke". Each smoke particle usually contains a single crystal.

The shape of the smoke depends on several parameters such as pressure, temperature and gas density. A schematic of a typical smoke is presented in Figure 2.7. The observed smoke is usually composed of four zones (except for the case of vaporization from a crucible). The first zone, referred to as inner zone is composed of particles smaller than that present in the intermediate zone (zone 2). The third zone, referred to as outer zone results. In most cases, the metal smoke can be divided in four zones: (1) the inner zone, (2) the intermediate zone, (3) the outer zone and (4) the vapor zone. However, let us note that in the case of vaporization from a crucible only a single region can be observed. Experimentally (Ohno et al. 1976), it was shown that particles in

the inner zone are smaller than that of the intermediate zone (located between the inner front and the outer zone). This is presumably due to the fact that the particle growth mechanism is assisted by the diffusion from the vapor zone below the inner zone. The outer zone is composed of the vapor formed below the inner zone and then convected upwards.
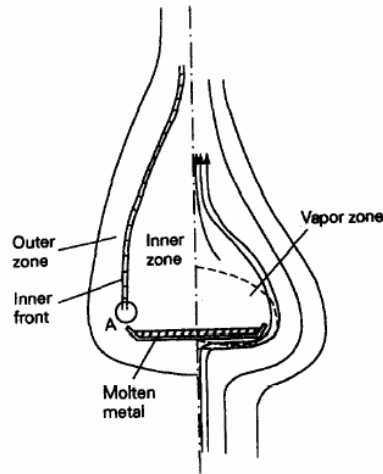
Figure 2.7: Schematic of a typical smoke.

Third, the condensed particles will grow and be transported onto a cold finger (or plate) prior to be collected. Particles can grow via tow different mechanisms corresponding to: (1) the absorption of other particles within the vapor zone and, (2) the coalescence of particles. The latter occurs mainly in the case of small particles. The powder is usually collected by scrapping it from its fixation surface. Let us note that the microstructure of the sample can be affected by the collection step. As shown in Figure 2.8, spiral shapes can result from the collection of the particles with the scrapper. The spirals are composed of nanograins with poor interface bonding (Agnew et al. 2000).
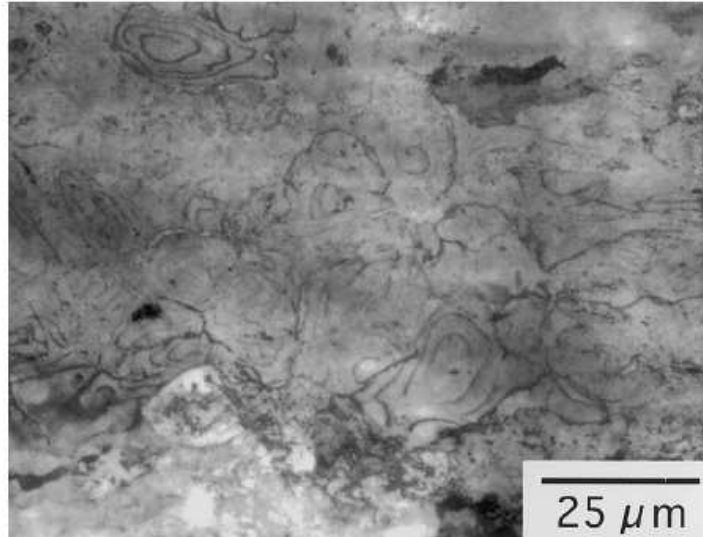
Figure 2.8: Spiral morphology revealed by chemical etching of compacted

nanocrystalline Cu.

Mechanical alloying

Mechanical alloying (MA) is a fairly simple process. It is a "top-down" approach which underlying concept is that an initially coarse microstructure in a powder form (with grain size in the range of several microns) can be refined via cyclic welding and fracture of the powder particles. A variety of mills are currently commercialized such as standard mills, shaker mills, planetary mills and ball mills. These are usually preferred to the other ones. A schematic of a ball mill is presented in Figure 2.9 (for the sake of simplicity, the metallic powder is not represented). The apparatus is composed of a sealed vial containing the powder to be refined. Steel balls are introduced into the vial and the rotating rod is activated at relatively high frequency (e.g. several hundreds of rpm). Energy is provided to the powder particles via contact with the milling balls. This leads to the continuous welding and fracture of the powder particle.
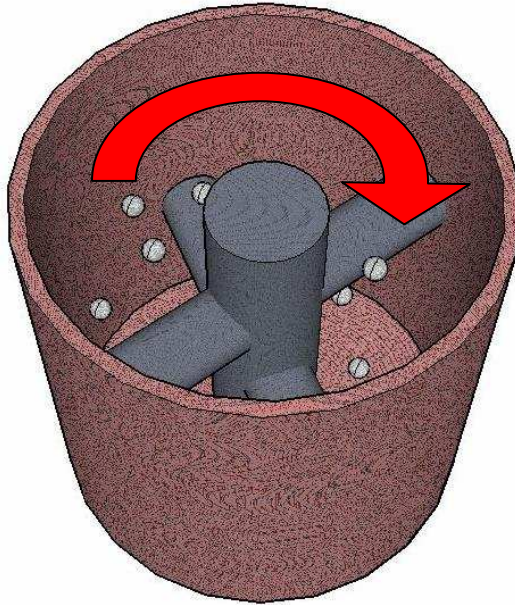
Figure 2.9: Schematic of a ball mill.

Each powder particle can contain several grains. Usually, in the case of cryomilling (milling in a liquid nitrogen environment), the first hours of milling are dominated by the welding of particles while the latest stages are dominated by the fracture of the powder. Hence, during the first hours of milling, the powder particles grow (but the grain size decreases continuously) while in the last hours of milling the particle size decreases. In order to avoid the coalescence of the powder, small quantities of control agents such as stearic acid or methanol are typically added into the vial (Khan, 2000).

The minimum grain size that can be achieved is dependent on several parameters such as the milling time, the type of powder, the ball size, the ball to powder ratio (in the

order of ~ 10 to 1). A plot of the evolution of grain size of a Fe powder with milling time

is presented in Figure 2.10 (extracted from Khan et al. 2000). It can observed that the

grain size significantly decreases prior to reaching a plateau (usually in the range of ~15-

20nm). This minimum grain size is referred to the steady state grain size. Interestingly, it

only shows a weak dependence on the milling temperature.
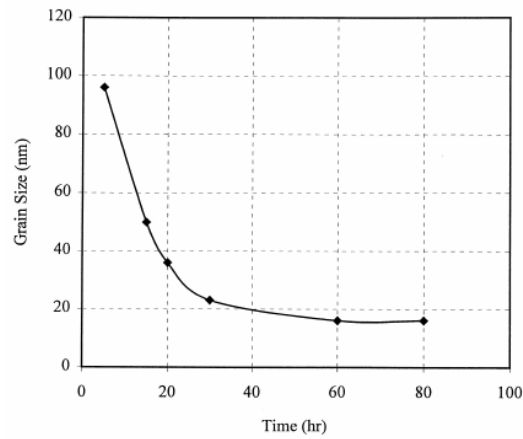
Figure 2.10: Experimental grain size versus milling time measurements for iron
powders.

The refinement in the grains composing the powder particles results from the

large strains applied to the particles when an entrapment event occurs. This leads to

severe plastic deformation within each particle. It was shown via X-ray analysis that

grain refinement occurs via the succession of three distinct stages (Fecht, 1992). First, the

initial powder containing micron-sized deforms plastically via dislocation activity (e.g.

storage, annihilation) localized in shear bands. A TEM bright field image of AIRu

powder after 10 minutes of milling is presented in Figure 2.11. One can observe the

presence of shear bands denoted with black arrows (Fecht, 2006). Second, low angle

grain boundaries are generated from the recombination of dislocation arrangements. In other words an initial grain becomes subdivided in subgrains. The grain boundaries are low misorientation angles type boundaries. Let us note that mechanical twins are usually created in this second stage (Huang et al. 1995). Finally, the third stage corresponds to the reorientation of the subgrains into large angle grain boundaries which leads to a refined microstructure. The stress imposed by the milling balls controls the resulting grain size. The generated grain boundaries are typically well ordered and present some noticeable curvature and strain. Let us note that this does not preclude the presence of less ordered regions within the cluster of grains composing the powder.

Figure 2.11: TEM bright field image of AIRu powder after 10 minutes of milling. The shear bands are shown with arrows.

In recent study aiming at establishing a clear link between the parameters used during the milling procedure (e.g., milling frequency) and the resulting microstructure, it was shown that the obtained microstructure is highly dependent on the shock energy

during an entrapment event (Boystov et al. 2007). Indeed, XRD measurements on NC Cu prepared with a planetary mill revealed that the dislocation density (in the order of $10^{16} \boldsymbol{m}^{-2}$), the ratio of edge to screw dislocations and twin density are non monotonically dependent on the shock energy. For example, the dislocation density increases linearly with shock energy until a critical value is reached at which the dislocation density decreases with an increase in the shock energy.

In order to reduce the contamination of the powder by the milling balls and to increase the rate of refinement, ball milling can be performed in a liquid hydrogen environment at temperatures in the neighborhood of ~70K. This process is referred to as cryomilling and has proved to lead to extremely high quality samples. Indeed considering the high surface to volume ration of nanoparticules, contamination of the powder is a critical issue. Precisely, the control agents and balls can introduce non negligible amount of impurities within the powder. For example, ball milling (with Cr balls) of TiAl powder at room temperature lead to the presence of O (0.77 wt. %), N (0.27 wt.%) and Cr (0.0021 wt. %) after 25 hours of milling (Bhattacharya et al. 2004).

As will be discussed in a subsection dedicated to the mechanical response of NC materials, one of the main difficulties consists of fabricating a material that reaches an acceptable strength/ductility compromise. Recently, it was shown that the cyclic combination of room temperature milling and cryomilling can lead to materials with low defect content, high strength, ductility larger than 10% and a narrow grain size distribution (Youssef et al. 2004). The resulting grain size distribution is presented in

Figure 2.12.
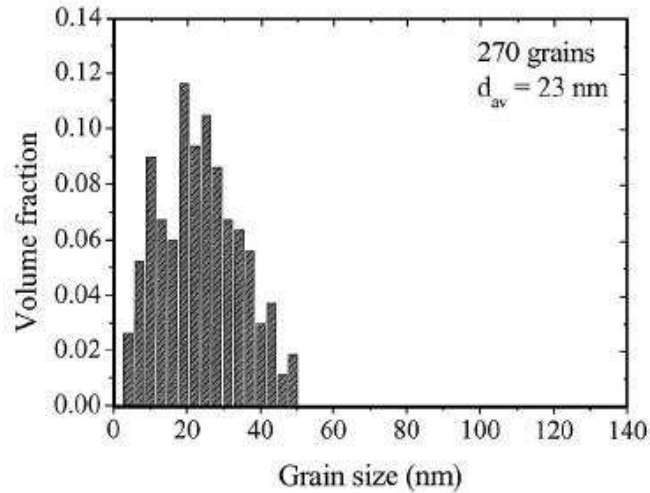
Figure 2.12: grain size distribution obtained after mixed cryomilling and room

temperature milling of Cu on a count of 270 grains.

Powder consolidation

Let us now briefly present the different consolidation techniques used to compact

powder nanoparticules. Several compaction routes can be used, such as cold compaction,

warm compaction, hot isostatic pressing (also referred to as HIPing) and sintering. The

objective is obviously to obtain a sample with maximum density and optimal particle

bonding that retains all of its nanofeatures. Let us note that the theoretical density cannot

be achieved since the density of grain boundaries is smaller than that of grain cores.

Indeed, grain boundaries typically exhibit excess volume (in the form of vacancies or

vacancy clusters), or as more appropriately termed by J.C.M. Li porosity (2007), which

prevent the consolidation of NC materials to the theoretical density of a crystal lattice.

The porosity of grain boundaries was suggested in transmission electron microscopy on

NC $Ni_{33}Zr_{67}$ produced by crystallization (Liu et al 1997). Also, Li et al. (1993) observed

47

the presence of nanovoids in grain boundaries on a NC Pd sample produced by IGC. The

consolidation of NC powders has greatly improved in the past decades and densities as

high as 99% can now be obtained (Jia et al. 2003). Moreover, it is desired to obtain a

good control on the grain size distribution. Indeed, it was shown in recent model by Zhu

et al. (2006) that the variance of the grain size distribution can affect the ultimate stress.

Precisely, supposing a log-normal distribution of the grain size, it was shown that the

ultimate stress of Ni could decrease by up to 25% when the variance is increased from 50

to 200.

Let us now briefly discuss three possible compaction procedures: (1) cold

compaction, (2) sintering and (3) hot isostatic pressing. Cold compaction simply consists

of submitting a powder placed in a die to high pressures (in the order of ~3GPa) at room

temperature or slightly above room temperature (T~300 C). The compact obtained is

usually refered to as Green compact and its properties depend on the initial powder

density, the die's geometry, and the pressure (Gutmanas 1990). The consolidation of the

powder results from the activity of viscoplastic deformation mechanisms such as grain

boundary sliding and vacancy diffusion (Gutmanas et al. 1994). Hence an increase in the

temperature facilitates the activity of these mechanisms resulting in higher densities.

However, since nanoparticules exhibit low thermal stability, increasing the temperature

may lead to a loss of the nanofeatures. Indeed, as discussed by Song et al. (2006), while

in the case of conventional materials grain growth is typically modeled with a constant

grain growth exponent (~ 2), NC materials exhibit time dependent grain growth exponent

ranging from to 2-4 which is representative or rapid grain growth above a critical

temperature.

Second, sintering corresponds to the application of high temperatures (below the melting point) to the powder without pressure. Sintering is usually preceded by a cold compaction step at low pressure leading to a Green compact with density in the neighborhood of 60-80% of the theoretical density (Gutmanas 1990). Typically sintering leads to a relative loss of the nanofeatures which results from the low temperature stability of nanoparticules. Hence, this compaction route is less often used than cold compaction or HIPing.

Hot isostatic pressing (HIPing) can be regarded as a compromise between cold compaction and sintering since it consists of applying moderate temperatures and isostatic pressure simultaneously to the compact. The applied temperatures are typically lower than that in sintering. Hence, grain growth is less prominent during the consolidation process. However, large grains in NC samples consolidated by HIPing are often observed (Tang et al. 2005). For example, Hayes et al. (2004) report a bimodal distribution on NC Al produced by cryomilling followed by HIPing.

Let us now present two one-step processes. First, severe plastic deformation will be exposed. Precisely, HPT and ECAP will be presented. Then, NC materials synthesis via electrodeposition will briefly be presented.

Severe plastic deformation

Severe plastic deformation procedures are top-down approaches that simply

consist of applying large strains to a bulk sample with conventional grain size in order to refine its microstructure. These approaches present the noticeable advantage of leading to specimens of relatively large dimensions with perfect density and negligible impurity content. Also, since a consolidation step is not necessary, severe plastic deformation is more time efficient. However, the major limitation of this approach is the minimum achievable grain size which typically lies at the border between the UF range and the NC range (d~80-100nm). There are numerous severe plastic deformation based procedures, HPT and ECAP being the most frequently used, that all rely on the core idea that the application of large strains to a sample will create a large number of dislocation which will refine the microstructure after rearrangement into high angle grain boundaries.

ECAP

A schematic of an equal channel angular pressing (ECAP) apparatus is presented in 2.13. ECAP consists of repeatedly extruding a sample bar (circular or squared) into a die containing two channels. Typically, the bar has relatively large dimensions (superior to a cm on each side). The channels form an inner angle ϕ and have an outer angle of curvature denoted by ψ (Langdon and Valiev 2006). While a single pass will lead to a highly inhomogeneous state of deformation within the bar, the application of several passes will homogenize the strain field and will consequently lead to a more homogeneous structure. This was observed in hardness measurements on ECAP processed Al which revealed increasing homogeneity of the Vickers's hardness with increasing number of passes (Xu et al. 2006)

The bar can be rotated in between passes. Each type of rotation defines one of the

four existing routes; (A) the sample is not rotated between passes, (B_A) the sample is alternately alternatively rotated by a +/-90 degree angle about its longitudinal axis (denoted by the green arrow in figure 2b), (B_C) the sample is rotated by a 90 degree rotation angle between passes and the rotation direction is kept constant and (C) the sample is rotated by 180 degree between passes.

The obtained microstructure will clearly depend on the selected processing route. For example, route A and C lead to elongated grains while route Bc leads to more equiaxed grains (Xu et al. 2006). However, as discussed in review by Langdon and Valiev (2006) the billet velocity has negligible influence on the resulting microstructure.
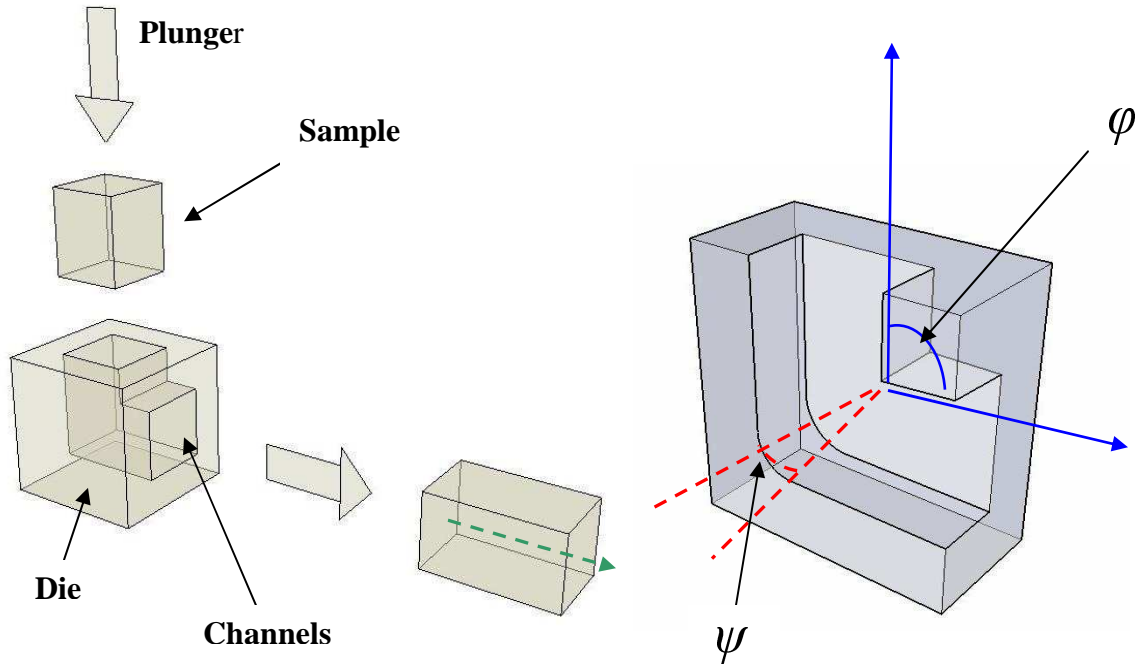
Figure 2.13: (a) Schematic of the ECAP process for a rod (b) cut of the die showing the channels geometry.

The strain imposed following each pass is clearly dependent on the number of passes and on the geometry of the die defined by its inner and outer angles. Using Iwashi.'s model (1996) one can observe a plot of the evolution of the net strain with respect to the inner and outer angle of the die with a number of passes equal to 1 (see Figure 2.14). Among others, one can see that the die angle ϕ has a very large influence on the net strain applied. Typically the die angle is slightly larger than 90 degrees for it has proved to lead to more equiaxed microstructures. Note here that while inner angles smaller than 90 degrees lead to larger strains, these geometries cannot be used since it leads, in most cases, to cracks in the billet (Langdon and Valiev 2006).
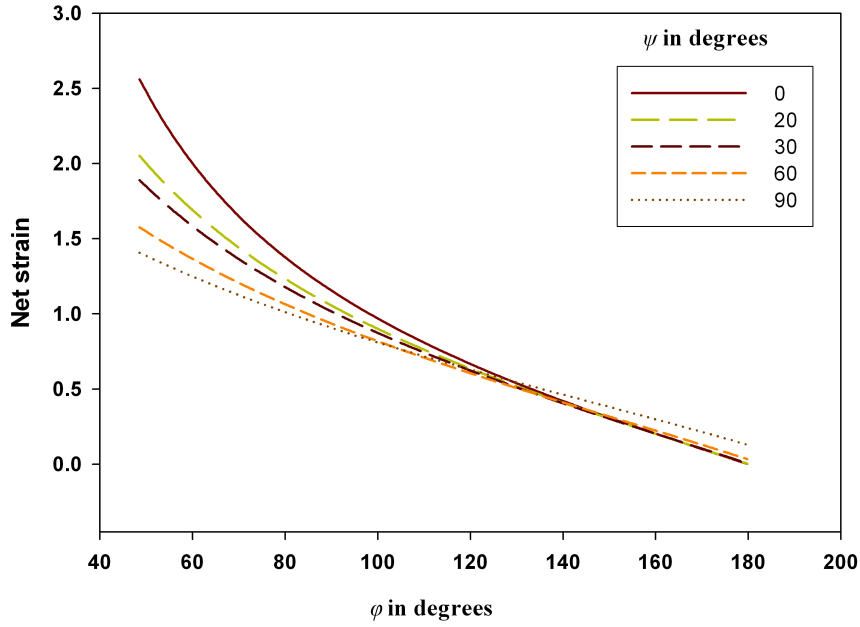
Figure 2.14: Evolution of the equivalent strain after 1 pass as a function of ϕ and ψ.

The details of the grain refinement process are still subject to debate. Though, it is suspected to result from the rearrangement of dislocations. Indeed, in the early stage of deformation, dislocations may create dislocation walls leading to the presence of elongated cells. Additional dislocations are then blocked on the subgrains walls. These cell walls will then break up and form high angle grain boundaries. This hypothesis emerges from the observation of the evolution of the grain boundary misorientation angles on Cu samples after 0, 2, 4 and 8 passes presented in Figure 2.15 (Mishra et al. 2007). While the initial microstructure is mainly composed of high angle grain boundaries, the low-angle-grain-boundary content increases sharply after 2 passes. Subsequent passes lead to an increase in the high-angle-grain-boundary content which suggests that grain refinement occurred respecting the aforementioned hypothesis. Hence,

53

grain refinement in ECAP processed materials would occur in a manner similar to that during ball milling.
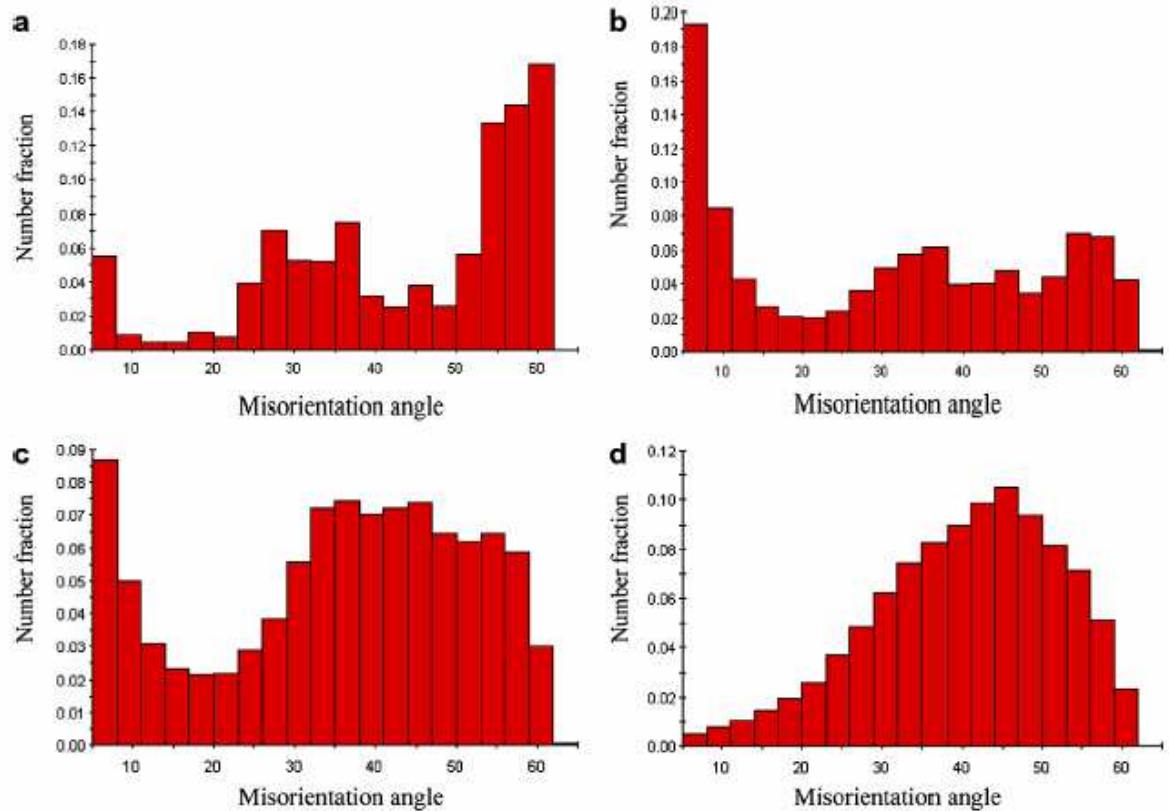
Figure 2.15: Evolution of the grain boundary misorientations angle in ECAP processed Cu sample (a) initial configuration, (b) after 2 passes, (c) after 4 passes and (d) after 8 passes.

HPT

The simultaneous application of high pressure and torsion to a bulk sample also results in the refinement of the initial microstructure. The apparatus, schematically presented in Figure 2.16, is simply composed of a die and of a plunger.

Samples are usually smaller than that processed via ECAP with diameter in the

range of ~2 cm and relatively small thickness in the order of ~0.2-10mm (Lowe and

Valiev 2000). Large strains are imposed to the sample via the application of pressure, in

the order of several GPa, and the application of large twists angles (up to ~5 turns).

Considering the geometry of the apparatus, one would expect to observe highly

inhomogeneous state of strain within the sample.
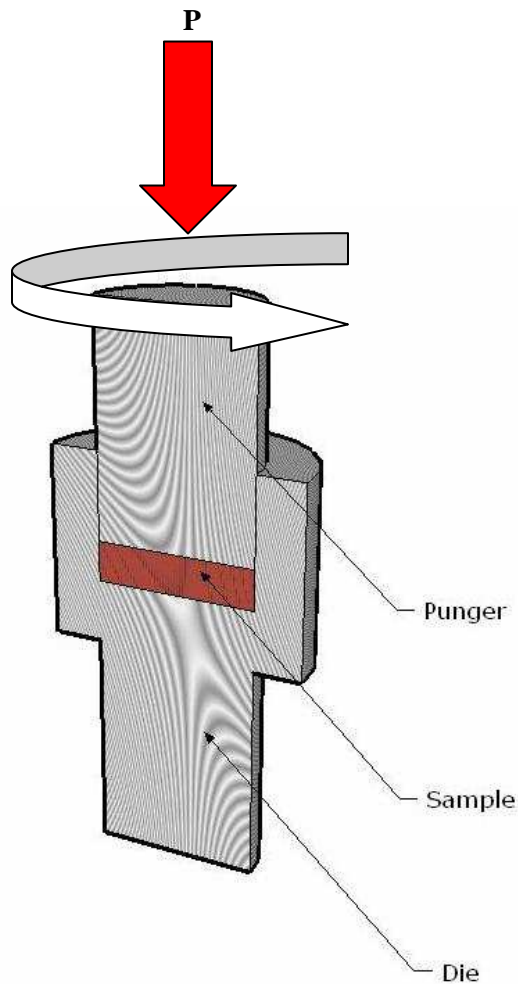
Figure 2.16: Schematic of the cut of an HPT apparatus

Grain refinement during HPT is similar to that occurring in ECAP. Precisely, microstructural evolution is dislocation driven and occurs via the formation of subgrains which will split to form high angle grain boundaries under the application of large strains (Fecht 1992). However due to the geometry of the apparatus, it is obvious that the center of the sample will sustain less deformation (in shear) compared to the extremities of the disk. As reported in HRTEM investigation by Liao et al. (2004), this results in a non homogeneous structure.

As reported by Jiang et al. (2000) the resulting microstructure presents a relatively strong texture. This is clearly suggested by the evolution of XRD patterns with increasing number of turns presented in Figure 2.17. The Cu sample was submitted to a high pressure of 5GPa. and XRD patterns were measured after 0, 1/2, 1 3 and 5 turns. While a randomly oriented sample typically exhibits a {111} to (200) peak high ratio of 2.17, it can be observed that this peak ratio increases with increasing number of turns. This shows that the resulting microstructure exhibits a well pronounced texture. Although dislocations are reported to be hard to find in the samples, some regions present high defect densities presumably due to dislocation debris. Zhu (2006) observed the presence of twins within HPT processed Cu samples. The mechanical twins found in the samples were reported to be formed of partial dislocation emitted by grain boundaries. Similar observations were reported by Liao et al. (2004a).
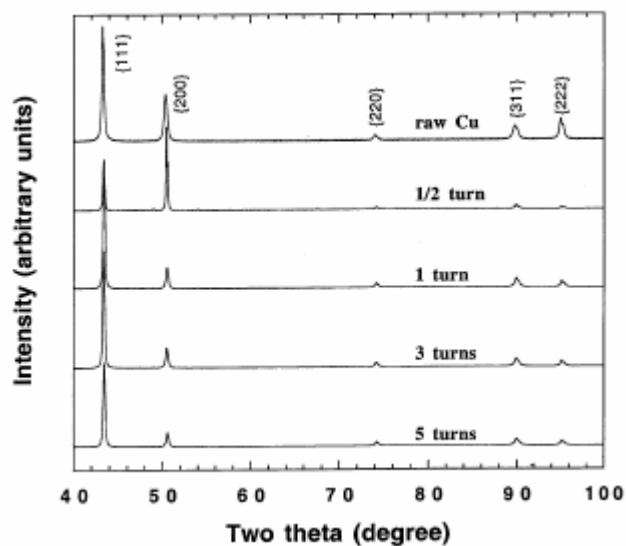
Figure 2.17: XRD diffraction patterns of Cu sample submitted to different turns.

Electrodeposition

Electrodeposition is a well known technique, used in many different fields, such as the automotive industry where thin layers of chromium are deposited in metallic parts in order to improve their resistance to corrosion. This process consists of introducing an anode (composed of the metal to be deposited) and a cathode in an electrolytic bath. The bath contains the metallic ions to be deposited. The anode and cathode are then submitted to a current. Deposition of the atoms composing the anode onto the cathode (substrate) occurs via oxidation of the anode. The novelty stands in the fact this process also allows the fabrication of NC materials with very small grain size, usually smaller than ~20nm, at a relatively high deposition rate (Cheung et al. 1995).

The grain size can be controlled by appropriately adjusting the bath composition, the pH, temperature and current intensity in order to promote grain creation rather than grain growth (Erb 1995). For example, in work by Ebrahimi et al. (1999) on the effect of

57

pH on the grain size of NC Ni, it was shown that the grain size decreases with an increase

in the pH. Also, the substrate can influence the grain size. Indeed, a Ni sample deposited

on a cold laminated Cu substrate will exhibit larger grain size than an Ni sample deposited

on a heat treated Cu sample (Ebrahimi et al. 2003).

Typically, the obtained grain size distribution is relatively sharp and the sample

will exhibit strong texture ((100) in the case of Ni) (Cheung et al. 1995). The texture

tends to decrease with decreasing grain size (Ebrahimi et al. 1999). Also, grain boundaries

do not exhibit major difference with respect to that found in conventional materials.

Electrodeposited samples typically have a lower purity than materials processed by other

approaches. Indeed the presence of oxygen atoms and sulfur atoms can usually be

detected. This will clearly affect the ductility of the sample.

Finally, the resulting samples exhibit large difference with that obtained by two –

step methods (Erb et al. 1997). For example, electrodeposited samples usually have a

Young's modulus similar to that of conventional materials while in the case of two step

methods difference up to 80% have been reported. However, let us note that hardness

measurements dot not exhibit a large dependence on the fabrication process (Erb et al.

1997).

Structure and observations

NC materials are composed of grain cores, also refered to as grain interiors, grain

boundaries and higher order junctions (triple junctions, quadruple junctions). Grain

boundaries and junctions form an interphase region as opposed to an interface region

58

with no attached thickness. A particular feature of NC materials stands in the high interphase/core volume fraction ratio. Indeed, a decrease in the grain size ineluctably results in an increase in the volume fraction of the interphase region. Supposing a tetracaidecahedral grain shape, which appears to be realistic, the volume fraction of interphase, grain boundaries and triple junctions can be estimated as follows (Sun et al. 2000):

$$f_{in} = 1 - \left[\frac{(d-w)}{w} \right]^3 \text{, } f_{gb} = \frac{3w(d-w)^2}{d^3} \text{, } f_{tj} = f_{in} - f_{gb} \qquad (2.6)$$

Here the subscripts *in, gb* and *tj* refer to the interphase, the grain boundaries and the triple junctions, respectively. Figure 2.18 presents a plot of the set of equations given in the above. It can be observed that the volume fraction of interphase (grain boundaries + triple junctions) becomes non negligible when the grain size is smaller than ~60 nm and clearly dominates that of the grain core when the grain size is smaller than ~12nm. Also, the volume fraction of triple junctions becomes non negligible solely when the grain size is smaller than ~10nm. Let us note that this simple model lies well with experiments. Indeed X-ray measurements on a sample with mean grain size 10 nm reveal a ~30% volume fraction of interphase (Birringer et al. 1989). Obviously, the high volume fraction of interphase region is of great importance and a section of this chapter will be entirely dedicated to grain boundary modeling. Let us now present the features of each constituent of NC materials.
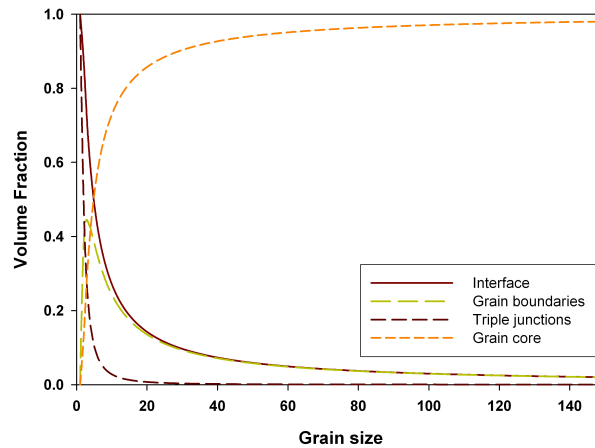
Figure 2.18: Evolution of volume fractions of interface, grain boundaries, triple junctions and grain cores with the grain size in nm.

Crystallites

Crystallites (grain cores) exhibit a well defined crystalline structure independently of the fabrication process. The crystallinity is maintained up to the grain boundaries. However, X-ray diffraction measurements on ECAP produced Cu samples have revealed a 0.04% decrease in the lattice parameter compared to that of conventional materials (Zhang et al. 1997). Hence, the lattice presents some strain which was suggested to result from the compressive stresses engendered by the presence of non-equilibrium grain boundaries Zhang et al. (1997). Although let us note that grain boundary dislocations were also suggested to be a plausible source of lattice strain (Ungar et al. 1998b). However, as will be discussed in next paragraph, grain interiors in NC materials do not exhibit a high density of dislocations. As discussed by Qin and Szpunar (2005) the noticeable lattice strain in crystallites, which presence is independent of the fabrication process, is localized near grain boundaries and may lead to internal stress fields within

the grain cores. Similar microstrains ranging from 0.21% to 0.04% were observed on and

on NC Ni produced by IGC (Schaeffer et al. 1995) and on amorphous $Fe_{33}Zr_{67}$ alloy (Sun

et al. 1996).

Also, crystallites present some peculiarities in terms of dislocation densities, twin

probability and stacking faults. First, the measure of dislocation density within NC

materials has been a major source of debates for years. Indeed, reported values ranged

from $10^{15} m^{-2}$ to zero. This issue will be clarified at the end of this discussion. In Figure

2.19, one can observe a high resolution TEM image of an electrodeposited Ni sample

with mean grain size ~30 nm deformation (Kumar et al. 2003). One can observe in the

bright and dark field images (2.19.a and 2.19.b) that the crystalline structure of the grain

core does not present any dislocations. In figure 2.19.c one can observe the presence of a

dislocation loop and the presence of a twin. Similarly, samples with small grain sizes

(d~20nm) processed by IGC exhibit a limited initial dislocation density (Straub et al.

1995). Recently, total dislocation density measurements (over the entire sample), on IGC

NC sample with grain size ~15nm reported densities in the order of $5.10^{15} m^{-2}$ with a

dislocation spacing in the order of the grain size (Ungar et al. 1998a). This signifies that

each grain initially contains zero to 1 dislocation. Finally, Langlois et al. (2005) reported

a severely reduced presence of dislocations within grain interiors of NC Cu samples

produced by consolidated nanopowders (via cold compaction, sintering and extrusion).

However, let us note that due to relaxation phenomena occurring at the free surfaces of

TEM samples, the observation of dislocations may be compromised. Nonetheless, it can

be concluded that the dislocation density within each grain is severely reduced in the as processed state.

However, this conclusion does not apply to samples produced via severe plastic deformation (e.g. ECAP, HPT). Indeed, dislocation densities in the range of $\sim 2.10^{15} m^{-2}$ were reported for 150nm grain ECAP processed Cu (Torre et al. 2005; Zhang et al. 1997). Qualitatively, the same conclusion was reached for NC Ni processed by HPT. Let us note though that these high dislocations densities are to be expected in the case of samples produced via severe plastic deformation. First, the grain sizes obtained usually lie in the UF regime were the dislocation loop length is still much lower than the grain size. Also, grain refinement results from dislocation activity, and as discussed in the above, dislocations remain present in some regions of the sample.
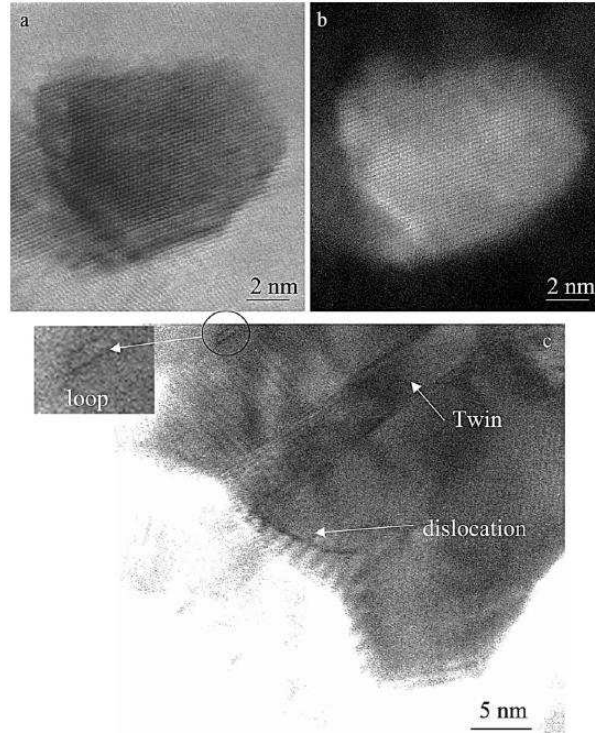
Figure 2.19: HRTEM image of a grain core with 20 nm diameter.

The above mentioned dislocation density measurements clearly suggest that the dislocation density and the resulting dislocation activity is severely reduced in NC materials. Hence, a change from dislocation glide dominated deformation to another type of mechanism is to be expected in the NC range.

Second, the presence of twins is seldom observed in NC materials. This can be observed in Figure 2.20, presenting a Cu grain core with a "giant step", the step is delimited by the arrowheads on the HRTEM image (Huang et al. 2003). This is a peculiarity of NC materials. Indeed, mechanical twins were observed in NC produced by

IGC, Cryomilling (Zhu 2006), and by severe plastic deformation (Liao et al. 2004 a and b). Ungar et al. (1998b) suggested the presence of mechanical twins (1 in every fifth grain) in electrodeposited Ni. Finally, Wu et al. (2007) reported HRTEM images of mechanical twins within grain cores of electrodeposited NC Ni post deformation.

On the contrary, the presence of twins in conventional F.C.C. materials, such as Cu or Al, is usually not expected since these materials present enough slip systems (12) for dislocation glide to be active. Moreover, Aluminum presents a high stacking fault energy which is not favorable to the presence of twins.
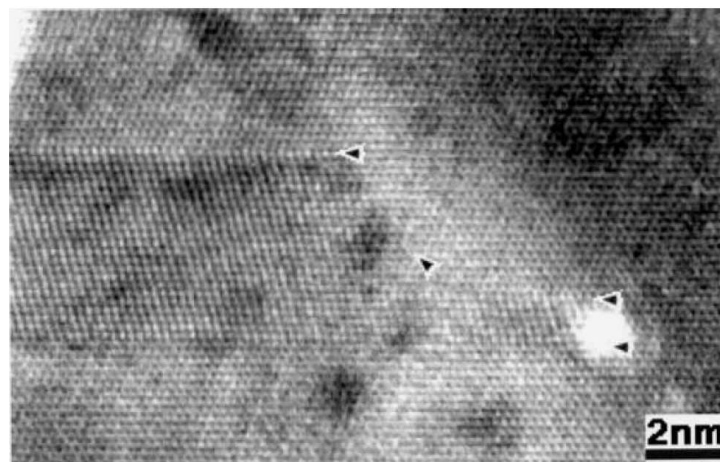
Figure 2.20: Cu cryomilled grain core containing a stepped twin.

Finally, the presence of stacking faults is rarely "observed" (via TEM experiments and XRD diffraction followed by calculation of the α_{warren} probability of faults). Indeed, the stacking fault probability was reported to be almost null in Cu and Pd samples with grain sizes smaller than ~25nm (Mingwei et al. 2003; Sanders et al. 1995).

Surprisingly, the stacking fault parameter increases with plastic deformation. A plot of the evolution of the stacking fault parameter with strain is presented in Figure 2.21 for and UF Pd sample and a 33nm grain NC IGC process Pd sample (Markmann et al. 2003). It can clearly be seen that in the stacking fault parameter of the NC sample is consistently higher than that of its UF equivalent and that it rises sharply at low strains prior to exhibiting a limited increase. These measurements are consequential since the increase in the presence stacking faults may suggest the activity of partial dislocations.
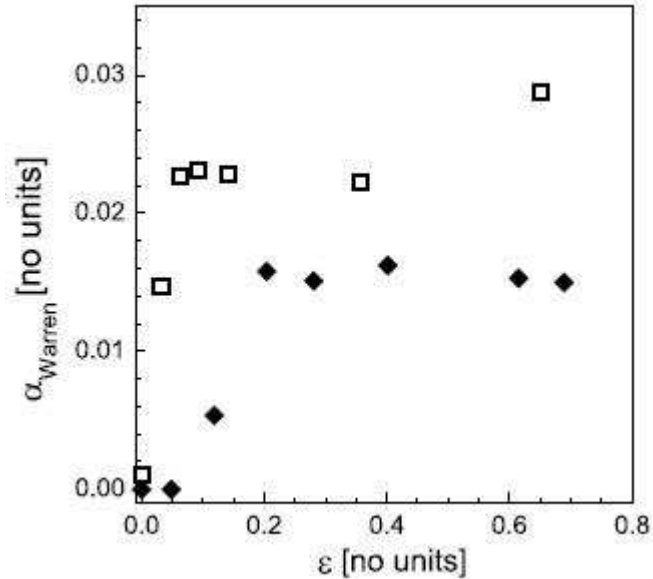
Figure 2.21: Evolution of the stacking fault parameter with strain for UFG PD (in bold) and nanocrystalline IGC Pd.

Grain boundaries and triple junctions

The microstructure of grain boundaries remains a major subject of debate in the community. Yet, it is commonly agreed that the thickness of grain boundaries, which ranges from 0.6nm to 1nm (i.e. ~3 to 4 lattice spacing's), is not dependent on the grain

size. Also, grain boundaries typically exhibit a lower density than that of the perfect

lattice. As extensively discussed by Qin et al. (1999 a and b), the lower density of grain

boundaries results from their particular microstructure (to be presented in this section)

and from the presence of vacancies and vacancy clusters. This is clearly dependent on

the fabrication process. Considering the volume fraction of grain boundaries and the

relative density of NC samples, an estimate of the grain boundary density can be obtained

via the use of a simple rule of mixture leading to densities ranging from ~65 to 95

percent of the theoretical density.

For the sake of comprehension, let us briefly discuss the most typical

representation of grain boundaries (this will be further detailed in upcoming subsection).

As mentioned in the first part of this chapter, dedicated to conventional materials,

dislocation can either be considered as statistical or geometrically necessary. The

presence of geometrically necessary dislocations is required to describe any remnant

lattice strain within a material. Since a grain boundary corresponds to the junction

between two grains with different misorientations, lattice strains are also localized at

grain boundaries which are typically regarded as regions of high density of geometrically

necessary dislocations.

However, in the case of NC materials, this general representation of grain

boundaries is not yet accepted by the community. Indeed two schools of thoughts are

opposed. In the first one, which the author does not belong to, grain boundaries are

thought to exhibit a high atomic disorder and to have a "structure" that could be qualified

as amorphous. In the second one, the structure of grain boundaries is similar to that of conventional materials. Hence, grain boundaries are considered to be the lieu of geometrically necessary dislocations and structural unit models (presented later in this chapter) are supposed to be applicable.

Let us discuss the implication of these schools of thoughts via the consideration of two limit cases; (1) a NC materials with grain size smaller than ~2nm and, (2) a bicrystal interfaces. In the first case, one would expect grain boundaries to exhibit a largely disordered structure since the position of each atom would be influenced by the neighboring atoms present in the grains. In the second case, it is well known that bicrystal interfaces often exhibit a well defined structure usually described with dislocation or disclination structural units (in the limit of the structural unit model). Indeed, the atoms present within the interface are influenced solely by two grains. In light of this short discussion, one would expect the microstructure of grain boundaries to vary from an ordered structure to a less ordered structure depending on the arrangement of the grains. Experimentally, this can be observed. A TEM image of a NC Pd sample with small grain size (~d=10nm) is presented in Figure 2.22 (Ranganathan et al. 2000). A well ordered grain boundary can be observed in region A-B. On the contrary region D-E does not present ant particular order. Also, interestingly, it can be seen that region B-C exhibits a grain boundary with a changing character.
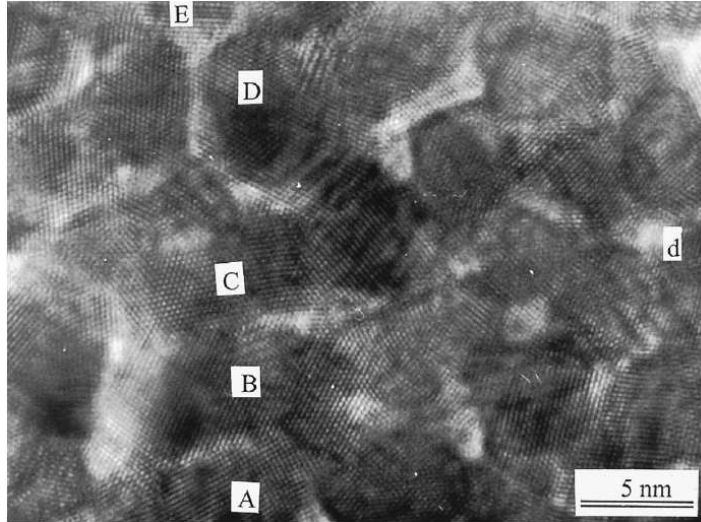
Figure 2.22: HRTEM image of a nanocrystalline Pd sample.

Let us recall that the description of the grain boundary microstructure is a complex exercise for it may depend largely on the fabrication process. Nonetheless, recent observations have revealed important features of grain boundaries in NC materials processed via HPT, ECAP and ball milling (Huang et al. 2003). Indeed, it was shown that most grain boundaries are high energy stepped or curved grain boundaries. This can be observed in Figure 2.23 (a) and (b) which presents a low angle grain boundary (2 degree misorientation angle). The presence of slightly disassociated dislocations can be observed in Figure 2.23a. These disassociated dislocations engender the presence of thin twins (stacking faults) within the adjacent grain cores. This emphasizes the effect of the grain boundary structure on the microstructure of grain cores.

Note that most NC samples have low angle grain boundary content much smaller than that of large angle grain boundaries. This was confirmed in recent work by Langlois et al. (2005) on bulk NC Cu prepared by a combination of IGC, sintering and extrusion. Also, let us recall that low angle grain boundaries are known to be possible dislocation

sources acting similar to a typical Frank and Read source.
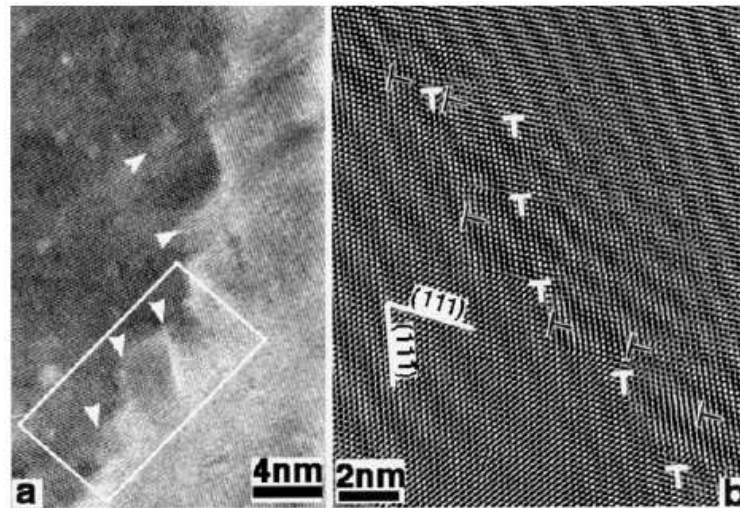
Figure 2.23: small angle grain boundary with steps and stacking faults (a) and zoom on the selected region revealing the presence of extrinsic stacking faults (b).

Facets and steps can also be observed in large angle grain boundaries. Figure 2.24 presents a TEM image of large angle grain boundary of a NC Cu prepared by cryomilling (Huang et al., 2005). Numerous steps, of height varying from 4 to 5 atomic layers, lying on the (111) plane can be observed. Let us note that these large steps can be assimilated as ledges which, as discussed in pioneering work by J.C.M Li, could act as dislocation sources.

Although not shown in previous TEM images, most defects such as pores and flaws are localized in the grain boundary regions. This was also observed in electrodeposited Ni samples (Dalla Torre et al. 2002). Observed flaws can seldom reach the micron size. For example, gas can remained trapped within NC samples during their

processing via physical vapor deposition. These defects are obviously expected to be of great influence on the response of NC materials
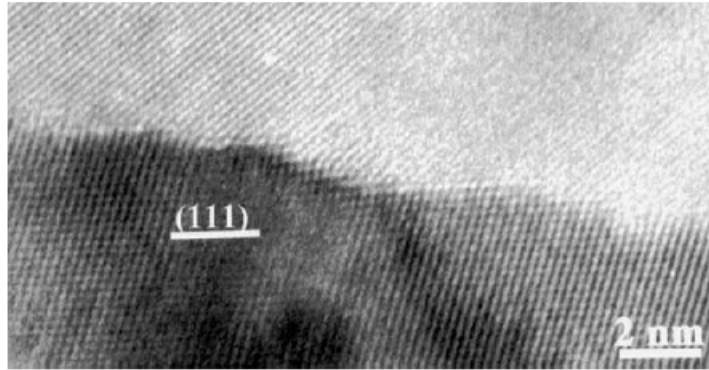
Figure 2.24: HRTEM image of a High angle stepped grain boundary in cryomilled Cu.

Finally, triple junctions which correspond to the regions of the sample where three grains intersect, commonly exhibit a disordered structure. This can be clearly observed in region d of Figure 2.22. This relatively high disorder is expected since atoms present in triple junctions are influenced by atoms belonging to three grains with different orientations. The open structure exhibited by triple junctions may also represent an appropriate "shortcut" for vacancies when diffusion mechanisms are activated. Similarly to grain boundaries, triple junctions are more prone to contain impurities than grain interiors.

Mechanical properties

The considerable research effort invested in NC was initially driven by the desire to fabricate novel materials with extremely high strength and improved ductility. This compromise is typically never reachable in conventional materials. While the objectives were reached in terms of strength, it will be shown here that so far the ductility of NC

materials is still limited. Although, let us note that recent cyclic cryomilling and room temperature milling procedures have contributed to greatly improve the ductility of the samples (Youssef et al. 2004). Similarly Wang et al. produced high tensile ductility nanostructured materials by developing a bimodal grain size distribution (Wang et al. 2002)

Interestingly, the refinement of conventional materials towards NC materials has also revealed interesting size effects. This is the case of the size dependence of elastic properties and more surprisingly of the strain rate sensitivity. All of these effects are discussed in following subsections.

Prior to presenting the size effects in the mechanical response of NC materials, it is important to re-emphasize the limitations, or more precisely the possible artifacts in experimental measures.

First, measurements are rarely reproducible. This is due to the fact that sample fabrication remains a delicate exercise that is performed mostly in academic laboratories. Hence, large variances in results emerge from the microstructural features of the samples. This precludes the use of any statistical analysis to estimate the properties and response of NC materials.

Second, some experimental procedures aver to be complex and the precision of the measures can be altered due to the use of particular techniques. To illustrate this discussion, let us focus on the stringent example of the measure of strength. Due to the small dimensions of samples, the measure of strength via tensile tests is not always

possible. Hence, an estimate of the material's strength is commonly obtained via hardness

measurements with the generally accepted approximation that the yield strength is equal

to a third of the hardness. This approximation consistently leads to measures of strength

higher than that obtained via tensile tests (at a given grain size). Simultaneously, the

quality of the sample, in terms of porosity, has a great influence on the measure of

strength. This can be observed in Figure 2.25 presenting the evolution of hardness

measurements with respect to the density of samples with same grain size (Sun et al.

2000). Clearly it can be seen that a change from a 99 percent density to a 99.5 percent

density results in a two fold increase in the measure of hardness.
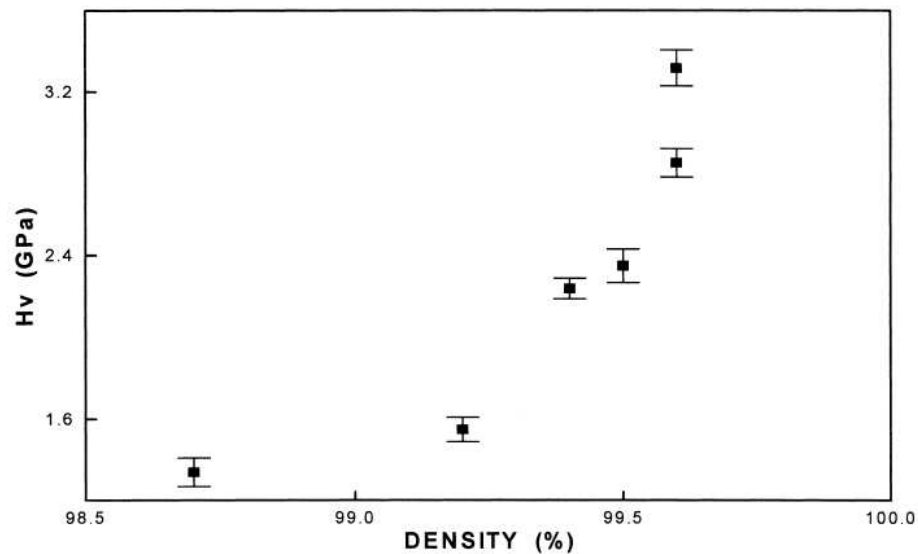
Figure 2.25: Hardness versus density of a powder compact.

Elastic properties

A size effect in the elastic response is expected to occur in NC materials. Indeed,

with decreasing grain size, the volume fraction of grain boundaries and triple junctions

increases. Since the structure of grain boundaries and triple junctions largely differ from

that of grain interiors, the elastic response of NC materials shall be affected by the size

effect. The size dependence of Young's modulus is presented in Figure 2.26. The

experimental points are extracted from several sources (Robinson et al. 1990; Nieman et

al. 1991; Sanders et al. 1997b; Wu et al. 1999; Ganapathi et al. 1991; Shen et al. 1995;

Kaye et al. 1978; Cheng et al. 2005). It can be observed that down to ~80nm grain size,

the Young modulus is not affected by the grain size. On the contrary, when the grain size

is smaller than ~40nm, a decrease in Young's modulus ranging from 10 to 50% can be

observed. Let us notice that some measures may present a bias due to poor consolidation.

Also, more data are required to confirm this trend. Therefore it is currently accepted that

a decrease in the grain size only leads to minor decrease in the elastic properties of NC

materials compared to that of conventional materials.
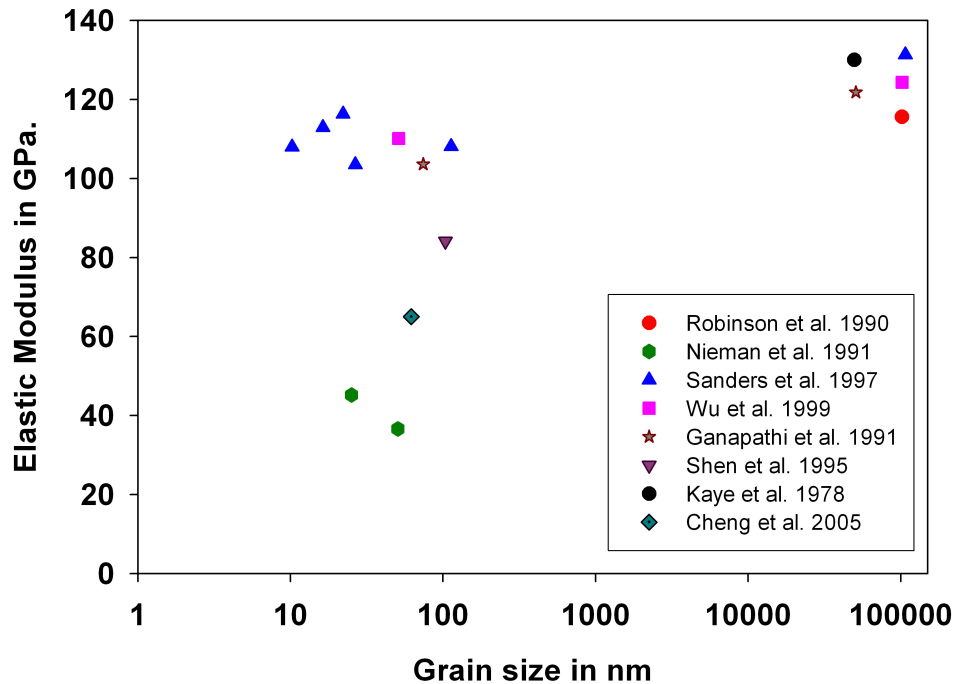
Figure 2.26: Experimental measurements of Young's modulus as a function of

grain size.

Yield stress

    As mentioned in Chapter 1, the yield stress of conventional materials is known to obey the Hall Petch law. A particular size effect occurs when the grain size is decreased below a critical grain size, in the neighborhood of ~25nm. Precisely, a breakdown of the Hall Petch law, characterized by a reduced and possibly negative Hall Petch slope, can be observed. Experimental data are presented in Figure 2.27. The dashed line represents the Hall-Petch law while points represents the experimental data extracted from several sources (Sanders et al. 1997a, Nieman et al. 1991, Conrad and Yang 2002, Hommel and Kraft 2001, Embury 1993, Fougere et al. 1992, Nieman et al. 1992, Cai et al. 2000, Chokshi et al. 1989, Merz and Dahlgren 1975, Chen et al. 2006, Youssef et al. 2004, Champion et al. 2003). Owing to the difficulty related to the fabrication processes and to the differences in methods used to measure the yield strength (e.g. compression tension, hardness), a noticeable scatter in the data can be observed. This has been source of debate in the community. However, in recent review by Meyers et al. (2006) it was clearly shown that the breakdown of the Hall Petch law is not an artifact. Indeed, a clear departure from the Hall Petch law can be observed when the grain size is in the neighborhood of ~25nm.
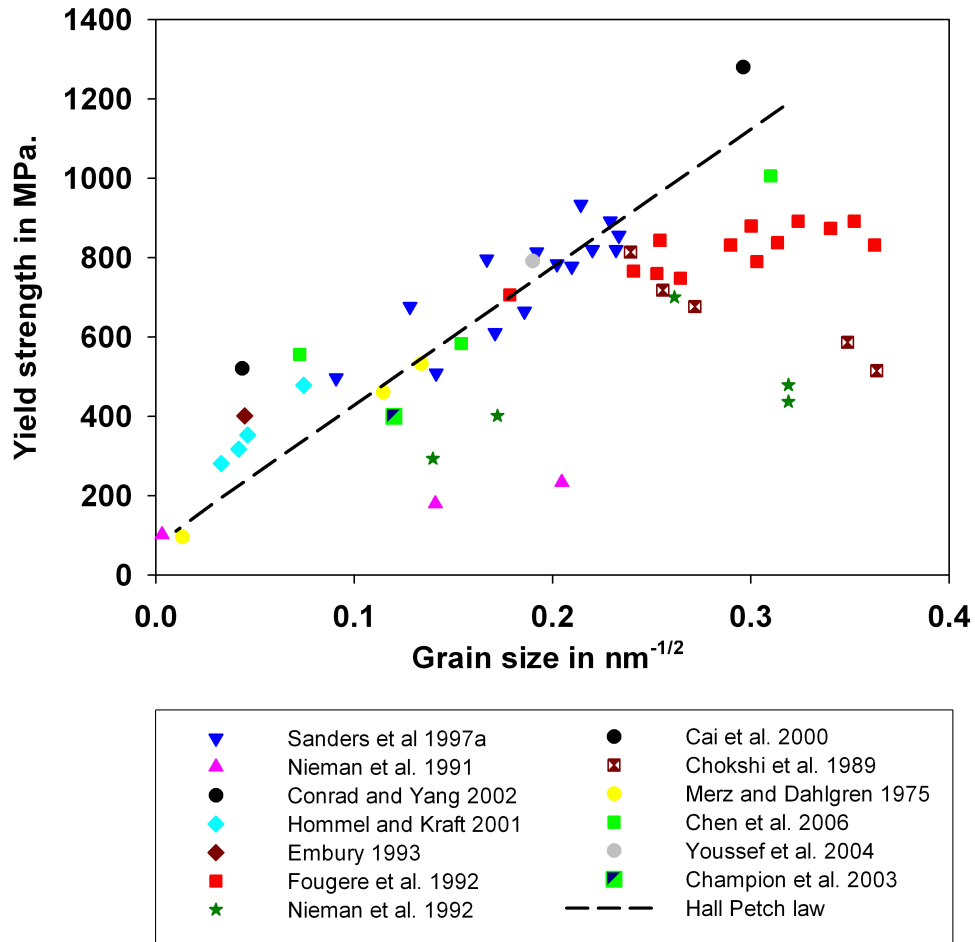
Figure 2.27: Experimental data presenting yield stress as the function of the inverse of the square root of the grain size.

Let us note that in work by Kumar et al. (2003), it was hypothesized that the yield strength vs. grain size plot can be divided in three regimes. The first regime, in which the Hall Petch law prevails, describes the size dependence of the yield strength of materials ranging from the conventional materials down to materials with grain size in the neighborhood of ~100nm. In the second regime, ranging from 100nm down to ~10nm

grained materials, a decrease in the Hall Petch slope occurs. Finally, in the third regime (d<~10nm) a decrease in the grain size leads to a decrease in the yield strength. This idealized vision of the size dependence of the yield strength is also suggested in models by Jiang and Weng (2004), Warner et al. (2006) and Benkassem, Capolungo et al. (2007).
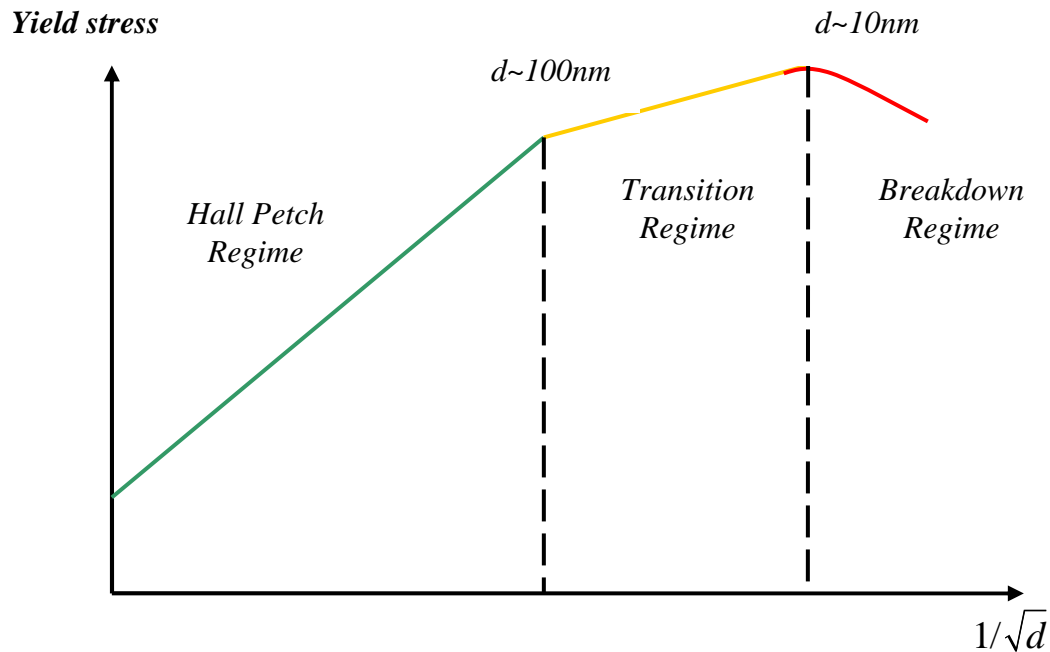
Figure 2.28: Plot of the expected grain size dependence of yield stress for ideal samples.

Inelastic response

Early tensile tests on NC materials revealed either limited ductility, in the order of ~3 percent, and a relatively high yield strength, or a higher ductility (yet smaller than that of conventional materials) and lower than expected yield strength. This is presented in Figure 2.29 extracted from Cheng et al. (2005). Red diamonds, pink stars, the blue

triangle, the grey cross and green squares are extracted from Nieman et al. (1992), Sanders et al. (1997a), Legros et al. (2000), Wang et al. (2003) and Cheng et al. (2005) respectively.

Consequently the capability of NC materials to achieve plastic deformation was subject to discussion. However, owing to the progress in consolidation techniques and to the amelioration of fabrication processes, a step forward towards a high ductility/ high strength compromise was made. Indeed, as can be observed in Figure 2.29, Cheng et al.' samples, produced via mixed cryomilling and room temperature milling, exhibit high strength (540-780MPa) and acceptable maximum elongation ranging from 6 to 12 percent. Similarly, Karaman et al. (2007) were successful in producing NC Cu samples (via equal channel angular extrusion) with ~100nm grain size and exhibiting high yield strength (~650 MPa.) and acceptable ductility in the neighborhood of 6 percent.
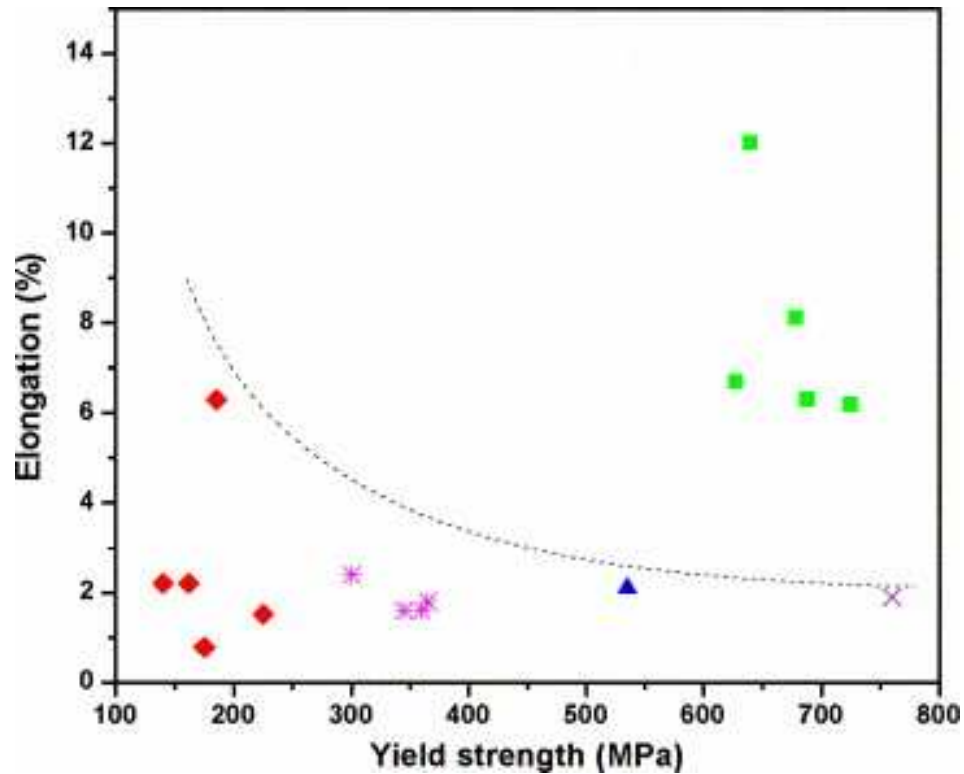
Figure 2.29: Experimental data presenting the yield strength vs. elongation plot.

Interestingly, the viscoplastic response of NC materials is different from that of conventional materials. Let us recall that within NC materials the dislocation density is severely reduced compared to that of conventional materials. Therefore, this suggests that NC deformation is dominated by a mechanism different from dislocation glide. Hence, a difference in the response of NC materials is expected. Figure 2.30 presents a comparison between the tensile response of a conventional Cu sample and of a NC Cu sample with 50nm grain size (Champion et al. 2003). While the coarse grain Cu exhibits typical strain hardening, this is not the case for the NC sample. Three regions can be distinguished in the response of the NC sample. Region 1 corresponds to a work hardening domain with decreasing strain exponent. Region 2 is a plastic yielding domain with constant flow

stress and region 3 is a plastic yielding domain with linear softening. The pseudo elastic-perfect plastic response of NC materials was also revealed by several other research groups in the case of samples prepared by equal channel angular pressing and by ball milling (Karaman et al. 2007, Cheng et al. 2005).
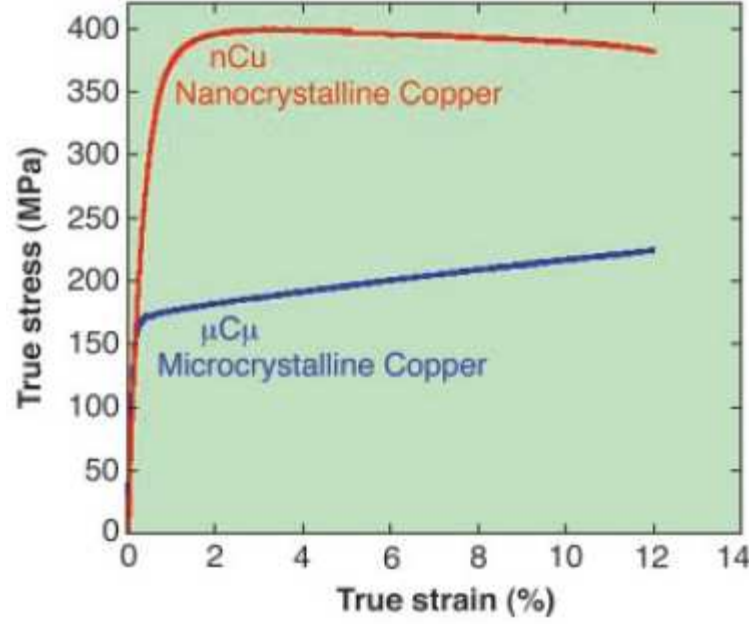
Figure 2.30: Experimental true stress true strain curve of nanocrystalline Cu with 50 nm grain size and coarse grain Cu.

The strain rate sensitivity of NC was reported to differ from that of conventional materials. The strain rate sensitivity can be related to the activation volume via the following expression (Asaro and Suresh 2005):

$$m = \frac{\partial \ln \sigma_f}{\partial \ln \dot{\varepsilon}} = \frac{\sqrt{3}kT}{v\sigma} \qquad (2.7)$$

Here k ,T v and σ refer to the Boltzmann constant, the absolute temperature, the activation volume and the uniaxial tensile stress, respectively. Typically, the strain rate sensitivity can be used to identify the deformation mechanism. For example, a value of m equal to 1 suggests the activity of Coble creep

Although the strain rate sensitivity exponent exhibits a dependence on the stress (it consequently evolves during deformation), it is usually considered constant during deformation. In the case of conventional Cu, m is usually equal to ~0,006. However, in NC materials the reported values of the strain rate exponent are much higher. For example, Cheng et al. (2005) obtained a value of 0,027 on a 62nm cryomilled Cu sample. Chen et al. (2006) report a strain rate sensitivity exponent equal to 0.06 on 10nm grained Cu prepared by magnetron sputtering. Similarly ECAP produced 300nm grain Cu exhibits a strain rate sensitivity coefficient equal to 0.025 with a 6.10^{-7}/s imposed strain rate (Wang and Ma 2004). . Hence, the change in the magnitude of the strain rate sensitivity of NC materials clearly suggests the activity of a novel plastic deformation mechanism.

A plot of the size dependence of the strain rate sensitivity with grain size is presented in Figure 2.31 (Asaro and Suresh, 2005). Red and blue marks correspond to literature data. Note here that in the case of the blue marks, the grain size is replaced by the twin width. One can notice that as the grain size decreases, the strain rate sensitivity increases. Also, from equation (2.7), the size dependence of the strain rate sensitivity suggests a decrease in the activation volume with increasing grain size. For example Armstrong and Rodriguez (2006) have shown a Hall-Petch type dependence of the activation volume.

Figure 2.31: Strain rate sensitivity parameter as a function of grain size.

Discussion

Let us briefly summarize the subsections related to the fabrication and response of NC materials, respectively. Two approaches can be used to fabricate NC materials. The first approach consists of synthesizing nanoparticules which are then compacted to form a sample. Inert gas condensation and ball milling fall in that category. The second approach consists of directly fabricating a bulk sample. ECAP, HPT and electrodeposition belong to this approach. The first approach typically leads to samples with smaller densities than the first approach due to the consolidation step.

In terms of defects, the dislocation density is severely reduced in NC materials. This constitutes a major difference with conventional materials. Also, depending on the fabrication process, twins are found in grain cores. The presence of these twins can, in some cases, be due to the geometry of the grain boundaries. Most of the impurities, such as oxygen and sulfur atoms in the case of electrodeposition, are located in triple junctions and grain boundaries. The former exhibits a structure with relatively high disorder while the later has a structure which can vary from well organized (e.g. structural units) to less ordered. Also, in the case of materials processed via HPT, ECAP and ball milling, grain boundaries typically exhibit large steps which can be assimilated as ledges of height 4 to 5 atomic layers. Most fabrication processes lead to high large angle grain boundary content. The resulting samples can be highly textured (depending on the fabrication process); this is particularly the case for samples produced by electrodeposition, HPT and ECAP. Although, the microstructure of NC samples is dependent on the fabrication process, some common features can be found in the mechanical response of all samples: (1) Independently of the fabrication process, the breakdown of the Hall-Petch law can always be observed. The critical grain size lies in the neighborhood of ~25 nm, (2) the strain rate sensitivity is dependent on grain size. Precisely a decrease in the grain size leads to an increase in strain rate sensitivity. This was observed on samples prepared by electrodeposition (Dalla Torre et al. 2002) and by ball milling (Cheng et al. 2005), (3) Dislocation activity decreases in the NC regime and may even become null when the grain size is smaller than ~10nm (Ke et al. 1995), (4) in grain boundaries, solely the inter-atomic distances depend on the grain size (Kumar et al. 2003). Triple junctions are always regions of high atomic disorder (Ranganathan et al. 2000).

Grain boundary modeling

Experimental results presented in the above clearly indicate that grain boundaries could have a great influence on the behavior of UF and NC materials. Here, the different models accounting for the grain boundary geometry and surface energy are briefly presented. This short review will be useful in upcoming chapter in which MD simulations are used to model the grain boundary dislocation emission mechanism.

A bicrystal interface, which corresponds to the simplest representation of a grain boundary, can be uniquely defined with 5 degrees of freedom. 3 degrees of freedom are necessary to describe the relative orientation of the two crystals and, two degrees of freedom are necessary to describe the relative orientation of the surface with respect to the grains. As shown in Figure 2.32 (Spearot et al. 2005), presenting MD predictions of the influence of the misorientation angle on the interface energy in the case of a pure tilt grain boundary, the relative misorientation of the two grains greatly influences the energy of the interface. Considering the large increase in the interface surface in NC materials, the initial state of NC materials is obviously at a higher energy state than that of conventional materials. It also clearly depends on the misorientations of the grains forming the grain boundaries. From a thermodynamic standpoint, this shall influence the capability of NC materials to store energy imposed by external conditions. Therefore, the response of NC materials is expected to be dependent on the grain boundary misorientations.
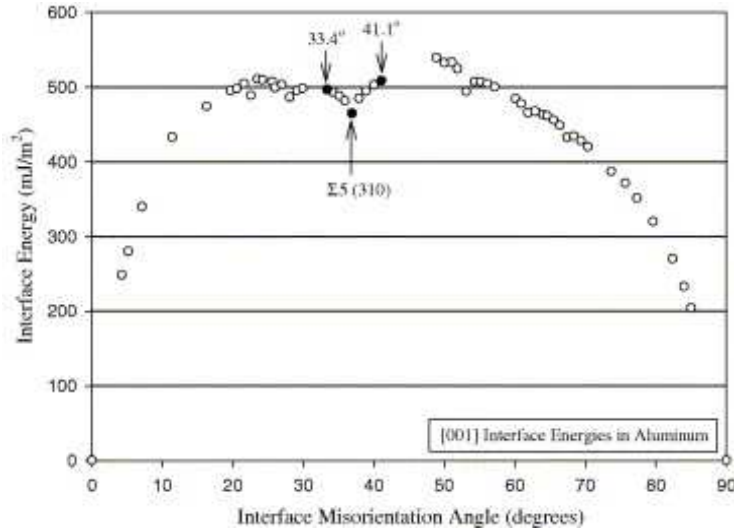
Figure 2.32: Evolution of the interface energy with respect to the misorientation angle.

In general, a grain boundary can be described geometrically with the use of one dimensional defect (e.g., dislocations, disclinations). In the particular case of tilt grain boundaries three families of models were developed to describe their surface energy; (1) dislocation based models, (2) structural unit's models and, (3) disclination based models. These models are presented briefly in what follows.

Dislocation models

In 1950, Read and Shockley introduced a two-dimensional model for the energy of an interface. Note that this model could very well be extended to a three-dimensional case.

The authors decomposed the grain boundary energy in two terms; a first term corresponding to the grain boundary core energy, and a second term resulting from elastic deformation in the surrounding of the grain boundary. The core of the grain boundary is defined as the thin zone of intersection of the grains. As mentioned by the authors, in the

84

case of large angle grain boundaries, the calculation of the grain boundary core energy

must be performed at the atomistic level. However, in the case of low angle grain

boundaries, closed formed solution can be obtained analytically.

First, the authors define a longitudinal axis (x-axis for example) and a vertical

axis (y-axis) associated with the grain boundary. Then, the dislocation densities on both

directions are calculated with the assumption that the lattice planes are equivalent to

dislocation flux lines. Recall here that grain boundaries can also be regarded as particular

arrangements of geometrically necessary dislocations. Considering first a single "y"

dislocation, the corresponding work term can be calculated by considering the effect of

all other "x" and "y" dislocations on its slip system. The work terms are equal to half the

lattice constant multiplied by the integral of the shear stress on the slip system. The

energy engendered by the "x" dislocations on the "y" dislocation, is supposed not to

depend on the position of the "y" dislocation and on the set of"x" considered. The same

procedure is performed for an "x" dislocation. Hence, the interface energy per unit length

is the sum, on the two types of slip systems, of the energy of a slip system multiplied by

the number of slip systems. Although each term is diverging, the sum of the two terms

converges. Finally, the following expression is obtained:

.

$$E_{él} = E_0 \theta \left(A - \ln \theta \right) \qquad (2.8)$$

θ is the misorientation between the two bicrystals. E_0 and A are given by :

$$E_0 = \frac{Ga}{4\pi(1-v)}\left(\cos\varphi - \sin\varphi\right) \tag{2.9}$$

$$A = A_0 - \frac{\sin 2\varphi}{2} - \frac{\sin\varphi \cdot \ln(\sin\varphi) + \cos\varphi \cdot \ln(\cos\varphi)}{\sin\varphi + \sin\varphi} \tag{2.10}$$

G, φ, a and v represent the shear modulus, the orientation of the grain boundary, the inverse of the plane flux density and Poisson's coefficient, respectively. A_0 is given by :

$$A_0 = 1\ln\left[\frac{a}{2\pi r_0}\right] \tag{2.11}$$

r_0 is the lower bound used for the integration of the shear stress. For the sake of rigor, this bound should be equal to the smallest distance at which the material is elastically deformed. The energy, at distances smaller than this bound (e.g., core energy), should be calculated at the atomistic level. However, in the case of low angle grain boundaries, the two energies (at distance lower and higher than the bound) have the same expression.

Although Read and Shockley's model is well suited for the calculation of the interface energy of low angles grain boundaries, the model is not adequate for large angle grain boundaries. This is due to the fact that in that case, the core energy (energy at distances smaller than lower integration bound for the shear stress) cannot be calculated with the set of equations in the above. For more details on the subject, the reader is referred to the work of Gleiter (1982). In order to overcome this limitation, structural units' models were developed.

Structural units models

In 1986, Wang et al. proposed a model for the evaluation of the interface energy of large angle grain boundaries. This model is an extension of Read Shockley's model based on the concept of structural units and on Baluffi's early model (1984).

Let us first define the concept of structural units which was first introduced by Sutton and Vitek (Sutton et al. 1980; Sutton et al. 1980; Sutton et al. 1981; Sutton et al. 1982). The structural unit model is based on molecular statics simulations and is limited to tilt grain boundaries. Let us note that this model cannot precisely describe all tilt boundaries.

Within a grain boundary misorientation range all grain boundaries with same medium plane (defining the grain boundary) are composed of a sequence of two structural elements (Sutton et al. 1980). Each structural element corresponds to a particular arrangement of a group of atoms. For example, in Figure 2.33, one can observe a tilt grain boundary composed of a sequence of C and D structural units (Spearot et al. 2005). At the bounds of the misorientation range, the grain boundaries are composed of only one repeated structural unit. For example, using the coincident site lattice (CSL) notation a $\Sigma 11$ (310) grain boundary is composed solely of A structural units, a $\Sigma 27$ (115) grain boundary is composed solely of B structural units and $\Sigma 89$ (229) grain boundary is composed of the sequence BBBA (Sutton et al. 1981).
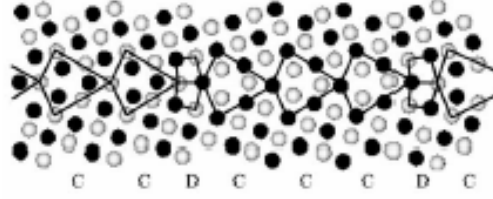
Figure 2.33: Grain boundary composed of a sequence of C and D structural units.

Following the work of Sutton and Vitek, Baluffi et al. (1984) developed a simple method for the calculation of particular properties of grain boundaries such as their energy and diffusivity. It is shown that the property of all grain boundaries (still in the tilt case) can be obtained from a finite number of simulations at the molecular level on structural units. Using this concept, Wang et al. (1986) developed a model of the energy of both low and large angle grain boundaries. Let E denote the total grain boundary energy. It can then be decomposed as the sum of the core energy, E_C, and the elastic deformation energy E_{el} (given by Read and Shockley's model):

$$E = E_{el} + E_C \tag{2.12}$$

The grain boundary core energy is obtained via Baluffi and Brokman's model. Precisely, Let us suppose that the grain boundary is composed of m structural units of type α and of n structural units of type β with m>n. The grain boundary core energy can be written as follows (note the interaction between the two types of structural units is accounted for):

$$E_C = E_C^\alpha + d_{\alpha\beta}\left(E_C^{\alpha\beta} - E_C^\alpha\right)l \qquad\qquad (2.13)$$

Here $d_{\alpha\beta}$, l, E_C^α, $E_C^{\alpha\beta}$ represent the length of an $\alpha\beta$ sequence, the average distance

between two dislocations within a grain boundary (given by Frank's formula), the energy

of an $\alpha\alpha$ sequence and the energy of an $\alpha\beta$ sequence, respectively. Introducing Frank's

formula in the above set of equation one obtains the following expression of the total

grain boundary energy:

$$E = E_{\acute{e}l} + E_C^\alpha + \frac{\Delta\theta}{b}d_{\alpha\beta}\left(E_C^{\alpha\beta} - E_C^\alpha\right) \qquad\qquad (2.14)$$

Let us note here that this expression depends on the grain boundary core radius. This

limitation is ineluctably inherited from Read and Shockley's model. Model predictions

are compared to numerical simulations in Figure 2.34a (the triangles corresponds to

points used to calculate the core radius) and to experimental measurements in Figure

2.34b. One can Notice that Wang et al.'s (1986) model is in almost perfect agreement

with numerical simulations. Indeed, the model can even predict the cusps in the evolution

of the interface energy. These cusps corresponds to case where the inter dislocation

distance is not a multiple of the inter-atomic distance. Finally the model predicts ratio of

the elastic energy of interfaces with (100) misorientation axis on that of interfaces with

(310) misorientations axis very close to experimental measures (Figure 2.34.b)
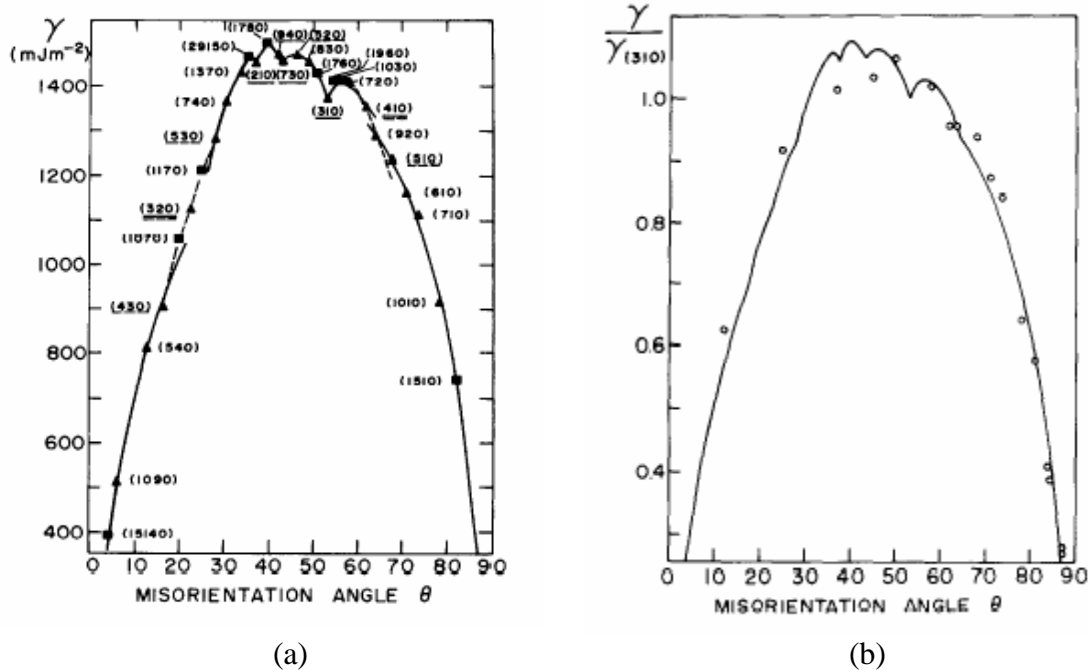
Figure 2.34: (a) Prediction of the evolution of the interface energy (b) ratio of the (100) to (310) misorientation energies.

Structural unit model are clearly more suited to describe the energy of grain boundaries since it applies to both low angle and large angle grain boundaries. However, these models cannot be extended to account for the effect of particular mechanisms, such as the emission or the penetration of a dislocation by/into a grain boundary. On the contrary disclination models have the capability to account for such effects (Hurtado et al. 1995).

Disclination models

Since the concept of disclination is not yet as widely known as that of dislocations, let us briefly recall the fundamentals of disclinations.

Disclinations

90

Disclination are one dimensional rotational defect bounding the surface of a cut to a continuous medium (Volterra 1907). Precisely, supposing a cylindrical medium, the undeformed faces of the volume are assumed to move by a distance u due to a rotation of angle w about a fixed axis. For ease of comprehension, one can consider that a disclination corresponds to the addition or to the subtraction of matter at the surface of a cut (see figure 2.35 extracted from Romanov 2003). A disclination is said to be positive if matter is subtracted to the medium and negative otherwise. Similarly to dislocations, disclinations engender long distance stress fields. While the strength of a dislocation is quantified by its Burger's vector, the strength of a disclination is described with its Frank vector (denoted w). The displacement of the undeformed surfaces is given by (De Wit 1973):

$$u = w \times (r - r_w)$$ (2.15)

Here, r and r_w denote the core radius and the distance between the rotation axis and the longitudinal axis of the cylinder. As in the case of dislocations which can have screw or edge character (Figure 2.35.a and b), disclinations can have a wedge or a twist character (Figure 2.35.c and d respectively).
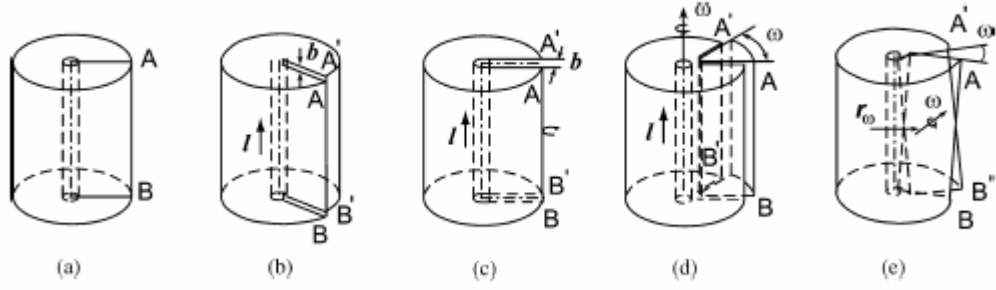
Figure 2.35: (a) Schematic of a cylindrical medium, (b) a screw dislocation, (c) an edge dislocation, (c) a wedge disclination and (d) a twist disclination.

All disclinations are geometrically equivalent to a particular arrangement of dislocations. For example, a negative wedge disclination can represent a dislocation wall. However, disclination models are equivalent to dislocations arrangements solely in terms of stress field or strain field (but not both). A discussed by Li, a disclination wall cannot have a unique strain field for an equivalent dislocation wall with same stress field. (Li 1972). For the sake of illustration, let us present the stress fields associated with a wedge disclination. These are given by (Huang et al. 1995):

$$\frac{1}{2}\left(\sigma_{xx} + \sigma_{yy}\right) = \frac{Gw}{2\pi(1-v)}\frac{1}{2}\left(\ln\frac{R^2}{x^2 + y^2} - 1\right) \tag{2.16}$$

$$\frac{1}{2}\left(\sigma_{xx} - \sigma_{yy}\right) = \frac{Gw}{2\pi(1-v)}\frac{1}{2}\left(\ln\frac{x^2 - y^2}{x^2 + y^2}\right) \tag{2.17}$$

$$\sigma_{xy} = \frac{Gw}{2\pi(1-v)}\frac{xy}{x^2 + y^2} \tag{2.18}$$

G , w , R , x and y denote the shear modulus, the disclination strength, the cylinder radius and the coordinates (centered with the cylinder longitudinal axis), respectively σ_j, (j=xx,yy,xy) are the stress components. The magnitude of the stress field is given by:

$$\sigma = \frac{Gw}{4\pi(1-v)}$$

As predicted by the above equations, disclination create large internal stress fields and have internal energies largely superior to that of a perfect crystal. However, the energy of particular disclination sequences, such as disclination dipoles, is much smaller (Romanov 2003).

Grain boundary energy models

The dislocation and structural unit models presented in the above rely on the calculation of the grain boundary core energy which should be calculated at the atomistic level via molecular statics simulations. In the case of the elastic deformation energy, the difficulty stands in the fact that the grain boundary core radius must be estimated. Disclination models are advantageous since they do not require the introduction of a grain boundary core radius. For example Li and Shih obtained the following expression of the elastic deformation energy of tilt grain boundaries (Li 1972; Shih et al. 1975).

$$E_{él} = \frac{Gw^2h}{32\pi^3(1-v)} f(\lambda) \tag{2.19}$$

G, w, v and h denote the shear modulus the disclination strength, Poisson's coefficient and the periodicity of the disclination wall.. $\lambda = \frac{\pi L_B}{h}$ where L_B is the length of the segment composed of the most frequent structural units. The function f is given by

$$f(\lambda) = -16 \int_0^\lambda (\lambda - v) \ln |2 \sin v| \, dv \tag{2.20}$$

As discussed by Nazarov et al. (2000) disclination models will always predict a physically acceptable value of the grain boundary energy, even in the case of so-called special grain boundaries (e.g. not appropriately described by the structural unit model). Indeed, dislocation structural units models can predict negative grain boundary energies which does not have any physical significance. Shih et al.'s model can be extended to account for additional effects. For example, Mikaekyan et al. (2000) extended this model to grain boundaries of finite length, Hurtado et al.(1995) introduced the effect of grain boundary dislocation emission on the grain boundary energy.

Deformation mechanisms

This section is dedicated to a presentation of all deformation mechanisms that have been suggested to contribute to the plastic deformation of UF and NC materials. Precisely, the mechanisms of Coble creep, Nabarro Herring creep, grain boundary sliding and grain boundary dislocation emission will be discussed as well as the size effect in the dislocation activity within grain interiors.

Relation to superplasticity

As mentioned in the section dedicated to the response of UF and NC materials, early experimental work suggested that mechanisms which are typically active in the case of creep responses, such as grain boundary sliding, could be active in NC materials and may lead to the softening of their response. For example, Yin et al. (2001) reported creep rates in the order of 11E-10/s at temperatures ranging from 290K to 373K. Similarly, Wang et al. (1997) reported creep rates suggesting the activity of grain boundary sliding at room temperature on NC Ni prepared by electrodeposition. This suggests that there could be an interesting relation between mechanisms that typically lead to superplastic response and the response of UF and NC materials.

In the case of creep tests, the deformation mechanisms based on vacancy diffusion or solid grain motion are activated at temperatures and imposed strains or stress largely different from which NC materials are subjected to. In the case of conventional materials, the domain of activity of these mechanisms can be plotted on a deformation map such as that proposed by Luthy (1979) (see Figure 2.36). For example, at low normalized temperature and low normalized shear stress, Coble creep dominates the creep response of a conventional material. At the same temperature, when the normalized shear stress is increased to 1.E-3, grain boundary sliding becomes active. Hence, with regards to Yin et al.'s experiments one would also expect grain boundary sliding as a possible plastic deformation mode.
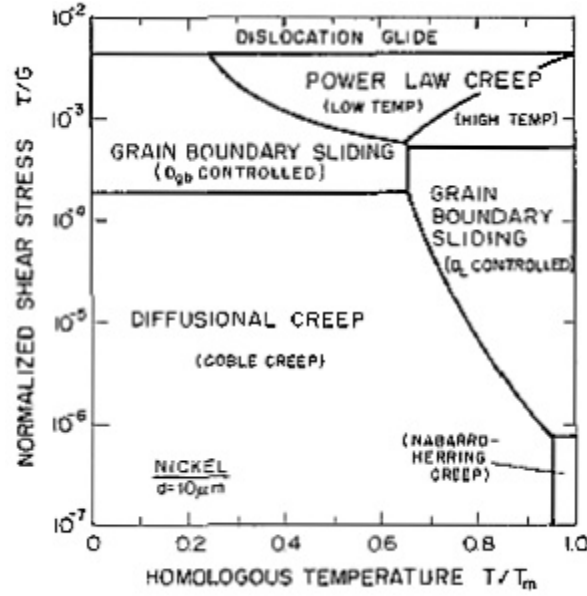
Figure 2.36: Luthy's deformation map.

Creep mechanisms are usually described with a phenomenological law accounting for some microstructural features of the material, such as grain size, and for the effect of temperature and stress. Typical creep laws are given by a relation of the form:

$$\dot{\varepsilon} = \frac{A \cdot D \cdot G \cdot b}{kT} \left(\frac{b}{d} \right)^{p} \left(\frac{\sigma}{G} \right)^{n} \tag{2.21}$$

Here *A, D, G, b, k, T* and *d* denote a numerical constant, the diffusion coefficient, the shear modulus, the magnitude of Burger's vector, Boltzmann's constant, the temperature and the grain size, respectively. σ denotes the applied stress, p and n are the size and stress exponents, respectively. The nature of the creep mechanism can usually be identified from the size and stress exponents. For example, if the stress exponent equals 1

and the size exponent is equal to 2 then the creep response is described by Nabarro herring creep.

Nabarro Herring creep (1948-1950) and Coble creep (1963) relate the effect of steady state vacancy diffusion along preferential paths. In the case of Nabarro Herring creep, vacancies diffuse through the grain interiors and engender plastic deformation within the grain at the macroscopic scale while in the case of Coble creep, vacancies diffuse along the grain boundary grain core interface (see Figure 2.37 extracted from Shah et al. 1998). Let us now describe the fundamentals of Coble creep and Nabarro Herring creep.
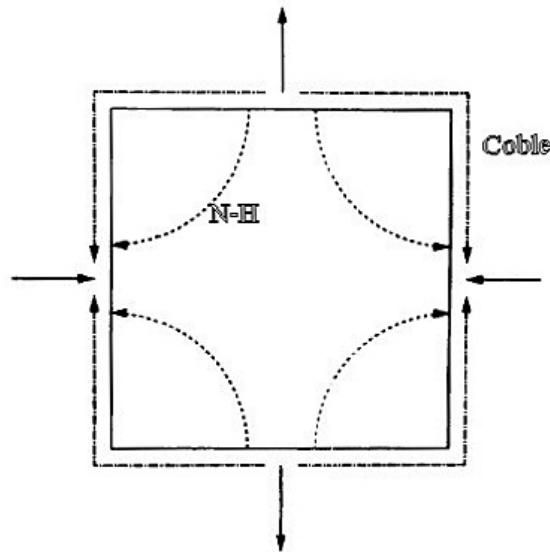
Figure 2.37: Vacancy diffusion paths during Coble creep and Nabarro Herring creep.

Nabarro Herring creep

Herring's model (1950) was first introduced to explain the quasi-viscous behavior of metallic wires in traction under small load and high temperatures. It models the transport of matter by diffusion within the grain interior. The author considers that the flux of matter results from a gradient of chemical potential which itself depends on the gradient of vacancies. Accordingly, the flux, denoted j, is written as:

$$j = -\left(\frac{n_L D}{kT}\right)\nabla\left(\mu - \mu_h\right) \tag{2.22}$$

Here $n_L, D, k, T,$ et $\nabla\left(\mu - \mu_h\right)$ denote the number of sites per unit volume, the self diffusion coefficient, Boltzmann constant, the temperature and the work per atom necessary to the input of a small amount of matter into the crystal. Supposing steady state diffusion, the gradient of the flux j must be equal to zero. Hence, the problem is equivalent to finding the appropriate boundary conditions on $\left(\mu - \mu_h\right)$. A solution is obtained via the minimization of the crystal's free energy with respect to the transfer of atoms between the crystal and the adjacent surface. With the above condition one obtains:

$$\mu - \mu_h = \mu_0 - p_{zz}\Omega_0 \tag{2.23}$$

Here μ_0, p_{zz} et Ω_0 denote the chemical potential of the source of atoms, the normal of the traction vector and the atomic volume. Finally, in the case of spherical grains, the normal component of the traction vector is proportional to the inverse of the square of the grain size.

Herring treated two different cases where the relaxation of the shear stress has not yet occurred and where it has occurred. One obtains for these cases, respectively:

$$\mu - \mu_h = \mu_0 - \frac{\Omega_0}{d^2} \sum_{i,j} \sigma_{ij} x_i x_j \qquad (2.24)$$

$$\mu - \mu_h = \mu_0 - \frac{5\Omega_0}{2d^2} \sigma_{xx} \left(x^2 - y^2 \right) \qquad (2.25)$$

where x_r r=i,j are the coordinates and d is the grain size. Finally, the creep law is obtained with the relation between the rate of displacement, the strain rate and the normal flux which is given by:

$$\frac{dr}{dt} = \sum_{i,j} \frac{1}{d} \dot{\varepsilon}_{ij} x_i x_j = \Omega_0 j_n \qquad (2.26)$$

Nabarro Herring's creep law reads:

$$\dot{\varepsilon}_{NH} = \frac{A_{NH} D_L G b}{kT} \left(\frac{b}{d} \right)^2 \left(\frac{\sigma}{G} \right) \qquad (2.27)$$

σ is the stress , d the grain size, G the shear modulus, b the magnitude of Burger's vector, D_L is the crystals diffusion coefficient, k denotes Boltzmann's constant, T is the temperature, A_{NH} is a numerical constant.

Coble creep

The fundamentals of Coble creep (1963) are similar to that of Nabarro Herring creep with the difference that in this case vacancy diffusion operates at the interface between grain interiors and grain boundaries. From Herring's reasoning it can be inferred that the deformation of the material results from the stress and temperature dependence of the vacancy concentration. Coble defines the gradient of the vacancy concentration as follows:

$$\Delta C = \frac{C_0 \cdot \sigma \cdot \Omega}{kT} \tag{2.28}$$

Here C_0, σ, Ω, k et T denote the initial equilibrium vacancy concentration, the stress normal to the grain boundary, the atomic volume, Boltzmann's constant and the temperature, respectively.

The boundary orientation is assumed constant during deformation. In doing so, both the volume conservation in the interface region and the discontinuity of stresses at the intersection of the crystals' facets are ensured. This condition holds when the creation of vacancies is uniform on each facet. In the case of spherical crystals, the creation and annihilation rate of vacancies are thus equal. This condition is met at 60 degrees on a hemisphere (e.g., both the top and bottom regions have the same area). Hence, the concentration gradient must be calculated at this angle. In the steady state regime and with Fick's law, the flux is given by:

$$J = D_v N w \frac{2\Delta C}{\pi d} d \sin 60 \qquad (2.29)$$

w and D_v denote the average grain boundary thickness and the coefficient of diffusion of grain boundaries. Finally, the expression of Coble creep is obtained via the relation between the volume change and the flux, one obtains:

$$J a_0^3 = \pi d^2 \frac{dd}{dt} = 7.4 D_v w \Delta C a_0^3 \qquad (2.30)$$

$$\dot{\varepsilon} = \frac{7.4 D_b \sigma w a_0^3}{\pi k T d^3} \qquad (2.31)$$

Discussion

First, let us recall that the activity of diffusion mechanisms is still subject to ongoing debate. On the one hand, Recent experiments (Li et al. 2004) have shown that early creep experiments may be flawed by poor crystal bonding and that NC materials shall not creep at room temperature. Similarly Yagi et al.' experiments (2006) on NC Au and Cu revealed that the creep response of cannot result from the activity of a vacancy diffusion mechanism. On the other hand, several models, motivated by early measurements revealing the activity of creep at room temperature, have shown that the activity of creep mechanisms could indeed lead to the softening in the plastic response of NC materials (Kim et al, 2000, 2001, Capolungo et al. 2005). Moreover MD simulations have also suggested the activity of Coble creep (Yamakov et al. 2002).

Also, triple junctions, owing to their particular atomic disorder, may constitute a shortcut for vacancy diffusion. Wang et al. (1995) introduced a creep law to describe triple junction creep. The fundamentals are similar to that explained in the above and the derivation of their model will not be recalled. The authors obtain the following expression of triple junction creep:

$$\dot{\varepsilon} = K_{tl} \frac{D_{tl} \cdot \Omega \cdot \sigma}{kT} \frac{w^2}{d^4} \tag{2.32}$$

Here K_{tl}, D_{tl}, Ω, w, k, σ and T denote a numerical constant, the coefficient of diffusion of triple junctions, the atomic volume, the average grain boundary thickness, Boltzmann's constant, the stress and the temperature in Kelvin, respectively.

The expression of Nabarro Herring creep, Coble creep and triple junction creep suggest that if diffusion phenomena are activated in NC materials, these three mechanisms should be dominant in different size regimes. For example, one would expect triple junction creep to become non negligible at small grain sizes (d~10nm).

Grain boundary sliding accommodated by diffusion

Similarly to diffusion mechanisms of vacancy diffusion, grain boundary sliding may be active in NC materials. Nowadays, the major part of the community agrees on the fact that grain boundary sliding is activated in NC materials (although it is yet to be observed unequivocally experimentally). For example Cai et al.'s (2001) creep test on electrodeposited Cu samples with ~30nm grain size and Kumar et al. (2003) tensile test suggest the activity of grain boundary sliding. The three open questions related to grain

boundary sliding are its possible accommodation by vacancy diffusion, its contribution to plastic deformation and its range of activity.

Typically, in conventional materials, the mechanism of grain boundary sliding accommodated by vacancy diffusion is referred to as Lifschitz sliding. Depending on whether the diffusion occurs within the grain cores or within the grain boundary/grain interior interface, the expression of Lifschitz sliding is given by

- In the case of diffusion at the grain boundary/grain interior interface :

$$\dot{\varepsilon}_{jg} \approx 2.E5 \cdot D_{jg} \frac{Gb}{kT}\left(\frac{b}{d}\right)^3\left(\frac{\sigma}{G}\right)^2 \tag{2.33}$$

- In the case of diffusion through the grain interiors:

$$\dot{\varepsilon}_c \approx 8.E6 \cdot D_c \frac{Gb}{kT}\left(\frac{b}{d}\right)^2\left(\frac{\sigma}{G}\right)^2 \tag{2.34}$$

Here $\dot{\varepsilon}_r$, D_r r=jg, c denote the average viscoplastic strain rate and the diffusion coefficients of grain boundaries and grain cores, respectively. b, k, T, d, G and σ denote the magnitude of Burger's vector, Boltzmann constant, the temperature, the grain size, the shear modulus and the stress, respectively. Let us note the similarities between the two expressions in the above and the expressions of Coble creep and Nabarro Herrring creep, respectively.

Grain boundary dislocation emission

Recent MD simulations on both two-dimensional columnar (Yamakov et al. 2001) and fully three-dimensional structures (Derlet et al. 2002) have revealed that grain boundaries could actively contribute to the viscoplastic deformation of NC materials via the emission of dislocations . Although, MD simulations are not representative of the quasi-static response of NC materials (due to the large difference in boundary conditions), the grain boundary dislocation emission mechanisms is still suspected to contribute in the quasi static regime for experiments, such as that of Kumar et al. (2003) on NC Ni fabricated via electrodeposition and the of Markmann et al.(2003), also suggest the activity of grain boundary dislocation emission.

Grain boundary dislocation emission mechanism was first introduced in early work by Li (1963). Unfortunately, until these novel MD simulations appeared, relatively little work was dedicated to this phenomenon. Hence, so far there is no model allowing the quantification of grain boundary dislocation emission on the macroscopic response of materials. A novel constitutive law describing the emission and penetration mechanism will be introduced in Chapter 5. However, let us note that Asaro and Suresh (2005) introduced a model at the continuum level allowing the description of the stability of an emitted dislocation. The proposed model is based on energetic considerations and accounts for the effect of the stacking faults resulting from the emission of partial dislocations. In particular, it is shown that the resolved shear stress necessary for an emitted dislocation to be "stable" increases with decreasing grain size. While the model is well suited to describe the effect of grain boundary dislocation emission within grain

interiors, it does not rigorously describe the dislocation emission mechanism in the region of emission. Moreover, several questions still require further investigation. Notably, those related to the nature of the primary grain boundary sources.

There are three possible types of grain boundary dislocation sources : (1) disclinations (Hurtado et al. 1995), (2) low angle grain boundaries which act in a manner similar to Frank and Read sources (Hirth et al. 1982), and (3) grain boundary ledges which can be represented as extraneous atomic layers located at the grain boundaries (steps). Since most grain boundaries are of large angle type, the contribution of low angle grain boundaries is typically not considered to be of primary importance.

As mentioned in the above, in work by Li (1963) it was already suggested that grain boundary ledges could emit dislocations. Murr and Venkatesh dedicated consequent effort to the experimental observation of grain boundary ledges (Venkatesh et al. 1976; Murr et al. 1978; Venkatesh et al. 1978; Murr 1981). Among other, it was reported that in high purity conventional materials, the activity of ledges (as dislocation donors) is dependent on the initial dislocation density within the grain cores. Indeed, stored dislocations within the grain cores engender stress fields at the grain boundaries which can prevent the emission of dislocations by grain boundaries.

Finally, as predicted in grain boundary models based on disclination structural units, a large angle grain boundary could also emit dislocations. For example, it was shown that the motion of a disclination dipole may result in the emission of dislocations

from the grain boundary considered. In model by Gutkin et al.(2003) based on the energy difference of a system composed of bicrystal prior and after dislocation emission, it is shown that, in several configurations (depending on the geometry of the grain boundary) , grain boundary dislocation emission can be energetically favorable. Let us note though that this model, and subsequent evolution (Gutkin et al. 2005), does not account for the fact that dislocations are emitted only on favorable slip systems. This was revealed in all MD and MS simulations. A model for the effect of grain boundary dislocation emission on the grain boundary microstructure was developed by Hurtado et al. (1995). The authors formulate two hypotheses as to the resulting grain boundary microstructure post emission: (1) dislocation emission leads to the creation of a negative disclination and (2) dislocation emission results in the generation of a negative dislocation within the source. Since the first hypothesis lead to unstable grain boundaries, the second approach was selected.

Numerous MD and MS studies were dedicated to grain boundary dislocations. Following first MD studies on two dimensional columnar NC materials with grain size ranging from 20 to 70 nm (Yamakov et al. 2001), grain boundary partial dislocation emission was brought to light. Precisely MD simulations performed by the team of Gleiter and Wolf showed that the dislocation emission process is decomposed into the emission of a leading Shockley partial dislocation, followed, or not, by the emission of the trailing partial dislocation, The authors suggested that the emission of the trailing partial dislocation depends on the whether or not the grain size is larger than the splitting distance between the two partial dislocations. This distance depends on the stacking fault

energy (Hirth et al. 1982). This suggests that when the grain size is small, solely the leading partial dislocation can be emitted which results in the creation of a stacking fault following its motion. Consequently, one would expect that a single leading partial dislocation could not be emitted in the case of high stacking fault energy materials such as aluminum. Fully three dimensional simulations on Cu and Ni NC materials with grain size ranging from 5 to 12 nm also reveal grain boundary partial dislocation emission (Derlet et al. 2002). However, it was suggested that the non emission of the trailing partial dislocation may result from a relaxation process within the grain boundary via atomic shuffling. In more recent work by the team of Van Swygenhoven (2004), a criterion based on the ratio of the stable to the unstable stacking fault energy is introduced to predict the emission of the trailing partial dislocation.

In order to investigate more closely the grain boundary dislocation emission mechanism, recent MD and quasicontinuum studies (e.g., finite elements couples with MS) focused on bicrystal interfaces. Spearot et al.'s simulations of a bicrystal interface under traction show that the emission of a dislocation loop from the interface can result in the creation of a ledge localized near the source (Spearot et al. 2005). In Figure 2.38 (Spearot et al. 2005), one can observe the emission of a trailing partial dislocation from a bicrystal interface. Atoms are colored with the central symmetry convention (e.g. solely atoms which do not belong to a particular lattice structure appear). These simulations confirm that dislocations are emitted solely on favorable slip systems. Also, the quasi-continuum mode developed by Sansoz and Molinari reveal that in some cases, atomic shuffling can precede the emission of a partial dislocation. This is especially the case

when the grain boundary contains E-structural units and is submitted to a pure shear constraint (Sansoz et al. 2005).
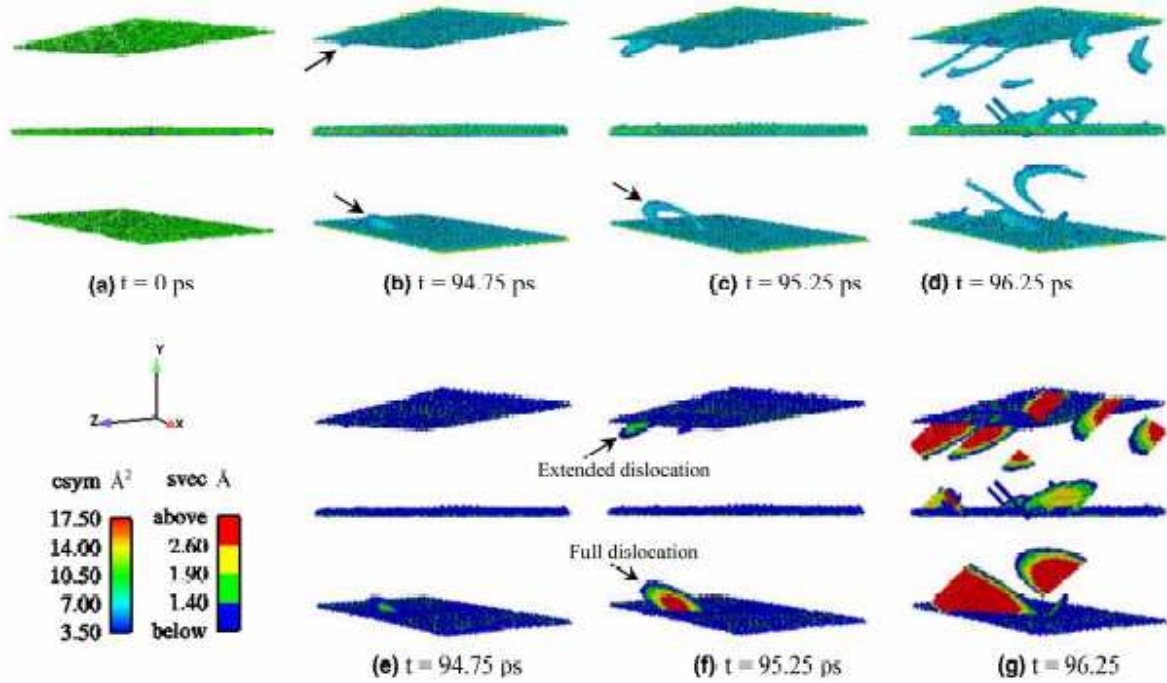
(Spearot et al. 2005)

Figure 2.38: Grain boundary dislocation emission simulated via MD.

Unaccomodated grain boundary sliding

As mentioned in the above, grain boundary sliding may be active in NC materials. This could be rationalized by the fact that dislocation activity is severely decreased in NC materials with small grain size. Hence, plastic deformation must occur via another mechanism. Also, dislocation emission by grain boundary may or not be active in NC materials. Supposing that this mechanism is indeed activated, its effect may not be sufficient to accommodate the imposed strain. Hence, grain boundary sliding appears as a

possible mechanism that could be activated in NC materials. As mentioned in the subsection dedicated to "superplastic" mechanisms. The possible accommodation of grain boundary sliding by diffusion mechanisms has been subject to debate. In the case where grain boundary sliding is not accommodated via vacancy diffusion, one would obviously expect to observe the debonding of the grain interiors. Indeed, Kumar et al. (2003) observed the creation and propagation of cracks during in situ tensile test on electrodeposited Ni sample. Although let us recall that samples produced via electrodeposition are more prone to have impurities within their grain boundaries which could promote the debonding of the grains. Modeling of the grain boundary sliding mechanism is rather complex and leads to controversial results. For example, Wei and Anand (2004) model the mechanism in a simple manner based on the hypothesis the grain boundary sliding is stress driven. Precisely, if the measure of the equivalent stress at the interface between grains is larger than a critical value, grain boundary sliding occurs. This model was implemented in a finite element simulation. The authors concluded that grain boundary sliding is the mechanism responsible for the softening in the plastic response of NC materials. However, Warner and Molinari (2006) revealed from quasicontinuum simulations that grain boundary sliding is similar to a stick slip mechanism. From these simulations the authors derive a simple expression of the stick skip sliding of grains which is implemented in a finite element simulation and concluded that grain boundary sliding alone is not responsible for the anomalous response of NC materials.

Discussion

From the above presentation of the microstructure and possible viscoplastic deformation mechanisms active in NC materials, it is clear that there is currently no rigorous understanding on the mechanisms engendering the particular response of NC materials. Consequently several questions are still subject to debate. The following discussion aims at rationalizing the change in the role of grain boundaries when the grain size of an F.C.C. metal is decreased to the NC regime. Also, a deformation map will be established to allow a better comprehension of the range of activity of the different mechanisms presented in the above.

Let us first discuss dislocation activity within the grain interiors. As previously mentioned, in the NC regime dislocation activity decreases with decreasing grain size. When the grain size is smaller than ~10nm, dislocation activity may even become null. In the case of conventional materials, strain hardening is a direct consequence of the activity of dislocations which density evolves during the deformation owing to the storage and annihilation of dislocations. When only dislocation-dislocation interactions are accounted for, the yield stress at zero Kelvin is typically written with Taylor's (1934) formula given by:

$$\hat{\sigma} = \alpha b M G \sqrt{\rho}$$

(2.35)

Here $\hat{\sigma}$, α, b, M, G and ρ denote the yield stress at zero Kelvin, a numerical constant which depends on the dislocation interaction, the magnitude of Burger's vector, Taylor's coefficient and the dislocation density, respectively. With the above formula, an

increase in the dislocation density leads to an increase in the yield stress which in turns

leads to strain hardening. Let us recall that this formula accounts solely for stored

dislocations and the generation of dislocations from the different possible sources are not

accounted for.

Looking more precisely at the activity of dislocation sources, such as the well

known Frank and Read sources, one can notice the emergence of size effects. Let us

recall that in a simple manner a Frank and Read source can be represented by a

dislocation line pinned at two end points. These sources are activated when the shear

stress applied on the dislocation line is larger than a critical value given by:

$$\tau_c = \frac{\mu \cdot b}{L}$$

(2.36)

Here μ, b, L and τ_c represent the shear modulus, the magnitude of Burger's vector, the

length of the dislocation line and the critical shear stress. Decreasing the grain size

directly leads to a confinement of the Frank and Read sources. Precisely, the length of the

source must at all times remain smaller than the grain size. Hence, the critical stress

required to activate a Frank and Read source will increase with decreasing grain size. At

a given grain size, a decrease in the dislocation activity is thus expected.

Also, the regions of stability of dislocations within NC materials may decrease

with decreasing grain size. Qin et al (1999) proposed a model for dislocation stability

based on the stress fields localized at grain boundaries due to the excess volume of grain

boundaries. This excess volume was measured experimentally on materials synthesized

with different processes (Van Petegem et al. 2003). At equilibrium, the stress applied by grain boundaries on a dislocation is equal to the Peierl stress. It is then shown (see Figure 2.39) that the ratio of dislocation equilibrium surface on the total surface decreases with grain size (Qin et al. 2002).

In Qin et al.'s (1999) conceptualization, the elastic modulus of grain boundaries, which is dependent on the excess volume, decrease with grain size. In conventional materials, grain boundaries have a role of barrier to dislocation motion and the number of dislocations that can pile up at the grain boundary is dependent on the grain boundary strength. The grain boundary strength decreases in the NC regime due to the increase in the excess volume. Thus grain boundaries are less efficient as barriers to dislocation motion and could even act as dislocation sinks.
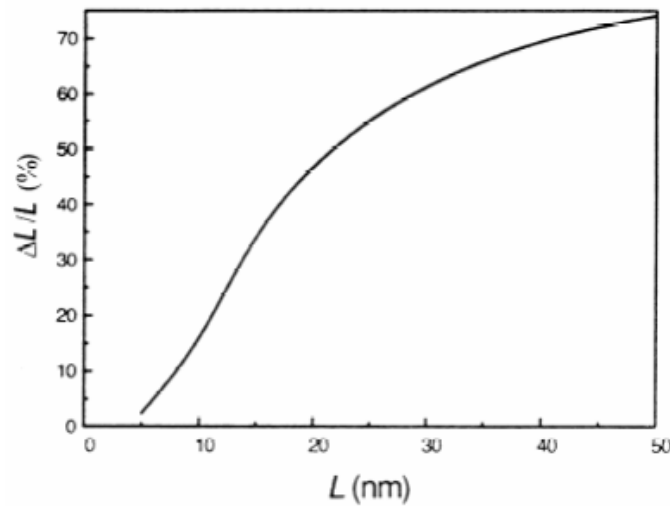
Figure 2.39: Ratio of the dislocation length stability over the grain size as a function of grain size.

Let us now discuss the size effect in the activity of grain boundary dislocation sources. In conventional F.C.C. materials the pile up of dislocations onto grain boundaries imposes stresses which prevent dislocations to be emitted from the grain boundaries. As mentioned in the above, the dislocation density is severely reduced in the UF and NC regime which will favorize the grain boundary dislocation emission. Moreover, since the stability of dislocations is also reduced in the NC regime, one would expect an emitted dislocation to end its trajectory in the grain boundary opposite to the source.

Deformation map

Let us present the range of activity of the mechanisms presented in previous sections (see Figure 2.40). In the case of conventional materials, plastic deformation is driven by dislocation glide and grain boundaries act solely as barriers to dislocations. When the grain size is decreased to the UF and NC regime, the role of grain boundaries and triple junctions changes for they can act as dislocation sources. Three types of grain boundary dislocation sources have been identified; (1) low angles grain boundaries, (2) large angle grain boundaries which are typically modeled with disclination structural units' models and (3) grain boundary ledges. From experimental measures of grain boundary misorientation distribution (Kumar et al. 2003; Iwasaki et al. 2004), it can be concluded that the role of low angle grain boundaries can be disregarded.

The effect and the presence of twins within the grain interiors are subject to studies and debate. For example, MD simulations on NC Al with 45 nm grain size reveal the activity of twinning. However, although the presence of twins can be observed in NC samples

(depending on the fabrication process) which tends to concur with MD simulations, the numerical results must be considered carefully. First, twinning is usually observed in materials subjected to dynamic loading and its activity is limited in high stacking fault energy materials such as Al. (Karaman., 2000). Consequently, MD results may not be representative of the quasi-static deformation of NC materials. Second, while two-dimensional simulations predict the presence and activity of twins, three-dimensional simulations predict the activity of twinning solely when twins are initially introduced in the model's geometry (Froseth et al. 2004).

The activity of vacancy diffusion mechanisms is also subject to debate. While many experiments reported creep rates in accordance with the Coble creep law, recent studies suggest that these measures are flawed by materials' artifacts. Also, let us note that as predicted by Kim et al. (2000) if vacancy diffusion is active in NC materials, Coble creep would dominate Nabarro Herring creep. This result is not surprising considering the size exponents in both constitutive laws.

Grain boundary sliding accommodated or not by vacancy diffusion could also be active in NC materials. This mechanism is suggested to be active in small grained NC materials (d<~20nm).
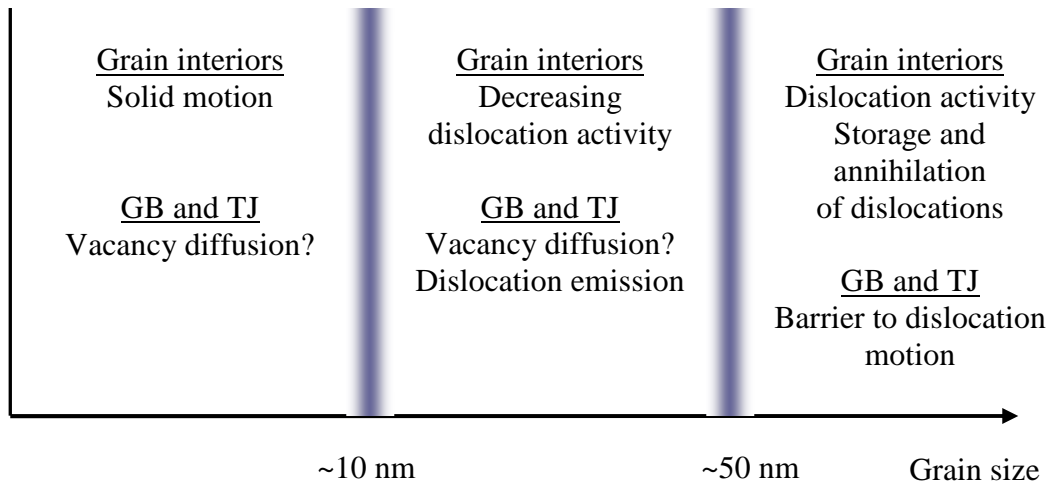
Figure 2.40: Deformation map

Let us note that question of the mechanism dominating NC deformation has been an open debate for more than a decade. In consequence to the advances in material synthesis, observations and modeling, the thoughts on the matter have evolved greatly. For example in 2003 (when this research project began), vacancy diffusion was largely thought to be dominant and discussion on grain boundary dislocation emission was beginning. Nowadays, diffusion mechanisms are not expected to play a major role in NC deformation and the most cited mechanisms are that of grain boundary sliding and grain boundary dislocation emission.

Size effect modeling

Let us discuss the fundamentals of the modeling of the size effect in the response of polycrystalline materials. Considering the many models available in the literature, this

section does not intend to be an extensive listing of all models but simply to present the type of modeling approaches used as well as their limitations.

Most models are based on two-phase composite approaches where the inclusion phase represents grain interiors and the matrix phase represents grain boundaries and triple junctions. In most cases the macroscopic response of the material is homogenized via a simple rule of mixture (Kim et al. 2000; Carsley et al. 1995; Konstantinidis et al. 1998). These approaches have the great advantage of being easy to implement numerically. However, their predictive capability is penalized by the simplicity of the homogenization procedure.

Due to the limited knowledge on the grain boundary structure, most models are based on the assumption that grain boundaries are amorphous and do not account for plastic deformation within the grain boundaries (Kim et al. 2001; Kim et al. 2001; Jiang et al. 2004; Capolungo et al. 2005). Let us note that 3-phase models, based on Christensen and Lo (1979) and Luo and Weng's (1987) early work, have also been introduced. Although this micromechanical scheme is more refined than traditional two-phase approaches, the predictions are limited by the description of the plastic deformation mechanisms.

In general the most complex issues related to the modeling of NC materials are; (1) the description at the microscopic levels of the deformation mechanisms and (2) the prediction of the macroscopic response of the material from the constitutive laws at the microscopic level. Indeed, since the mechanisms occurring in NC materials occur at the

atomistic level, where MD and MS aver of great use, an interpretation of the atomistic

motions must be performed to develop a constitutive law at the microscopic level. Also,

since the constitutive laws are valid at the microscopic scale, a scale transition from the

micro to macro must be performed. This scale transition can be performed either via

finite elements (Warner and Molinari 2006) or via micromechanics. However, both scale

transition approaches are limited. For example in the case of finite element simulations,

the first step usually consists of meshing a representative model of the microstructure.

Owing to the existence of interface elements in most commercially available codes, the

mechanism of grain boundary sliding can be modeled relatively simply. However, the

mechanism of dislocation emission cannot (so far) be modeled for dislocation densities

shall be nodal unknown. Hence, a complex finite element framework with additional

degrees of freedom would be necessary (Chapter 6 will present such a framework). In

the case of micromechanics, while the emission of dislocations could be accounted for,

the unaccomodated sliding of grains cannot be accounted for. This is due to the fact that

elasto-viscoplastic models with imperfect interfaces have not yet been developed (a novel

model will be presented in the following chapter). Also, traditional Eshelbian

micromechanical schemes can rarely account for non ellipsoidal grain shapes.

References

Agnew, S.R., Elliott, B.R., Youngdahl, C.J., Hemker, K.J., Weertman, J.R. (2000).
      "Microstructure and mechanical behavior of nanocrystalline metals". Materials
      Science and Engineering A 285: 391-396.

Armstrong, R.W., Rodriguez, P. (2006). "Flow stress/strain rate/grain size coupling for
      fcc nanopolycrystals". Philosophical magazine 86: 5787 – 5796.

Asaro, R.J., Suresh, S. (2005) "Mechanistic models for the activation volume and rate
      sensitivity in metals with nanocrystalline grains and nano-scale twins". Acta
      Materialia, 53:3369-3382.

Ashby, M. F. (1970). "The deformation of plastically non homogeneous materials." Philosophical magazine 21: 399-424.

Balluffi, R. W. and P. D. Bristowe (1984). "On the structural unit/grain boundary dislocation model for grain boundary structure." Surface Science 144(1): 28-43.

Benkassem, S., Capolungo, L., Cherkaoui, M. (2007). "Mechanical properties and multi-scale modeling of nanocrystalline materials". Acta Materialia in press.

Bhattacharya, P., Bellon, P., Averback, R.S., Hales, S.J. (2004)." Nanocrystalline TiAl powders synthesized by high-energy ball milling: effects of milling parameters on yield and contamination". Journal of Alloys and Compounds 368: 187–196.

Birringer, R. (1989). "nanocrystalline materials". Materials Science and Engineering A 117: 33-43.

Boystov, O., Ustinov, A.I., Gaffet, E., Bernard, F. (2007). "Correlation between milling parameters and microstructure characteristics of nanocrystalline copper powder prepared via a high energy planetary ball mill". Journal of Alloys and compounds 432: 103-110.

Cai, B., Q. P. Kong, Kong, Q.P. Lu, L., Lu, K. (2000). "Low temperature creep of nanocrystalline pure copper." Materials Science and Engineering A 286: 188-192.

Cai, B., Q. P. Kong, Cui, P., Lu, L., Lu, K. (2001). "Creep behavior of cold-rolled nanocrystalline pure copper." Scripta Materialia 45: 1407-1413.

Capolungo, L., C. Jochum, et al. (2005). "Homogenization method for strength and inelastic behavior of nanocrystalline materials." International journal of plasticity 21: 67-82

Carsley, J. E., J. Ning, Milligan, W.W., Hackney, S.A, Aifantis, E.C. (1995). "A simple, mixture based model for the grain size dependence of strength in nanophase metals". Nanostructured materials 5: 441-448.

Cermelli, P., Gurtin, M.E. (2002). "Geometrically necessary dislocations in viscoplastic single crystals and bicrystals undergoing small deformations". International Journal of Solids and Structures 39: 6281–6309.

Champion, Y., Langlois, C., Guerin-Mailly, S., Langlois, P., Bonnentien, J. L., Hytch, M. J. (2003). "Near-perfect elastoplasticity in pure nanocrystalline copper". Science 300: 310-311.

Chen, J.,Lu, L., Lu, K. (2006). "Hardness and strain rate sensitivity of nanocrystalline Cu". Scripta Materialia 11: 1913-1918

Cheng, S., E. Ma, Wang, Y.M., Kecskes, L.J., Youssef, K.M., Koch, C.C., Trociewitz, U.P., Han, K. (2005). "Tensile properties of in situ consolidated nanocrystalline Cu." Acta Materialia 53: 1521-1533.

Cheong, K. S. ,E. P. Busso (2004). "Discrete dislocation density modelling of single phase FCC polycrystals aggregates". Acta materialia 52: 5665-5675.

Cheung, C., F. Djuanda, et al. (1995). "Electrodeposition of nanocrystalline Ni-Fe alloys." Nanostructured Materials 5: 513-523.

Chokshi, A. H., A. Rosen, Karch, J., Gleiter, H. 1989. On the validity of the hall-petch relationship in nanocrystalline materials. Scripta Metallurgica 23 (10), 1679-1683.

Christensen, R. M., Lo, K.H.(1979). "Solutions for the effective shear properties in three phase sphere and cylinder models." Journal of the mechanics and physics of solids 27: 315-330.

Coble, R. L. (1963). "A Model for Boundary Diffusion Controlled Creep in Polycrystalline Materials." Journal of Applied Physics 34(6): 1679-1682.

Conrad, H. and Di. Yang (2002). "Effect of an electric field on the plastic deformation kinetics of electrodeposited Cu at low and intermediate temperatures". Acta Materialia 50: 2851-66

Dalla Torre, F., H. Van Swygenhoven, Schaublin, R., Spatig, P., Victoria, M. (2002). "Nanocrystalline electrodeposited Ni: microstructure and tensile properties." Acta materialia 50: 3957-3970.

Derlet, P. M., Van Swygenhoven, H. (2002). "length scale effects in the simulation of deformation properties of nanocrystalline metals." Scripta materialia 47: 719-724.

De Wit, R. (1973). J. Res. National Bureau of Standards.A **77**: 607.

Ebrahimi, F, Ahmed, Z., Li, H.Q. (2006). "Tensile Properties of Electrodeposited Nanocrystalline FCC Metals". Materials and Manufacturing Processes 21: 687–693.

Ebrahimi, F., Ahmed Z. (2003). "The effect of substrate on the microstructure and tensile properties of electrodeposited nanocrystalline nickel." Materials Characterization 49: 373-379.

Ebrahimi, F., G. R. Bourne, et al. (1999). "Mechanical properties of nanocrytsalline nickel produced by electrodeposition." Nanostructured Materials 11: 343-350.

Embury, J.D., Lahaie, D.J. (1993), in: M. Natasi, et al. (Ed.), Mechanical Properties and Deformation Behavior of Materials Having Ultrafine Microstructure, Kluwer Academic Publisher, Netherlands, 287.

Erb, U. (1995). "Electrodeposited nanocrystals: synthesis, structure, properties and future applications". Canadian Metallurgical Quarterly 34: 275-280.

Erb, U., G., Palumbo, et al. (1997). "Electrodeposited vs. consolidated nanocrystals: differences and similarities." Nanostructured Materials 9: 261-270.

Estrin, Y. (1998). "Dislocation theory based constitutive modelling: foundations and applications." Journal of the materials processing technology 80-81: 33-39.

Estrin, Y. and H. Mecking (1984). "A unified phenomenolgical description of work hardening and creep based on one parameter models". Acta metallurgica 32: 57-70.

Fecht, H.J. (1992). "Synthesis and properties of nanocrystalline metals and alloys prepared by mechanical attrition." Nanostructured Materials 1: 125.

Fecht, H.J, (2006). "Nanostructured Materials and Composites Prepared by Solid State Processing". 73-112.

Fougere GE, Weertman JR, Siegel RW, Kim S. (1992). "Grain-size dependent hardening and softening of nanocrystalline Cu and Pd". Scripta Metallurgica 26:1879–1883.

Froseth, A., H. Van Swygenhoven, et al. (2004). "The influence of twins on the mechanical properties of nc-Al." Acta materialia 52: 2259-2268.

Ganapathi, S.K., Aindow, M.,Fraser, M.L. and Rigney, D.A (1991). 'Clusters and cluster-assembled materials', MRS Symp Proc., Vol. 206, 593 – 598; 1991, Warrendale, PA, Materials Research Society.

Gleiter, H. (1982). "On the structure of grain boundaries in Metals". Materials science and engineering 52: 91-131.

Granqvist, C.G. and R.A. Buhrman. (1976) "Ultrafine metal particles". Journal of Applied Physics, 1976. 47: p. 2200.

Gutkin, M. Y., I. A. Ovid'Ko, et al. (2003). "Transformation of grain boundaries due to disclination motion and emission of dislocations pairs." Materials science and engineering A339: 73-80.

Gutkin, M. Y., I. A. Ovid'Ko, Skiba N.V.(2005). "Grain boundary sliding and lattice dislocation emission in nanocrystalline materials under plastic deformation". Physics of the Solid State 47: 1662-1674.

Gutmanas, E.Y. (1990). "Materials with fine microstructure by advance powder metallurgy". Progress in Materials Sience 34:261-366.

Gutmanas, E.Y., Trusov, L.I., Gotman, I. (1994). "Consolidation, microstructure and mechanical properties of nanocrystalline metal powders.", NanoStructured materials 4: 893-901.

Hayes, R. W. Witkin, D., Zhou, Fei, Lavernia, E. J. (2004). "Deformation and activation volumes of cryomilled ultrafine-grained aluminum". Acta Materialia 52: 4269-4271.

Herring, C. (1950). "Diffusional Viscosity of a Polycrystalline Solid." Journal of Applied Physics 21: 437-445.

Hirth, J. P. and J. Lothe (1982). Theory of dislocations. New York.

Hommel, M., Kraft, O. (2001). "Deformation behavior of thin copper films on deformable substrates".Acta Materialia 49:3935-3947.

Huang, J. Y., Wu, Y.K., Ye, H.Q. (1995). "Deformation structures in ball milled copper". Acta materialia 44: 1211-1221.

Huang, J.Y., Liao, X.Z., Zhu, Y.T. (2003). "Grain boundary structure of nanocrystalline Cu processed by cryomilling". Philosophical magazine 83: 1407-1419.

Hurtado, J. A., Elliot, B.R., Shodja, H.M., Gorelikov, D.V., Campbell, C.E.
Lippard, H.E., Isabell, T.C., Weertman, J.(1995). "Disclination grain boundary model with plastic deformation by dislocations." Materials Science and Engineering A 190: 1-7.

Iwasaki, H., K. Higashi, et al. (2004). "Tensile deformation and microstructure of a nanocrystalline Ni-W alloy produced by electrodeposition." Scripta materialia 50: 395-399.

Iwahashi, Y., Wang, J., Horita, Z.; Nemono, M.; Langdon, T.G. (1996). "Principle of equal-channel angular pressing for the processing of ultra-fine grained materials". Scripta Materialia 35:143.

Jia, D., Ramesh, K.T., Ma, E. (2003). "Effects of nanocrystalline and ultrafine grain sizes on constitutive behavior and shear bands in iron". Acta Materialia 51: 3495-3509.

Jiang, B., Weng, G.J. (2004). "A generalized self consistent polycrystal model for the yield strength of nanocrystalline materials". Journal of the mechanics and physics of solids 52: 1125-1149.

Jiang, H., Zhu, Y.T., Butt, D.P., Alexandrov, I.V., Lowe, T.C. (2000). "Microstructural evolution, microhardness and thermal stability of HPT-processed Cu". Materials Science and Engineering A 290 : 128-138.

Karaman, I., H. Sehitoglu, et al. (2000). "Modeling the deformation behavior of Hadfield steel single and polycrystals due to twinning and slip." Acta materialia 48: 2031-2047.

Kaye, G.W.C. and Laby, T.H.: 'Tables of physical and chemical constants', 14th edn, 31; 1978, New York, Longman.

Ke, M., S. A. Hackney, et al. (1995). "Observations and measurement of grain rotation and plastic strain in nanostructured metal thin films." Nanostructured materials 5: 689-697.

Khan, A. S., Zhang, H., Takacs, L. (2000). "Mechanical response and modeling of fully compacted nanocrystalline iron and copper". International journal of plasticity 16: 1459-1476.

Karaman, I., Haouaoui, M., Maier, H.J. (2007). "Nanoparticle consolidation using equal channel angular extrusion at room temperature". Journal of Materials Science 42: 1561-1576.

Kim, H. S., Y. Estrin, Bush, M.B. (2000). "Plastic deformation behaviour of fine grained materials." Acta materialia 48: 493-504.

Kim, H. S., Y. Estrin, Bush, M.B.. (2001). "Constitutive modelling of strength and plasticity of nanocrystalline metallic materials." Materials science and engineering A316: 195-199.

Koch, C.C. (2007). "Structural nanocrystalline materials: an overview". Journal of Materials Science 42:1403–1414.

Kocks, U. F. (1976). "Laws for work hardening and low temperature creep". Transactions of the ASME: 76-85.

Kocks, U. F. and H. Mecking (2003). "Physics and phenomenology of strain hardening." Progress in materials science 48: 171-273.

Konstantinidis, D. A., Aifantis, E.C. (1998). "On the "anomalous" hardness of nanocrystalline materials". Nanostructured materials 10: 1111-1118.

Kuhlman-Wilsdorf, D. (1962). "A new theory of work hardening". Transactions of the Metallurgical Society of AIME 224: 1047.

Kumar, K. S., H. Van Swygenhoven, et al. (2003). "Mechanical behavior of nanocrystalline metals and alloys." Acta materialia 51: 5743-5774.

Langdon, T.G., Valiev, R.Z. (2006). "Principles of equal-channel angular pressing as a processing tool for grain refinement". Progress in Materials Science 51: 881-981.

Langlois, C., Hytch, M.J., Lartigue-Korinek, S., Champion, Y. (2005). "Synthesis and Microstructure of Bulk Nanocrystalline Copper". Metallurgical and Materials Transactions 36:3451.

Legros, M., Elliott, B.R., Rittner, M.N., Weertman J.R., Hemker, K.J. (2000). Philosophical Magazine A 80: 1017.

Li, J.C.M. (2007). "Grain boundary impurity and porosity effects on the yield strength of nanocrystalline materials". Applied Physics Letters 90: 41912-1.

Li, J. C. M. (1972). "Disclination model of high angle grain boundaries". Surface science 31: 12-26.

Li, Y.J., Blum, W. and Breutinger, F., (2004). "Does nanocrystalline cu deform by coble creep near room temperature". Materials science and engineering A 387-389:585-589.

Li , D.X., Ping, D.H., Qin , X.Y. Wu, X.J. (1993). "HREM study of the microstructure in nanocrystalline materials". Materials Letters 18: 29-34.

Liao, X. Z., Zhao, Y. H., Zhu, Y.T., Valiev, R. Z. and D. V. Gunderov (2004a). "Grain-size effect on the deformation mechanisms of nanostructured copper processed by high-pressure torsion". Journal of Applied Physics 96: 636-640.

Liao, X.Z., Y. H. Zhao, S. G. Srinivasan, Y. T. Zhu, R. Z. Valiev, and D. V. Gunderov, (2004b). "Deformation twinning in nanocrystalline copper at room temperature and low strain rate". Applied Physics Letters 84: 592-594.

Liu, D., Umemoto, M., Deng, W., Xiong, L. Y., Ping, D. H., Lu, K. (1997). "Characterization of nanocrystalline $Ni_{33}Zr_{67}$ alloy". Journal of Applied Physics 81: 1103-1108.

Loss, H. V. (1901). "The flow of metal". Journal of the Franklin Institute 6: 456-464.

Lowe, T.C. and R.Z. Valiev (2000). "Producing nanoscale microstructures through severe plastic deformation." JOM, 52: 27.

Luo, H. A., Weng, G.J. (1987). "On Eshelby's inclusion problem in a three phase sphreically concentric solid and a modification of Mori-Tanaka's method." Mechanics of materials 6: 347-361.

123

Luthy, H., R. A. White, et al. (1979). "Grain boundary sliding and deformation mechanism maps". Materials Science and Engineering 39(2): 211-216.

Markmann, J., Bunzel, P., Rosner, H., Liu, K.W., Padmanabhan, K.A., Birringer, R., Gleiter, H., Weissmuller, J. (2003). "Microstructure evolution during rolling of inert-gas condensed palladium." Scripta Materialia. 49: 637-644.

Mecking, H., Kocks, U.F. (1981). "Kinetic of flow stress and strain hardening". Acta metallurgica 29: 1865-1875.

Merz, M.D., Dahlgren, S.D. (1975). "Tensile strength and work hardening of ultrafine-grained high-purity copper".Journal of Applied Physics 46: 3235-3237

Meyers, M.A., Mishra, A., Benson, D.J. (2006). "Mechanical properties of nanocrystalline materials". Progress in Materials Science 51: 427-556.

Mikaelyan, K. N., I. A. Ovid'ko, et al. (2000). "Disclination-structural-unit model of quasiperiodic tilt boundaries of finite extent." Materials Science and Engineering A 288: 61-65.

Mingwei, C.,Ma, E.;Hemker, K.J.; Sheng, H., Wang, Y.; Cheng, X.(2003). "Deformation twinning in nanocrystalline aluminum". Science 300: 1275-1277.

Mishra, A., Kad, B.K., Gregori, F., Meyers, M.A. (2007). "Microstructural evolution in copper subjected to severe plastic deformation: Experiments and analysis". Acta Materialia 55:13-28.

Morimoto, H., Sakata, H. (1962)." Electron diffraction study of evaporated films of nickel and cobalt". Journal of the Physics society of Japan 17: 136-145.

Morris, D.G. (1998), Mechanical behavior of nanostructured materials, Trans Tech Publication Ltd.

Murr, L. E. (1981). "Strain induced dislocation emission from grain boundaries in stainless steel". Materials science and engineering 51: 71-79.

Murr, L. E., Venkatesh, E. (1978). "Contrast phenomena and indentification of grain boundary ledges". Metallography 11: 61-79.

Nabarro, F. R. N. (1948). "Report of conference on Strength of Solids." Physical Society London.

Nazarov, A. A., Shenderova, O.A., Brenner, D.W. (2000). "On the disclination-structural unit model of grain boundaries". Materials Science and Engineering A 281: 148-155.

Nes, E. (1997). "Modelling of work hardening and stress saturation in FCC metals". Progress in materials science 41: 129-193.

Nieman GW, Weertman J.R., Siegel RW (1991). "Mechanical behavior of nanocrystalline Cu and Pd". Journal of Materials Research 6:1012–27.

Nieman GW, Weertman J.R., Siegel RW (1992). "Mechanical behavior of nanocrystalline metals". NanoStructured Materials 1:185-190.

Nishikawa, S., Asahara, G. (1920). "Some studies of metals by means of X-rays". Journal of the Franklin Institute 189: 688.

Ohno, T., Yatsuya, S., Uyeda R. (1976). "Formation of ultrafine metal particles by gas-evaporation technique. III. Al in He, Ar and Xe, and Mg in mixtures of inactive gas and air". Japanese Journal of Applied Physics 15:1213-1217.

Qin, W., Chen, Z.H., Huang, P.Y., Zhuang, Y.H. (1999). "Crystal lattice expansion of nanocrystalline materials". Journal of Alloys and compounds 292: 230-232.

Qin, W., Chen, Z.H., Huang, P.Y., Zhuang, Y.H (1999). "Dislocation pileups in nanocrusyalline materials." Journal of alloys and compounds 289: 285-288.

Qin, W., Y. W. Du, Chen, Z.H., Gao, W.L. (2002). "Dislocation stability and configuration in the crystallites of nanocrystalline materials." Journal of alloys and compounds 337: 168-171.

Qin, W., Szpunar, J.A. (2005). "Origin of lattice strain in nanocrystalline materials". Philosophical Magazine Letters 85: 649–656.

Ranganathan, S., R. Divakar, Raghunathan, V.S. (2000). "Interface structures in nanocrystalline materials". Scripta materialia 27: 1169-1174.

Read, W. T. and W. Schockley (1950). "Dislocations models of crystal grain boundaries." Physical Review 78(3): 275-289.

Robinson, P. and Mankins, W.L.(1990).'ASM metals handbook' 10th edn, Vol. 2 'Properties and selection: non-ferrous alloys and special purpose materials', 266, 437; Metals Park, OH, ASM International.

Romanov, A. E. (2003). "Mechanics and physics of disclinations in solids." European Journal Of Mechanics A/Solids 22: 727-741.

Sanders, P.G., Witney, A.B., Weertman, J.R., Valiev, R.Z., Siegel, R.W. (1995). "Residual stress, strain and faults in nanocrystalline palladium and copper". Journal of Engineering and Applied Science A204(1-2): 7-11.

Sanders, P. G., Eastman, J.A., Weertman, J.R. (1997a). "Elastic and tensile behavior of nanocrystalline copper and palladium." Acta metallurgica 45: 4019-4025.

Sanders, P. G., M. Rittner, Kiedaisch, E., Weertman, J.A., Kung, H., Lu, Y.C. (1997b). "Creep of nanocrystalline Cu, Pd, and Al-Zr." Nanostructured Materials 9(1-8): 433-440.

Schaefer, H.E., Wttrschum, R., Gessmann, T.Stick1, G., Scharwaechter, P, Frank, W., Valiev, R.Z., Fecht, H.-J., C. Moelle (1995). "Diffusion and free volumes in nanocrystalline Pd". Nanostructured Materials. 6:869-872.

Shah, S. and A. H. Chokshi (1998). "The significance of diffusional flow in ultrafine-grained materials." Colloids and Surfaces A 133: 57-61.

Shen, T.D., Koch, C.C., Tsui, T.Y., Pharr, G.M. (1995). "On the elastic moduli of nanocrystalline Fe, Cu, Ni, and Cu-Ni alloys prepared by mechanical milling/alloying". Journal of Materials. Research 10: 2892– 2896.

Shih, K. K., Li, J.C.M. (1975)." Energy of grain boundaries between cusp misorientations" Surface science 50: 109-124.

Song, X. Zhang, J., Li, L., Yang, K., Liu, G. (2006). "Correlation of thermodynamics and grain growth kinetics in nanocrystalline metals". Acta materialia 54:5541-5550.

Spearot, D. E., K. I. Jacob, McDowell, D.L. (2005). "Nucleation of dislocations from [001] bicrystal interfaces in aluminum." Acta materialia Acta Materialia 53: 3579-3589.

Stokes, R.J., Cottrel, A.H. (1954). "Work softening in aluminium crystals". Acta metallurgica 2: 341-342.

Straub, W.M., et al. (1995). "High resolution transmission electron micrsocopy study of nanostructured metals". nanostructured materials, 6: 571-576.

Sun, X.K., et al. (2000a). Preparation and mechanical properties of highly densified nanocrystalline Al. Metallurgical and Materials Transactions A (Physical Metallurgy and Materials Science), 31A(3A): 1017.

Sun, X., et al. (2000b)."Microhardness of bulk and higher density nanocrystalline copper obtained by hot compaction". Materials Chemistry and Physics 63 : 82-87.

Sun, N.X., Zhang, K.; Zhang, X.H.; Liu, X.D. Lu, K. (1996). "Nanocrystallization of amorphous $Fe_{33}Zr_{67}$ alloy" . Nanostructured Materials 7: 637-649

Sutton, A. P., Balluffi, R.W., Vitek, V. (1981). "On intrinsic secondary grain boundary dislocation arrays in high angle symmetrical tilt grain boundaries." Scripta Metallurgica 15(9): 989-994.

Sutton, A. P, Vitek, V. (1980). "On the coincidence site lattice and DSC dislocation network model of high angle grain boundary structure." Scripta Metallurgica 14: 129-132.

Sutton, A. P.,Vitek, V. (1980). "On the use of the energy-misorientation relationship of grain boundaries in modelling grain boundary defects and properties." Scripta Metallurgica 14: 563-567.

Sutton, A. P. and V. Vitek (1982). "An atomistic study of tilt grain boundaries with substitutional impurities." Acta Metallurgica 30(11): 2011-2033.

Tang, F., Hagiwara, M., Schoenung, J.M. (2005)."Formation of coarse-grained inter-particle regions during hot isostatic pressing of nanocrystalline powder". Scripta Materialia 53: 619-624.

Taylor, G. I. (1934). "The mechanism of plastic deformation of crystals: Part 1 theoretical." Proceedings of the Royal Society A CXLV(362-387).

Torre, F.D., Spatig, P., Schaublin, R., Victoria, M. (2005). "Deformation behaviour and microstructure of nanocrystalline electrodeposited and high pressure torsioned nickel". Acta Materialia 53: 2337-2349.

Ungar, T., Ott, S., Sanders, P.G., Borbely, A., Weertman, J.R. (1998a). "Dislocations, grain size and planar faults in nanostructured copper determined by high resolution X-ray diffraction and a new procedure of peak profile analysis". Acta Materialia, 46: 3693.

Ungar, T., Revesz, A., Borbely (1998b). "Dislocations and Grain Size in Electrodeposited Nanocrystalline Ni Determined by the Modified Williamson-Hall and Warren-Averbach Procedures". Journal of Applied Crystallography 31: 554-558

Uyeda, R. (1991)." Studies of ultrafine particles in Japan: crystallography. Methods of preparation and technological applications". Progress in Materials Science 35. 1-96.

Van Petegem, Dalla Torre, F., Segers, D., Van Swygenhoven, H. (2003). "Free volume in nanostructured Ni." Scripta materialia 48: 17-22.

Van Sygenhoven, H., Derlet, P.M.,Froseth, A.G. (2004). "Stacking fault energies and slip in nanocrystalline metals". Nature 3:399-403.

Volterra, V. (1907). "Annales Ecole Normale Supérieure de Paris". 24: 401.

Venkatesh, E. S., Murr, L.E. (1976). "Variations in grain boundary ledge structure with thermomechnical treatment in high purity aluminum." Scripta metallurgica 10: 477-480.

Venkatesh, E. S., Murr, L.E. (1978). "The influence of grain boudanry ledge density on the flow stress in Nickel." Materials science and engineering 33: 69-80.

W. (1898). "The metallographist : A quarterly publication devoted to the study of metals, with special reference to their physics and microstructure, their industrial treatments and applications. Edited by Albert Sauveur. Published by the Boston Testing Laboratories, 446 Tremont Street, Boston, Mass., U. S. A." Journal of the Franklin Institute 146(1): 76.

Wang, G.W, Vitek, V. (1986). "Relationships between grain boundary structure and energy".Acta Metallurgica 34: 951-960.

Wang, Y., Ma, E. (2004)." Temperature and strain rate effects on the strength and ductility of nanostructured copper". Applied Physics Letters 83: 3165-3167.

Wang, Y. Chen, M. Zhou, F. Ma, E. (2002). "High tensile ductility in a nanostructured metal". Nature 419: 912-915.

Wang, N., Wang, Z.,Aust, K.T., Erb, U. (1997). "Room temperature creep behavior of nanocrystalline nickel produced by electrodeposotion technique". Materials science and engineering A 237: 150-158.

Wang, N., Wang, Z., Aust, K.T., Erb, U. (1995). "Effect of grain size on mechanical properties of nanocrystalline materials". Acta Metallurgica et Materialia 43: 519-528.

Wang, Y. M., K. Wang, Wang, K.; Pan, D., Lu, K., Hemker, K.J., Ma, E. (2003). "Microsample testing of nanocrystalline copper". Scripta materialia 48: 1581-1586.

Warner, D. H., Sansoz, F.,Molinari, J. F. (2006). "Atomistic based continuum investigation of plastic deformation in nanocrystalline copper". International Journal of Plasticity 4: 764-774.

Wei, Y. J., Anand, L. (2004). "Grain-boundary sliding and separation in polycrystalline metals: application to nanocrystalline fcc metals". Journal of the Mechanics and Physics of Solids 52:2587-2616.

Witkin, D.B. and E.J. Lavernia (2006). "Synthesis and mechanical behavior of nanostructured materials via cryomilling." Progress in Materials Science 51: 1.

Wu, X.J., Du, L.G., Zhang, H.F., Liu, J.F., Zhou, Y.S., Li, Z.Q., Xiong, L.Y., Bai, Y.L. (1999). Nanostructured Materials 12: 221 – 224

Wu, X., Ma,, E., Zhu, Y.T. (2007). "Deformation defects in nanocrystalline nickel". Journal of Materials Science 42:1427–1432

Xu, S., Zhao, G. Luan, Y., Guan, Y. (2006). "Numerical studies on processing routes and deformation mechanism of multi-pass equal channel angular pressing processes". Journal of Materials Processing Technology 176: 251-259.

Yamakov, V., D. Wolf, Phillpot, S. R., Gleiter, H. (2001). "Lenght scale effects in the nucleation of extended dislocations in nanocrystalline Al by molecular dynamics simulation." Acta materialia 49.

Yamakov, V., Wolf, D., Phillpot, S. R., Gleiter, H. (2002). "Grain-boundary diffusion creep in nanocrystalline palladium by molecular-dynamics simulation". Acta Materialia 50:61-73.

Yagi, N., Rikukawa, A., Mizubayashi, H., Tanimoto, H. (2006). "Deformation by grain rotations in nanocrystalline fcc-metals". Materials Science and Engineering: A 442: 323-327.

Yin, W. M., S. H. Whang, et al. (2001). "Creep behavior of nanocrystalline nickel at 290 and 373 K". Materials Science and Engineering A 301: 18-22.

Youssef, K. M.,Scattergood, R. O., Murty, K. L., Koch, C. C. (2004). "Ultratough nanocrystalline copper with a narrow grain size distribution". Applied Physics Letters 6: 929-931.

Zhang, K., I.V. Alexandrov, and K. Lu. (1997) The X-ray diffraction study on a nanocrystalline Cu processed by equal-channel angular pressing. Kona, HI, USA: Elsevier.

Zhonghao, J., L. Jianshe, et al. (1995). "A dislocation density approximation for the flow stress-grain size relation of polycrystals." Acta Metallurgica et Materialia 43: 3349-3360.

Zhu, B., Asaro, R.J., Krysl, P., Zhang, K., Weertman, J.R. (2006) "Effects of grain size distribution on the mechanical response ofnanocrystalline metals: Part II." Acta Materialia 54: 3307–3320.

Zhu, Y.T. (2006). "Deformation twins formed in nanocrystalline materials". Materials Science Forum 503-504:125-32

CHAPTER 3

SCALE TRANSITION

The fundamentals of continuum micromechanics are recalled in this chapter. As previously mentioned, micromechanics is a technique allowing the scale transition from the microscopic scale, at which the local constitutive laws are written, to the macroscopic scale which we are interested into. Generally, it can be regarded as a particular averaging method relying on fundamental physics. Let us note here that micromechanic is a very vast field. Therefore, this review clearly does not intend to be exhaustive. For complete review on the subject the reader is referred to books by Qu and Cherkaoui (2006), Mura (1987) and Suquet (2003).

In a first section, the fundamentals of Eshelby's solution to the so-called inclusion problem will be briefly exposed. This substantial advance in the field of micromechanics has lead to subsequent evolutions aiming at treating complex cases such as that of elastic-viscoplastic composite media. Then, two secant-self-consistent micromechanical schemes, used in next chapter, will be derived (Cherkaoui et al. 2000, Berbenni et al. 2004).

Finally, two novel micromechanical schemes are presented. First, a three-phase-scheme valid solely in the viscoplastic regime and accounting for jump conditions at interfaces is introduced (Benkassem, Capolungo et al. 2007). This scheme clearly allows a more precise description of the effect of interphases on NC materials.

Second, a two-phase homogenization scheme based on the field fluctuation method and on the field translation method is developed (Capolungo et al. 2007). This scheme is valid in the elastic-viscoplastic regime and accounts for the effect of slightly weakened interfaces which will allow the treatment of unaccomodated grain boundary sliding.

Throughout this chapter, bold Latin letters will refer to fourth order tensors, bold Greek letters will refer to second order tensors unless otherwise specified. Capital letters will denote macroscopic quantities and small letters will refer to local quantities. The subscripts i,j,k,l (with i,j,k,l=1,2,3) will refer to the components of the tensor considered. For example, the tensors ε, σ will denote local strains and stress, respectively and $\mathbf{E}, \mathbf{\Sigma}$ will denote their macroscopic equivalents. ε_{ij} denotes the ij component of the local strain tensor noted ε. The superscripts e,vp, eff and * will refer to the elastic, viscoplastic, effective and eigenstrain part of a tensor. The superscripts I, M and C will refer to the inclusion phase, the matrix phase and the coating phase, respectively. Also, the superscript • and bar will refer to time derivatives and spatial averages, respectively.

Principle of micromechanics

The objective of continuum micromechanics is to predict the macroscopic response of a material from the local constitutive laws of each constituent of the material. The general procedure micromechanics rely on is presented in Figure 3.1. The change of scales is typically performed in three steps: (1) choice of a representative volume element (RVE),

(2) finding a relation between the local fields to the global fields and, (3) homogenization. The RVE must be large enough such that its overall properties are representative of the composite material.

Depending on whether strain or stress is imposed on the RVE the second step is referred to as the localization or as the concentration step, respectively. Homogenization can be assimilated as the use of local constitutive laws followed with an averaging technique (Bornert 1996). Precisely, the volume average of the local stress and strain fields must be equal to their macroscopic equivalent. This condition is referred to as the macrohomogeneity condition. It is a direct consequence of the choice of the RVE and is written formally as follows:

$$\Sigma = \frac{1}{V} \int_V \sigma(r) dr \text{ and } E = \frac{1}{V} \int_V \varepsilon(r) dr \qquad (3.1)$$
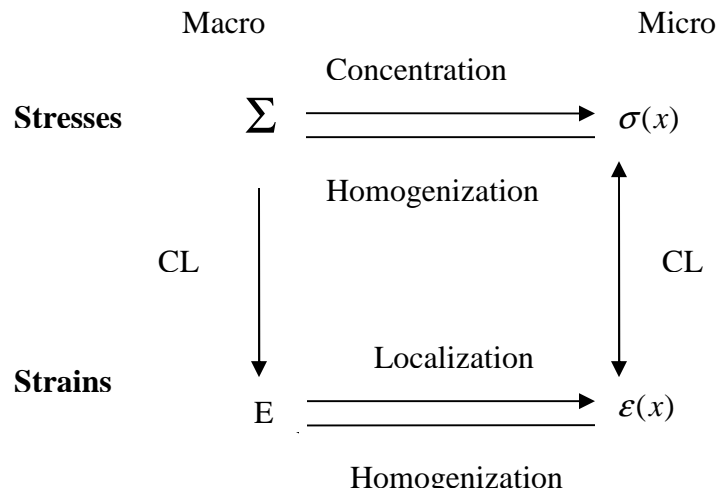
Figure 3.1: Methodology of the scale transition.

All micromechanical schemes presented in this chapter rely on pioneering work by Eshelby (1957) who developed a solution to the 'inclusion problem' in which an elastic ellipsoidal inclusion is embedded in an infinitely-large elastic matrix. Both matrix and inclusion phase have the same elastic constants but the inclusion phase sustains a stress free strain (Eigenstrain). Eshelby's solution which will be presented in the following section relates the eigenstrain to the local strain in the inclusion. This allows the prediction of the overall elastic response of the biphased material.

While Eshelby's solution to the inclusion problem leads to exact solutions in the case of time independent behaviors, exact solutions cannot be found in the case of time-dependent responses (e.g., viscoelastic behaviors, viscoplastic behaviors, time dependent elastic-plastic). Consequently, approximations to the real response of the material are to be obtained in these cases. As discussed by Molinari et al. (1997), two types of methodology were developed: (1) field fluctuation approaches and (2) incremental approaches. The first method is traditionally referred to as the secant approach while the second method is referred to as the tangent approach.

The first approach relies on Kroner, Budiansky and Wu's (KBW) work which is based on the local fluctuation of the plastic strain in the neighborhood of the spatially-independent strain rate in the homogeneous equivalent medium (Kroner 1961; Budiansky et al. 1962). The solution proposed by KBW relates the global plastic strain to the local ones via an elastic term. This ineluctably leads to overestimated predictions of the overall response. The incremental approach was developed by Hill (1965) who related the strain

and stress rates via an elastic-plastic modulus tensor. Essentially, this corresponds to a linearization of the constitutive laws followed by the use of Eshelby's solution. As detailed in work by Tome (1999), tangent approaches generally lead to softer predictions of the overall response of the material.

Since these two approaches rely on approximations they are both subject to debate. First, the field fluctuation approach implicitly considers plastic strains as eigenstrains, which is not entirely true (Masson and Zaoui 1999). Hence, the use of Eshelby's solution is often debated. Second, the incremental approach is based on the linearization of the constitutive laws which could penalize the accuracy of the predictions.

Numerous extensions of the field fluctuation and of the incremental approaches have been proposed over the past decades. Kroner's approaches are typically preferred to Hill's approaches for the linearization of elastic-viscoplastic constitutive laws avers to be complex. Weng (1981) proposed an extension of the KBW approach to treat the case of the creep response of materials. The author justified the use of Eshelby's solution on the basis that creep strain is independent on the stress rate and can thus be assimilated as an eigenstrain. An elastic-viscoplastic micromechanical schemes was also developed by Cherkaoui et al. (2000) in which both the fluctuations in the elastic and viscoplastic responses are taken into account. This scheme will be derived in upcoming section for it is used in Chapter 4 dedicated to the prediction of the effect of diffusion mechanisms. Recently, a softer elastic-viscoplastic self-consistent scheme based on the field fluctuation approach was developed by Berbenni et al. (2004). Note that the field

translation method was previously introduced in work by Sabar et al. (2002). This scheme is used in Chapter 5, dedicated to grain boundary assisted deformation, and will be presented in upcoming section.

Also, in contribution by Masson and Zaoui (1999), a Hill's inspired scheme was developed in which the elastic-viscoplastic problem is transformed into a thermoviscoelastic problem. Although this scheme leads to softer predictions than that of Berbenni et al.'s scheme, its implementation is far more complex. Also this model does not allow the treatment of the case of anisotropic materials. This affine procedure was later used and extended in work by Lebensohn et al. (2004) in order to treat the problem of anisotropic polycrystals with voids.

The inclusion problem

A solution to the inclusion problem was introduced in Eshelby's pioneering work (Eshelby 1957) who found the overall elastic response of a homogeneous material, with elastic tensor C composed of an inclusion embedded in a matrix of infinite dimensions (see Figure 3.2). Additionally to the elastic strain, the inclusion phase sustains an eigenstrain. The terminology eigenstrain refers to a stress-free strain such as a thermal strain, a phase transformation strain etc.

In this section, a solution to the problem of an elastic homogeneous media composed of an inclusion sustaining an eigenstrain embedded in a matrix of infinitely large dimensions is presented. Second, this solution to the inclusion problem is used to solve the problem of a linear elastic composite material.
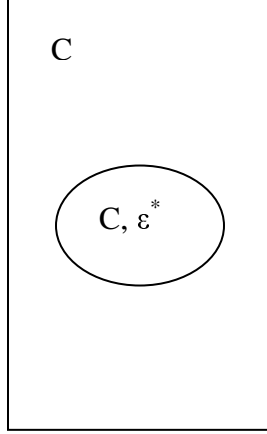
Figure 3.2: Representative volume element of the inclusion problem.

The eigenstrain problem

The objective here is to relate the local strain within the inclusion phase to the eigenstrain. Let us consider the inclusion phase. Hence, the superscript *I* will be omitted for simplicity of the notations. First, let us decompose the strain field in the inclusion phase as the sum of the elastic strain and of the eigenstrain which is supposed homogeneous within the inclusion:

$$\varepsilon_{ij} = \varepsilon_{ij}^{e} + \varepsilon_{ij}^{*} \qquad (3.2)$$

The deformation in the inclusion phase must respect the compatibility condition. Hence, if u denotes the displacement vector, the compatibility condition reads, in the case of small deformation:

$$\varepsilon_{ij} = \frac{1}{2}\left(u_{i,j} + u_{j,i}\right) \tag{3.3}$$

Using the local linear elastic constitutive law (e.g. Hooke's law) where c denotes the local elastic tensor modulus, equation (3.2) becomes:

$$\sigma_{ij} = c_{ijkl}\varepsilon_{kl}^{e} = c_{ijkl}\left(\varepsilon_{kl} - \varepsilon_{kl}^{*}\right) \tag{3.4}$$

Using the compatibility condition and the symmetry of the elastic tensor (e.g., $c_{ijkl} = c_{klij} = c_{ijlk}$) one obtains the following equation:

$$\sigma_{ij} = c_{ijkl}\left(u_{k,l} - \varepsilon_{kl}^{*}\right) \tag{3.5}$$

Neglecting any dynamic effect and body forces, the equilibrium condition reads:

$$\sigma_{ij,j} = 0 \tag{3.6}$$

Finally, Navier's equation is established by introducing the equilibrium condition into equation (3.5):

$$c_{ijkl}u_{k,lj} - c_{ijkl}\varepsilon_{kl,j}^* = 0 \tag{3.7}$$

The solution to the above equation is obtained via the use of Green's function which is

solution to:

$$c_{ijkl}G_{km,lj}(x-x') + \delta_{im}\delta(x-x') = 0 \tag{3.8}$$

Here $\delta(x-x')$ is the Dirac function which takes the value 1 when x=x' and the value 0

everywhere else. G_{km}, with $\boldsymbol{G}$ denoting Green's operator, is the displacement produced in

the direction k when a force of value unity is applied in the i*th* direction. Note that the

proof of (3.8) is based on the use of Fourier equation and can be found elsewhere (Mura,

1987, Qu and Cherkaoui 2006). Multiplying (3.8) by the *i*th component of the

displacement and integrating the resulting equation on the volume of the RVE leads to

the following relation of the eigenstrain problem:

$$\varepsilon_{ij}(r) = S_{ijkl}^E \varepsilon_{kl}^* \tag{3.9}$$

Here $\boldsymbol{S}^E$ denotes Eshelby's tensor which is given by:

$$\boldsymbol{S}^E = \boldsymbol{P} : \boldsymbol{C} \tag{3.10}$$

Here $\boldsymbol{P}$ a fourth order modified green operator related to Greens functions as follows:

$$P = \int_{\Omega} \Gamma(r - r') dr' \tag{3.11}$$

Here Ω denotes the volume of the inclusion. Indeed since the matrix does not sustain any eigenstrain the volume integral performed on (3.8) becomes an integral on the inclusion's volume. Also the fourth order tensor $\Gamma(r - r')$ is given by:

$$\Gamma_{ijkl}(r - r') = \frac{1}{2}\left[G_{ki,jl}(r - r') + G_{kj,il}(r - r') + G_{li,jk}(r - r') + G_{lj,ik}(r - r') \right] \tag{3.12}$$

The details of the derivation of the solution to Navier's equation are presented in Appendix A. The solution to the inclusion problem can be used to solve the case of 2-phase inhomogeneous elastic materials. Traditionally the equivalent inclusion method is used. A solution to such a problem is exposed in the following section. However, the solution procedure is based on the fluctuation method. This method will be used in subsequent schemes to solve elastic-viscoplastic problems both in the case of a 2-phase and a 3-phase material's topology.

Linear elastic bi-phased composite material

Consider the problem of a linear elastic material containing a non-homogeneous inclusion. The material is composed of two different phases (e.g., a matrix phase and an inclusion phase) with different elastic tensors. Let us transform this problem into an equivalent problem (see Figure 3.3). The equivalent problem is the following; at any

point within the RVE, the elastic tensor fluctuates in the neighborhood of a value C (it can be considered as an average value of the elastic tensor over the entire volume) that will be evaluated from the self-consistent scheme. The deviation is denoted with δC.
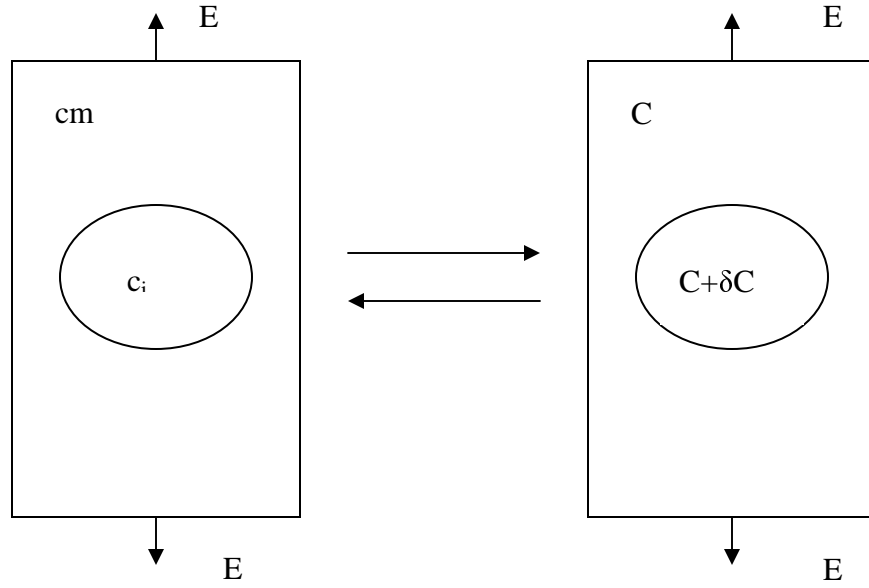
Figure 3.3: Schematic of the linear elastic non homogenous inclusion problem.

Let us derive Navier's equation in the case of the equivalent problem. Recall that the deformation fields and the stress fields must be compatible and at equilibrium at all times. These conditions are written as follows:

$$div\boldsymbol{\sigma} = 0 \tag{3.13}$$

and

$$\boldsymbol{\varepsilon} = \nabla^s \boldsymbol{u} \qquad (3.14)$$

here ∇^s denote the gradient operator. At any point within the material, the local constitutive law is written as follows:

$$\boldsymbol{\sigma}(r) = \boldsymbol{c}(r) : \boldsymbol{\varepsilon}(r) \qquad (3.15)$$

Here r denotes the position of the point. Local fields must respect the macrohomogeneity conditions given by:

$$\int_r \boldsymbol{\sigma}(r')dr = \bar{\boldsymbol{\sigma}} = \boldsymbol{\Sigma} \qquad (3.16)$$

And

$$\int_r \boldsymbol{\sigma}(r')dr = \bar{\boldsymbol{\sigma}} = \boldsymbol{\Sigma} \qquad (3.17)$$

The decomposition of the elastic tensor into the sum of a tensor $\boldsymbol{C}$ and a fluctuation term is written as follows:

$$\boldsymbol{c}(r) = \boldsymbol{C} + \delta\mathbb{C}(r) \qquad (3.18)$$

Similarly, the compliance tensor, denoted $s(r)$, is decomposed into a constant compliance tensor S and a fluctuation term $\delta S(r)$:

$$s(r) = S + \delta S(r) \tag{3.19}$$

Using the constitutive law and both the compatibility and equilibrium conditions one obtains Navier's equation written as follows:

$$C_{ijkl} u_{k,lj} + \left(\delta C_{ijkl} u_{k,l} \right)_{,j} = 0 \tag{3.20}$$

The solution to the equation in the above is found via the use of Green's operator in a manner similar to that exposed in Appendix A. After some algebra, one obtains:

$$\varepsilon_{ij}(r) = E_{ij} - \int_V \Gamma_{ijkl}(r - r') \delta C_{klmn}(r') \varepsilon_{mn}(r') dV \tag{3.21}$$

Here, Γ denotes Green's modified operator given in equation (3.12). In equation (3.21), one can recognize the expression of convolution products, denoted with $\otimes$. Hence, the previous equation can be written in the following form:

$$\varepsilon(r) = E - \Gamma \otimes \delta C : \varepsilon \tag{3.22}$$

Navier's equation can also be written in terms of Kunin's projection operators which are written as follows (Kunin, 1981):

$$\boldsymbol{\Pi}^C = \boldsymbol{\Gamma} : \boldsymbol{C} \tag{3.23}$$

Here, $\boldsymbol{\Pi}^C$ denotes Kunin's operator which has the following properties corresponding to the equilibrium and compatibility conditions, respectively:

$$div(\boldsymbol{\sigma}) = 0 \Leftrightarrow \boldsymbol{\Pi}^C \otimes \boldsymbol{S} : \boldsymbol{\sigma} = 0 \tag{3.24}$$

And

$$\boldsymbol{\varepsilon} = \nabla^s \boldsymbol{u} \Leftrightarrow \boldsymbol{\Pi}^C \otimes \boldsymbol{\varepsilon} = \boldsymbol{\varepsilon} - \boldsymbol{E} \tag{3.25}$$

Finally the solution to Navier's equation also referred to as the integral equation, reads:

$$\boldsymbol{\varepsilon} = \boldsymbol{E} + \boldsymbol{\Pi}^C \otimes \delta\mathbf{S} : \boldsymbol{c} : \boldsymbol{\varepsilon} \tag{3.26}$$

A complete derivation of the integral equation using Kunin's operator is presented in Appendix B. The above relation links the macroscopic strain to the local strain at any point. In terms, this leads to the localization relation.

However, this relation must be averaged in a self-consistent manner to uniquely define the elastic compliance tensor $\boldsymbol{S}$. First, let us decompose the above equation into

the sum of a local term, denoted with subscript *L*, and of a non-local term, denoted with subscript *NL*:

$$\boldsymbol{\varepsilon} = \boldsymbol{E} + \boldsymbol{\Pi}_L^C \otimes \boldsymbol{\delta S} : \boldsymbol{c} : \boldsymbol{\varepsilon} + \boldsymbol{\Pi}_{NL}^C \otimes \boldsymbol{\delta S} : \boldsymbol{c} : \boldsymbol{\varepsilon}$$ (3.27)

Recalling the following property of the convolution product; $f \otimes \delta(r - r') = f$, the local term in (3.27) can be written as a simple double dot product instead of a convolution product. The evaluation of the non-local term is of great complexity. It can be avoided if S is chosen such that the volume average of $\boldsymbol{\delta S} : \boldsymbol{c} : \boldsymbol{\varepsilon}$ is equal to zero. This particular choice is the core basis of the self-consistent approximation. Expanding the volume average of this term and using the macrohomogeneity condition, one obtains:

$$\overline{(s - S) : c : \varepsilon} = \bar{\varepsilon} - S : \overline{c : \varepsilon} = E - S : \Sigma = 0$$ (3.28)

Hence the elastic compliance is equal to the material's effective elastic compliance $S = S^e$. Consequently the self-consistent approximation consists of transforming the original problem into an equivalent problem in which the inclusion has an elastic compliance that fluctuates in the neighborhood of the material's effective compliance and the matrix's compliance is equal to the material's effective compliance. The localization relation is obtained by neglecting the non local-terms of equation (3.27) and introducing the value of the non local elastic compliance. Note here that the non local terms are neglected since the expression presented here below is to be averaged on the

volume of the RVE which will directly set the non local term to zero. After some algebra one obtains the localization relation:

$$\left[I + \Gamma : (c - C^e) \right] : \varepsilon = E \tag{3.29}$$

The localization relation is typically written as follows:

$$\varepsilon = A^{ce} : E \tag{3.30}$$

Owing to the macrohomogeneity condition, this relation applies to both the inclusion and the matrix phase. Moreover, the average of the localization tensors (e.g., of both the inclusion and the matrix phase) must be equal to the fourth order identity tensor. A^{ce} is the fourth order localization tensor given by:

$$A^{ce}(r) = \left[I + \Gamma(r - r') : (c(r) - C^e) \right]^{-1} \tag{3.31}$$

Let us note that since inclusions are supposed ellipsoidal, the localization tensor is equal to its average on the inclusion's volume and does not depend on the position. Also, analytical expressions of the localization tensors can easily be found in the case of isotropic materials. The derivation of the closed forms of the localization tensors in the case of elasticity and viscoplasticity are presented in Appendix C. Hence, the average of the localization relation on the inclusion and matrix volume are given by:

$$\boldsymbol{\varepsilon}^r = \boldsymbol{A}^{ce,r} : \boldsymbol{E} \qquad\qquad \text{with } r = I, M \qquad\qquad (3.32)$$

Here the localization tensor averaged on the inclusion or on the matrix volume is given by:

$$\boldsymbol{A}^{ce,r} = \left[\boldsymbol{I} + \boldsymbol{S}^E : \left(\boldsymbol{C}^e\right)^{-1} : \left(\boldsymbol{c}^r - \boldsymbol{C}^e\right) \right]^{-1} \qquad \text{with } r = I, M \qquad\qquad (3.33)$$

The value of the effective elastic tensor (and its inverse), can now be found via the use of the local constitutive laws and the macrohomogeneity conditions. The effective material's response is simply given by:

$$\boldsymbol{\Sigma} = \boldsymbol{C}^e : \boldsymbol{E} \qquad\qquad\qquad\qquad (3.34)$$

Recall that the volume average of the local stress is equal to the macroscopic stress, using the constitutive laws one obtains:

$$\overline{\boldsymbol{\sigma}} = \overline{\boldsymbol{c} : \boldsymbol{\varepsilon}} = \overline{\boldsymbol{c} : \boldsymbol{A}^{ce}} : \overline{\boldsymbol{\varepsilon}} \qquad\qquad\qquad (3.35)$$

This step corresponds to the homogenization step. The effective elastic tensor is thus found by identification. One obtains:

$$\boldsymbol{C}^e = \overline{\boldsymbol{c} : \boldsymbol{A}^{ce}} \qquad\qquad\qquad\qquad (3.36)$$

For the sake of completeness, let us expand expression (3.36).

$$\boldsymbol{C}^e = f^I c^I \boldsymbol{A}^{ceI} + f^M c^M \boldsymbol{A}^{ceM} \qquad (3.37)$$

Note here that both localization tensors are explicitly dependent on the effective elastic modulus tensor. Hence, equation (3.37) needs to be solved numerically. The derivation of the closed form of equation (3.37) is presented in appendix C.

Time dependent responses

The fundamentals of micromechanics derived in the previous section can be extended to the case of time dependent response. In the present section, two micromechanical schemes used in Chapter 4 will be recalled.

The first scheme developed by Cherkaoui et al. (2000) is a two- phase elastic-viscoplastic self-consistent scheme corresponding to an extension to the KBW model to the case of materials with inhomogeneous elastic response. Throughout this thesis this scheme will be referred to as 2PEVP.

The second scheme to be exposed was introduced by Berbenni et al. (2004). It is an extension of the 2PEVP scheme based on translated fields, and will be referred to as the 2PEVPT scheme. While the 2PEVP model accounts for the heterogeneity in the plastic responses with elastic terms, the 2PEVPT scheme allows softer predictions owing to its accommodation of the plastic heterogeneities.

2PEVP

Consider a RVE similar to that shown in Figure 3.3 where both constituents are capable of plastic deformation. Locally, the strain rate can be decomposed into the sum of the elastic strain rate and the viscoplastic strain rate:

$$\dot{\varepsilon} = \dot{\varepsilon}^e + \dot{\varepsilon}^{vp} \tag{3.38}$$

The local constitutive law reads:

$$\dot{\sigma} = c : \dot{\varepsilon}^e \tag{3.39}$$

Using the decomposition of the elastic tensor modulus (and its inverse) presented in previous section, the double dot product of the local stress rate with the spatially constant compliance tensor is written as:

$$S : \dot{\sigma} = S : c : \dot{\varepsilon}^e = (s - \delta S) : c : \dot{\varepsilon}^e = \dot{\varepsilon} - \dot{\varepsilon}^{vp} - \delta S : c : \dot{\varepsilon} \tag{3.40}$$

Using the properties of Kunin's projection operator one obtains the following:

$$\Pi^C \otimes S : \dot{\sigma} = \dot{\varepsilon} - \dot{E} - \Pi^C \otimes \dot{\varepsilon}^{vp} - \Pi^C \otimes \delta S : c : \dot{\varepsilon}^e = 0 \tag{3.41}$$

The equation in the above relates the local strain rate to the macroscopic strain rate and to the local elastic and viscoplastic strain rates. Let us now decompose the viscoplastic

strain rate into the sum of two contributions: (1) a contribution which is independent of the position (but not independent on time t), this contribution can be seen as a spatial average of the viscoplastic strain rate, and (2) a fluctuation dependent on the position in the neighborhood of the first contribution. With this hypothesis one can write the local viscoplastic strain rate as follows:

$$\dot{\boldsymbol{\varepsilon}}^{vp}(r) = \dot{\boldsymbol{E}}^{vp} + \boldsymbol{\delta}\dot{\boldsymbol{\varepsilon}}^{vp}(r) \tag{3.42}$$

Notice the presence of the projection of (3.42) in (3.41). Introducing the above equation in (3.41), and using the compatibility conditions, one obtains the following integral equation:

$$\dot{\boldsymbol{\varepsilon}} = \dot{\boldsymbol{E}} + \boldsymbol{\Pi}^C \otimes \left[\delta \boldsymbol{S} : \boldsymbol{c} : \dot{\boldsymbol{\varepsilon}}^e + \delta\dot{\boldsymbol{\varepsilon}}^{vp} \right] \tag{3.43}$$

Let us note that two terms are to be evaluated in this expression: (1) the constant compliance tensor and, (2) the spatially invariant viscoplastic strain rate. These two terms are obtained via the self-consistent approximation. Indeed, the above equation can be decomposed into the sum of a local term and of a non-local term which spatial average is set to zero.

$$\overline{\delta \mathrm{S} : \boldsymbol{c} : \dot{\boldsymbol{\varepsilon}}^e + \boldsymbol{\delta}\dot{\boldsymbol{\varepsilon}}^{vp}} = 0 \tag{3.44}$$

After some algebra involving the use of the macrohomogeneity condition, one obtains the self-consistent estimate of the two unknown tensors, namely:

$$S = S^e \tag{3.45}$$

And

$$\dot{E}^{vp} = \dot{E}^{vpe} \tag{3.46}$$

Finally, with the above estimates, the localization relation is written as follows:

$$\dot{\varepsilon}(\rho) = A^{ce}(r):\dot{E} + A^{ce}(r):\Gamma^{ce}(r-r'):\left[c(r):\dot{\varepsilon}^{vp}(r) - C^e:\dot{E}^{vpe}\right] \tag{3.47}$$

The values of the effective compliance tensors and strain rate tensor are obtained simply with use of the macrohomogeneity conditions which consists of averaging the local constitutive laws over the RVE volume. Precisely, recalling that in the case of an ellipsoidal inclusion the localization tensors are constant in each phase the average of (3.47) on the inclusion's volume leads to:

$$\dot{\varepsilon}^I = \frac{1}{\Omega}\int_\Omega \dot{\varepsilon}(r)dr = \frac{1}{\Omega}\int_\Omega A^{ce}:\dot{E}dr + A^{ce}:\frac{1}{\Omega}\int_\Omega \Gamma dr:\left[c:\dot{\varepsilon}^{vp} - C^e:\dot{E}^{vpe}\right] \tag{3.48}$$

In the above equation one can notice the presence of the fourth order tensor $\boldsymbol{P}$ which is related to Eshelby's tensor. Hence, one obtains, after some algebra:

$$\dot{\boldsymbol{\varepsilon}}^{I} = \boldsymbol{A}^{ceI} : \dot{\boldsymbol{E}} + \boldsymbol{A}^{ceI} : \boldsymbol{S}^{E} : \left(\boldsymbol{C}^{e}\right)^{-1} : \left[\boldsymbol{c}^{I} : \dot{\boldsymbol{\varepsilon}}^{vpI} - \boldsymbol{C}^{e} : \dot{\boldsymbol{E}}^{vpe}\right] \qquad (3.49)$$

Let us note that the second term on the right hand side accounts for the inhomogeneity in the viscoplastic response which is weighted solely with elastic terms. This leads to slightly overestimated viscoplastic responses. Equation (3.49) is typically written in as follows

$$\dot{\boldsymbol{\varepsilon}}^{I} = \boldsymbol{A}^{ceI} : \dot{\boldsymbol{E}} + \boldsymbol{a}^{I} \qquad (3.50)$$

Where the second order tensor $\boldsymbol{a}^{I}$ is given by:

$$\boldsymbol{a}^{I} = \boldsymbol{A}^{ceI} : \boldsymbol{S}^{E} : \left(\boldsymbol{C}^{e}\right)^{-1} : \left[\boldsymbol{c}^{I} : \dot{\boldsymbol{\varepsilon}}^{vpI} - \boldsymbol{C}^{e} : \dot{\boldsymbol{E}}^{vpe}\right] \qquad (3.51)$$

As can be observed in the above equation, Kroner's scheme (1961) can be obtained simply by considering the case of a 2-phase material with homogeneous elastic response. Finally, the effective viscoplastic strain rate and elastic modulus tensor are obtained with use of the macrohomogeneity condition giving:

$$\boldsymbol{C}^{e} = f^{I} \boldsymbol{c}^{I} \boldsymbol{A}^{ceI} + f^{M} \boldsymbol{c}^{M} \boldsymbol{A}^{ceM} \qquad (3.52)$$

151

And

$$\dot{E}^{vpe} = f^I A^{ceI} : S^E : \left(C^e \right)^{-1} : c^I : \dot{\varepsilon}^{vpI} + \left(1 - f^I \right) A^{ceM} : S^E : \left(C^e \right)^{-1} : c^M : \dot{\varepsilon}^{vpM} \qquad (3.53)$$

2PEVPT

Let us now briefly expose the derivations of the 2PEVPT model introduced by Berbenni et al. (2004). In order to derive this scheme, one must proceed in two steps: (1) consider a purely viscous case and, (2) using the translated field method in the case of an elastic-viscoplastic material.

Viscoplastic self-consistent scheme

Consider the case of a two-phase viscoplastic material. The local constitutive laws are then written as follows:

$$\dot{\varepsilon}^{vp} = m : \sigma \qquad (3.54)$$

Here m denotes the fourth order viscosity tensor with inverse b. Similarly the macroscopic response is written as follows:

$$\dot{E}^{vpe} = M^e : \Sigma \qquad (3.55)$$

Here M^e denotes the fourth order macroscopic viscosity tensor with inverse denoted with

$\boldsymbol{B}^e$. Note here that in order to distinguish the elastic case from the viscoplastic case, the superscript B will be used to denote the viscoplastic case. Let us recall the expression of Kunin's projection operators, denoted $\boldsymbol{\Pi}^B$ in the case of viscoplasticity:

$$\boldsymbol{\Pi}^B = \boldsymbol{\Gamma}^B : \boldsymbol{B} \tag{3.56}$$

Here $\boldsymbol{B}$ is a spatially invariant inverse of the viscosity tensor. $\boldsymbol{\Gamma}^B$ is Green's operator in the viscoplastic case. The equilibrium and compatibility conditions are written as follows, respectively:

$$div(\boldsymbol{\sigma}) = 0 \Leftrightarrow \boldsymbol{\Pi}^B \otimes \boldsymbol{M} : \boldsymbol{\sigma} = 0 \tag{3.57}$$

And

$$\boldsymbol{\varepsilon} = \nabla^s \boldsymbol{u} \Leftrightarrow \boldsymbol{\Pi}^C \otimes \dot{\boldsymbol{\varepsilon}}^{vp} = \dot{\boldsymbol{\varepsilon}}^{vp} - \dot{\boldsymbol{E}}^{vp} \tag{3.58}$$

Here the tensor $\boldsymbol{M}$ is given by the decomposition of the local viscosity tensors (the same relation is also valid for the inverse of the viscosity tensors):

$$\boldsymbol{m}(r) = \boldsymbol{M} + \delta\boldsymbol{m}(r) \tag{3.59}$$

Here, $\boldsymbol{M}$ and $\delta\boldsymbol{m}(r)$ denote the spatially invariant viscosity tensors and its fluctuation, respectively. Using the equilibrium and compatibility conditions the integral equation can

be obtained in a manner similar to that presented in the case of a composite elastic material:

$$\dot{\boldsymbol{\varepsilon}}^{vp} = \dot{\boldsymbol{E}}^{vp} + \boldsymbol{\Pi}^B \otimes \boldsymbol{\delta m} : \boldsymbol{b} : \dot{\boldsymbol{\varepsilon}}^{vp} \tag{3.60}$$

Using the decomposition of the integral equation into a local and a non-local part and the self-consistent approximation, one obtains the localization relation given by:

$$\dot{\boldsymbol{\varepsilon}}^{vp} = \boldsymbol{A}^{Be} : \dot{\boldsymbol{E}}^{vpe} \tag{3.61}$$

with

$$\boldsymbol{M} = \boldsymbol{M}^e \tag{3.62}$$

And

$$\boldsymbol{A}^{Be} = \left[\boldsymbol{I} + \boldsymbol{S}^E : \left(\boldsymbol{B}^e \right)^{-1} : (\boldsymbol{b} - \boldsymbol{B}^e) \right]^{-1} \tag{3.63}$$

Similarly to the elastic composite material's case, the effective viscosity tensors are obtained via use of the macrohomogeneity condition. Therefore it will not be recalled here.

Field translation

A solution to the elastic-viscoplastic case can be obtained with use of the previously developed scheme. Let us now consider a two-phase elastic-viscoplastic material. Suppose the decomposition of the local strain rate tensor (which is dependent on both time, t, and position, r) into the sum of a first term independent on time, but dependent on position, which can be seen as a local value averaged on time in the neighborhood of which a second term, corresponding to local fluctuations, and thus depending on both time and position, will evolve:

$$\dot{\boldsymbol{\varepsilon}}^{vp}(r,t) = \dot{\tilde{\boldsymbol{\varepsilon}}}^{vp}(r) + \delta\dot{\boldsymbol{\varepsilon}}^{vp}(r,t) \tag{3.64}$$

Here $\dot{\tilde{\boldsymbol{\varepsilon}}}^{vp}$ and $\delta\dot{\boldsymbol{\varepsilon}}^{vp}$ denote the time invariant term and the fluctuation term, respectively. From the decomposition of the strain rate into the sum of the elastic strain rate and the viscoplastic strain rate, the macroscopic constitutive law can be written:

$$\dot{\boldsymbol{E}} = \boldsymbol{S}:\dot{\boldsymbol{\Sigma}} + \dot{\tilde{\boldsymbol{E}}}^{vp} \tag{3.65}$$

Here the tensor $\dot{\tilde{\boldsymbol{E}}}^{vp}$ is the translated viscoplastic tensor solution of the fictitious viscoplastic problem which is related to the time invariant local viscoplastic strain rate field via the previously derived viscoplastic localization relation (Sabar et al. 2002):

$$\dot{\tilde{\boldsymbol{\varepsilon}}}^{vp} = \boldsymbol{A}^{Be}:\dot{\tilde{\boldsymbol{E}}}^{vpe} \tag{3.66}$$

This field can be projected with use of Kunin's operator. Also, using the decomposition of the elactic tensor and the solution to the elastic problem, one obtains the expression of the integral equation given by:

$$\dot{\boldsymbol{\varepsilon}} = \dot{\boldsymbol{E}} + \boldsymbol{A}^{Be} : \dot{\tilde{\boldsymbol{E}}}^{vp} - \dot{\tilde{\boldsymbol{E}}}^{vp} + \boldsymbol{\Pi}^{C} \otimes \left[\boldsymbol{\delta S} : \boldsymbol{c} : \dot{\boldsymbol{\varepsilon}}^{e} + \boldsymbol{\delta\dot{\varepsilon}}^{vp} \right] \tag{3.67}$$

Finally, the unknown tensors are estimated via the self-consistent approximation:

$$\boldsymbol{S} = \boldsymbol{S}^{e} \tag{3.68}$$

And

$$\dot{\tilde{\boldsymbol{E}}}^{vp} = \dot{\boldsymbol{E}}^{vpe} \tag{3.69}$$

Introducing, the above results the localization relation reads

$$\dot{\boldsymbol{\varepsilon}} = \boldsymbol{A}^{Ce} : (\dot{\boldsymbol{E}} - \dot{\boldsymbol{E}}^{vpe}) + \boldsymbol{A}^{Ce} : \boldsymbol{A}^{Be} : \dot{\boldsymbol{E}}^{vpe} + \boldsymbol{A}^{Ce} : \boldsymbol{S}^{E} : \boldsymbol{S}^{e} (\boldsymbol{c}\dot{\boldsymbol{\varepsilon}}^{vp} - \boldsymbol{C}^{e} : \boldsymbol{A}^{Be} : \dot{\boldsymbol{E}}^{vpe}) \tag{3.70}$$

It can be noticed that the above localization relation accommodates the inhomogeneity in the viscoplastic response not only in terms of elastic constants but also with the viscoplastic localization tensors, $\boldsymbol{A}^{Be}$, obtained in the case of a viscoplastic biphased composite material. Consequently this scheme leads to softer response than that obtained with use of the 2PEVP scheme.

156

Novel models

Let us now introduce two novel micromechanical schemes based on the three-phase approach initially introduced by Christensen and Lo (1979) and on the two-phase model for slightly weakened interfaces introduced by Qu (1993). These two schemes will be used in Chapter 5.

A first model, developed in cooperation with Saad Benkassem (Benkassem Capolungo et al. 2007) and corresponding to an extension of work by Cherkaoui (2000) on micromechanics of mobile interfaces is presented. As discussed by Cherkaoui (1996), three-phases models are more suited to precisely describe the effect of interfaces (typically modeled as thin layers of interphase) on the response of polycrystalline aggregates. This scheme will be referred to as 3PVP (3 Phase Visco Plastic). While it allows interface motion, which is appropriate to treat mass transfer and diffusion problems, it does not account for the relative sliding

The second model, which will be referred to as 2PEVPWI (2 Phase Elastic Visco Plastic with Weakened interface), is valid in the case of elastic-viscoplastic materials. It is based on the translated field approach (Sabar et al. 2002) and inspired by Qu's early work on slightly weakened interface (1993). Therefore, the case of imperfect interface bonding can be treated. An application will be shown in Chapter 5 where the effect of unaccomodated grain boundary sliding will be briefly treated.

The topology of the three-phase model, introduced by Christensen and Lo (1979), relies on the assumption that the real material can be represented by a volume element including a single coated inclusion embedded in a homogeneous equivalent medium. This is clearly an extension of the composite sphere model. In the case of NC materials, the inclusion phase represents grain cores while the coating phase represents both grain boundaries and triple junctions.
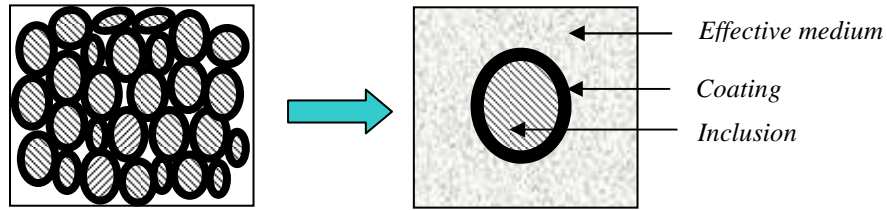
Figure 3.4: Schematic of topology of the three phase problem.

3PVP model

<u>Localization relations</u>

The macroscopic behaviour of the material is purely viscoplastic and can be written as follows:

$$\dot{\boldsymbol{E}} = \boldsymbol{M}^e : \boldsymbol{\Sigma}$$

(3.71)

Similarly, within the inclusion and coating phase the local constitutive laws are written as follows:

$$\dot{\varepsilon}^r = \boldsymbol{m}^r : \boldsymbol{\sigma}^r \qquad\qquad \text{with } r{=}I,C \qquad\qquad (3.72)$$

The local strain rates will be related to the macroscopic strain rate via the localization relations:

$$\dot{\varepsilon}^r = \boldsymbol{A}^r : \dot{\boldsymbol{E}} \qquad\qquad \text{with } r{=}I,C \qquad\qquad (3.73)$$

Here, $\boldsymbol{A}^r$ represents the fourth order concentration tensor which expression will be derived in the following. Using the macrohomogeneity condition, the effective inverse of the viscosity tensor, $\boldsymbol{B}^e$, can be expressed in function of its local equivalent and of the average localization tensor in the inclusion phase:

$$\boldsymbol{B}^e = \boldsymbol{b}^C + f^I \left(\boldsymbol{b}^I - \boldsymbol{b}^C \right) : \boldsymbol{A}^I \qquad\qquad (3.74)$$

Here f^I denotes the volume fraction of the inclusion phase which is given by:

$$\frac{V^I}{V^{IC}} = \frac{f^I}{f^I + f^c} = f^I \qquad\qquad (3.75)$$

Here V^I and V^{IC} denote the volume of the inclusion and of the coated inclusion, respectively. Similarly one can define the volume fraction of the coating phase as follows:

$$\frac{V^C}{V^{IC}} = \frac{f^c}{f^I + f^c} = f^c \tag{3.76}$$

Here V^C denotes the volume of the coating phase. Let us now derive the expression of the localization tensors. At any point within the material the viscosity tensor can be decomposed into the sum of a spatially constant term, which is equal to the effective viscosity via the use of the self-consistent approximation, and of a fluctuation term engendered by the viscoplastic heterogeneity introduced by the inclusion and its coating:

$$\boldsymbol{b}(r) = \boldsymbol{B}^e + \delta\boldsymbol{b}(r) \tag{3.77}$$

The concentration tensors are then determined via the simultaneous use of the integral equation (Dederich et al., 1973; Eshelby, 1961; Hill, 1983) and of interfacial operators (Walpole 1978, Hill 1983). With the above decomposition of the viscosity tensor, the integral equation is given by:

$$\dot{\boldsymbol{\varepsilon}} = \dot{\boldsymbol{E}} - \int_V \boldsymbol{\Gamma}(r - r') : \delta\boldsymbol{b}(r') : \dot{\boldsymbol{\varepsilon}}(r') \, dr' \tag{3.78}$$

Where r is an arbitrary point, $\boldsymbol{\Gamma}(r - r')$ denotes Green's modified operator. Heavyside step functions are introduced to describe the fluctuating part of the inverse of the viscosity tensors:

$$\theta^I(r) = \begin{cases} 1 \ if \ r \in V^I \\ 0 \ if \ r \notin V^I \end{cases} \quad and \quad \theta^{IC}(r) = \begin{cases} 1 \ if \ r \in V^{IC} = V^I + V^C \\ 0 \ if \ r \notin V^{IC} \end{cases} \quad (3.79)$$

Accordingly, the volume of the coating is described by the following Heavyside function:

$$\theta^C(r) = \theta^{IC}(r) - \theta^I(r) \quad (3.80)$$

Hence, the fluctuating term $\delta \boldsymbol{b}(r)$ in equation can be written as:

$$\delta \boldsymbol{b}(r) = \Delta \boldsymbol{b}^I \theta^I(r) + \Delta \boldsymbol{b}^C \theta^C(r) \quad (3.81)$$

Where $\Delta \boldsymbol{b}^I = \boldsymbol{b}^I - \boldsymbol{B}^e$ and $\Delta \boldsymbol{b}^C = \boldsymbol{b}^C - \boldsymbol{B}^e$. Introducing the above decomposition into the integral equation one obtains

$$\dot{\boldsymbol{\varepsilon}} = \dot{\boldsymbol{E}} - \int_{V^I} \Gamma(r-r') : \Delta \boldsymbol{b}^I(r') : \dot{\boldsymbol{\varepsilon}}(r') dr' - \int_{V^C} \Gamma(r-r') : \Delta \boldsymbol{b}^C(r') : \dot{\boldsymbol{\varepsilon}}(r') dr' \quad (3.82)$$

Let us introduce the interaction tensor defined as the integral of Green's modified operator in the coated inclusion volume. It is written as follows:

$$\boldsymbol{T}(\boldsymbol{B}^e) = \int_{V^{IC}} \Gamma(r-r') dr' \quad (3.83)$$

Introducing (3.83) into (3.82) and taking the average of the resulting equation on the

coated inclusion's volume one obtains the localization relation:

$$\dot{E} = \frac{V^I}{V^{IC}} \left\{ \boldsymbol{I} + \boldsymbol{T}\left(b^{\mathit{eff}}\right) : \Delta \boldsymbol{b}^I \right\} : \dot{E}^I + \frac{V^C}{V^{IC}} \left\{ \boldsymbol{I} + \boldsymbol{T}\left(b^{\mathit{eff}}\right) : \Delta \boldsymbol{b}^C \right\} : \dot{E}^C \qquad (3.84)$$

For (3.84) to be complete, a relationship between the local averaged strain rates in the

inclusion and in the effective medium must be introduced via the use of interfacial

operators which are presented below.

Interfacial operators

   In this section, interface relations between 2 phases are presented in a general case. The

superscript 1 and 2 refer to phase 1 and phase 2, respectively. A schematic of such an

interface is given in Figure 3.5.
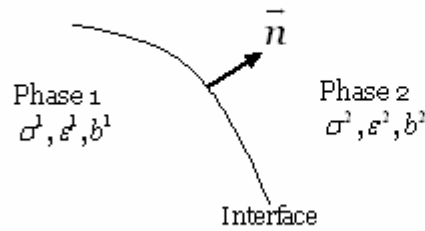
Figure 3.5: schematic of an interface.

   The relatively small thickness of the coating (~1nm) justifies the use of the thin layer

assumption. Moreover, perfect bonding is assumed between the inclusion and its coating.

Accordingly, the displacement across an interface must be continuous and must respect the following equation.

$$\left[u_i \right] = 0 \quad , u_i^2 - u_i^1 = 0 \quad \text{with } i=1,3 \tag{3.85}$$

Where $\left[\cdot \right]$ denotes a jump across the inclusion/coating interface and u denotes the displacement vector. From the continuity of the traction vector one obtains:

$$\left[\sigma_{ij} \right] n_j = \left(\sigma_{ij}^1 - \sigma_{ij}^2 \right) n_j = 0 \tag{3.86}$$

Where n_i is the outward unit normal on the interface. Hadamard's compatibility conditions (1903) for a moving interface Σ are given by:

$$\left[v_i \right] = -\left[u_{i,j} \right] n_j w_\alpha n_\alpha \tag{3.87}$$

where v_i is the velocity of particles at S , w_α denotes the propagation velocity of the interface Σ, n_α is the normal on the surface Σ, $u_{i,j}$ is the displacement gradient and n_j the normal to the element of surface dS. Moreover, since the interface is stationary one obtains $w_\alpha = 0$ and $\left[v_i \right] = 0$. At an arbitrary point $r(x_i)$ of the interface, the compatibility condition $du_i = u_{i,j} dx_j$ added to the continuity of displacement along the

boundary imposes the following condition on the jump of the gradient of the displacement:

$$\left[u_{i,j}\right]dx_j = \left(u^1_{i,j} - u^2_{i,j}\right)dx_j = 0 \; ; \quad \text{or} \quad \left[u_{i,j}\right] = u^1_{i,j} - u^2_{i,j} = \lambda_i n_j \tag{3.88}$$

From the symmetry of the strain tensor, the jump in the strain rate $\left[\dot{\varepsilon}_{ij}\right]$ across the interface is given by:

$$\left[\dot{\varepsilon}\right] = \dot{\varepsilon}^1 - \dot{\varepsilon}^2 = \frac{1}{2}\left(\lambda_i n_j + \lambda_j n_i\right) \tag{3.89}$$

Here λ_i is a proportionality factor corresponding to the magnitude of the jump. From the equilibrium condition and with the use of the local constitutive laws one obtains:

$$\boldsymbol{b}^1 : \dot{\boldsymbol{\varepsilon}}^1 n_j = \boldsymbol{b}^2 : \dot{\boldsymbol{\varepsilon}}^2 : n_j \tag{3.90}$$

Introducing (3.89) into (3.90) leads to:

$$\left[\boldsymbol{b}^1 - \boldsymbol{b}^2\right] : \dot{\boldsymbol{\varepsilon}}^1 n_j = \boldsymbol{b}^2 : n_l n_j \lambda_k \tag{3.91}$$

The strain rate jump across the interface is obtained from (3.91) and given by:

$$\lambda_i = K_{ik}^{-1} n_l \left[\boldsymbol{b}^1 - \boldsymbol{b}^2 \right] : \dot{\boldsymbol{\varepsilon}}^1 \tag{3.92}$$

Here Christofells's matrix is denoted by $K_{ik} = \boldsymbol{b}_{ijkl}^2 n_l n_j$. Introducing (3.92) into (3.89) one

obtains the expression of strain rate jump across the interface:

$$\dot{\boldsymbol{\varepsilon}}^2 - \dot{\boldsymbol{\varepsilon}}^1 = \boldsymbol{P}^2 : \left[\boldsymbol{b}^1 - \boldsymbol{b}^2 \right] : \dot{\boldsymbol{\varepsilon}}^1 \tag{3.93}$$

where $\boldsymbol{P}^r$ with r=1, 2, denotes the interfacial operator, introduced by Hill (1983) and

dependent of the unit normal $\vec{n}$.

Localization tensors

In what follows the interface relations developed in the previous section are applied to

the topology of the three-phase model which will lead to the expressions of the

localizations tensors. Applying (3.93) to the case of the coated inclusion problem leads

to:

$$\dot{\boldsymbol{\varepsilon}}^C (r) = \dot{\boldsymbol{\varepsilon}}^I (r') + \boldsymbol{P}^C : \Delta \boldsymbol{b}^{IC} : \dot{\boldsymbol{\varepsilon}}^I (r') \tag{3.94}$$

Where $r \in \mathrm{V}^C$ and $r' \in \mathrm{V}^I$; $\Delta \boldsymbol{b}^{Ic} = \boldsymbol{b}^I - \boldsymbol{b}^c$. Let us suppose the local strain rate in the

inclusion to be homogeneous and evaluate the average strain rate within the coating, one

obtains:

$$\dot{\boldsymbol{E}}^C = \dot{\boldsymbol{E}}^I + \boldsymbol{T}^C\left(\boldsymbol{b}^C\right):\Delta\boldsymbol{b}^{IC}:\dot{\boldsymbol{E}}^I$$

(3.95)

Where the interaction tensor is written as follows:

$$\boldsymbol{T}^C\left(\boldsymbol{b}^C\right) = \frac{1}{V^C}\int_{V^C}\boldsymbol{P}^C dr$$

(3.96)

Finally, the localisation tensors in each phase are simply obtained by introducing (3.95) into(3.84); one obtains:

$$\boldsymbol{A}^I = \left[\begin{array}{l} f^I\left(\boldsymbol{I}+\boldsymbol{T}\left(b^{e\!f\!f}\right):\Delta\boldsymbol{b}^I\right)+ \\ + f^c\left(\boldsymbol{I}+\boldsymbol{T}\left(b^{e\!f\!f}\right):\Delta\boldsymbol{b}^c\right):\left(\boldsymbol{I}+\boldsymbol{T}^c\left(b^c\right):\left(\Delta\boldsymbol{b}^{IC}\right)^{-1}\right) \end{array}\right]^{-1}$$

(3.97)

and

$$\boldsymbol{A}^c = \left[\boldsymbol{I}+\boldsymbol{T}^c\left(b^c\right):\Delta\boldsymbol{b}^{Ic}\right]:\boldsymbol{A}^I$$

(3.98)

The algebra leading to the above equations is similar to that developed by Cherkaoui et al. (1995). In conclusion, the complete localization relations are obtained by introducing the above localization tensors in the localization relations (3.61). Also, the effective viscosity tensor is obtained with use of the expression of the localization tensor of the inclusion phase. As can be seen this scheme shall lead to softer prediction of the

viscoplastic response than that of the two phase viscoplastic model presented previously. This is due to the fact that the heterogeneity of the viscoplastic strain rates is accommodated with the use of interaction tensors.

2PEVPWI model

The problem of elastic-viscoplastic coated inclusions with imperfect interfaces (which could potentially lead to material failure via grain boundary sliding in the case of NC Materials) requires the solution of two complex sub-problems: (1) the development of an appropriate self-consistent scheme valid in the case of coated inclusions with elastic-viscoplastic behaviors and, (2) the development of relations accounting for the effect of imperfect interfaces on the relative state of deformation in the different constituents.

In the case of problem (1), generalized self-consistent schemes, also referred to as three phase models, were developed in the particular case of purely elastic or purely viscoplastic behaviors (e.g. 3PVP) and solutions can be obtained in the case of perfect interfaces. Accordingly, the existing solutions need to be extended to the case of elastic-viscoplastic behaviors.

The proposed procedure for the solution of problem (1) and (2) is presented in Figure 3.6 (Capolungo et al. 2007). As detailed in the introduction to this chapter, the effective response of the material can be related to the local response of the constituents via the localization relation which is to be obtained via the consecutive use of two schemes for the following problems: (1) two-phase composite composed of inclusions

and coating with imperfect interface, where Qu's development (1993) can be easily

extended and, (2) two-phase composite composed of homogenized coated inclusions and

the homogenous material solution of the three-phase viscoplastic problem. In other

words, the interface relations in a three phase problem are obtained by the consecutive

solutions of two approximated bi-phase problems.

The solution obtained in the pure viscoplastic case will then be translated, in the

same sense as defined by Sabar et al. (2002), to solve the elastic-viscoplastic solution.

```
┌─────────────────────────────┐
│  Mori Tanaka scheme for the │
│  coating/inclusion materials│
│   with imperfect interface  │
└─────────────────────────────┘
               │
               ▼
┌─────────────────────────────┐
│ Self-consistent scheme for the│
│    homogenized coated        │
│  inclusion/homogeneous       │
│ materials with perfect interface│
└─────────────────────────────┘
               │
               ▼
┌─────────────────────────────┐
│      Evaluation of the      │
│     localization relation   │
└─────────────────────────────┘
               │
               ▼
┌─────────────────────────────┐
│    Solution for the pure    │
│      viscoplastic case      │
└─────────────────────────────┘
               │
               ▼
┌─────────────────────────────┐
│      Translation of the     │
│       viscoplastic field    │
│          solution           │
└─────────────────────────────┘
               │
               ▼
┌─────────────────────────────┐
│    Development of the       │
│  integral equation in the   │
│  elastic-viscoplastic case  │
└─────────────────────────────┘
               │
               ▼
┌─────────────────────────────┐
│   Application of the self-  │
│         consistent          │
│        approximation        │
└─────────────────────────────┘
               │
               ▼
┌─────────────────────────────┐
│   Solution for the elastic- │
│       viscoplastic case     │
└─────────────────────────────┘
```

Figure 3.6: Schematic of the scale transition procedure.

Prior to solving the problem of coated inclusions with imperfect interfaces in the case of elastic-viscoplastic behaviors, let us treat the case of pure viscoplastic behaviors.

Interface relations

Considering the complexity of the approach, the interface relation will be approximated in two steps (see Figure 3.7). First, the discontinuity between the inclusion and the coating will be treated. This interface is not perfect and allows relative sliding of the inclusions with respect to the coating is allowed. The behavior of the homogenized coated inclusion will be extracted from the application of a Mori Tanaka scheme. Second, the homogeneous medium/homogeneous coated inclusion discontinuity is treated. In this case the interface is perfect. Linking the solutions of step 1 and step 2 will lead to the desired expression of the localization relation. However, let us note here that the inclusion/coating relation is clearly approximated in this approach.
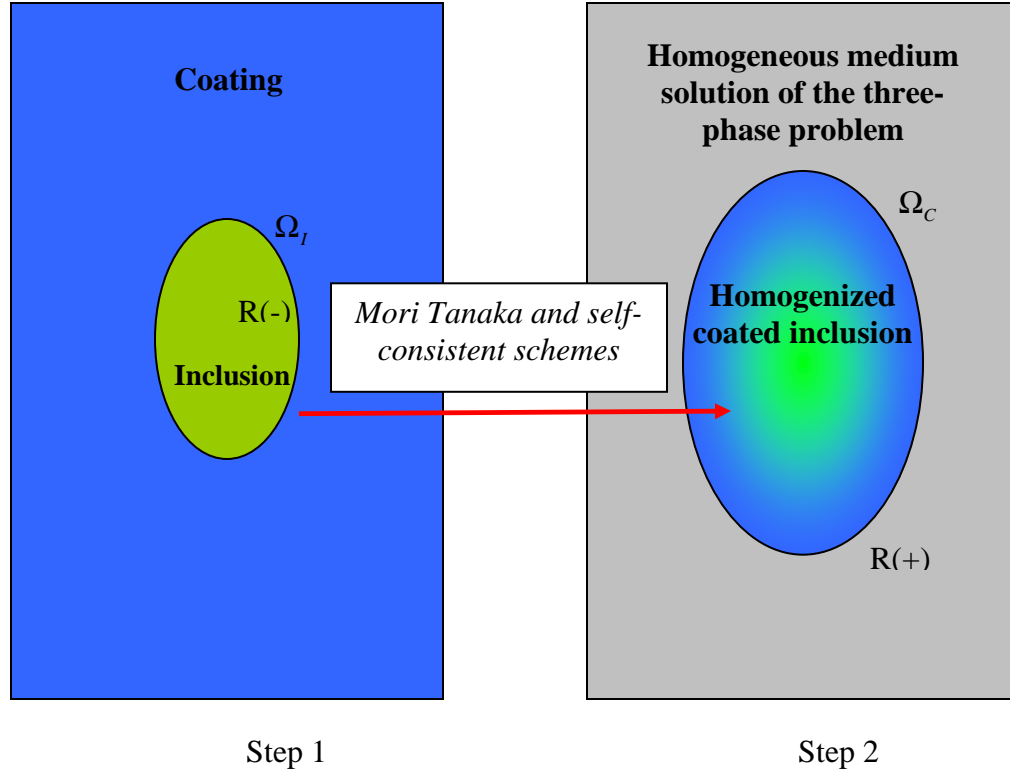
Figure 3.7: Schematic of the two steps used to solve the 3-phase viscoplastic problem.

Coating/inclusion interface

For the sake of clarity let us recall that the problem to be solved in this section

corresponds to the case of a two-phase material composed of an inclusion phase

embedded in a matrix phase. Also, in this case the inclusion coating interface is not

perfect. Across the coating/inclusion interface the traction vector remains continuous,

hence:

$$\Delta\sigma_{ij}n_j \equiv [\sigma_{ij}(S^+) - \sigma_{ij}(S^-)]n_j = 0 \quad , \tag{3.99}$$

Here the superscripts + and – denotes the respective positive and negative sides of the interface. $\boldsymbol{n}$ denotes the vector normal to the interface. The jump condition across the interface is given here in a manner similar to that proposed by Qu (1993) and relates the jump in the displacement to the stress at the interface with a tensor η_{ij} :

$$\Delta u_i \equiv u_i(S^+) - u_i(S^-) = \eta_{ij}\sigma_{jk}n_k \quad , \tag{3.100}$$

Here, η_{ij} represents the compliance of the interface and is given by:

$$\eta_{ij} = \alpha\delta_{ij} + (\beta - \alpha)n_i n_j \tag{3.101}$$

For the sake of illustration a sliding law is proposed. This law will be discussed in details in Chapter 5. Note that in the case where $\beta = 0$, the relative motion of the coating with respect to the inclusion will not lead to void creation. α could be given by a formula of the following form:

$$\alpha = \frac{\delta_c}{\sigma_c\left(1 - \dfrac{\sum_i [u_i]}{\delta_c}\right)} \tag{3.102}$$

Here δ_c and σ_c denote a critical distance and a critical stress, respectively. This expression simply corresponds to the converse of that proposed by Warner and Molinari

172

(2006) for the description of the stick-slip mechanism. The proposed scheme could be easily adapted to other types of sliding conditions. From the equilibrium condition and the viscoplastic constitutive laws, the following equation can be established at any point r within the RVE:

$$b_{ijlk}^{C} \frac{\partial^2 G_{km}^{\infty}(r,r')}{\partial x_l \partial x_j} + \delta_{im} \delta(r-r') = 0 \tag{3.103}$$

Here, $\boldsymbol{b}^{*}$ is a viscosity tensor to be determined with the use of self consistent scheme. It corresponds to the viscosity tensor of the homogenized coated inclusion. Let us note that this equation corresponds to Navier's equation in the viscoplastic case which is to be solved via the use of Green's functions. Hence the derivation of this equation is essentially the same as that of (3.20)

Let us use Green's equivalent function, $\boldsymbol{G}^{\infty}$, in the case of pure viscoplastic behaviors, defined as follows:

$$\int_{\Omega} \dot{u}_i(r) b_{ijkl}^{C} \frac{\partial^2 G_{km}^{\infty}(r,r')}{\partial x_l \partial x_j} d\Omega(r) = \begin{cases} -\dot{u}_m(r') & r' \in \Omega \\ \\ 0 & r' \notin \Omega \end{cases} \tag{3.104}$$

Where $\delta(\mathbf{x})$ is the three-dimensional Dirac delta function. Also, let us integrate the following equation on a volume, denoted with Ω, and multiply it by the displacement rate vector, one obtains:

173

$$\int_{\Omega} \dot{u}_i(r) b_{ijkl}^* \frac{\partial^2 G_{km}^\infty(r,r')}{\partial x_l \partial x_j} d\Omega(r) = \begin{cases} -\dot{u}_m(r') & r' \in \Omega \\ \\ 0 & r' \notin \Omega \end{cases} . \tag{3.105}$$

Using the divergence theorem, one can rewrite the volume integral in (3.105) as:

$$\int_{\Omega} \dot{u}_i(r) b_{ijkl}^C \frac{\partial^2 G_{km}(r,r')}{\partial x_l \partial x_j} d\Omega(r)$$

$$= \int_S \dot{u}_i(r) b_{ijkl}^C \frac{\partial G_{km}(r,r')}{\partial x_l} n_j dS(r) - \int_V \dot{u}_{i,j}(r) b_{ijkl}^C \frac{\partial G_{km}(r,r')}{\partial x_l} d\Omega(r) \tag{3.106}$$

Where S is the surface of Ω, and n_i is the unit outward normal of S. Next, multiplying (3.103) by $G_{im}(r,r')$ and integrating the result over the volume Ω leads to:

$$\int_{\Omega} G_{im}^\infty(r,r') b_{ijkl}^C \dot{u}_{k,lj}(r) d\Omega(r) - \int_{\Omega} G_{im}^\infty(r,r') \left(b_{ijkl}^C - b_{ijkl}^I \right) \dot{\varepsilon}_{kl,j}(r) d\Omega(r) = 0 \tag{3.107}$$

Using the divergence theorem, the first term of the above equation can be written as follows:

$$\int_{\Omega} G_{im}^\infty(r,r') b_{ijkl}^C \dot{u}_{k,lj}(r) d\Omega(r)$$

$$= \int_S G_{im}^\infty(r,r') b_{ijkl}^C \dot{u}_{k,l}(r) n_j dS(r) - \int_{\Omega} \frac{\partial G_{im}^\infty(r,r')}{\partial x_j} b_{ijkl}^C \dot{u}_{k,l}(r) d\Omega(r) \tag{3.108}$$

174

Subtracting (3.105) from (3.108), one obtains:

$$
\begin{aligned}
&\int_S \left(G_{im}^\infty(\mathbf{x},\mathbf{y}) b_{ijkl}^C \dot{u}_{k,l}(\mathbf{x}) - \dot{u}_i(\mathbf{x}) b_{ijkl}^C \frac{\partial G_{km}(\mathbf{x},\mathbf{y})}{\partial x_l} \right) n_j dS(\mathbf{x}) \\
&- \int_\Omega G_{im}^\infty(\mathbf{x},\mathbf{y}) \left(b_{ijkl}^C - b_{ijkl} \right) \dot{\varepsilon}_{kl,j}(\mathbf{x}) d\Omega(\mathbf{x}) \\
&= \begin{cases} \dot{u}_m(\mathbf{y}) & \mathbf{y} \in \Omega \\ \\ 0 & \mathbf{y} \notin \Omega \end{cases}
\end{aligned}
\tag{3.109}
$$

Using the divergence theorem, the above equation becomes:

$$
\begin{aligned}
&\int_S b_{ijkl}^C \left(G_{im}^\infty(\mathbf{x},\mathbf{y}) \left(\dot{u}_{k,l}(\mathbf{x}) - \left(I_{klmn} - \left(b_{klpq}^C \right)^{-1} b_{pqmn} \right) \dot{\varepsilon}_{mn}(\mathbf{x}) \right) - \dot{u}_i(\mathbf{x}) \frac{\partial G_{km}(\mathbf{x},\mathbf{y})}{\partial x_l} \right) n_j dS(\mathbf{x}) \\
&+ \int_\Omega \frac{\partial G_{im}^\infty(\mathbf{x},\mathbf{y})}{\partial x_l} \left(b_{ijkl}^C - b_{ijkl} \right) \dot{\varepsilon}_{kl}(\mathbf{x}) d\Omega(\mathbf{x}) \\
&= \begin{cases} \dot{u}_m(\mathbf{y}) & \mathbf{y} \in \Omega \\ \\ 0 & \mathbf{y} \notin \Omega \end{cases}
\end{aligned}
$$

$$
\tag{3.110}
$$

When r' belongs to the inclusion, the constitutive relation can be identified, within the above expression. Hence, equation (3.110) can be written as follows:

$$\dot{u}_m(r') = \int_{S^-} \left(G_{im}^\infty(r,r')\sigma_{kl} - b_{ijkl}^C \dot{u}_i(r)\frac{\partial G_{km}(r,r')}{\partial x_l} \right) n_j dS(r)$$

$$+ \int_{\Omega_I} \frac{\partial G_{im}^\infty(r,r')}{\partial x_l} \left(b_{ijkl}^C - b_{ijkl} \right) \dot{\varepsilon}_{kl}(r) d\Omega_I(r) \qquad (3.111)$$

If Ω is exterior to Ω_I, then one obtains the following relation:

$$0 = \int_{S^+} \left(G_{im}^\infty(r,r')\sigma_{kl} - b_{ijkl}^C \dot{u}_i(r)\frac{\partial G_{km}(r,r')}{\partial x_l} \right) n_j dS(r) \qquad (3.112)$$

Subtracting (3.111) to equation (3.112) one obtains:

$$\dot{u}_m(r) = \int_S \left(b_{ijkl}^C \Delta \dot{u}_i(r')\frac{\partial G_{km}(r,r')}{\partial y_l} \right) n_j dS(r')$$

$$+ \int_V \frac{\partial G_{im}^\infty(r,r')}{\partial y_l} \left(b_{ijkl}^C - b_{ijkl} \right) \dot{\varepsilon}_{kl}(r') dV(r') \qquad (3.113)$$

Hence one introduces the expression of the jump of the displacement rate. Differentiating the above expression and supposing the homogeneity of the strain rate tensor within the inclusion, one obtains:

$$\dot{u}_{m,n}(\mathbf{x}) = \int_S \left(b_{ijkl}^C \Delta \dot{u}_i(\mathbf{y})\frac{\partial G_{km}(\mathbf{x},\mathbf{y})}{\partial y_l \partial x_n} \right) n_j dS(\mathbf{y}) + \int_V \frac{\partial G_{im}^\infty(\mathbf{x},\mathbf{y})}{\partial y_l \partial x_n} \left(b_{ijkl}^C - b_{ijkl} \right) \dot{\varepsilon}_{kl}(\mathbf{y}) dV(\mathbf{y})$$

$$(3.114)$$

Hence, the strain rate in the inclusion is given by:

176

$$\dot{\varepsilon}_{ij}(\mathbf{x}) = T_{ijmn}\left(B\right)\left(b^C_{mnkl} - b^I_{mnkl}\right)\dot{\varepsilon}^I_{kl} + \int_S b^C_{mnkl}\Delta\dot{u}_k(\mathbf{y})\Gamma^\infty_{ijmn}(\mathbf{y},\mathbf{x})n_l dS(\mathbf{y}),$$

(3.115)

Introducing interfacial conditions, one obtains:

$$\dot{\varepsilon}_{ij}(\mathbf{x}) = T\left(b^C_{mnpq}\right)\left(b^C_{pqkl} - b^I_{pqkl}\right)\dot{\varepsilon}^I_{kl} + \int_S b^C_{mnkl}\dot{\eta}_{kp}\sigma_{pq}n_q\Gamma^\infty_{ijmn}(\mathbf{y},\mathbf{x})n_l dS(\mathbf{y})\quad.$$

(3.116)

In (3.116), the derivative of the stress tensor is supposed negligible considering that it is in the order of the second time derivative of the strain tensor while the derivative of the interface coefficient is in the same order as that of the strain rate. In order to pursue the analytical developments, the stress state along the interface is supposed constant and equal to the stress state in the inclusion. Hence, introducing the constitutive law in the inclusion into (3.116), one obtains:

$$\dot{\varepsilon}_{ij} = T_{ijpq}\left(b^C\right)\left(b^C_{pqkl} - b_{pqkl}\right)\dot{\varepsilon}_{kl} + b^C_{mnkl}b^I_{pqab}\dot{\varepsilon}^I_{ab}\int_S \dot{\eta}_{kp}n_q\Gamma^\infty_{ijmn}(\mathbf{y},\mathbf{x})n_l dS(\mathbf{y})$$

(3.117)

Averaging (3.117) on the inclusion's volume and accounting for the boundary conditions via superposition, one obtains:

$$\dot{\varepsilon}^I_{ij} = T_{ijpq}\left(b^C\right)\left(b^C_{pqkl} - b^I_{pqkl}\right)\dot{\varepsilon}^I_{kl} + \dot{\varepsilon}^I_{ab}b^I_{pqab}b^C_{mnkl}T_{ijmn}\left(b^C\right)\int_S \dot{\eta}_{kp}n_q n_l dS(\mathbf{y}) + \dot{\varepsilon}^C_{ij}$$

(3.118)

Similarly to early work by Qu, let us approximate the above integral by its average value. Hence, one obtains:

$$\dot{\varepsilon}_{ij}^{I} = T_{ijpq}\left(b^{C}\right)\left(\left(b_{pqkl}^{C} - b_{pqkl}^{I}\right) + b_{pqab}^{C} R_{abmn} b_{mnkl}^{I}\right)\dot{\varepsilon}_{kl}^{I} + \dot{\varepsilon}_{ij}^{C} \qquad (3.119)$$

Note here that the macroscopic strain rate is not written in the above expression. Also **R** is given by:

$$R_{mnpq} = \frac{1}{4\Omega}\int_{S}\left(\dot{\eta}_{mp}n_{q}n_{n} + \dot{\eta}_{mq}n_{p}n_{n} + \dot{\eta}_{np}n_{q}n_{m} + \dot{\eta}_{nq}n_{p}n_{m}\right)dS(\mathbf{y}) \qquad (3.120)$$

Expressions of **R** are given in Qu and Cherkaoui (2006). From (3.119), one obtains the following averaged localization tensor:

$$A_{ijlk}^{Ivp} = \left[I_{ijkl} - T_{ijpq}\left(b^{C}\right)\left(\left(b_{pqkl}^{C} - b_{pqkl}^{I}\right) + b_{pqab}^{C} R_{abmn} b_{mnkl}^{I}\right)\right]^{-1} \qquad (3.121)$$

The effective viscosity tensor of the composite material is obtained simply by use of the macrohomogeneity conditions. Namely, one obtains;

$$\mathbf{b}^{IC} = \left(1 - f\right)\mathbf{b}^{C} + f\mathbf{b}^{I} : \mathbf{A}^{Ivp} \qquad (3.122)$$

Homogenized coated inclusion/Homogeneous medium interface

178

Following the same reasoning as in the above and recalling that in this case the homogenized coated inclusion /homogeneous the interface is perfect, one obtains the following expression of the strain rate on the S^+ interface:

$$\dot{\varepsilon}_{kl}^{IC} = T_{ijpq}\left(b^e\right)\left(b_{pqkl}^e - b_{pqkl}^{IC}\right)\dot{\varepsilon}_{kl}^{IC} + \dot{E} \tag{3.123}$$

b_{pqkl}^e is determined such that the average of the localization tensors is equal to the identity tensor. Let us recall the expression of the localization tensor in this case:

$$A_{ijkl}^{vpIC} = \left(I_{ijkl} - T_{ijpq}\left(b^e\right)\left(b_{pqkl}^e - b_{pqkl}^{IC}\right)\right)^{-1} \tag{3.124}$$

Strain rate jump

From (3.119) and (3.123) the local strain rates in the inclusion and in the coating can be related. Indeed, the spatial average of the strain rate tensors within the inclusion and coating (in the two phase model) must be equal to the strain rate within the homogenized coated inclusion:

$$f\dot{\varepsilon}_{ij}^{I} + (1-f)\dot{\varepsilon}_{ij}^{C} = \dot{\varepsilon}_{ij}^{IC}$$

Hence,

$$\left(A_{ijkl}^{vpIC}\right)^{-1}\dot{\varepsilon}_{kl}^{IC} = \dot{E}_{ij} = f\left(A_{ijkl}^{vpIC}\right)^{-1}\dot{\varepsilon}_{kl}^{I} + (1-f)\left(A_{ijkl}^{vpIC}\right)^{-1}\dot{\varepsilon}_{kl}^{C}$$

Using the result from Mori Tanaka' scheme, one obtains

$$\dot{E}_{ij} = (1-f)\left(A_{ijkl}^{vpIC}\right)^{-1}\left(A_{klmn}^{Ivp}\right)^{-1}\dot{\varepsilon}_{mn}^{I} + f\left(A_{ijkl}^{vpIC}\right)^{-1}\dot{\varepsilon}_{kl}^{I}$$

One obtains the following relation

$$\dot{\boldsymbol{\varepsilon}}^{I} = \left[(1-f)\left(\boldsymbol{A}^{vpIC}\right)^{-1} : \left(\boldsymbol{A}^{Ivp}\right)^{-1} + f\left(\boldsymbol{A}^{vpIC}\right)^{-1}\right]^{-1} : \dot{\boldsymbol{E}}$$

$$(3.125)$$

Here f is the volume fraction of inclusion used in the first self consistent scheme. From the equation in the above one obtains the expression of the localization relation.

$$\dot{\boldsymbol{\varepsilon}}^{I} = \boldsymbol{B}^{I} : \dot{\boldsymbol{E}}$$

with

$$\left(\boldsymbol{B}^{I}\right)^{-1} = (1-f)\left(\boldsymbol{A}^{vpIC}\right)^{-1} : \left(\boldsymbol{A}^{Ivp}\right)^{-1} + f\left(\boldsymbol{A}^{vpIC}\right)^{-1}$$

$$(3.126)$$

From the localization relation in the above, the viscoplastic problem can be completely solved.

Elasto-viscoplastic solution

180

Let us now treat the elastic-viscoplastic case via the use of translated fields in a manner similar to that proposed by Sabar et al.(2002). As seen in the case of the 2PEVPT model, the integral equation is written as follows:

$$\dot{\boldsymbol{\varepsilon}} = \dot{\boldsymbol{E}} + \boldsymbol{\Pi}^C \otimes \left(\delta s : c : \dot{\boldsymbol{\varepsilon}}^e + \dot{\boldsymbol{\varepsilon}}^{vp} \right) \tag{3.127}$$

Let us decompose the local viscoplastic strain $\dot{\boldsymbol{\varepsilon}}^{vp}$ as the sum of an invariant term, denoted $\dot{\boldsymbol{e}}^{vp}$ and solution of the viscoplastic problem and a fluctuation term $\delta\dot{\boldsymbol{\varepsilon}}^{vp}$:

$$\dot{\boldsymbol{\varepsilon}}^{vp} = \dot{\boldsymbol{e}}^{vp} + \delta\dot{\boldsymbol{\varepsilon}}^{vp} \tag{3.128}$$

As mentioned in the above the invariant term is assumed to be the translated solution field respecting:

$$\dot{\boldsymbol{e}}^{vp} = \boldsymbol{B} : \dot{\boldsymbol{X}} \tag{3.129}$$

The field $\dot{\boldsymbol{X}}$ is to be found via the self consistent scheme. Also, the translated field must respect the compatibility condition given by:

$$\boldsymbol{\Pi}^C \otimes \dot{\boldsymbol{e}}^{vp} = \dot{\boldsymbol{e}}^{vp} - \dot{\boldsymbol{X}} \tag{3.130}$$

Where Kunin's projection operators are given by:

$$\mathbf{\Pi}^C = \mathbf{\Gamma}^C : \mathbf{C} \tag{3.131}$$

Introducing the above relations into the integral equation, one obtains:

$$\dot{\boldsymbol{\varepsilon}} = \dot{\boldsymbol{E}} + \mathbf{\Pi}^C \otimes \left(\delta \boldsymbol{s} : \boldsymbol{c} : \dot{\boldsymbol{\varepsilon}}^e + \delta \dot{\boldsymbol{\varepsilon}}^{vp} \right) + \boldsymbol{B} \dot{\boldsymbol{X}} - \dot{\boldsymbol{X}} \tag{3.132}$$

Using the self-consistent approximation, the unknown field can be identified:

$$\dot{\boldsymbol{X}} = \dot{\boldsymbol{E}}^{vp} \tag{3.133}$$

Hence, the integral equation becomes:

$$\dot{\boldsymbol{\varepsilon}} = \dot{\boldsymbol{E}} + \mathbf{\Pi}^C \otimes \left(\delta \boldsymbol{s} : \boldsymbol{c} : \dot{\boldsymbol{\varepsilon}}^e \right) + \mathbf{\Pi}^C \otimes \left(\dot{\boldsymbol{\varepsilon}}^{vp} - \boldsymbol{B} : \dot{\boldsymbol{E}}^{vp} \right)$$
$$+ \left(\boldsymbol{B} - \boldsymbol{I} \right) : \dot{\boldsymbol{E}}^{vp} \tag{3.134}$$

Averaging the above equation on the coated inclusion volume and with the self-consistent approximation, one obtains:

$$\dot{\boldsymbol{\varepsilon}} = \boldsymbol{A}^{CeE} : (\dot{\boldsymbol{E}} - \dot{\boldsymbol{E}}^{vpe}) + \boldsymbol{A}^{CeE} : \boldsymbol{B} : \dot{\boldsymbol{E}}^{vpe} + \boldsymbol{A}^{CeE} : \boldsymbol{S}^E : \boldsymbol{S}^e (\boldsymbol{c} \dot{\boldsymbol{\varepsilon}}^{vp} - \boldsymbol{C}^e : \boldsymbol{B} : \dot{\boldsymbol{E}}^{vpe})$$

$$\tag{3.135}$$

For the sake of simplicity, let us assume that the averaged local viscoplastic strain rate can still be related with (3.125). Similarly, the averaged local elastic strain rates can

be related via the equivalent to (3.125) in the case of pure elastic behavior. Hence, A^{CeE} is the elastic equivalent of the localization tensor $\boldsymbol{B}$. Hence, a complete solution can be found in the case of elasto-viscoplasticity.

Reference

Benkassem, S., Capolungo, L., Cherkaoui, M. (2007). "Mechanical properties and multi-scale modeling of nanocrystalline materials". Acta Materialia in press.

Berbenni, S.Favier, V. Lemoine, X. Berveiller, M. (2004). "Micromechanical modeling of the elastic viscoplastic behavior of polycrystalline steels having different microstructures". Materials science and engineering A 372: 128-136.

Bornert, M. (1996). "Morphologie microstructurale et comportement mecanique; caracterisation experimentales, approches par bornes estimations autocoherantes generalisees."Ph.D. thesis Ecole Nationale des Ponts et Chaussees Paris.

Budiansky, B., Wu (1962). "Theoretical prediction of plastic strains of polycrystals". Proceedings of the 4th U.S. National congress of applied mechanics, ASME 1175.

Capolungo, L., Benkassem, S. Cherkaoui, M., Qu, J. (2007). "Coated inclusions with elastic-viscoplastic behaviors and imperfect interfaces: application to nanocrystalline materials". *In preparation.*

Cherkaoui, M., Sun, Q., Song, G.Q. (2000). "Micromechanics modeling of composite with ductile matrix and shape memory alloy reinforcement". International journal of solids and structures 37: 1577-1594.

Cherkaoui, M., Sabar, H., Berveiller, M. (1996). "Elastic composite with coated reinforcements: a micromechanical approach for non homothetic topology". International Journal of Engineering science 33:829:843.

Cherkaoui, M., Sabar, H., Berveiller, M. (1996). "Elastic behavior of composites with coated inclusions: micromechanical approach and applications". Composites Science and Technology 56: 877-882.

Cherkaoui, M., Berveiller, M. (2000). "Moving inelastic discontinuities and applications to martensitic phase transition". Archive of Applied Mechanics 70: 159-181.

Christensen, R.M., Lo, K.H. (1979). "Solutions for the effective shear properties in three phase sphere and cylinder models". Journal of the mechanics and physics of solids 27:315-330.

Dederich, P.H. and R. Zeller (1973). Z. Physik 103: 259.

Eshelby, J.D. (1957). "The determination of an ellispoidal inclusion and related problems". Proceedings of the Royal Society of London A 241: 376-396.

Eshelby, J.D. (1961). "Elastic inclusions and inhomogeneities". Progress in Solid Mechanics, ed. I.N. Sneddon and R. Hill., Amsterdam.

Hadamard, J. (1903). "Lecon sur la propagation des ondes et les equations de l'hydrodynamique ", C.d.c.d. France, Editor.

Hill, R. (1965). "Continuum micro-mechanics of elastoplastic polycrystals". Journal of the mechanics and physics of solids 13:89.

Hill, R. (1983). "Interfacial operators in the mechanics of composite media". Journal of the mechanics and physics of solids 31.

Kroner,E.(1961). "Zur plastichen verformung des vielkristalls". Acta metallurgica 9:155.

Kunin, I. A. (1981). "An algebra of tensor operators and its applications to elasticity". International Journal of Engineering Science 19: 1551-1561.

Lebensohn, R. A., Tome, C. N., Maudlin, P. J. (2004). "A selfconsistent formulation for the prediction of the anisotropic behavior of viscoplastic polycrystals with voids". Journal of the Mechanics and Physics of Solids 52: 249-278

Molinari, A., Ahzi, S., Kouddane, R. (1997). "On the self consistent modeling of elastic plastic behavior of polycrystals". Mechanics of materials 26:43-62.

Masson, R., Zaoui,A. (1999). "Self consistent estimates for the rate dependent elastoplastic behaviour of polycrystalline materials". Journal of the mechanics and physics of solid 47: 1543-1568.

Mura, T. (1987). "Micromechanics of Defects in Solids". Kluwer Academic ISBN: 9024732565

Qu, J., Cherkaoui, M. (2006). "Fundamentals of Micromechanics of Solids". Wiley ISBN-10: 0471464511.

Qu, J, (1993). "The effect of slightly weakened interfaces on the overall elastic properties of composite materials". Mechanics of Materials 14: 269-281.

Sabar, H. Berveiller, M., Favier, V. Berbenni, S. (2002). "A new class of micro-macro models for elastic-viscoplastic heterogeneous materials". International Journal of Solids and Structures 39: 3257-3276.

Suquet, P. (2003). "Continuum Micromechanics". Springer ISBN-10: 3211829024.

Tome, C. (1999). "Self-consistent polycrystal models: a directional compliance criterion to describe grain interactions". Modelling and Simulation in Materials Science and Engineering 7: 723-738.

Walpole, J. (1978). "A coated inclusion in an elastic medium". Math Proc Camb 83

Weng, G.J., (1981). "A self consistent relation for the time dependent creep of polycrystals". Journal of apllied mechanics 48:41-46.

CHAPTER 4

DIFFUSION BASED MECHANISMS

This chapter focuses on the modeling of the effect of diffusion mechanisms on the size effect of polycrystalline materials with a F.C.C. structure. First, the effect of Coble creep, corresponding to the steady state diffusion of vacancies along the grain boundary/ grain core interface, will be studied via the use of the 2PVP model. Second, the simultaneous effect of Lifshitz sliding and Coble creep will be investigated.

Coble creep

This section is dedicated to the effect of Coble creep on the response of UF and NC materials (Capolungo et al. 2004; Capolungo et al. 2005). The first problem to be considered is that of the material's topology. Considering the fact that grain boundaries and grain cores have a distinct structure from that of the grain interior and the fact that the volume fraction of triple junctions is negligeable for grain size larger than ~10nm, the material is represented as a two-phase composite. The inclusion phase represents grain cores and the matrix phase represents both grain boundaries and triple junctions (see Figure 4.1).

The response of grain interiors is dominated by two deformation mechanisms: (1) dislocation glide and (2) Coble creep. The effect of Nabarro Herring creep is not accounted for since it was shown in work by Kim et al. (2001) that its contribution is negligeable compared to that of Coble creep. As a first approach, the behavior of the

matrix phase is assumed elastic- prefect plastic. Note here that a constitutive law for the grain boundaries will be introduced in Chapter 5.

This model is limited to the case of spherical inclusions and the bonding between inclusions and matrix is assumed perfect (e.g. unaccomodated grain boundary sliding is not considered). Finally, the material is assumed isotropic and not compressible. The scale transition is performed via the use of the 2PEVP model presented in Chapter 3. The model is applied to the case of pure Cu for which numerous experimental data is available. Finally, model predictions in the quasi-static regime and at ambient temperature are compared to experimental data available in the literature.
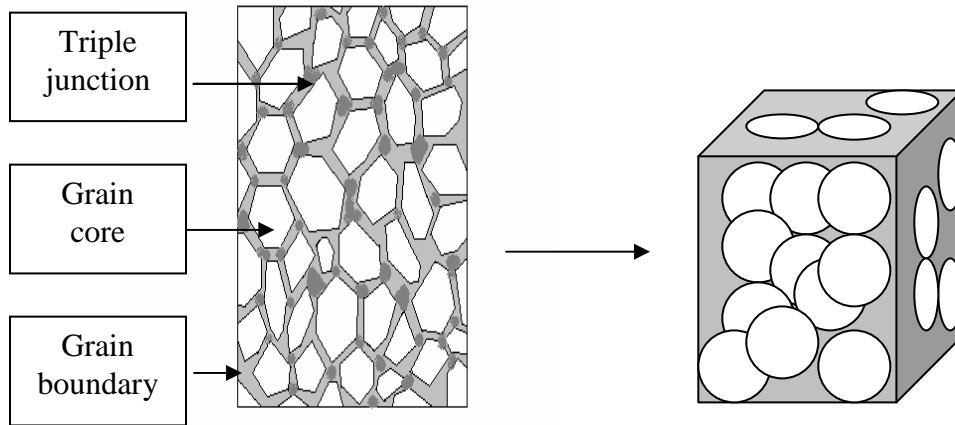
Figure 4.1: Schematic of the equivalent material.

In this chapter, the superscripts I and M will refer to the inclusion and matrix phase, respectively. Also, ε, σ and $\dot{\varepsilon}$, $\dot{\sigma}$ will refer to the strain and stress tensors and their rates, respectively. Σ and E denote the macroscopic stress and strain tensors respectively.

Although this first model was implemented solely in the one dimensional case, the mathematical developments will be presented in the general three-dimensional case.

Constitutive law of the inclusion phase

Plastic deformation within the inclusion phase is driven by the glide of dislocations and by the Coble creep mechanism (hence the inclusion phase is composed of the crystals and of the grain boundary/grain core interface). Let us note here that the size effect in the dislocation activity is not considered in this first model. In consequence, the model will lead to overestimated predictions of the hardening response of the inclusion phase in the NC regime. The constitutive law of the inclusion phase is elastic-viscoplastic and given by:

$$\dot{\boldsymbol{\sigma}}^I = \boldsymbol{C}^I : \left(\dot{\boldsymbol{\varepsilon}}^I - \dot{\boldsymbol{\varepsilon}}^{I,vp} \right) \tag{4.1}$$

Here, $\dot{\boldsymbol{\varepsilon}}^{I,vp}$ and $\boldsymbol{C}^I$ represent the second order viscoplastic strain rate tensor and the fourth order elastic moduli tensor, respectively. Plastic flow is assumed isotropic and described by the Prandtl Reuss flow rule given by:

$$\dot{\boldsymbol{\varepsilon}}^{I,vp} = \frac{3}{2} \frac{\dot{\varepsilon}_{eq}^{I,vp}}{\sigma_{eq}^I} s_{ij}^I \tag{4.2}$$

Here $\dot{\varepsilon}_{eq}^{I,vp}$, σ_{eq}^I and s_{ij}^I denote the equivalent strain rate, Von Mises equivalent stress ($\sigma_{eq}^I = \sqrt{3/2 s_{ij}^I s_{ij}^I}$) and the deviatoric part of the stress tensor. The equivalent viscoplastic

strain rate which accounts for both the effect of dislocation glide, denoted with superscript *dis*, and the effect of Coble creep, denoted with superscript *co*, and is written as the sum of the contribution of both mechanisms:

$$\dot{\varepsilon}_{eq}^{vpI} = \dot{\varepsilon}^{dis} + \dot{\varepsilon}^{co} \tag{4.3}$$

The formalism developed by Kim et al. is used to describe the effect of the dislocation glide mechanism given by a power law (Estrin 1998; Kim et al. 2000; Kim et al. 2001):

$$\dot{\varepsilon}^{dis} = \dot{\varepsilon}^{*} \left(\frac{\sigma_{eq}^{I}}{\sigma_0} \right)^{m} \rho^{-m/2} \tag{4.4}$$

Here, $\dot{\varepsilon}^{*}$, σ_0, m and ρ denote a numerical constant, a stress term relating of the effect of the microstructure on the glide of dislocations and the hardening exponent and the dislocation density normalized with respect to the initial dislocation density, respectively. Let us note that for the sake of simplicity no distinction is made between statistically stored dislocations and geometrically necessary dislocations (hence the effect of strain gradients is not considered). The evolution of the density of stored dislocations with deformation is given by:

$$\frac{d\rho}{d\varepsilon^{dis}} = C + C_1 \sqrt{\rho} - C_2 \rho \tag{4.5}$$

189

Let us note that the above expression is based on work by Estrin et al. (1984) and accounts for the effects of both stored dislocations and grain boundaries on the dislocation storage mechanism. Dynamic recovery is described with the third term on the right hand side of equation (4.5). Hence, C_1 is a numerical constant and C is given by:

$$C = M \cdot \frac{b}{d} \left(\frac{M \cdot \alpha \cdot G}{\sigma_0} \right)^2 \tag{4.6}$$

Here, M, b, G denote Taylor's factor, the magnitude of Burger's vector and the shear modulus, respectively. α is a numerical constant accounting for the dislocation-dislocation interactions. The thermally activated dislocation annihilation mechanism is given by the following power law:

$$C_2 = C_{20} \left(\frac{\dot{\varepsilon}^{dis}}{\dot{\varepsilon}_0} \right)^{-1/n} \tag{4.7}$$

In equation (4.7), C_{20} and $\dot{\varepsilon}_0$ are numerical constants. As will be shown in Chapter 5, the ratio of C_{20} and C_1 defines, at a given grain size, the value of the saturation stress. The exponent m and n account for the thermally activated nature of the dislocation glide mechanism and of the recovery mechanisms, respectively. Hence these two parameters are inversely proportional to the temperature. Let us note that an exponential expression of the thermally activated mechanisms would be more accurate.

Finally, the expression of the effect of vacancy diffusion is given by the equation of

Coble creep (1963) and written as follows:

$$\dot{\varepsilon}^{co} = \frac{14 \cdot \pi \cdot \Omega_c \cdot w \cdot D_{bd}^{sd} \cdot \sigma_{eq}^{I}}{k \cdot T \cdot d^3}$$ (4.8)

Here T, k, d, Ω_c and D_{sd}^{bd} denote the temperature, Boltzmann's constant, the grain size,

the atomic volume and the grain boundary self-diffusion coefficient, respectively.

Constitutive law of the matrix phase

Let us now describe the constitutive law of the matrix phase and let us recall that

this model is a first attempt to estimate both the predictive power of the micromechanical

scheme and the effect of diffusion mechanisms. Hence, although grain boundaries cannot

be considered to have a gas like structure, with no particular organization of the atoms,

the response of grain boundaries will be supposed as that of an amorphous material.

Typically, the flow stress in amorphous materials ranges between 50 to 70% of Young's

modulus. Experimental data report values ranging between 60 to 70% of Young's

modulus of the perfect crystal. Here the flow stress will be estimated equal to 800 MPa..

When Von Mises stress is smaller than the previously mentioned critical value, the

response of the matrix phase is thus given by a simple linear elastic law:

$$\dot{\sigma}^M = C^M : \dot{\varepsilon}^M$$ (4.9)

Here, C^M is the fourth order elastic tensor modulus of the matrix phase.

Effective material

The macroscopic response of the material is obtained via the use of the 2PEVP model (Cherkaoui et al. 2000) presented in Chapter 3. Since the derivations of the self-consistent scheme were developed in the previous chapter, solely the critical equations are recalled and adapted for the problem studied. Let us recall that the approximation consisting of including both grain boundaries and triple junctions into the same matrix phase shall not penalize the accuracy of the model for the contribution of triple junctions becomes relevant solely when the grain size is smaller than ~10nm. The macroscopic response of the material is elastic-viscoplastic and given by:

$$\dot{\Sigma} = C^{eff} : \left(\dot{E} - \dot{E}^{vp} \right)$$
(4.10)

Here C^{eff} denotes the fourth order effective elastic moduli tensor. The components of these tensors are given by the self-consistent approximation. The localization relations are given by:

$$\dot{\varepsilon} = A^{r} : \dot{E} + a^{r} \text{ with } r=I,M$$
(4.11)

In equation (4.11) the fourth order concentration tensors denoted with A^{r}, account for the effect of the heterogeneity in the elastic responses. The second order tensors denoted with a^{r} account for the heterogeneity in the anelastic responses of the matrix and inclusion phase. With use of the homogenization scheme, the following expressions of the localization tensors are obtained

$$A^r = \left[I + S^E : \left(C^{eff} \right)^{-1} : \left(C^r - C^{eff} \right) \right]^{-1} \qquad \text{with } r=I,M \qquad (4.12)$$

$$a^I = A^I : S^E : \left(C^{eff} \right)^{-1} : \left(C^{eff} : \dot{\varepsilon}^{vpI} - C^{eff} : \dot{E}^{vp} \right) \qquad (4.13)$$

$$a^M = -A^M : S^E : \dot{E}^{vp} \qquad (4.14)$$

In the above equations, S^E denotes Eshelby's tensor. Finally, the effective viscoplastic strain rate tensor is given by:

$$\dot{E}^{vp} = f \cdot \left(C^{eff} \right)^{-1} : A^I : C^I : \dot{\varepsilon}^{vpI} \qquad (4.15)$$

Here f denotes the inclusion phase's volume fraction which is given by:

$$f = \frac{(d - w)^3}{d^3} \qquad (4.16)$$

The above equation results directly from the spherical inclusion assumption.

Results

The model presented in previous section is applied to the case of pure copper in uni-axial traction and in the quasi-static regime. Since both phases are supposed isotropic the set of equation (4.11) to (4.16) can be further developed analytically. This leads to relatively

193

simple formulae. Also the numerical solution is obtained in a fairly simple manner via an explicit scheme. The self-consistent approximation is solved with the bisection method. The grain sizes simulated range from several microns to 10 nm. The effect of the applied strain rate is studied. Precisely, tensile test are simulated with the following strain rates; 1.E-5/s, 1.E-4/s, and1.E-3/s.

Constant evaluation

The following numerical constants were used:

$C_{20} = 18.5, \mu_I = 42100$ MPa., $\mu_M = 25260$ MPa., $\sigma_0 = 160$ MPa. , $\Omega_c = 1.18E^{-29}, m = 230, n = 12.25$

, $b = .246$ nm, $k = 1.38E^{-23}$ $M = 3.06, \alpha = .33, T = 300K, G = 42100$MPa .

The shear modulus in the inclusion phase is set equal to that of conventional copper. Indeed, in the case of an infinite grain size, the volume fraction of the matrix phase tends to zero and the response of the material is entirely driven by the response of the inclusion phase. The shear modulus of the matrix phase is equal to 60% of the shear modulus of the inclusion phase. The parameters σ_0 and n are obtained by curve fitting of available data. Let us note that σ_0 depends on the initial dislocation density, which is not known a priori, and influences the value of plastic flow. All other numerical data sited in the above are extracted from Kim et al. (2000 and 2001).

Response of the inclusion phase

This section is dedicated to the response of the inclusion phase. The effects of the evolution of the relative contribution of Coble creep and dislocation glide, of the grain size and of the strain rate are studied.

Figure 4.2 (a) and (b), presents the equivalent viscoplastic strain rate of both

Coble creep and dislocation glide as a function of grain size. In case (a) the applied strain

rate is 1.E-5/s while in case (b) the applied strain rate is 1.E-3/s. One can observe that in

the first case, dislocation glide drives the deformation until a grain size d~300nm is

reached at which the effect of Coble creep becomes non negligeable. Indeed, the

contribution of the Coble creep mechanism increases with decreasing grain size and

dominates that of dislocation glide when the grain size is smaller than ~85nm. Also, it

can be noticed that the contribution of the inclusion phase (e.g. Coble creep+dislocation

glide) decreases in the NC regime. This result is expected since the volume fraction of

grain boundaries increases in the NC regime.
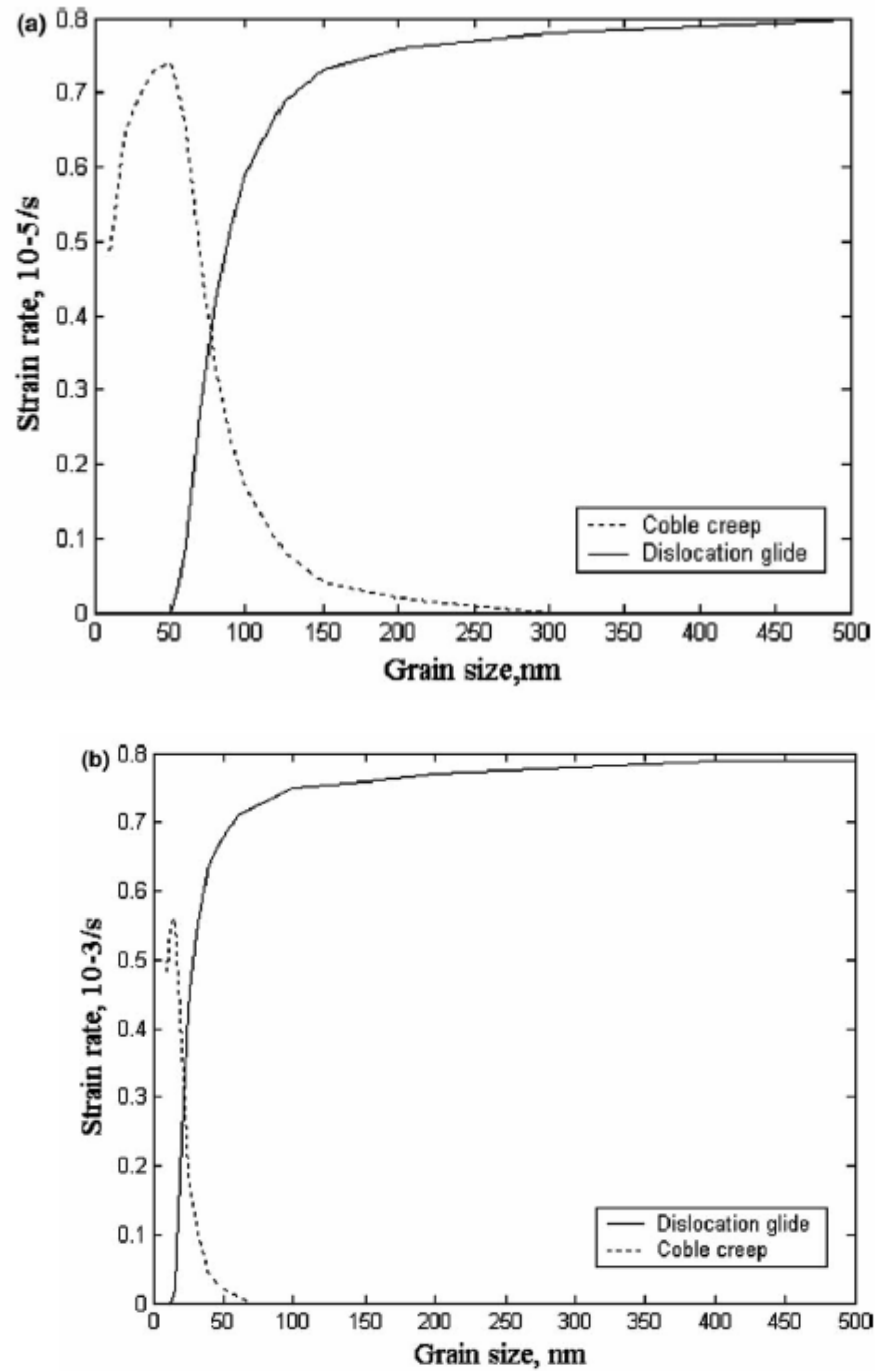
Figure 4.2 Evolution of the contributions of equivalent viscoplastic strain rate of the

dislocation glide and Coble creep mechanisms as a function of grain size for two applied

strain rates: (a) 1E-5s and (b) 1.E-3/s.

The evolution of the response of the inclusion phase with strain rate is presented in Figure 4.3. The grain size used in these simulations is 1000 nm. It can be observed that an increase in the macroscopic strain rate, leads to a more pronounced strain hardening within the inclusion phase. As mentioned in previous discussion, when the grain size is equal to 1000 nm the contribution of Coble creep is negligeable. Hence, plastic deformation is driven by dislocation glide which is dependent on the dislocation density and increases with increasing strain rates.
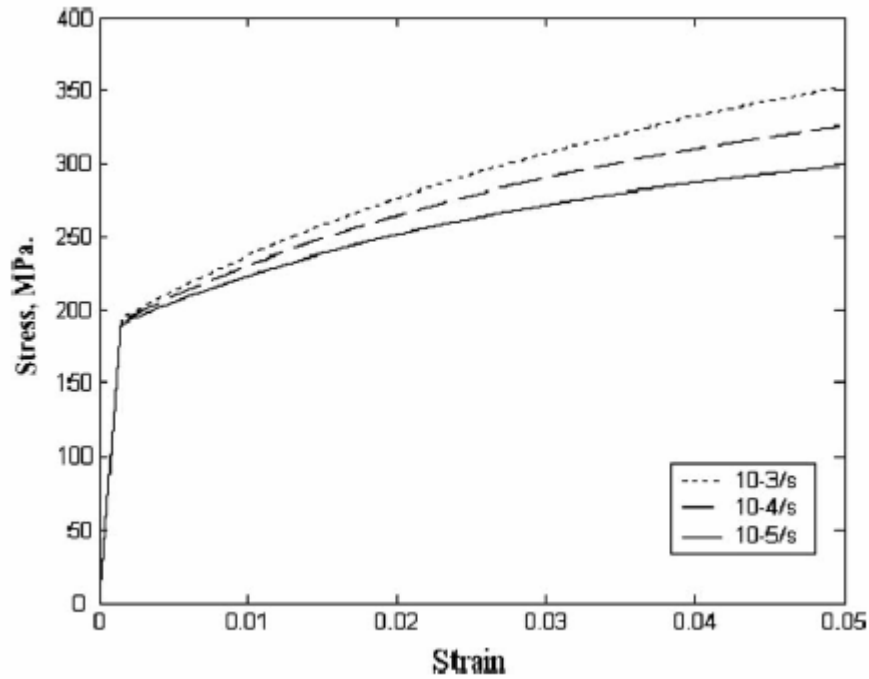
Figure 4.3: Stress-strain curves of the inclusion phase with 1.E-5/s, 1.E-4/s and 1.E-3/s imposedd strain rate and d=1000 nm grain size.

Finally, the size effect on the response of the inclusion phase is presented in Figure 4.4. The imposed strain rate is set equal to 1.E-3/s. When the grain size is equal to

1000 nm and 100nm the inclusion phase presents a typical strain hardening response. The increased hardening of the 100nm grain inclusions is due to the decrease in the mean free path of dislocation which is engendered by the decrease in the grain size. When the grain size is equal to 10nm, one can notice that the inclusion phase presents a softened behavior compared to that of 100 nm grain inclusion. This is due to the fact that Coble creep dominates the deformation of 10nm grain inclusions.
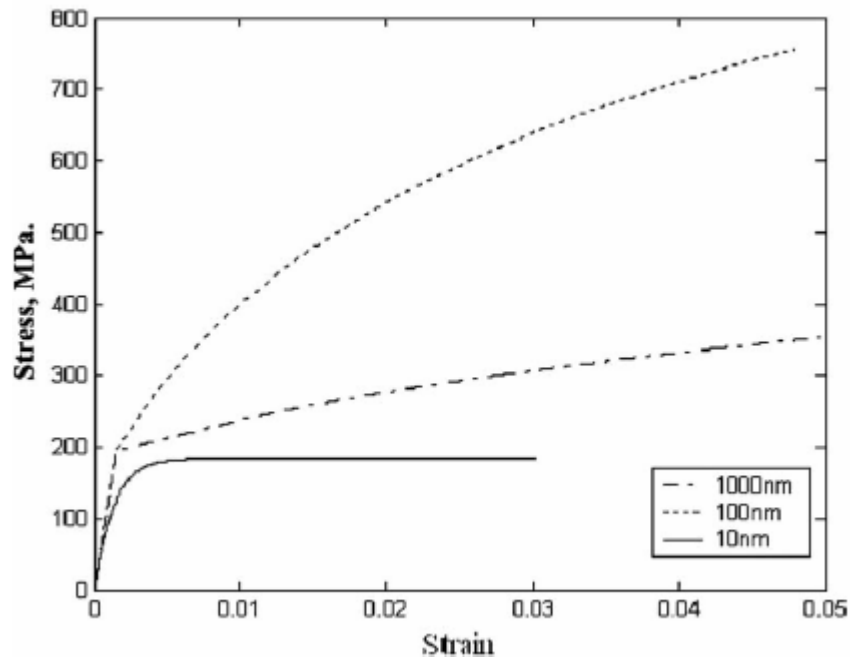
Figure 4.4 Stress-strain curve of the inclusion phase for different grain sizes; 1000, 100 and 10 nm.

Response of the matrix phase

Let us now briefly present the response of the matrix phase. Since the response of the matrix phase is elastic-perfect plastic, it does not present any dependence on strain rate or

grain size. This can be clearly observed in Figure 4.5 which presents stress-strain curves

of the matrix phase with the three different strain rates.
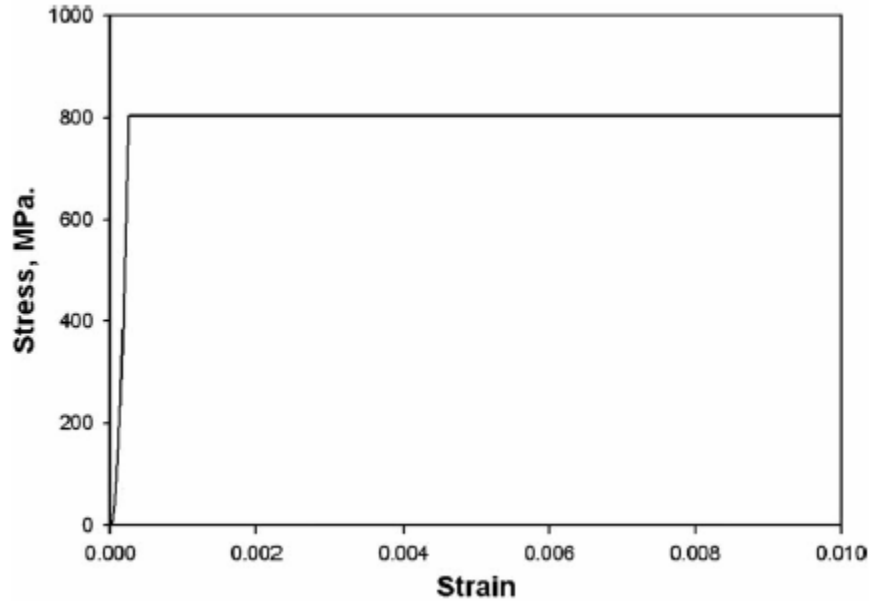
Figure 4.5: Stress strain curve of the matrix phase.

Effective response of the material

 The tensile response of the material is presented for different grain sizes (e.g. 1000, 1000

and 10 nm) in Figure 4.6. The macroscopically imposed strain rate is 1.E-3/s. One can

notice that in the case of large grain sizes (1000nm and 100nm); the hardening of the

material is more pronounced with decreasing grain size. Indeed, for these grain sizes, the

contribution of the matrix phase to the deformation is negligeable. Hence, the

macroscopic response of the material is expected to be similar to that of the inclusion

phase. When the grain size is equal to 10nm, both the inclusion and the matrix phase have

a non negligeable role. The plastic response of the inclusion phase is dominated by the Coble creep mechanism and the matrix phase has an elastic-perfect plastic response.

The effect of strain rate on the macroscopic response of the material is presented in Figure 4.7. The grain size is set to 1000nm. Hence the response is largely dominated by the response of the inclusion phase which is dominated by dislocation activity.

The model is compared to experimental data (Sanders et al. 1996; Youngdahl et al. 1997) in Figure 4.8. The strain rate imposed in the simulations is 1.E-3/s. One can observe that the elastic response and the beginning of the plastic response of UF and NC materials are predicted with acceptable accuracy. However, it can be observed that when that when the deformation exceeds 1%, the model overestimates of the plastic response of the material. This will be discussed in the conclusion of this chapter.

Finally, Figure 4.9 presents the evolution of the flow stress at 0.5 percent deformation with respect to the inverse of the square root of the grain size. The model leads to a good prediction of the evolution of flow stress with grain size. One can notice that down to ~100nm the flow stress increases with decreasing grain size. The Hall-Petch breakdown is also successfully predicted when the grain size is smaller than ~100nm. Also, the critical grain size at which the breakdown of the Hall-Petch law occurs decreases with increasing strain rate.
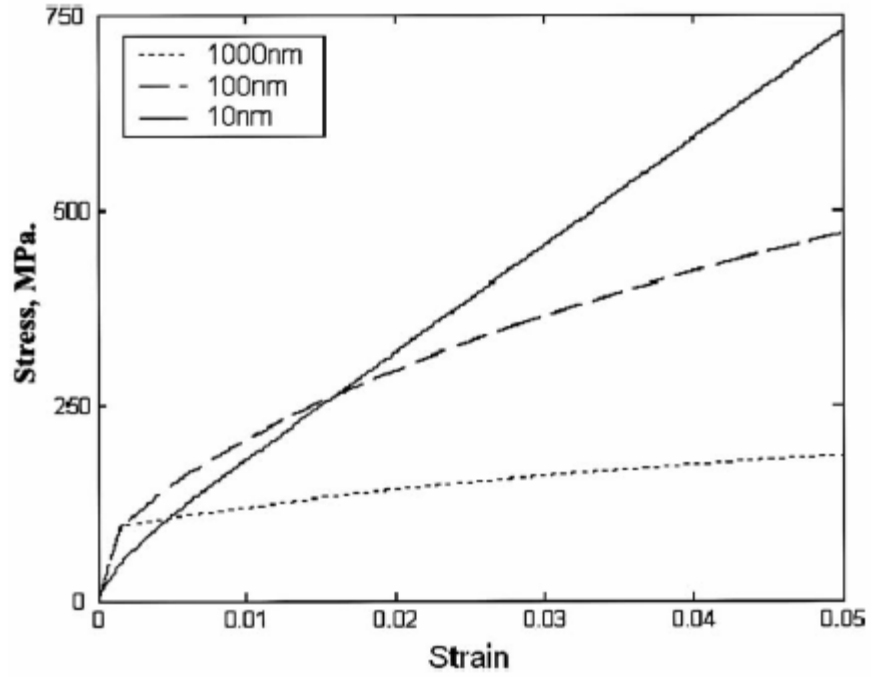
Figure 4.6: Stress strain curves of the material with three different grain sizes (1000, 100

and 10 nm).
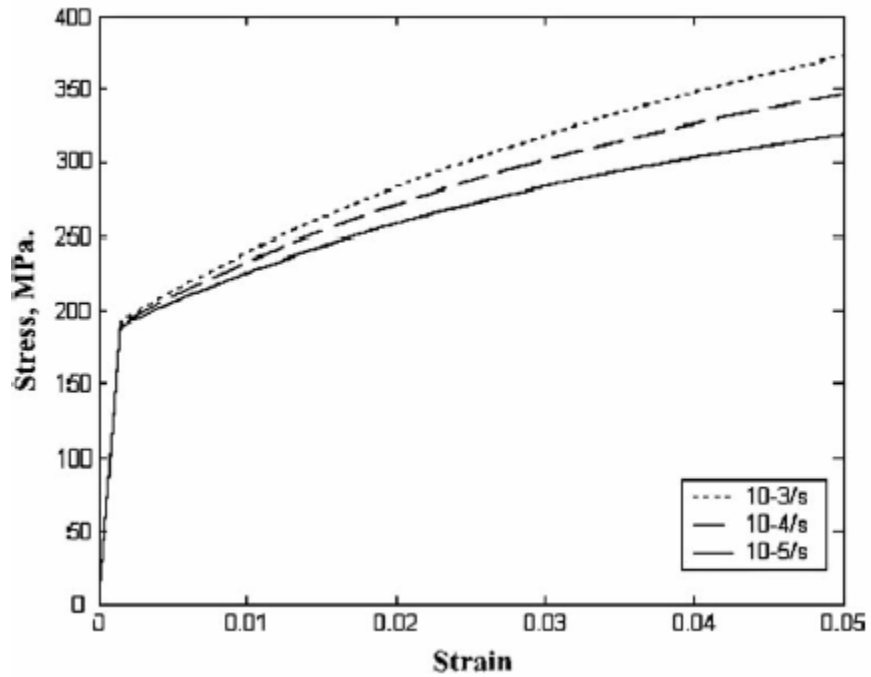
Figure 4.7: Macroscopic stress strain curves for three different strain rates.
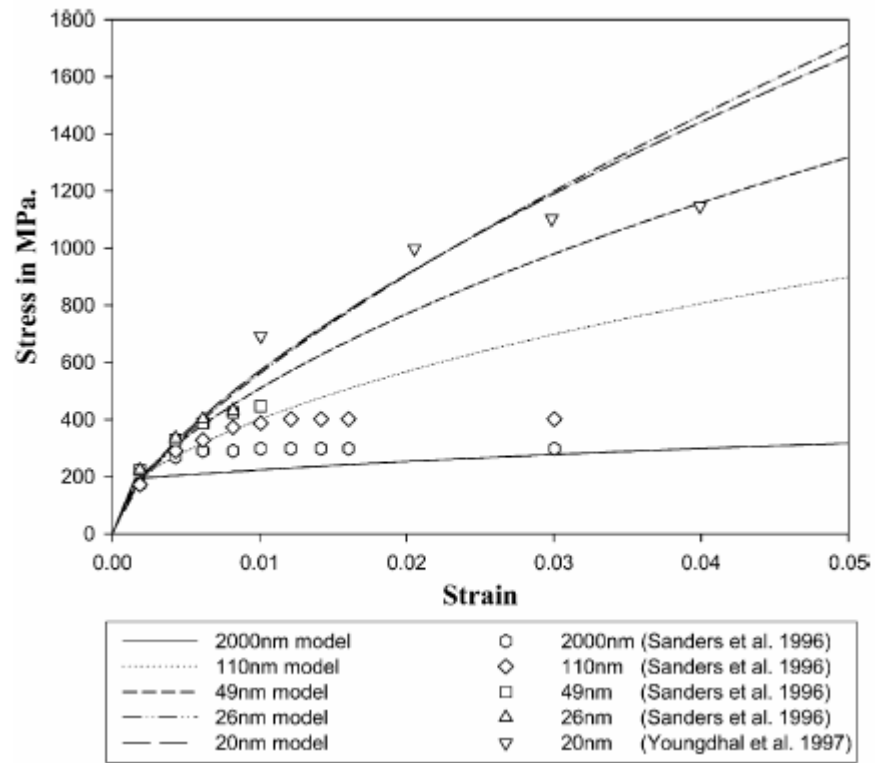
Figure 4.8: Comparison of model predictions with experimental data.
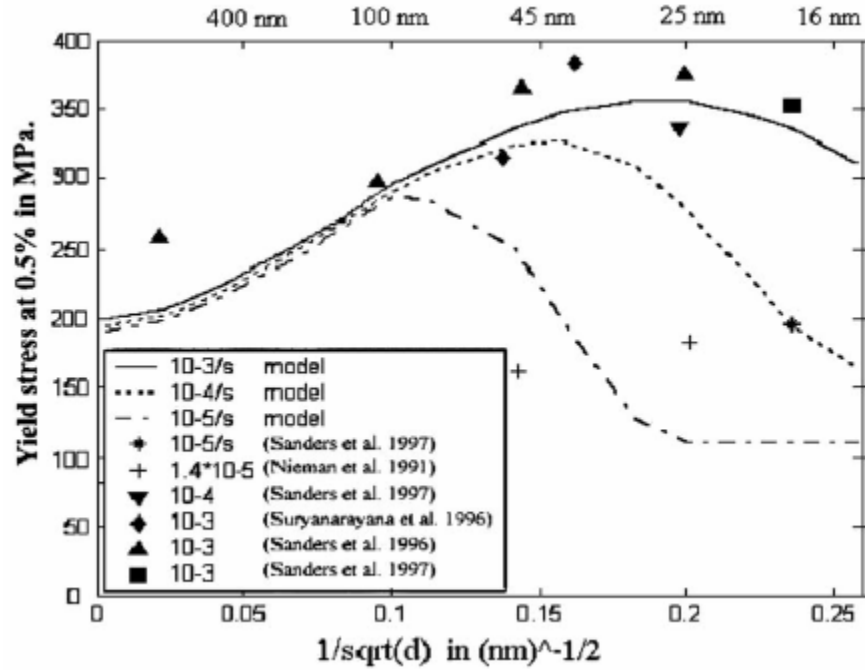
Figure 4.9: Evolution of the yield stress with the inverse of the square root of the grain

size. Experimental data are extracted from (Nieman et al. 1991; Sanders et al. 1996;

Surayanarayana et al. 1996; Sanders et al. 1997).

Coble creep and Lifschitz sliding

This section is dedicated to the modeling of the simultaneous effect of Coble

creep and vacancy diffusion accommodated grain boundary sliding (e.g. Lifschitz

sliding). Similarly to the previous section, the material is represented as a two-phase

composite material. The same assumptions as in the case of the study of the effect of

Coble creep alone are made; inclusions are supposed spherical and debonding between

the two phases is not allowed. The inclusion phase represents grain interiors while the

matrix phase encompasses grain boundaries, triple junctions and the grain boundary grain

core interface (with zero thickness). The behavior of the inclusion phase is driven by the

203

mechanism of dislocation glide while the matrix phase deforms via the simultaneous effect of Lifschitz sliding and Coble creep.

Constitutive law of the inclusion phase

The inclusion phase has an elastic-viscoplastic behavior given by:

$$\dot{\boldsymbol{\sigma}}^I = \boldsymbol{C}^I : \left(\dot{\boldsymbol{\varepsilon}}^I - \dot{\boldsymbol{\varepsilon}}^{I,vp} \right) \tag{4.17}$$

Supposing an isotropic response of the inclusion phase, the viscoplastic strain rate tensor is related to the equivalent viscoplastic strain rate via the Prandtl Reuss flow rule. The local viscoplastic strain rate accounts solely for the effect of dislocation glide and is written as:

$$\dot{\varepsilon}_{eq}^{vpI} = \dot{\varepsilon}^{dis} \tag{4.18}$$

Here $\dot{\varepsilon}^{dis}$ is given by (4.4) and the evolution of the dislocation density is given by (4.5).

Constitutive law of the matrix phase

The mechanisms of Coble creep and of Lifschitz sliding are taken into account in the description of the behavior of the matrix phase which has an elastoplastic constitutive law written as follows:

$$\dot{\boldsymbol{\sigma}}^M = \boldsymbol{C}^M : \left(\dot{\boldsymbol{\varepsilon}}^M - \dot{\boldsymbol{\varepsilon}}^{M,vp} \right) \tag{4.19}$$

Here C^M is the elastic tensor of the matrix phase and $\dot{\varepsilon}^{M,vp}$ is the viscoplastic part of the strain rate tensor of the matrix phase. It is related to its equivalent quantity via the modified Prandtl Reuss flow rule and takes into account the contribution of both grain boundary sliding and Coble creep.

$$\dot{\varepsilon}_{eq}^{M,VP} = \dot{\varepsilon}^{co} + \dot{\varepsilon}^{gbs} \qquad (4.20)$$

Here the superscripts 'co' and 'gbs' respectively refer to Coble and grain boundary sliding, respectively. The contribution of Coble creep is given by equation (4.8) while the contribution of grain boundary sliding accommodated by vacancy diffusion along the grain boundary grain core interface is given by (Luthy et al. 1979):

$$\dot{\varepsilon}_{gbs} \approx 10^8 \frac{D_{gb}}{d^3} b \left(\frac{\sigma_{eq}^I}{E} \right)^2 \qquad (4.21)$$

Here E is Young's modulus of the inclusion phase, d is the grain size, D_{gb} is the diffusion coefficient of the grain boundaries.

Constitutive law of the matrix phase

The model presented in the above was applied to pure copper. The numerical data used in the simulations are the following; $\mu_I = 21.45 GPa.$, m=230, n=8.25, $\sigma_{0,I} = 220 MPa.$,

$\dot{\varepsilon}_I^* = 0.005/s$, M=3.06, $\alpha = 0.33$, G=42.1GPa., $C_1 = 52.86$, $C_{20} = 18.5$, $\dot{\varepsilon}_0 = 1/s$,

$\Omega_c = 1.18e - 29$, $D_{bd} = 2.6e - 20$, T=300K, E=130GPa., w=1.5nm.

In figure 4.10, one can see a comparison between the predictions of the model,
represented by lines, and various experimental studies (Sanders et al. 1996; Youngdahl et
al. 1997), represented by dots. Stress strain curves were plotted for various grain sizes. A
decrease in the grain size engenders an increase in the strain hardening. However when
the grain size reaches 20 nm, strain hardening is less pronounced than when d=26 nm.
This results from a change in the mechanism dominating the deformation. When
d>20nm., the glide of dislocation dominates the deformation while when d<20nm
diffusion mechanisms take over the dislocation glide which engenders a decrease in the
strain hardening. The model is in agreement with experimental results in the first stage of
deformation. When the strain is larger than a few percent, the model underestimates the
global stresses.

In figure 4.11, one can see the evolution of yield stress with grain size. The predictions of
the current model are represented by lines while experimental results are represented by
dots. The yield stress increases linearly down to a critical grain size which is
approximately equal to 40 nm. Once this critical threshold is reached, the breakdown of
the Hall Petch law occurs. The model predicts values of the yield stress lower than the
one given by experimental data. Recall that this model takes into account both Coble
creep and grain boundary sliding accommodated by vacancy diffusion along the grain
interior/ grain boundary interface. Hence, at very small grain sizes a redundancy in the
diffusion phenomenon might occur. Also, the equations used to describe the two

phenomena are based on a steady state creep rate which clearly overestimates the effect

of diffusion. Hence, the model is expected to underestimates the stress fields.
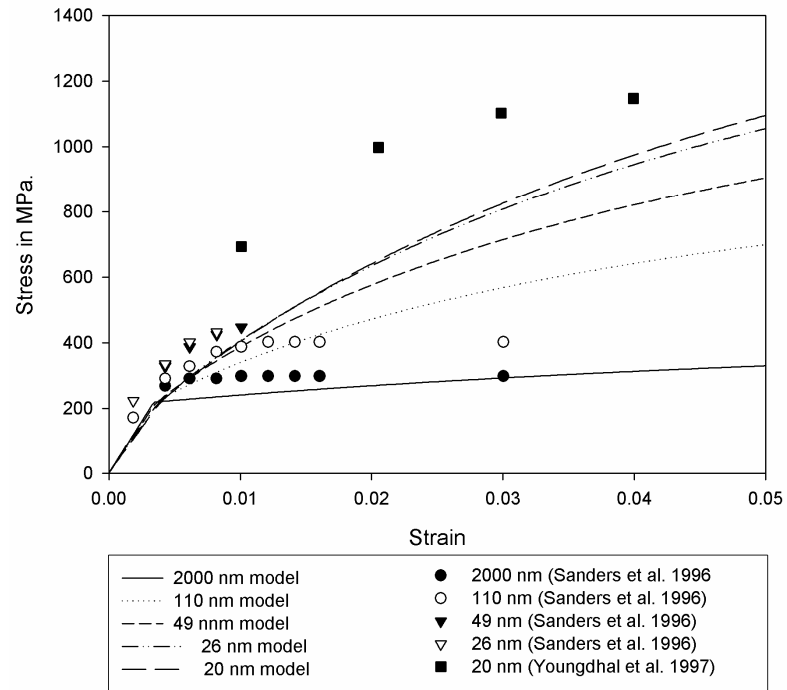
Figure 4.10 Stress Strain curves for different grain sizes.
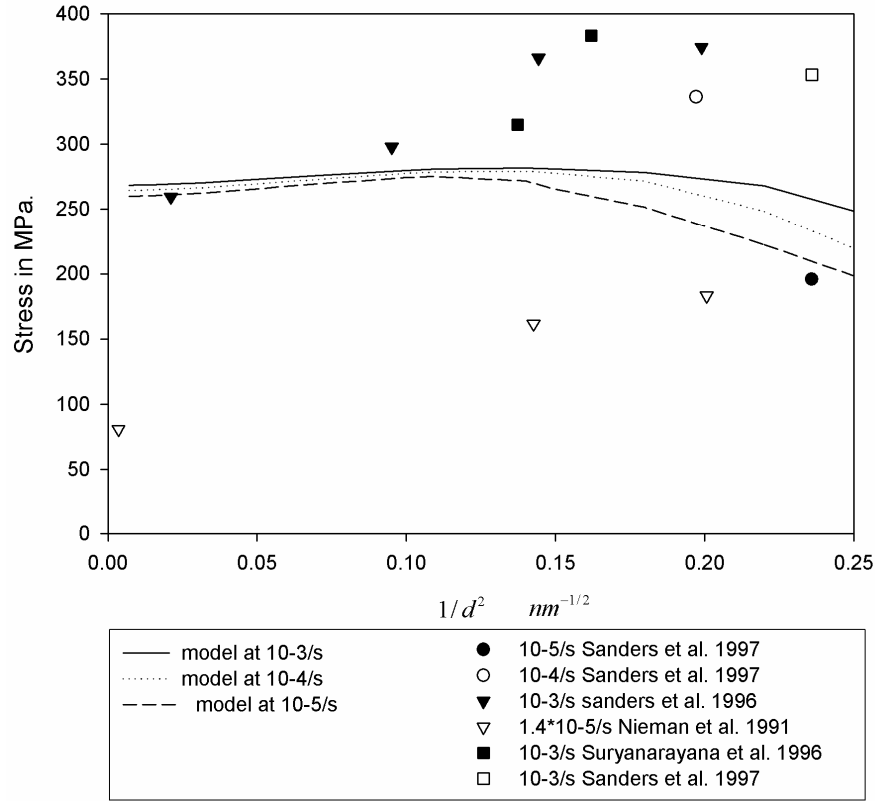
Figure 4.11: Evolution of the yield stress with grain size.

Summary and discussion

In this chapter, two models were introduced to describe the possible effects of diffusion based phenomena (Coble creep and Lifschitz sliding). It can be clearly concluded that the simultaneous effect of Coble creep and Lifshitz sliding leads to an overestimated softening of the plastic response of NC materials

.

However, the first model accounting for the sole effect of vacancy diffusion along the grain interior/grain boundaries interface reveals that, on the condition that vacancy diffusion mechanisms are indeed activated in NC materials, the mechanism of Coble

creep could lead to the experimentally observed softening of the plastic response of NC

materials. Moreover, the model also sheds light on a critical limitation; plastic

deformation is clearly overestimated when the deformation is larger than 1%. Although

this issue does not affect the predicted Hall Petch slope, it suggests that the 2PEVP

scheme used to perform the scale transition may not adequate for use in the present

problem. Also, as discussed in Chapter 1, the description of plastic deformation in grain

interiors, based on the formalism developed in early work of Kocks, Mecking and Estrin,

leads to underestimated Hall Petch slopes in the conventional regime. Hence, the

description of plastic deformation within the grain interiors needs further refinement to

precisely describe the Hall Petch law. This limitation will be investigated in following

chapter

References

Capolungo, L., M. Cherkaoui, et al. (2004). Homogenization method for strength and inelastic behavior of nanocrystalline materials. Size effects on material and structural behavior at micron and nanometer-scales, Hong Kong, Kluwer Academic Publisher.

Capolungo, L., C. Jochum, et al. (2005). "Homogenization method for strength and inelastic behavior of nanocrystalline materials." International journal of plasticity 21: 67-82.

Cherkaoui, M., Q. Sun, et al. (2000). "Micromechanics modeling of composite with ductile matrix and shape memory alloy reinforcement." International journal of solids and structures 37: 1577-1594.

Coble, R. L. (1963). "A Model for Boundary Diffusion Controlled Creep in Polycrystalline Materials." Journal of Applied Physics 34(6): 1679-1682.

Estrin, Y. and H. Mecking (1984). "A unified phenomenolgical description of work hardening and creep based on one parameter models." Acta metallurgica 32: 57-70.

Estrin, Y. (1998). "Dislocation theory based constitutive modelling: foundations and applications." Journal of the materials processing technology 80-81: 33-39.

Kim, H. S., Y. Estrin, Bush, M.B. (2000). "Plastic deformation behaviour of fine grained materials." Acta materialia 48: 493-504.

Kim, H. S., Y. Estrin, Bush, M.B. (2001). "Constitutive modelling of strength and plasticity of nanocrystalline metallic materials." Materials science and engineering A316: 195-199.

Nieman, G. W., Weertman J.R., Siegel R.W. (1991). "Mechanical behavior of nanocrystalline Cu and Pd." Journal of materials research 6: 1012-1027.

Sanders, P. G., J. A. Eastman, Weertman, J.R (1996). Processing and Properties of Nanocrystalline Materials. Warrendale, PA, TMS.

Sanders, P. G., Eastman, J.A., Weertman, J.R (1997). "Elastic and tensile behavior of nanocrystalline copper and palladium." Acta metallurgica 45: 4019-4025.

Surayanarayana, R., Frey, R., Sastry, S.M.L.,Waller, B.E., Bates, S.E., Buhro, W.E. (1996). "Deformation, recovery, and recrystallization behavior of nanocrystalline copper produced from solution-phase synthesized nanoparticles." Journal of alloys and compounds 11: 449-457.

Youngdahl, C. J., Sanders, P. G., Eastman, J.A., Weertman, J.R. (1997). "Compressive yield strengths of nanocrystalline Cu and Pd." Scripta materialia 37: 809-813.

CHAPTER 5

GRAIN BOUNDARY ASSISTED DEFORMATION

This chapter is dedicated to grain boundary assisted deformation which, as mentioned in Chapter 1, plays a major role in the response of NC materials. The first part of this chapter aims at revealing some interesting aspects of the elastic deformation of bicrystal interfaces. This work results from collaboration with Dr. Spearot who kindly performed all molecular dynamics simulations used in this chapter.

The second part of this chapter aims at investigating the viscoplastic response of NC materials. In particular, a novel constitutive law is introduced to describe the mechanism of grain boundary dislocation emission and penetration. Also, a hierarchal scale transition technique is developed to link molecular simulations on bicrystal interfaces to the previously mentioned constitutive law. These molecular dynamics simulations are also used to investigate the activity of grain boundary ledges. Finite elements simulations are performed to estimate stress heterogeneities which cannot be predicted with Eshelbian micromechanics. Finally, an unaccomodated grain boundary sliding model is developed to estimate its effect on NC deformation.

Elastic deformation mechanisms

The objective of this section is to study the discrete atomic motion of bicrystal interfaces and the evolution of their excess energy when submitted to a uniaxial tensile

deformation (Spearot, Capolungo et al. 2007). This study is limited to the elastic regime. The plastic regime will be subject investigated in following section. Let us note that this work has for long term objective to study the relationship between interface stress and interface free energy in the case where the well known Shuttlewoth equation does not apply.

Let us recall that the Shuttleworth equation, which is based on the Gibbs Duhem equation, holds in the case where no load is applied perpendicular to the interface plane. For solid-solid interfaces, the derivation of the Shuttleworth equation (1950) requires the assumption of coherency and mechanical equilibrium at the interface (Muller et al. 2004). Precisely, the Shuttleworth equation is first based on the thermodynamic equilibrium of an interface which excess energy, dW^{exc}, is typically given by (Muller and Saul 2004):

$$dW^{exc} = \left[\delta\varepsilon_{ij}^{\parallel} s_{ij} + \sigma_{ij}^{\perp} \delta e_{ij} \right] S_{AB}$$
(5.1)

Here S_{AB} denotes the area of the interface. $\delta\varepsilon_{ij}^{\parallel}$ and $\sigma_{ij}^{\perp}$ denotes the infinitesimal change in strain parallel to the interface and the stress perpendicular to the interface. s_{ij} and δe_{ij} denote the interfacial excess stress (parallel to the interface) and the infinitesimal change in the interfacial excess strain (perpendicular to the interface). The effect of perpendicular components is then neglected and this leads to a relation between the interface stress (which components are all parallel to the interface), the interface energy and its derivative with respect to the interface strain (which components are all parallel to the interface). Clearly, the Shuttleworth equation does not allow to treat the

212

case where the interface is stretched normally to its plane. Such a study would aver useful in order to introduce a precise description of the effect of interfaces (grain boundaries for example) in a generalized self-consistent scheme.

In order to study a wide range of grain boundary interfaces, six interfaces, with low order coincident site lattice content, are constructed about the [100] misorientation axis: , $\Sigma 5$ (210) 53.1^o, $\Sigma 5$ (310) 36.9^o, $\Sigma 13$ (320) 67.4^o, $\Sigma 13$ (510) 22.6^o,$\Sigma 17$ (410) 28.1^o and $\Sigma 17$ (530) 61.9^o.

Model geometry and simulation methodology

The geometric model is presented in Figure 5.1.(a) and the interface dimensions are presented in table 5.1 The MD simulations are performed on copper symmetric tilt boundaries about the [100] crystallographic axis. Mishin et al. (2001) embedded atom potential is used to describe the inter-atomic bonds between atoms. Periodic boundary conditions are enforced in all directions. Note that the periodic boundary conditions lead to the presence of two half interfaces, with structure similar to the central one, on the periodic border. The model dimensions are specified in order not to influence the predictions by the image forces resulting from the presence of the upper and lower interfaces.
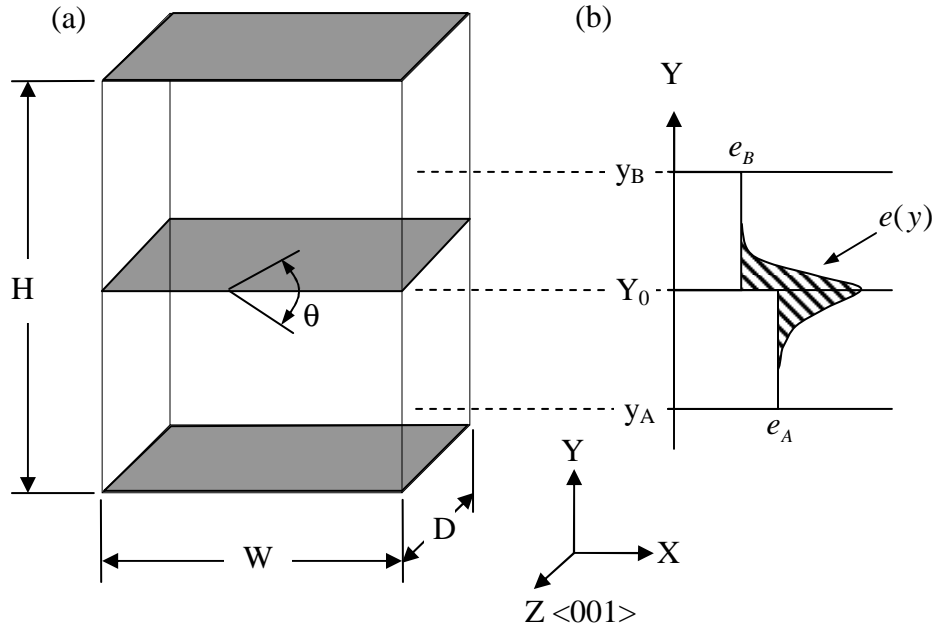
Figure 5.1: Schematic illustration of (a) the bicrystal interface model used in this work and (b) the concept of excess energy at the interface between two crystalline regions.

First, the initial interface configuration is obtained via molecular statics calculations using a non linear conjugate gradient method. The resulting interface structures are compared to high resolution transmission electron microscopy images. The initial configuration is then equilibrated using MD in the isobaric-isothermal ensemble at a pressure of 0 bar and a temperature of 10 K. For further details on the above described procedure, the reader is referred to Spearot (2005) who performed all molecular simulations presented in this chapter. Therefore, all figures presented in this section are extracted from (Spearot, Capolungo et al. 2007). Second, stresses of 1, 2, 3, 4 and 5GPa, are applied to the normal of the boundary plane (Y-direction). Note here that in order to remain in the elastic regime; the applied stresses are lower than the stress required for

dislocation emission to be activated. Throughout the simulations, the X and Z direction

boundaries are stress-free. The thermodynamic equilibrium is held for 100 ps in order to

minimize the fluctuations in the excess quantitities.

Table 5.1. Bicrystal interface misorientations and model dimensions.

Interface	Angle	Width, W (nm)	Height, H (nm)	Depth, D (nm)	Interface Structure	Number of atoms
Σ13 (510)	22.6^{o}	18.43	22.12	14.46	|CDD|	494,400
Σ17 (410)	28.1^{o}	17.88	23.85	14.46	|CD.CD|	518,400
Σ5 (310)	36.9^{o}	17.15	22.86	14.46	|C|	477,600
Σ29 (730)	46.4^{o}	19.27	22.03	14.46	|B'B'C|	516,320
Σ5 (210)	53.1^{o}	17.78	22.63	14.46	|B'.B'|	489,280
Σ5 (210)	53.1^{o}	17.78	45.27	14.46	|B'.B'|	982,080
Σ5 (210)	53.1^{o}	17.78	67.90	14.46	|B'.B'|	1,474,880
Σ17 (530)	61.9^{o}	18.97	21.08	14.46	|A$_s$B'|	485,280
Σ13 (320)	67.4^{o}	18.25	23.46	14.46	|AB'.AB'|	519,680

Interface excess energy

The interface energy, denoted E^{int}, is defined as the energy within the boundary of

the two crystalline regions, in excess of the intrinsic energy of the bulk lattices. A

schematic of the principle is given in Figure 5.1.(b). The excess interface energy is given by:

$$E^{\text{int}} = \int_{y_A}^{y_B} e(y) dy - e_A (Y_0 - y_A) - e_B (y_B - Y_0) \quad .$$

(5.2)

Here $e(y)$, e_A and e_B denote the energy profile normal to the interface, the bulk energy in region A (lower crystalline region) and the bulk energy in region B (upper crystalline region), respectively. The vertical locations Y_0, y_A and y_B are defined schematically in Fig. 5.1.b. Equation (5.2) is adapted to the case of a discrete system by replacing the integral terms by sums on all atoms of the region considered.

$$E^{\text{int}} = \sum_{i=1}^{N_A} [e_i - e_A] + \sum_{i=1}^{N_B} [e_i - e_B]$$

(5.3)

Here, N_A and N_B are the number of atoms in regions A and B, respectively. The bulk energies, e_A and e_B, are determined by averaging the e_i of a group of atoms positioned sufficient far away from the interface such that the presence of the boundary is not detected. Using e_A and e_B, an excess energy is computed for every atom within the interface model; the sum of these excess energies is defined as the total interface energy.

Bicrystal interface evolution

Let us now discuss the atomistic rearrangement of the six different simulated structures. The energy profile, after energy minimization and isobaric-isothermal

equilibration, of the Σ5 (210) 53.1° boundary is presented in figure 5.2 (a) for which only the first two atomic layers are used on the Z-direction. Recall that periodic boundary conditions are used in all directions. In Figure 5.2. (b) one can observe an image of the simulated structure where the atoms are colored by their excess energy $e_i - e_{bulk}$. It can be observed that the interface can be described as a sequence of B'.B' structural units. Interestingly, the structure presents a slight asymmetry. This can be observed in Figure 5.2.(a) where the atoms in the layer above the interface (denoted by +1) have a higher energy than that of the atoms in the layer below the interface (denoted by -1). Also, from the plots of the energy profile after energy minimization and after thermodynamic equilibration (Figure 5.2.a), it can be concluded that the observed asymmetry does not result from the thermal equilibration.

Figure 5.2: (a) Interface energy profile for a Σ5 (210) interface in copper after energy minimization and isobaric-isothermal equilibration. (b) Structure of the Σ5 (210) interface after NPT equilibration showing the slight asymmetry of the boundary. Atoms are colored by excess energy.

The energy profiles of the Σ5 (210) interface at 1.0, 3.0 and 5.0 GPa applied stresses are presented in Figure 5.3.(a). While most layers see their energy increase, this is especially the case of layer (0), several layers decrease in energy upon increasing the applied stress. This can be observed in layers (+1) and (-1). In terms of atomistic motion, one can observe that the initial asymmetry is removed upon loading the bicrystal. Indeed,

when the applied stress is equal to 5 GPa. atoms in the (+1) and (-1) layers are aligned (see Figure 5.3(b)).
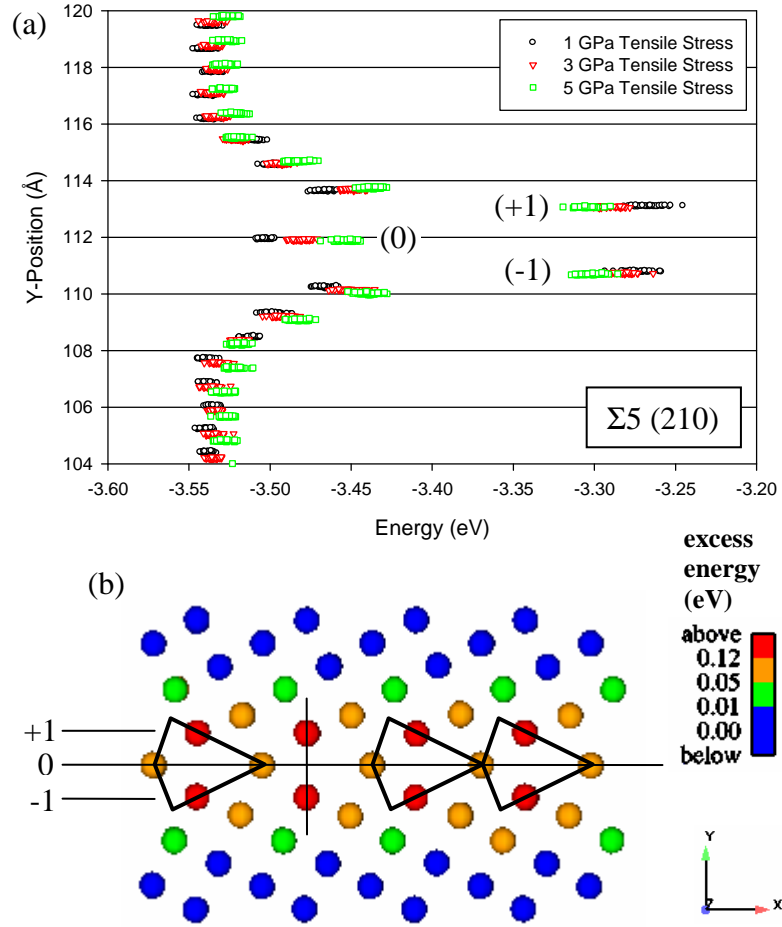
Figure 5.3:(a) Energetic evolution of the atomic layers in the vicinity of the Σ5 (210) interface showing that atomic layers may increase or decrease in energy during deformation. (b) Structure of the Σ5 (210) interface at a tensile stress of 5.0 GPa demonstrating that the interface asymmetry has been removed by the tensile deformation.

The energy profile of the $\Sigma 5$ (310) 36.9° boundary after both energy minimization en isobaric-isothermal equilibration is presented in Figure 5.4.(a). As in the previous case, solely the first two atomic layers are used. Contrary to that of the $\Sigma 5$ (210) boundary, the $\Sigma 5$ (310) interface has a perfectly symmetric structure even though the {001} and {002} layers have different structural configurations. From Figure 5.4.(b) it can be concluded that, as expected, the $\Sigma 5$ (310) 36.9° boundary is composed uniquely of C structural units. Also, it can be observed that atoms composing the (0) plane can have two possible energy states; (1) a low energy state corresponding to atoms positioned in the {001} layer and (2) a higher energy state corresponding to atoms in the {002} layer. Let us note that atoms in the lower energy state serve as intersections between C structural units. The high and low energy layers are denoted $(0)_A$ and $(0)_B$, respectively. Finally, as presented in Figure 5.5(a) thermal vibration does not lead to major changes in the energy profiles.
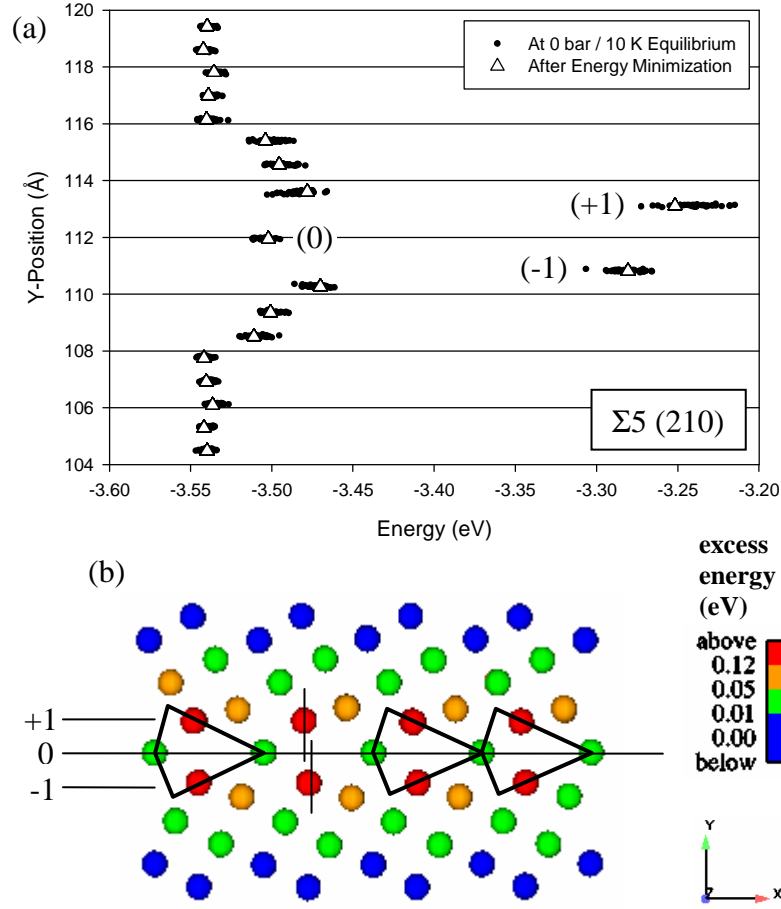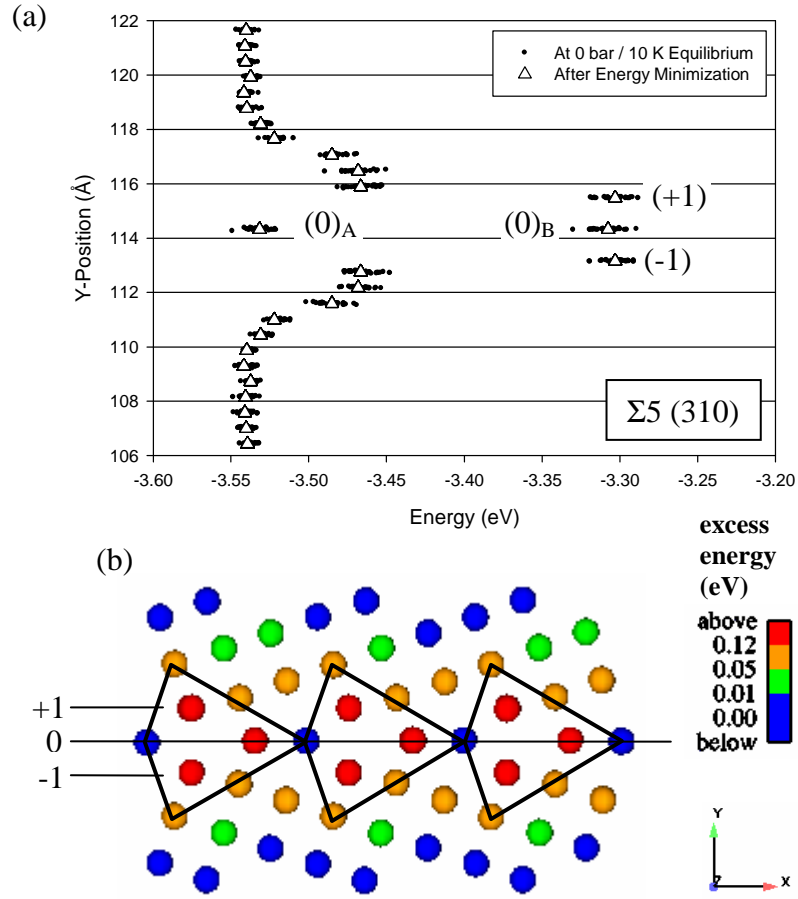
Figure 5.4: (a) Interface energy profile for a Σ5 (310) interface in copper after energy minimization and isobaric-isothermal equilibration. (b) Structure of the Σ5 (310) interface after equilibration showing the interface structural units. Atoms are colored by excess energy.

The evolution of the interface energy profile after loading at 1.0, 3.0 and 5.0 GPa is presented in Figure 5.5 (a). While most atomic layers have an increasing energy with increasing loading, the three layers with the largest initial energy, $(0)_B$, $(+1)$ and (-1), decrease in energy. Interestingly, the simulations reveal a unique behavior of the Σ5 (310) interface. Precisely, when the applied load reaches a critical threshold stress between 3.25

and 3.5 GPa, atoms within the $(0)_A$ layer bifurcate in the Y-direction. An image of the bifurcation event is presented in Figure 5.5.(b) in which the tensile stress is equal to 5.GPa. We speculate that this bifurcation event, which can also be observed in layers (+4) and (-4) with same critical threshold stress, may trigger the anelastic deformation of the interface and may be facilitated by the expansion of the structural unit during elastic deformation. Indeed, it was shown via MD simulations that in the case of C structural units composed interfaces, a shift normal to the boundary plane occurs during the dislocation nucleation event. Similarly to the previously studied interface, the interface scale effect was studied and did not reveal any artifacts in the simulations.
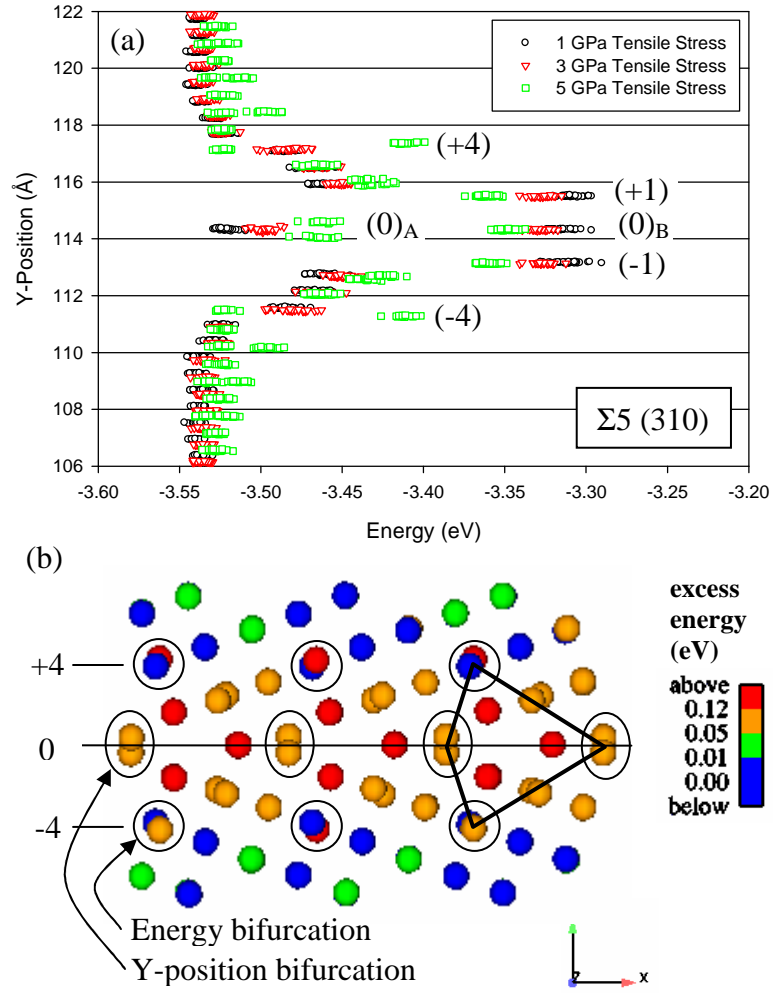
Figure 5.5: (a) Energetic evolution of the atomic layers in the vicinity of the Σ5 (310) interface. Bifurcation of the $(0)_A$, (+4) and (-4) layers is identified as an evolution mechanism. (b) Structure of the Σ5 (310) interface at a tensile stress of 5.0 GPa showing the discrete changes in interface structure during the deformation process.

In the same manner the energy profiles of the copper Σ13 (320) 67.4^o , Σ13 (510) 22.6^o , Σ17 (410) 28.1^o and Σ17 (530) 61.9^o boundaries subjected to 1.0, 3.0 and 5.0

GPa. where investigated. Although not shown here, the MD simulations revealed that the

$\Sigma13$ (320), $\Sigma17$ (530) are composed of |AB'.AB'| and B' structural units displaced by

one atomic layer in the Y-direction, respectively. In the case of the $\Sigma17$ (530) the

particular structure composed of displaced B' structural units clearly shows the limits of

the structural unit model. Moreover the simulations also revealed that the "bifurcation

event does not occur for these interfaces. On the contrary, the $\Sigma13$ (510) and $\Sigma17$ (410)

which are composed of |CDD| and |CD.CD| structures exhibit the occurrence of the

bifurcation phenomenon at threshold stresses 1.75 GPa and ~2.25GPa. Therefore it can

be concluded that the presence of C structural units affects the occurrence of the

bifurcation event which is to be discussed in following section.

Evolution of the Excess Interface Energy

Let us now rationalize the occurrence of the bifurcation events via energetic

considerations. First, the bulk energy of the opposing lattice regions is calculated by

averaging the energy of atoms sufficiently far away from the boundary (see Figure

5.6.(a)). As expected the energy input to the bicrystal results in an increase in the bulk

energy.

Second, the excess interface energy , normalized with respect to the interface energy

obtained after isobaric-isothermal equilibration, is calculated for each load and each

boundary presented in this work (See Figure 5.6.(b)). The data are also divided by the

surface of the model in order to obtain excess energy per area. It can be noticed that both

$\Sigma5$ boundaries exhibit a decreasing excess energy with increasing load. Let us recall that

a decrease in the interface energy does not imply that the total energy of the system

decreases but that the energy of the bulk lattice region increases more rapidly than that of

the interface. Hence, energy storage within these grain boundaries is less efficient that of the perfect lattice. This may results from the special geometric constraints imposed on atoms that compose the $\Sigma5$ (210) and $\Sigma5$ (310) interfaces. Indeed, the crystallographic constraint of the B' and C structural units limits the lateral contraction during uniaxial tension as compared with the $\Sigma13$ and $\Sigma17$ boundaries examined in this work, which contain regions of 'perfect' lattice (A or D structural units) between the B' and C structural features. Interestingly, in Figure 5.6.(b) it can be noticed that the occurrence of the bifurcation event leads to an increase in the interface excess energy. Hence, the elastic bifurcation event can be considered as an energy storage enhancement mechanism. Since the energy stored in grain boundaries directly affects the grain boundary dislocation mechanism, which is thermally activated, the discrete atomic bifurcation event may be of great importance on the elastic and viscoplastic deformation of NC materials. Also, the "bifurcation" event which physically corresponds to a redistribution of the energy of the interface with its surrounding, shall lead to a softening in the elastic response of the interface. This shall be the case if the interfaces were constrained in terms of displacement rather than stress. Interestingly the structure observed during the energy redistribution may correspond to metastable configurations which could result in a pseudo elastic response of the interface. This will be subject to future studies.

To verify the conclusion that the geometric constraints imposed by the B' and C structural units affect the efficiency of energy storage during elastic deformation, additional MD simulations are performed on a $\Sigma29$ (730) 46.4^{o} interface, which energy minimization predicts has a |B'B'C| structure. The evolution of the excess interface

225

energy for the Σ29 interface is shown in Figure5.9 (b) in comparison with the other boundaries considered in this work. Clearly, the excess interface energy of the Σ29 (730) boundary decreases during uniaxial tensile deformation. Furthermore, the effect of elastic bifurcation on the excess interface energy can be identified in Fig. 5.9.(b) as a brief increase in the excess interface energy between 2 and 3 GPa. Visual inspection of the interface structure during deformation confirms that the elastic bifurcation event does initiate between 2 and 3 GPa; however, the magnitude of the local variation in the Y-position (for example) is not as significant as that in the Σ5 (310) interface shown in Fig. 6(a).
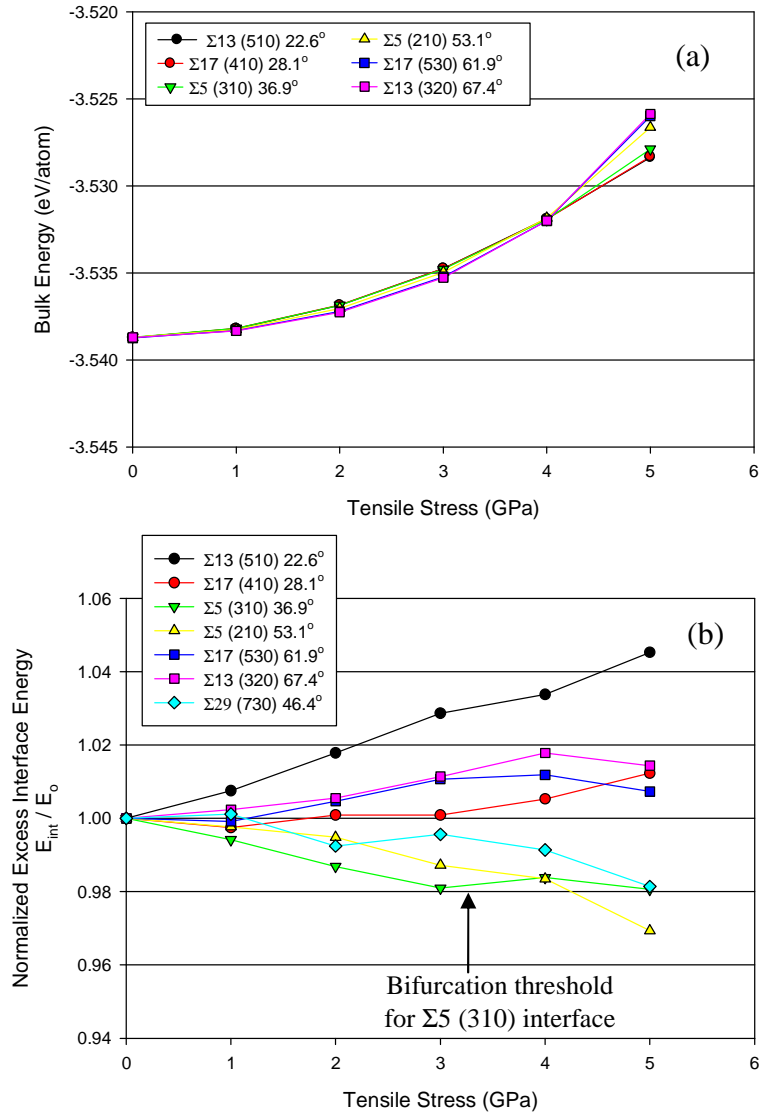
Figure 5.6: (a) Bulk energy as a function of applied tensile stress; (b) normalized excess interface energy as a function of applied tensile stress. Boundaries which contain B' and C structural units show a decrease in excess interface energy, while $\Sigma 13$ and $\Sigma 17$ boundaries show an increase in excess energy.

Viscoplastic deformation

This section is dedicated to the study and modeling of the viscoplastic deformation of NC materials. As mentioned in Chapter 1, grain boundary assisted deformation, via the emission and penetration of dislocations by/within grain boundaries and the relative sliding of grains, may be of primary importance. Therefore, this section is composed of two subsections; a first section in which the activity of grain boundary dislocation emission and penetration is studied, and a second section in which the activity of grain boundary sliding is considered. The modeling of the effect of grain boundary dislocation emission and penetration is based on a hierarchal scale transition technique to be presented in what follows.

Also, both two-phase and three-phase representations of the material will be used. In all cases, the inclusion phase will represent grain interiors. In the case of two-Phase models, the matrix phase will represent grain boundaries and triple junctions while in the case of 3-phase models, the matrix phase will represent the effective medium and grain boundaries and triple junctions will be encompassed in the coating phase.

Grain boundary dislocation emission and penetration

The methodology used to model the effect of grain boundary dislocation emission and penetration is presented in Figure 5.7 (Capolungo et al. 2005, 2007a, 2007b). The methodology relies on the solution of three distinct steps: (1) equivalent representation of the material, (2) atomistic simulations and (3) homogenization. In the first step an equivalent representation of the material is chosen. For example, the material can be

represented as a two-phase composite or as a three-phase composite as discussed in Chapter 3. From the representation of the material, constitutive laws for each phase must be developed which leads to step 2 consisting of informing the continuum based constitutive laws with use of molecular dynamics simulations. As will be shown, in the case of constitutive laws based on statistical mechanics the bridging between the atomistic scale and the scale of the continuum may be performed. Finally, as discussed in Chapter 3, the local constitutive laws are used to predict the macroscopic response of the material.

Let us now present the constitutive laws of the grain interiors and grain boundaries for which solely the effect of grain boundary dislocation emission and penetration are accounted for.

.
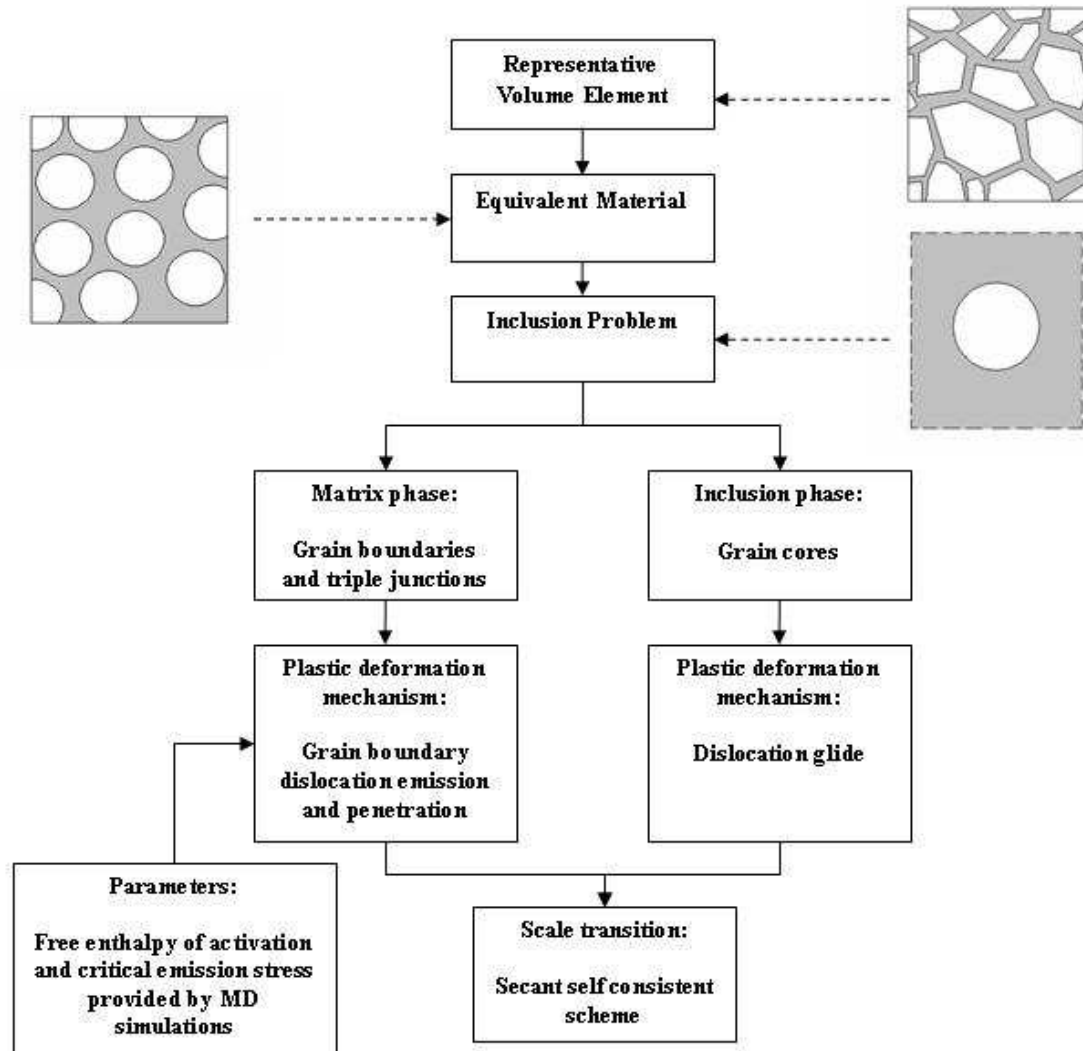
Figure 5.7: Schematic of the methodology.

<u>Continuum modeling</u>

grain interiors

This model aims at capturing the size effect in the elastic-viscoplastic deformation of pure F.C.C. polycrystalline materials with grain sizes ranging from several microns down to a few nanometers. Therefore, the behavior of grain interiors results from the activity of dislocations. Precisely, it is assumed here that dislocation glide is the only

mechanism active in grain interiors. Let us note though, that as discussed in Chapter 1, dislocation activity in NC materials is severely reduced. Hence, the proposed model will clearly lead to overestimated response of nanosized grain interiors. This issue will be discussed in Chapter 6. Considering the time and temperature dependence of dislocation glide, the constitutive law of the grain interiors is elastic-viscoplastic and written as follows:

$$\dot{\boldsymbol{\sigma}}^{I} = \boldsymbol{C}^{I} : \left(\dot{\boldsymbol{\varepsilon}}^{I} - \dot{\boldsymbol{\varepsilon}}^{I,vp} \right) \tag{5.4}$$

Here, $\boldsymbol{C}^{I}$ $\dot{\boldsymbol{\varepsilon}}^{I,vp}$ and $\dot{\boldsymbol{\varepsilon}}^{I}$ are the fourth order elastic modulus tensor of the crystallites, the second order viscoplastic strain rate tensor and the second order deformation tensor respectively. Supposing isotropic hardening, the equivalent viscoplastic strain rate $\dot{\varepsilon}_{eq}^{I,VP}$ can be related to the viscoplastic strain rate via Prandtl Reuss flow rule:

$$\dot{\boldsymbol{\varepsilon}}^{I,vp} = \frac{3}{2} \left(\frac{\dot{\varepsilon}_{eq}^{I,vp}}{\sigma_{eq}^{I}} \right) \boldsymbol{\sigma}_{dev}^{I} \tag{5.5}$$

Here, $\boldsymbol{\sigma}_{dev}^{I}$ and σ_{eq}^{I} denote the deviatoric part of the stress tensor and the equivalent stress defined by $\sigma_{eq}^{I} = \sqrt{3/2 \left(\boldsymbol{\sigma}_{dev}^{I} : \boldsymbol{\sigma}_{dev}^{I} \right)}$, respectively. Using a power law for the description of the thermally activated dislocation glide mechanism, one can write the equivalent viscoplastic strain rate as follows:

$$\dot{\varepsilon}_{eq}^{I,VP} = \dot{\varepsilon}_0 \left(\frac{\sigma_{eq}^I}{\sigma_f} \right)^m$$

(5.6)

Recall that *m,* the strain rate sensitivity coefficient, represents both shape and area of the dislocation glide resistance diagram. From experimental data, sited in Chapter 1, the hardening coefficient *m* is size dependent. Cheng et al. (2005) proposed the following model in which the size effect arises from both the size dependence in the activation volume and in the flow stress:

$$m = \frac{\sigma_f \times \Lambda \times \xi \times b}{k_b T}$$

(5.7)

where k_b, T, b, ξ, l^* and σ_f' are the Boltzmann's constant, the temperature, Burger's vector, the distance swept by a dislocation during an activation event, the obstacle spacing and the flow stress at zero K, respectively. Let us recall that in conventional materials *m* traditionally ranges in the neighborhood of ~150 while in the case of NC materials reported values range in the neighborhood of ~30 (Cheng et al., 2005). Also, equation (5.7) is weighted with a proportionality factor included in ξ in order to account for the fact that the statistical treatment of dislocations naturally leads to overestimated values of the dislocation mean free path. This was clearly discussed in review by Kocks and Mecking (2003)

While in models presented in Chapter 4 the flow stress at zero Kelvin accounted solely for the effect of stored dislocations, in the present model the stress field engendered by the lattice distortion present at grain boundaries is taken into account. Hence, the expression of the flow stress at zero Kelvin shall be written as the sum of three terms (Wei et al., 2004):

$$\sigma_f = \sigma_0 + \sigma_{dis} + \sigma_{GB} \tag{5.8}$$

where $\sigma_{dis} = \alpha G M b \sqrt{\rho}$ and $\sigma_{GB} = \beta / \sqrt{d}$ and represent the stress engendered by stored dislocations and grain boundaries, respectively. Here α, G, M and ρ denote a numerical constant, the shear modulus, the Taylor factor and the dislocation density, respectively. Note here that no distinction between statistically stored dislocation and geometrically necessary dislocation is made. Also, σ_0 denotes a lattice friction term which is typically neglected. Let us note that equation (5.8) introduces a size effect through the term σ_{GB}. The size dependence of σ_{GB} arises from the fact that F.C.C. metals abide the Hall-Petch at zero Kelvin.

The evolution of the dislocation density is driven by the simultaneous effect of: (1) athermal storage and, (2) dislocation annihilation. Let us recall that several models for the dislocation storage have been proposed. For example, Kocks and Mecking (2003) introduced a percolation model while Nes (1997) suggested that dislocation storage occurs via the absorption of dislocations into subgrain walls leading to a change in the

dislocation density within these walls. The present approach is based on a statistical description of the phenomenon. Therefore the storage of dislocations is written as follows:

$$\frac{d\rho^+}{d\varepsilon_{eq}^{I,vp}} = \frac{M}{b\Lambda} \qquad (5.9)$$

where M is the Taylor factor, Λ and ρ^+ represent the mean free path of mobile dislocations and stored dislocation density, respectively. $\varepsilon^{I,vp}$ is the equivalent plastic strain in the grain interiors. The dislocation mean free path is typically written as the harmonic average of two terms; a first term Λ^* representing the effect of stored dislocations, and a second term Λ^{**} representing the effect of grain boundaries as barrier to dislocation motion leading to $\Lambda^{**} = d$. Hence, equation (5.9) can be written as follows:

$$\frac{d\rho^+}{d\varepsilon_{eq}^{I,vp}} = M\left(\frac{1}{bd} + \frac{1}{b\Lambda^*}\right) \qquad (5.10)$$

Equation (5.10) defines stage II of strain hardening. Using the concept of material scaling which relates the dislocation density to the geometry of substructures present within the grains, the previous equation can be written in the following form:

$$\frac{d\rho^+}{d\varepsilon_{eq}^{I,vp}} = M\left(\frac{1}{bd} + \frac{\psi\sqrt{\rho}}{b}\right) \qquad (5.11)$$

Here ψ is a proportionality factor.

The thermally activated dynamic recovery mechanism, which leads to a softening in the plastic response of the crystallites, is given the following empirical law introduced by Estrin and Mecking (1984):

$$\frac{d\rho^-}{d\varepsilon_{eq}^{I,vp}} = -k_{20}\left(\frac{\dot{\varepsilon}_{eq}^{I,vp}}{\dot{\varepsilon}_*}\right)^{-1/2} \cdot \rho \tag{5.12}$$

where n is inversely proportional to the temperature, with a reported value of 21.25 at 300 K (Estrin and Mecking, 1984), k_{20}^* is a numerical constant, ρ^- denotes the annihilated dislocation density and $\dot{\varepsilon}_*$ denotes a normalization strain rate. Grouping the effects of dislocation storage and dislocation annihilation together, one obtains the following expression of the evolution of dislocation density with the local equivalent viscoplastic strain:

$$\frac{d\rho}{d\varepsilon_{eq}^{I,vp}} = M\left(\frac{1}{bd} + \frac{\psi\sqrt{\rho}}{b}\right) - k_{20}\left(\frac{\dot{\varepsilon}_{eq}^{I,vp}}{\dot{\varepsilon}_*}\right)^{-1/n} \rho \tag{5.13}$$

To be consistent with the notations used in most strain hardening models (Kocks, 1976; Estrin and Mecking, 1984), equation (5.13) will be written as follows:

$$\frac{\partial \rho}{\partial \varepsilon^p} = M\left(\frac{k}{d} + k_1\sqrt{\rho} - k_2\rho\right) \tag{5.14}$$

where

$$k = \frac{1}{b} \ , \ k_1 = \frac{\psi}{b}, k_2 = k_{20}\left(\frac{\dot{\varepsilon}_{eq}^{I,vp}}{\dot{\varepsilon}_*}\right)^{-1/n} \tag{5.15}$$

Hardening rate

Let us discuss the effect of the term σ_{GB} introduced in the expression of the flow stress at zero Kelvin given by equation (5.8). Also, let us recall that the models presented in previous chapter could not successfully lead to an acceptable Hall Petch slope in the conventional regime. Hence, let us compare the hardening rates obtained with the present model, the Kocks and Mecking (K-M) model and the Estrin and Kock (E-K) 'hybrid' model. The derivation of the hardening rates obtained in the case of the K-M and E-K model are presented in detail in article by Estrin and Mecking (1984). Also, let us recall that in the upcoming derivations, the strain rate sensitivity parameter *m* is supposed constant. Moreover, in both the K-M and E-K model the flow stress at zero Kelvin is given by $\sigma_f = \alpha MGb\sqrt{\rho}$. The K-M model does not account for the size effect in the storage of dislocation and is given by: $\frac{d\rho}{d\varepsilon^p} = M\left(k_1\sqrt{\rho} - k_2\rho\right).$ Kocks and Mecking report the following expression of the hardening rate $\theta = \frac{d\sigma}{d\varepsilon^p}$:

$$\theta = \theta_{II}\left(1 - \frac{\sigma}{\sigma_s}\right) \tag{5.16}$$

where θ_{II}, σ_s and σ correspond to the stage II strain hardening rate, the saturation stress, and the stress in the tensile direction respectively, and are given by:

$$\theta_{II} = \frac{1}{2} M^2 \alpha Gb k_1 \left(\frac{\dot{\varepsilon}^p}{\dot{\varepsilon}_0} \right)^{1/m} \tag{5.17}$$

$$\sigma_s = \alpha MGb \frac{k_1}{k_{20}} \left(\frac{\dot{\varepsilon}^p}{\dot{\varepsilon}_0} \right)^{1/m} \left(\frac{\dot{\varepsilon}^p}{\dot{\varepsilon}_*} \right)^{1/n} \tag{5.18}$$

Recall that no size effect was taken into account in the early development of Kocks and Mecking (K-M). Therefore, Estrin and Kocks introduced a size effect in the evolution of the dislocation density given by: $\frac{d\rho}{d\varepsilon^p} = M \left(\frac{k}{d} + k_1 \sqrt{\rho} - k_2 \rho \right)$. This Hybrid model leads to the following expression of the hardening rate:

$$\theta = \frac{M}{\sigma} \frac{k_2}{2} \left(\sigma_s^h \right)^2 \left[1 - \kappa + \kappa \frac{\sigma}{\sigma_s^h} - \left(\frac{\sigma}{\sigma_s^h} \right)^2 \right] \tag{5.19}$$

where the saturation stress σ_s^h and κ are defined as follows

$$\sigma_s^h = \alpha MGb \frac{k_1}{k_2} \frac{\dot{\varepsilon}^{p^{\frac{1}{m}}}}{\dot{\varepsilon}_0} \kappa^{-1} \quad , \quad \kappa = 2 \left[1 + \left(1 + \frac{4kk_2}{dk_1^2} \right)^{\frac{1}{2}} \right]^{-1} \tag{5.20}$$

237

Let us now present the resulting Haasen plot. Figure 5.8 presents a Haasen plot extracted from two tensile tests on a 20 micron and 110 nm CU samples (Sanders et al. 1997). It can be noticed that a decrease in the grain size leads to a shift in the maximum value of on the plot, and in the saturation stress. Also let us recall that as argued by Kocks and Mecking the hybrid model cannot predict accurate values of the hall Petch slopes. This was clearly exhibited in models presented in Chapter 4.
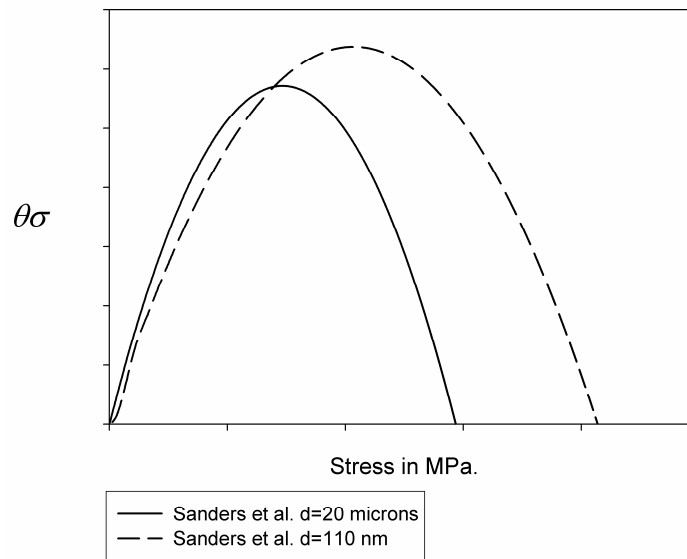
Figure 5.8: Experimental Haasen plot.

Figure 5.9 presents Haasen plots predicted by hybrid model introduced by Estrin and Kocks. The same two grain sizes considered in previous plot are used in the simulations and the constants used in the model where chosen to obtain a best fit of the experimental stress strain curves. The limitations of the Hybrid model can be clearly seen for the two curves do not have same starting point as their experimental equivalents and the shifts in the maximum values cannot be predicted.
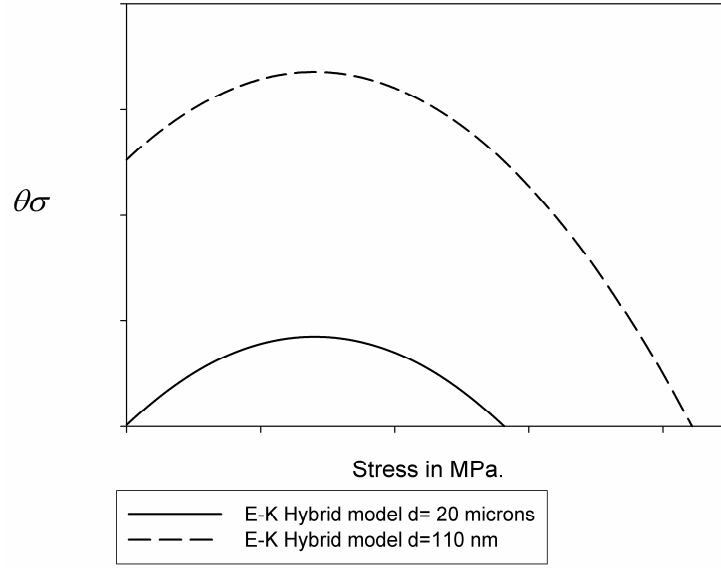
Figure 5.9: Haasen plot from Estrin et al.'s hybrid model.

We now consider the size dependence of the hardening coefficient, which has a major influence on creep behavior. The present model incorporates the effect of long range obstacles on the flow stress at zero Kelvin. After some algebra (the details of the derivation are presented in Appendix C), the model yields the following set of equations for the hardening behavior at constant plastic stain rate:

$$
\theta = \frac{Mk_2\sigma_s^2}{2\left[\sigma\left(\frac{\dot{\varepsilon}^p}{\dot{\varepsilon}_0}\right)^{-1/m} - \frac{\beta}{\sqrt{d}}\right]}\left[1 - \left(\frac{\sigma}{\sigma_s}\right)^2 - 2\left(1 - \frac{\sigma}{\sigma_s}\right)(1+Z)\left(1+Z+\left(1+\frac{4k_2k}{d}\right)^{\frac{1}{2}}\right)^{-1}\right]
$$

(5.21)

Or equivalently,

239

$$\theta = \frac{Mk_2\left(\sigma_s\right)^2}{2\left(\sigma\left(\dfrac{\dot{\varepsilon}^p}{\dot{\varepsilon}_0}\right)^{-1/m} - \dfrac{\beta}{\sqrt{d}}\right)} \cdot \left(\frac{\dot{\varepsilon}_{eq}^p}{\dot{\varepsilon}_0}\right)^{\frac{-1}{m}}\left(1 - \left(\frac{\sigma}{\sigma_s}\right)^2 - 2\left(1 - \left(\frac{\sigma}{\sigma_s}\right)\right)(1+Z)\left(1 + Z + \left(1 + \frac{4kk_2}{d\left(k_1\right)^2}\right)^{\frac{1}{2}}\right)^{-1}\right)$$

(5.22)

Here the saturation stress is given by:

$$\sigma_s = \frac{\alpha MGbk_1}{2k_2}\left(1 + \frac{2\beta k_2}{\alpha MGbk_1\sqrt{d}} + \left(1 + \frac{4k_2k}{dk_1^2}\right)^{\frac{1}{2}}\right)$$

(5.23)

with

$$Z = \frac{2\beta k_2}{\alpha MGbk_1\sqrt{d}}$$

(5.24)

It can be readily seen that the present model reduces to the E-K model if the contribution of long range obstacles is neglected, i.e., $\beta = 0$. Introducing the effect of grain boundaries on the flow stress at zero Kelvin will lead to a shift in the maximum of the Haasen plot. Moreover, as described in equation (5.23), the saturation stress, which defines the maximum stress achievable, will be more likely to increase with a decrease in the grain size.

grain boundaries

In order to quantify the sole contribution of grain boundary dislocation emission, the contribution of grain boundary sliding is neglected and plastic deformation, in the matrix

phase (in the case of 2-phase models) or in the coating (in the case of 3 phase models), is assumed to be driven by the emission of dislocations by grain boundaries and triple junctions, which shall be activated at small grain sizes (d<100 nm). The simultaneous contribution of grain boundary sliding and grain boundary dislocation emission will be discussed in future section. Dislocation emission is thermally activated as shown by MD simulations. Since the presence of dislocation forests is less energetically favorable at small grain sizes, an emitted dislocation is expected to travel through the crystallite and to end its trajectory in the opposite grain boundary, causing mass transfer within the grain boundary (see Figure 5.10). Recent MD simulations have shown that following the emission of a dislocation, a grain boundary ledge is created at the nucleation site (Spearot et al. 2005). No long distance mass transfer was observed near the dislocation source. Hence, in the present conceptualization, the effect of dislocation emission on plastic deformation is assumed negligible compared to that of penetration of dislocation into a grain boundary. Let us note that mass transfer does occur both in the neighborhood of the dislocation source and in the region of penetration of the emitted dislocation. As stated above, the mass transfer following the emission process is local and its contribution on the macroscopic response is neglected. Hence, the current model will not insure time reversibility. Specifically, it is supposed that a nucleated dislocation will have two local effects: (1) creation of a dislocation source (ledge) at the nucleation site, which is neglected in the present approach and, (2) creation of mass diffusion within the opposite grain boundary. The latter is responsible for the plastic deformation of grain boundaries. Grain boundary ledges are considered to be the primary dislocation source. This

hypothesis will be investigated in upcoming section dedicated to MD simulations on bicrystal interfaces.
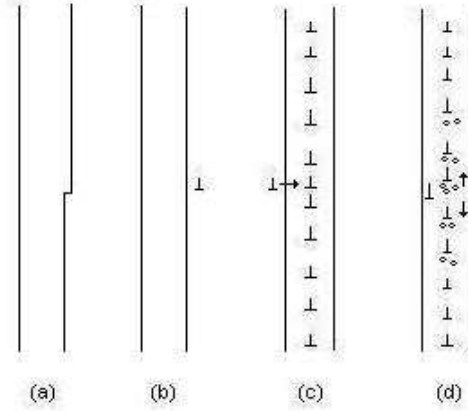
Figure 5.10: Schematic of the mechanisms of emission of dislocation by grain boundaries.

Assuming that every emitted dislocation penetrates the opposite grain boundary, the equivalent viscoplastic strain in the phase including grain boundaries and triple junctions, $\dot{\varepsilon}_M^{eq}$, can then be written as the product of the activation rate for the penetration of a dislocation and the probability of success of emission of dislocations. Experimentally, little dislocation debris is found in samples, indicating that when dislocation emission occurs, full dislocation loops are emitted. Since the trailing partial dislocation is expected to follow the emission of the leading partial it is considered that the critical event is the emission of the leading partial dislocation. Therefore one can write:

$$\dot{\varepsilon}_{eq}^{M} = N_s \dot{\varepsilon}_0^{M} \exp\left(-\frac{\Delta G_0\left(\theta_{mis}\right)}{k_B T}\left(1-\left(\frac{\sigma_{eq}^{M}}{\sigma_c^{M}\left(\theta_{mis}\right)}\right)^{p}\right)^{q}\right) \tag{5.25}$$

where, $\dot{\varepsilon}_0^{M}$ and N_s are the average strain rate caused by the penetration of a dislocation and the number of nucleation sites, respectively. The parameters k, T, σ_{eq}^{M}, and σ_M^{c} represent Boltzmann's constant, the temperature in Kelvin, the equivalent stress in the matrix phase defined by $\sigma_{eq}^{M} = \sqrt{3/2\left(\sigma_{dev}^{M} : \sigma_{dev}^{M}\right)}$ where σ_{dev}^{M} denotes the deviatoric stress tensor, and the critical-emission stress, respectively. The non-dimensional parameters p and q describe the evolution of the enthalpy of activation with the local stress.

The probability of successful emission is described with a Boltzmann distribution. Therefore, ΔG_0 denotes the free enthalpy of activation, corresponding to the energy that must be provided at zero Kelvin to a dislocation for it to move from a stable configuration in the grain boundary to an unstable configuration with positive driving force outside the grain boundary. The unstable configuration is reached once the dislocation has been emitted and has traveled a *minimum* distance such that upon suppressing the load, it would not return to its emission site. Since dislocation emission is a local process, the free enthalpy of activation and the critical emission stress at zero Kelvin are both dependent on the geometry of the grain boundary. For simplicity, the geometry is described by a tilt boundary with tilt angle θ_{mis} (see equation (5.25) and Figure 5.11). A more refined description of the geometry would take into account the five degrees of freedom in grain boundaries.

The average strain rate engendered by a single penetration event, denoted by $\dot{\varepsilon}_0^M$, can be evaluated by approximating the interaction between the emitted dislocation and the interfaces as a soft collision. Let m_{dis} be the effective mass of a dislocation, m_{GB} the total mass of matter in the interface affected by the collision characterized by the length parameter L (see Figure 5.11), $\vec{v}_{dis}$ the velocity vector of the penetrating dislocation and $\vec{v}_{GB}$ the average velocity vector of mass diffusion in the grain boundary area characterized by L. One can then obtain from the conservation of momentum:

$$m_{dis}\vec{v}_{dis} = \left(m_{dis} + m_{GB}\right)\vec{v}_{Gb} \tag{5.26}$$

Let θ be the angle between the slip plane and the longitudinal axis of the grain boundary, referred to as the x-axis (see figure 5.11). The mass transferred into the interfaces via penetration of a dislocation will have two effects, whose relative contributions will depend on θ: (1) mass transfer along the longitudinal axis of the grain boundary and, (2) mass transfer along the transversal axis of the grain boundary. The latter could possibly lead to the creation of a grain boundary ledge. Since most grain boundaries are large angle boundaries in NC materials, the transversal component of the velocity will be neglected.
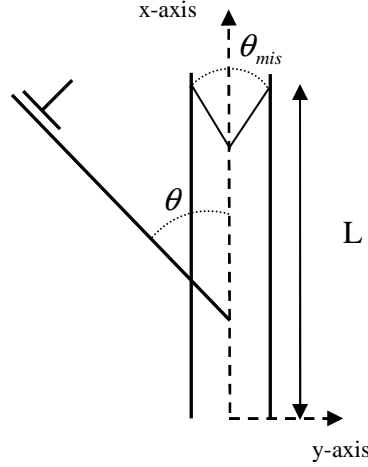
Figure 5.11: Schematic of the penetration of a dislocation.

Projecting equation (5.26) onto the longitudinal axis and dividing the average velocity by the length of the grain boundary region affected by the mass transfer, L, to obtain a strain rate, one obtains:

$$\dot{\varepsilon}_{GB}^0 = \frac{m_{dis}}{m_{dis} + m_{GB}} \frac{v_{dis} \sin \theta}{L} \tag{5.27}$$

where L is proportional to the grain boundary length. The proportionality factor is denoted by κ. Hence, L is written as follows: $L = \kappa d$. This choice is motivated by the fact that triple junctions are expected to act as barrier to the mass motion. It is known that the dislocation velocity v_{dis} is given by:

$$v_{dis} = v_0 \left(\frac{\sigma_{eq}^I}{\sigma_c^I} \right)^m \tag{5.28}$$

245

where v_0 is a proportionality factor. The number of nucleation sites per unit GB area is supposed not to be size dependent. However, the total number of the nucleation sites of the representative volume element increases with decreasing grain size, because of the increasing total surface area. Therefore, the number of nucleation sites will be written as follows:

$$N_s \propto \frac{n_{ledge}}{\pi d^2} = \frac{\delta}{d^2} \tag{5.29}$$

where δ is a proportionality factor. Combining the above equation one obtains the following expression of the expression of the equivalent viscoplastic strain rate:

$$\dot{\varepsilon}_{eq}^M = \frac{\chi}{d^3} \left(\frac{\sigma_{eq}^I}{\sigma_c^I} \right)^m \exp\left(-\frac{\Delta G_0 \left(\theta_{mis} \right)}{k_B T} \left(1 - \left(\frac{\sigma_{eq}^M}{\sigma_c^M \left(\theta_{mis} \right)} \right)^p \right)^q \right) \tag{5.30}$$

where

$$\chi = \frac{m_{dis} v_0 \delta \sin(\theta)}{\left(m_{dis} + m_{GB} \right) \kappa} \tag{5.31}$$

Using Prandtl-Reuss's flow rule, the viscoplastic strain rate tensor can be related to the equivalent plastic strain rate defined in (5.31). One obtains:

$$\dot{\boldsymbol{\varepsilon}}^{M,vp} = \frac{3}{2}\left(\frac{\dot{\varepsilon}_{eq}^{M}}{\sigma_{eq}^{M}}\right)\boldsymbol{\sigma}_{dev}^{M} \tag{5.32}$$

Finally, the constitutive behavior of the matrix phase is given by:

$$\dot{\boldsymbol{\sigma}}^{M} = \boldsymbol{C}^{M} : \left(\dot{\boldsymbol{\varepsilon}}^{M} - \dot{\boldsymbol{\varepsilon}}^{M,vp}\right) \tag{5.33}$$

where $\boldsymbol{C}^{M}$ is the fourth order elastic tensor of the matrix phase.

Although the proposed approach will enable the evaluation of the contribution of grain boundary dislocation emission, the overall response of the material is expected to be overestimated due to several limitations. Indeed, the contribution of sliding mechanisms, which engender a softening in the behavior of the material, is neglected. Moreover, a criterion describing the decrease in dislocation activity, which could emerge from the lower initial dislocation density within the crystallites of NC materials, needs to be developed. Considering the fact that dislocation activity ceases when the grain size is smaller than approximately 10 nm, the model will clearly not be valid when d<10nm. Finally, the constitutive law describing the dislocation emission process is limited to an average misfit angle between adjacent grains. The use of a statistical distribution could improve the model predictions.

As mentioned in the introduction to this chapter, the scale transition from microscopic scale, at which the constitutive laws were developed, to the macroscopic scale is to the macroscopic scale is to be performed via the use of Eshelbian micromechanical schemes (e.g., 2PEVPT, 3PVP etc.) which, as mentioned in Chapter 3, cannot predict stress heterogeneities within a phase. This is due to the fact that in all the models developed, the grain interiors are assumed spherical. Therefore, equation (5.30) is modified to account for these stress heterogeneities:

$$\dot{\varepsilon}_{eq}^{M,vp} = \frac{\chi}{d^3} \left(\frac{\sigma_{eq}^I}{\sigma_c^I} \right)^m \exp \left(-\frac{\Delta G_0 \left(\theta_{mis} \right)}{k_B T} \left(1 - \left(\frac{K \cdot \sigma_{eq}^M}{\sigma_c^M \left(\theta_{mis} \right)} \right)^p \right)^q \right) \qquad (5.34)$$

Here the parameter K accounts for the stress heterogeneities within the inclusion phase. Specifically, it can be seen from the above equation that an increase in the stress within the grain boundaries will lead to an increase in the activity of grain boundary dislocation emission.

In order to assess of the stress heterogeneities within the grain boundaries, a simple 2-phase model is created via the finite element method (Abaqus). Hence, in this simulation, grain cores are described with the constitutive law presented in equations (5.4) to (5.14) and the grain boundaries and triple junctions are described with the set of equations presented in the above (with a stress heterogeneity factor set to 1). Also in equation (5.34), the ratio $\left(\sigma_{eq}^I / \sigma_f \right)^m$ in equation (40) is assumed constant and equal to 0.8. Hence, the behaviour of grain boundaries in the finite element simulation is softer than

that described in the micromechanical based model. As presented in Figure 5.12, the

simulation reveals high stress heterogeneities at triple junctions; a maximum factor of 3 is

predicted (corresponding to the ratio of the maximum value of the Von Mises stress over

its minimum value within the same boundary). These simulations are in agreement with

work by Meyers et al. (1982). However, let us note that these 2-D simulations will clearly

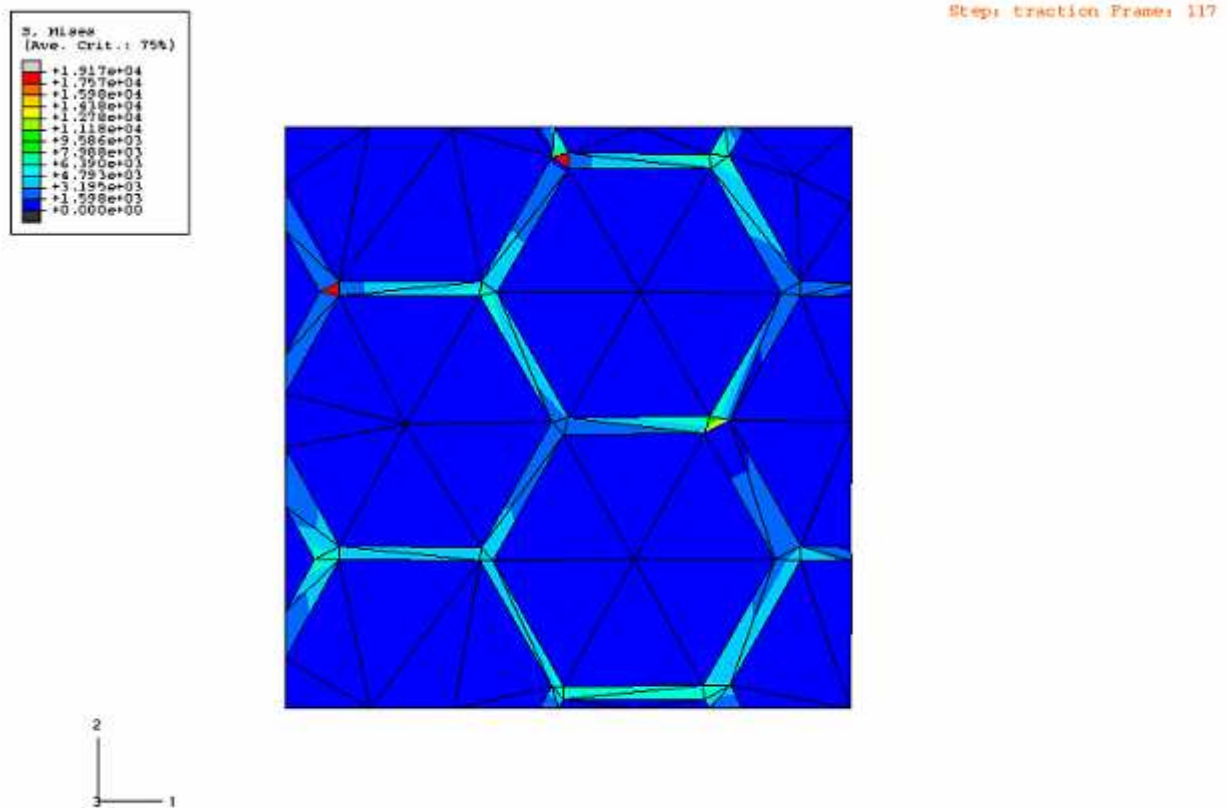lead to overestimation of the stress concentrations.

Figure 5.12: Finite element simulations of a NC Cu sample; contour plot of the

Von Mises equivalent stress.

While most parameters in equation (5.34) can be estimated via theoretical reasoning's (to be presented in the following section), the free enthalpy of activation and the critical emission stress at zero Kelvin need particular attention for these two parameters control the rate of emissions of dislocations. Let us recall that both the free enthalpy of activation and the critical emission stress are dependent on the geometry of the grain boundary (e.g., misfit angles between the two grains composing the grain boundary). A scale transition from the atomistic scale to the microscopic scale can be performed via the evaluation of these parameters with molecular dynamics simulations. Therefore, MD simulations are performed on a $\Sigma 5$ {210} boundary. This will lead to estimates of the free enthalpy of activation and critical emission stress. These simulations clearly need to be extended to more grain boundary structures in order to draw general conclusions on the activity of grain boundary dislocation emission. Recall that grain boundary dislocation emission is a thermally activated mechanism which is described here with a methodology similar to that presented in Chapter 1.

Although further details will be given on the calculation of the two parameters describing the grain boundary dislocation emission mechanism, let us present the fundamentals of the estimation procedure. First, in the case of the critical emission stress, MD simulations are performed on a bicrystal interface subjected to a tensile stress. In order to decrease the effect of thermal fluctuations, the simulations are performed at 10K. The critical emission stress is then equal to the stress, resolved on the slip system on which dislocation emission occurs, at which the nucleation of a leading partial dislocation can be observed. Second, the free enthalpy of activation corresponds to the energy that

must be brought to the system (e.g, grain boundary), without additional input from thermal fluctuation, for a dislocation to be nucleated and to move at a sufficient distance for it to reach and unstable configuration with positive driving force. The following subsection will describe the details of the MD simulations which were all performed by Dr. D. Spearot. In order to investigate the effect of ledges, which were considered to be the primary grain boundary dislocation sources, two Σ5 {210} boundary are considered. The first boundary is a perfect planar while the second grain boundary contains a ledge.

Atomistic modeling

Model geometry and resulting structures

A schematic illustration of the 'planar' and 'stepped' interface models is presented in Figure 5.13. Recall that as in the case of the study of the details of the atomic motion during elastic stretch of an interface, the Σ5 {210} 53.1^o results from a symmetric tilt rotation Φ of opposing lattices around the [001] crystallographic axis. In the case of the stepped geometry, two pure ledges of heights ℓ_H equal to two times the repeating length of the supperlattice site for this misorientation are created along the interface plane.

The dimensions of the interface models are prescribed as necessary to enforce periodic boundary conditions in all directions (X, Y and Z) and are presented in Table 5.2. The effect of the model dimensions will be discussed later in this section
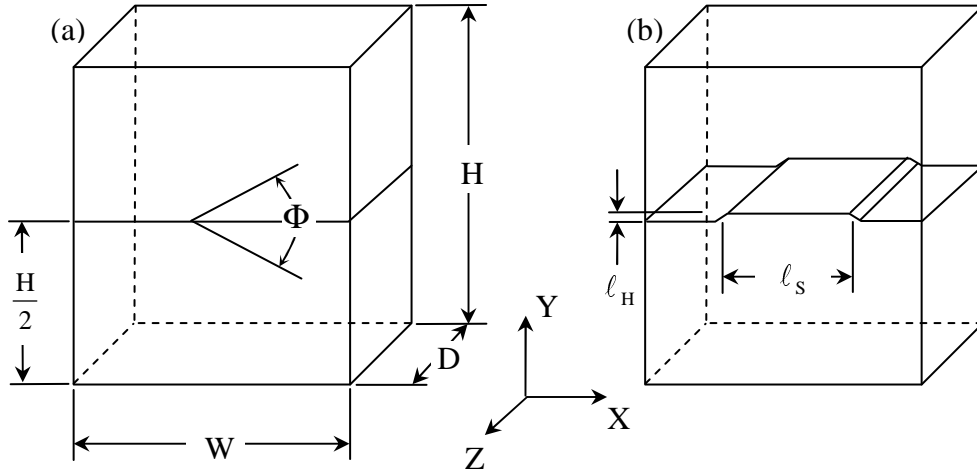
251

Figure 5.13: Schematic of the grain boundary interface models (a) perfect planar boundary and (b) boundary with ledge of height ℓ_H.

The bicrystal models are constructed similarly to those constructed in the first part of this chapter (dedicated to elasticity). Specifically, the initial configuration is obtained via MS calculations followed by isobaric-isothermal equilibration at 0 Bar and 10 Kelvin. The dynamic of the system is driven by the Melchionna et al. (1993) equations of motion for the NPT ensemble. The bicrystal is subjected to tensile stresses in the Y-direction and the motions of the boundaries are calculated from the prescribed system stresses. As in the case of elasticity, the boundaries perpendicular to the interface are stress-free. Finally Mishin et al. (2001) embedded atom potential is used.

Table 5.2. Interface model dimensions considered in the current work.

Interface Type	Width, W (nm)	Height, H (nm)	Depth, D (nm)	Ledge Height (nm)	Ledge Spacing (nm)	Number of atoms
Planar (Σ5)	19.4	22.6	16.2	n/a	n/a	533,760
Stepped (Σ5)	19.4	22.6	16.2	0.79	9.7	533,760
Stepped 2X (Σ5)	38.8	22.6	16.2	0.79	19.4	1,067,520

Detailed views of the planar and stepped Σ5 {210} interfaces are presented in Figure 5.14 (a) and (b), respectively. The viewing direction is along the [001] crystallographic axis (Z-direction) and atom positions are projected into the X-Y plane for clarity. Snapshots of the atomic configurations at the interface are taken after the isobaric-isothermal equilibration procedure at 0 bar and 10 K. The structure of each interface can be readily identified by shading atoms according to their respective {001} atomic plane, as indicated in the legend of Figure 5.14.
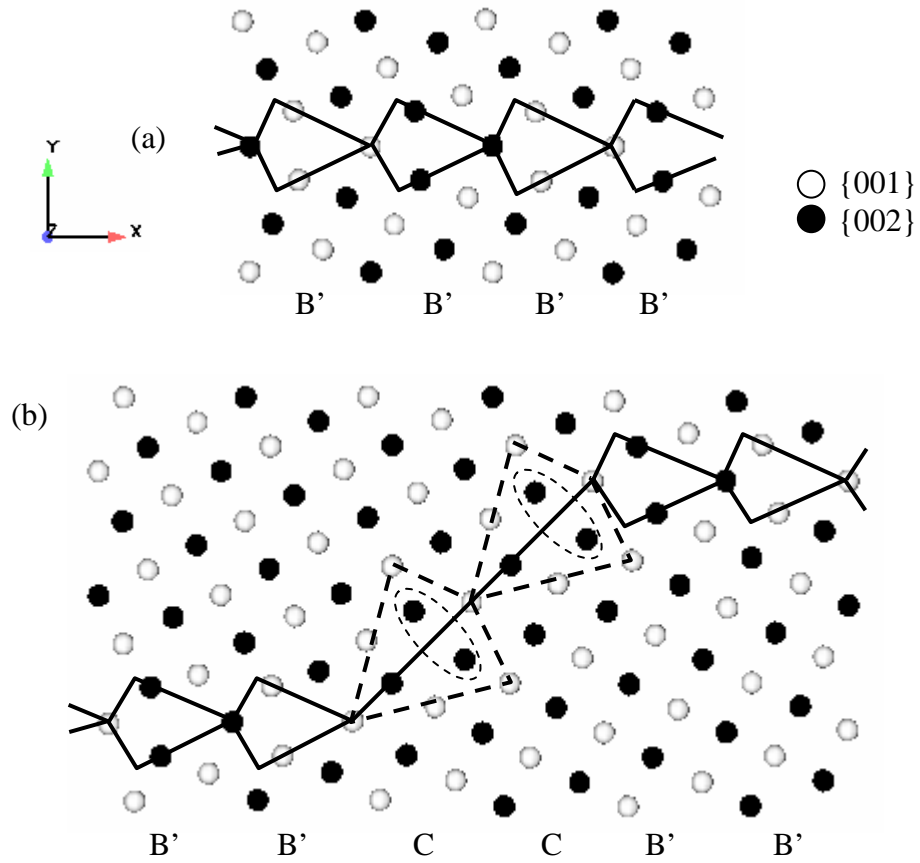
Figure 5.14: (a) view of the planar interface and (b) view of the stepped interface.

Similarly to work by Bachurin et al. (2003), the planar interface is composed of B'

structural units. From Figure 5.14 (b) it can be noticed that the ledge is formed at a 45°

angle relative to the positive X-direction which results from the symmetry of the lattice

misorientations between the two crystals. The ledge height is equal to ~7.9 Å.

interestingly; one can also notice the presence of C structural units along the step.

Dislocation nucleation

Let us now present the methodology used to estimate the free enthalpy of activation

and the critical emission stress. The latter is obtained via the application of a sequence of

increasing tensile stresses (normal to the interface) starting at a minimum applied stress

of 5GPa.. The simulations were run for 100 ps and the stress was increased by 0.1 to 0.2

GPa if dislocation nucleation did not occur with the initially applied stress.

Figure 5.15 (a, b and c) present snapshots of the nucleation process from a planar

interface at different increasing simulations times. The centrosymmetry parameter is used

to color atoms (Kelchner et al., 1998). One can notice that the simulations reveal that, as

expected, the leading partial dislocation is emitted on one of the primary {111}/<112>

slip systems. Also, the MD simulations can successfully capture realistic dislocation

loops with both edge and screw characters. Note here that the core of the dislocation (in

blue) remains connected to the interface by an intrinsic stacking fault (appearing in

green). As discussed in Chapter 1 the simulation does not allow the prediction of the

trailing partial dislocation. Finally, the calculation of the resolved shear stress necessary

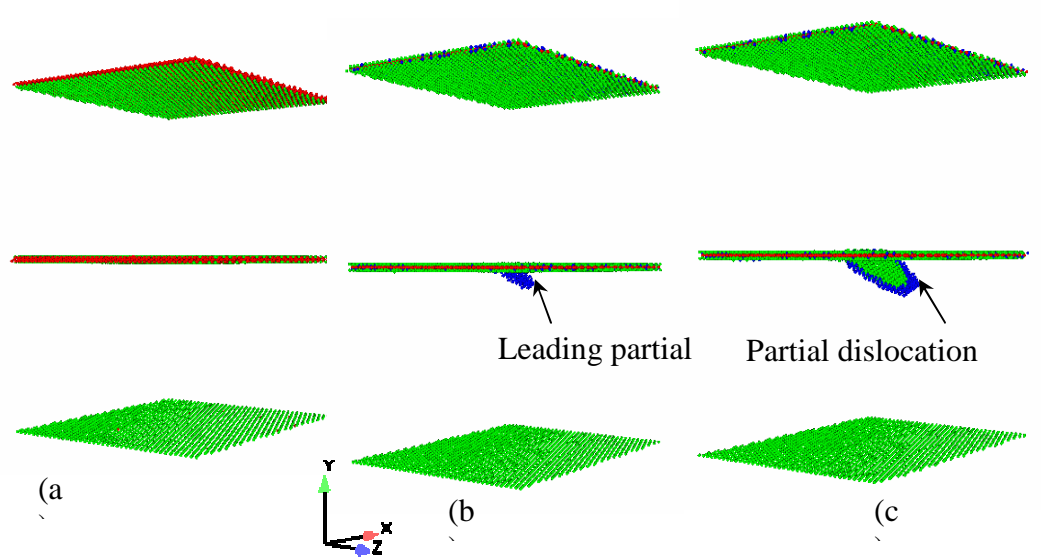for dislocation emission is equal to 2.58 GPa.

Leading partial   Partial dislocation

(a   (b   (c

Figure 5.15: Snapshots of the nucleation of a dislocation from a planar interface at an applied stress of 6.1GPa.

Figure 5.16 (a, b and c) presents snapshots of the dislocation nucleation from the stepped interface. Interestingly, one can notice that dislocation nucleation occurs at the interface ledge. Similarly to the case of the planar interface, the nucleation event is localized on one of the primary {111}<112> slip systems and the leading partial dislocation is connected to the interface by an intrinsic stacking fault. Also, one can notice that once emitted, the dislocation expands onto regions away from the ledge. The resolved shear stress necessary for the activation of dislocation nucleation from the stepped interface is equal to 2.45 GPa. This value is smaller than that reported in the case of the planar interface. However, this information alone is not sufficient to assess of the nature of the primary dislocation sources (e.g., stepped or planar interface). Therefore,

256

the calculation of the free enthalpy of activation is necessary and detailed in what follows.
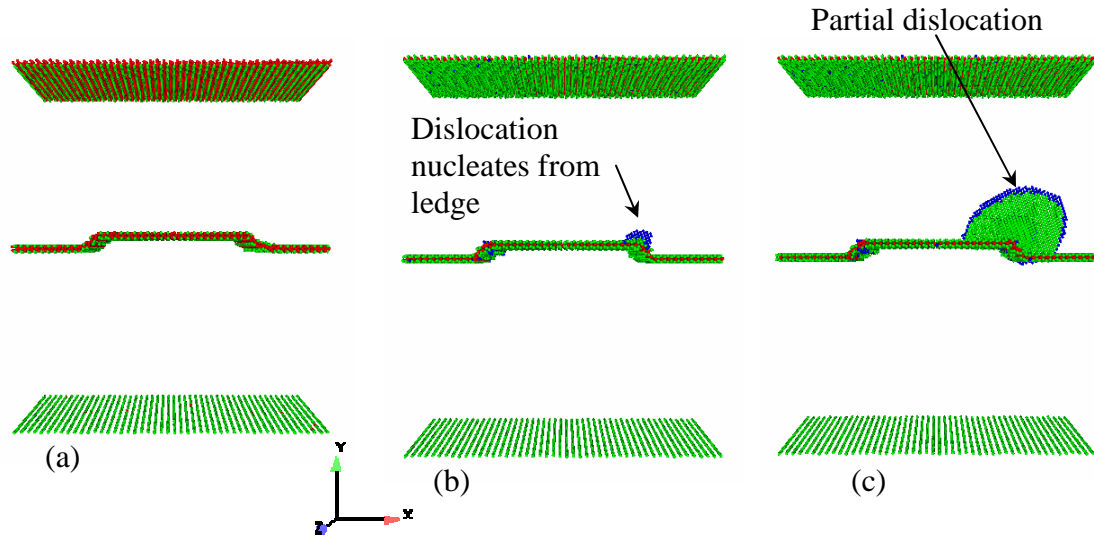

Figure 5.16: Snapshots of the nucleation of a dislocation from a stepped interface.

The free enthalpy of activation corresponds to the change in energy of the interface from the initial configuration to the configuration in which the emitted dislocation becomes unstable with positive driving force. Physically, this signifies that upon releasing the stress, an emitted dislocation in the unstable configuration with positive driving force will not come back into its source. However, since the interface and lattice stretch contribute to the change in total energy, the free enthalpy of activation cannot be obtained directly. Hence, in order to eliminate these artifacts, the excess energy is used to reach an estimate of the free enthalpy of activation. Precisely, the free enthalpy of activation corresponds to the change in excess energy of the interface from the initial configuration to the configuration in which the dislocation is emitted. The excess energy at each time step is

calculated with equation (5.3). A plot of the evolution of the bulk energy of both the planar and stepped interfaces is presented in Figure 5.17.(a). Prior to the occurrence of the dislocation emission event, the bulk energy increases with time which is expected since energy is brought to the system via the external boundary conditions. However, one can observe a decrease in the bulk energy which occurs when the emission event is activated. This is to be expected since dislocation emission is a plastic process.

The evolution of the interface energy, defined as the sum of the excess energies over all the atoms within the bicrystal, is presented in Figure 5.17.(b). It can be seen that the interface energy decreases with increase time. However, a slight increase in the interface energy can be observed prior to the emission event. Also, a sharp decrease in the interface energy occurs after the emission of the leading partial dislocation. Recall that in previous section, in which solely the elastic response of interfaces was studied, the bifurcation event was brought to light. Therefore, these increases in the interface excess energy may be associated with particular atomic motion. Recall that atomic shuffling was exhibit in quasicontinuum simulations of bicrystal interfaces composed of E structural units. Also, let us recall that the decrease in interface energy does not signify that the total energy of the interface decreases. As argued by Muller and Saul (2004), a negative change in the interface energy is engendered by a change from an initial state where stresses are applied to a final state which corresponds to the relaxed state. Considering the fact the energy change obtained via MD represents the energy barrier for dislocation emission to occur, the negative of the change in the interface energy is taken as the approximate of the free enthalpy of activation. Recall that as discussed in review by Kocks, Argon and Ahsby (1975), the rigorous value of free enthalpy of activation shall be

258

calculated from the energy of the emitted dislocation only. Finally, the following values of the free enthalpy of activation for the planar and stepped interfaces are obtained: 173.2 mJ/m^2 and 103.8 mJ/m^2.
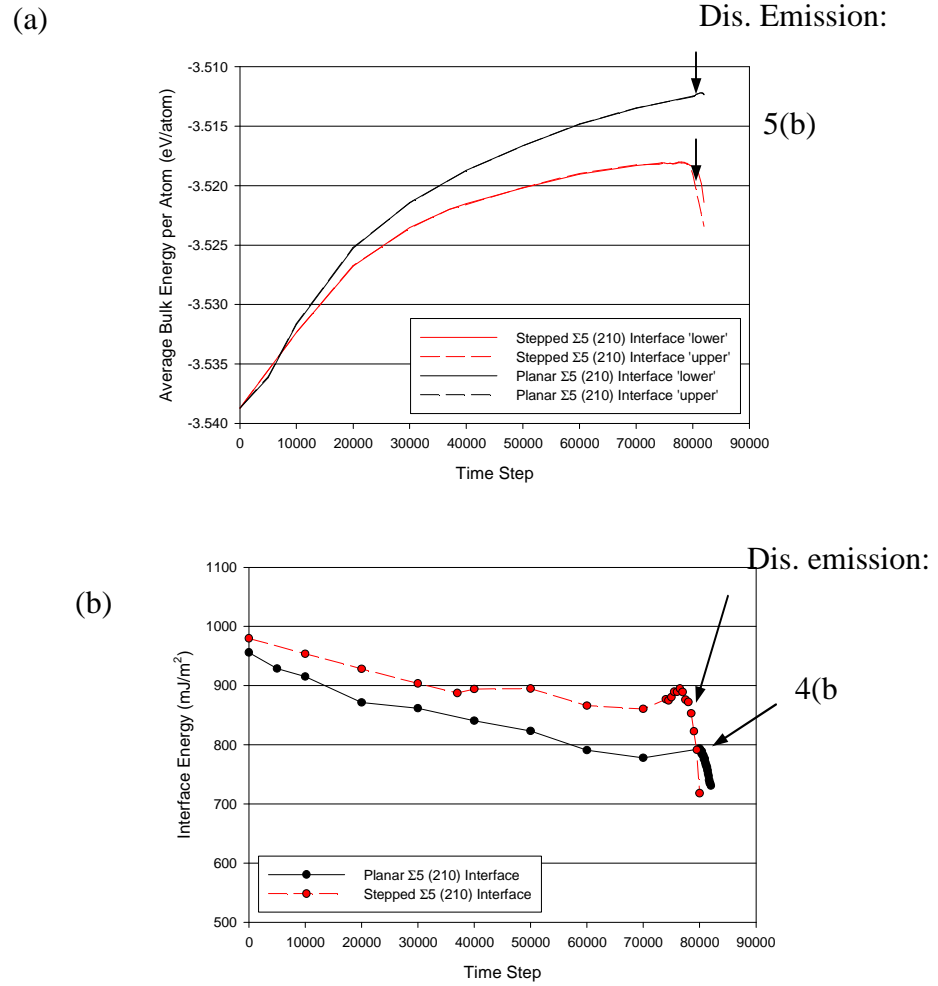

Figure 5.17: (a) evolution of the bulk energy with time and (b) evolution of the interface energy with time.

In summary, the free enthalpy of activation and the critical emission stress were estimated in the case of a planar and stepped copper Σ5 {210} 53.1^o planar. The MD

simulations reveal that both the free enthalpy of activation and the critical emission

stresses are lower in the case of the stepped interface. Let us now recall that these two

parameters are used in the continuum model, presented in the previous section (see

equation (5.34)), in order to describe the probability of successful dislocation emission.

Since the model is based on a Boltzman distribution of the emission process, the

probability of successful emission, P, is given by the exponential term of equation (5.34):

$$P = \exp\left(-\frac{\Delta G_0\left(\theta_{mis}\right)}{k_B T}\left(1-\left(\frac{K \cdot \sigma_{eq}^M}{\sigma_c^M\left(\theta_{mis}\right)}\right)^p\right)^q\right) \qquad (5.35)$$

This equation accounts for the stress and temperature dependence of the probability of

successful emission. The parameters p and q, describing the shape and area of dislocation

emission resistance diagram, are chosen in order to obtain a sharp profile of the diagram.

Hence $p=1$ and $q=1.5$. A plot of the probability of successful emission with respect to the

equivalent stress in the grain boundaries in the case of the planar and stepped interfaces

for two grain sizes (100nm and 10nm) is presented in Figure 5.18. Recall that the free

enthalpy of activation obtained via MD is given per unit area. It must be multiplied by the

grain boundary area. It can be observed that the stepped interface is more prone to emit

dislocations than the planar interface. This element suggests that the assumption that

grain boundary ledges are the primary dislocation sources may be correct. Let us note

that only one misorientation was considered. Hence, the MD simulations should be

extended to more misorientation angles in order to rigorously confirm that grain

boundary ledges are the primary dislocation sources in NC materials. Also, as exhibited

in HRTEM images NC materials fabricated via severe plastic deformation (e.g. HPT, ECAP) and ball milling present stepped grain boundaries. However, it can also be noticed that high stresses are necessary for dislocation emission to be activated.
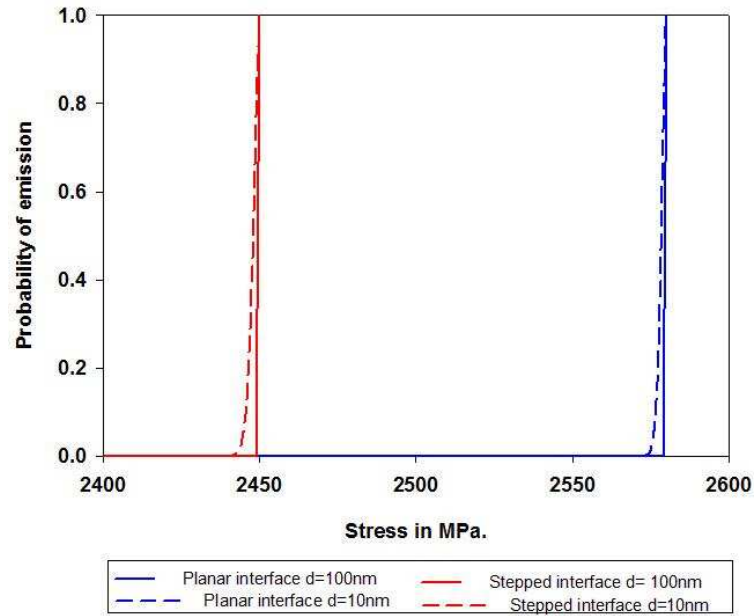
Figure 5.18: Probability of successful dislocation emission versus stress for a perfect planar interface and a stepped interface at 100 nm and 10 nm grain sizes.

Figure 5.19 presents the effect of the stress heterogeneity factor on the probability of dislocation emission from a stepped grain boundary. As expected, an increase in the stress heterogeneity factor leads to the activation of grain boundary dislocation emission at lower stresses.
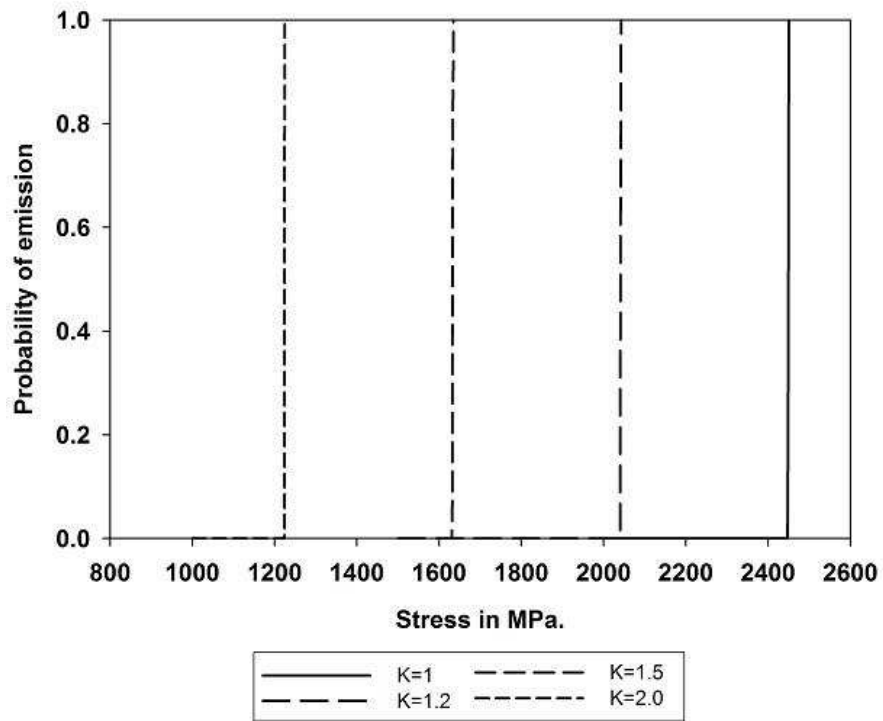
Figure 5.19: Effect of stress heterogeneities on the probability of successful emission from a stepped interface.

Effect of grain boundary dislocation emission

The macroscopic response of polycrystalline materials with grain sizes ranging from the conventional regime to the NC regime can be predicted from the constitutive law of grain interiors and of grain boundaries (accounting for grain boundary dislocation emission). Here the 2PEVPT model presented in Chapter 3 is used to perform the scale transition from the microscopic scale to the macroscopic scale. For the sake of brevity the localization relations will not be recalled. Inclusions are assumed spherical with volume fraction f:

$$f = \left[\frac{(d-w)}{d} \right]^3 \qquad\qquad (5.36)$$

Here d is the grain size and w is the grain boundary thickness.

The model was applied to pure copper for which a relatively large number of experimental data is available. The following parameters, describing the behavior of the inclusion phase, were mostly from Estrin et al.'s work (Estrin and Mecking, 1984): $\alpha = .33$, Taylor's factor $M = 3.06$, Burger's vector $b = .256E-9$ m, $\mu^I = 38400 MPa.$ (Sanders et al., 1997), $\dot{\varepsilon}_0 = 0.005/s$ and $n = 21.25$ at room temperature and is inversely proportional to the temperature.

$\xi = 3.507E-4$ was determined such that the hardening coefficient, m, reaches a value of 230 when the grain size is in the order of several microns, consistent with the work of Estrin and Mecking (Estrin and Mecking 1984).

The term, accounting for the effect of long range obstacles on the flow stress at zero Kelvin introduced in equation (5.8), was chosen to be consistent with the Hall-Petch coefficient, e.g., $\beta = 0.11\, MPa \cdot m^{-1/2}$.

The parameters defining the evolution of the dislocation density were fitted, using equations (5.22) and (5.23), to appropriately describe experimental data provided by

Sanders et al. on 20 micron grain size polycrystalline Cu (Sanders et al., 1997), leading to the following results; $k_0 = \frac{1}{b} = 3.5E9$ m^{-1}, $k_1 = 1.E10$ m^{-1} and $k_{20} = 330$.

Let us suppose the ratio of the mass densities of grain boundaries over that of a perfect crystal to be equal to .85, typical values range from .75 to .89 (Fitzsimmons et al., 1995). The mass density is 8.96 g/cm^3 for the perfect crystal of Cu. The grain boundary volume is size dependent and is approximated as a hollow sphere of thickness w surrounding an inclusion. We approximated the effective dislocation mass as the rest mass of a screw dislocation m_{os} as given by (Bitzek and Grumbsch, 2005):

$$m_{dis} \approx m_{os} = \frac{\mu b^2}{4\pi C_t^2} \ln\left(\frac{R}{r_0}\right) \tag{5.37}$$

where r_0 and R are the lower and upper integration limit and the transverse wave speed is given by.

$$C_t = \sqrt{\frac{\mu^I}{\rho}} \tag{5.38}$$

Hence, one obtains $m_{dis} = 3.15\, pN \cdot ps^2 / \overset{o}{A}^2$ (Bitzek and Grumbsch, 2005). Since the dislocation velocity cannot exceed $C_t/3$ (without quantum effects) and the ratio of the equivalent stress in the inclusion phase over the flow stress at zero K is at most equal to .99, one can estimate $v_0 = 0.03$ such that the maximum dislocation velocity is equal to $C_t/3$.

As the grain size decreases, the dislocation mass becomes closer to the grain boundary

mass, which will increase the effect of the incoming dislocation.

Finally, a 45 degree penetration angle is assumed, and the proportionality factor

ς is set to $\varsigma = 1/2$. The parameter δ is set to 40. Note here that these parameters can be

adjusted since the penetration angle depends on the relative position of the active slip

system with respect to the longitudinal axis of the grain boundary.

Using the reasoning developed by Wang et al. (2003), the shear modulus of the

matrix phase can be evaluated. The elastic moduli of the matrix region are estimated from

an atomic potential method. Using the Lennard Jones potential and supposing the ratio of

the density of the matrix phase over that of a perfect crystal to be .85, one

obtains $\mu^M = 11140 MPa$. Finally, the grain boundary thickness, w, is estimated as 1 nm

(Kim et al., 2000).

The effect of grain size, strain rate and temperature are predicted and compared to

experiments when relevant data are available in pure tension. Note that the stress

heterogeneity factor is set to 1 unless otherwise mentioned.

Effect of grain size

The predicted macroscopic stress-strain curves under uniaxial tension at 1.E-3/s

strain rate are presented in Figure 5.20. Four grain sizes were simulated: 1 micron, 100

nm, 20 nm and 10 nm. In agreement with Sanders et al.(1997) experimental study on the

elastic behavior of nanocrystalline materials, in which a decrease of Young's modulus,

ranging from 13 to 16 % was exhibited upon decreasing the grain size from 20 microns to 26 nm, the present model predicts a decrease in the macroscopic Young's modulus of 19 % when the grain size is decreased from 1 micron to 20 nm.
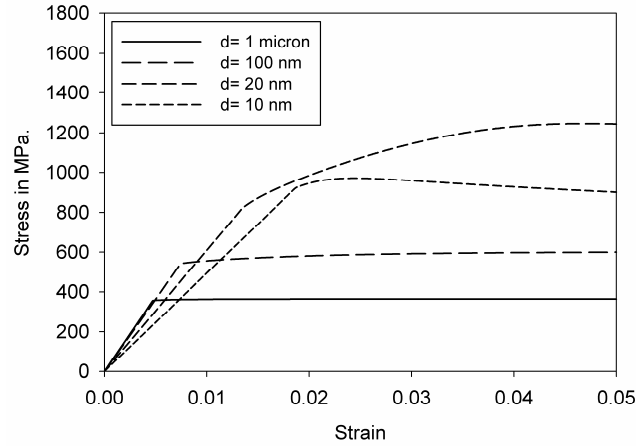
Figure 5.20: Stress-strain curves at different grain sizes and 10E-3/s strain rate.

The softening in the plastic response with decreasing grain sizes can be explained by observing the responses of the constituents presented in Figure 5-21 and Figure 5-22. Since the volume fraction of the matrix phase becomes non negligible when the grain size is in the range of ~20nm, it is noticed that down to 20 nm grain size, the macroscopic response is very similar to that of the inclusion phase. In Figure 5-21, it is also noticed that at small grain sizes (d<100nm), substantial increase in the yield strength of the inclusion phase is seen which is a consequence of the long range stresses due to the presence of grain boundaries.

Moreover, a comparison of figure 5-21 and figure 5-22 reveals that for grain size in the order of 100 nm and below, the matrix phase is relatively harder than the inclusion phase. Therefore, when the grain size is decreased the maximum deformation of the matrix phase increases. Since the critical emission stress depends on the geometry of the grain boundary region, some grain boundaries could have a harder character while others could have a softer character leading to easier emission of dislocations. Grain boundaries with a harder character might be more likely to initiate cracks. Also, let us note that the response of the phase accounting for grain boundaries is similar to an elastic-prefect plastic response. Recall that NC materials with a small grain size exhibit the same type of response. Hence, on the condition that grain boundary dislocation emission is activated, the grain boundary phase could contribute to the observed elastic-perfect plastic response of NC materials.

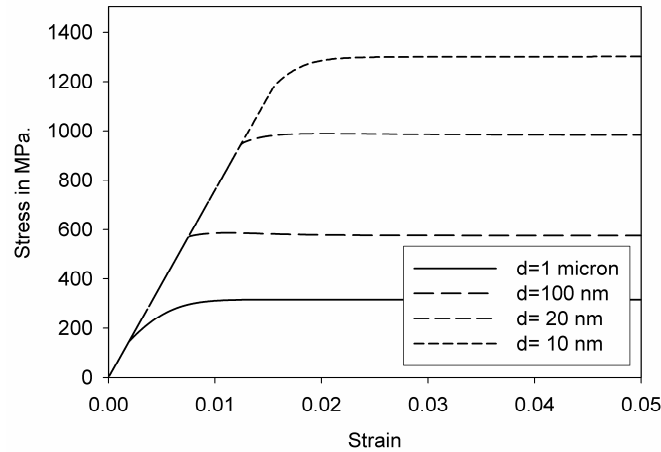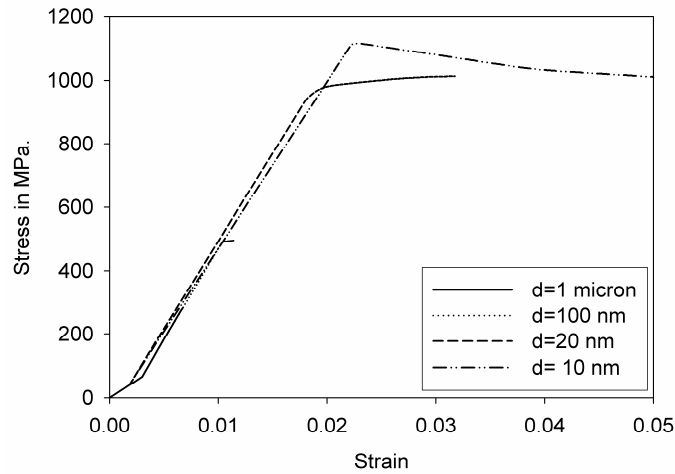Figure 5.21: Stress-strain curves of the inclusion phase at different grain sizes and 10E-3/s strain rate.

Figure 5.22: Stress-strain curves of the matrix phase at different grain sizes and 10E-3/s

strain rate.

Shown in Figure 5.23 is the comparison between the model predictions and the relevant experimental data from (Sanders et al., 1997; Cheng et al., 2005). When compared to Sanders et al.'s experimental results on 110 nm grained Cu, the model predicts much larger values for the yield stress and consequently for the remaining part of the stress-strain curve. However, as mentioned Chapter 2, large discrepancies are often found in experimental results.

The present model is in very good agreement with the experimental data from Cheng et al. (2005) on high purity 62 nm grain copper, although some minor discrepancies are seen near the initial plastic regime. The substantial increase in the yield stress predicted in the present model is mostly due to the fact that the long range stress caused by the presence of grain boundaries are accounted for through the 'Hall-Petch' dependence of the flow stress at zero Kelvin (see equation (5.8)).

The size dependence of the hardening coefficient cannot be appropriately described with the Cheng's modified model described by the evolution of the mean free path of dislocations (equation (5.9)).
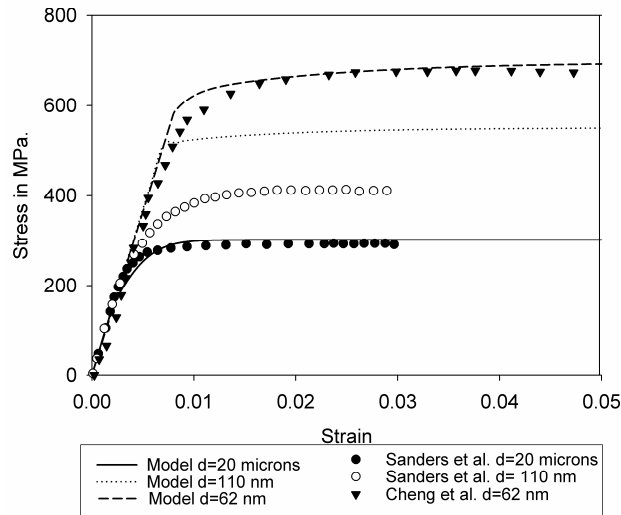
Figure 5.23: Comparison with experimental work at different grain sizes

Effect of strain rate and temperature

The effects of strain rate and temperature on the response of NC materials are presented in Figure 5.24 and Figure 5.25. Similarly to the case of coarse grained materials, an increase in the strain rate leads to a harder response of the material. At low temperatures, since less energy is brought to the material by thermal fluctuation, the probability of successful glide is smaller than in a material subjected to the same loading but at higher temperature. This engenders a harder response of the material.
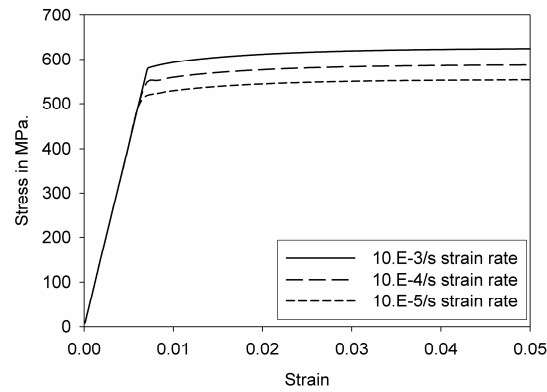
Figure 5.24: Stress strain curves at different strain rates,

with d=100 nm.
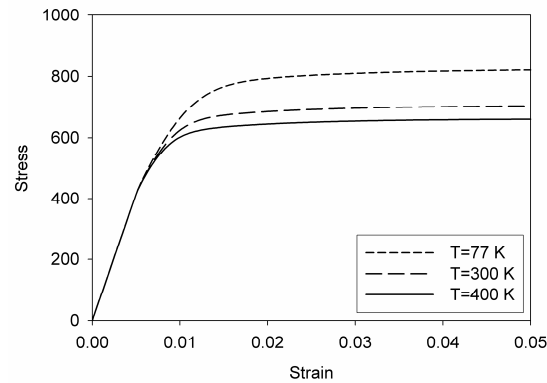
Figure 5.25: Stress-strain curves at different temperatures, with d=62 nm.

Creep behavior

In what follows, the effects of grain size, stress and temperature on the creep behavior of

the material are simulated. The material is loaded at constant strain rate ($\dot{E} = 1.E - 3/s$) until

the desired creep stress is reached. In Figure 5.26 and Figure 5.27, one can observe the

response of the material, with a critical stress set to 400 MPa, at different grain sizes: 100

nm, 60 nm and 20 nm and the evolution of the macroscopic strain rate with respect to time,

270

respectively. One can observe that the strain rate decreases rapidly once the desired

macroscopic stress is reached leading to creep rates in the order of 10E-10/s. In the case of

very small grain sizes (d=20 nm), the material does not deform under constant stress. This

is due to the fact that the material is still in its elastic regime. Hence, the material cannot

sustain any deformation due to viscous effects.
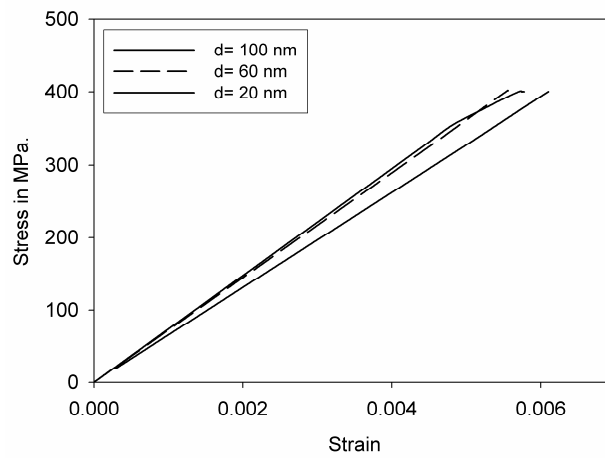
Figure 5.26: Stress strain curves at different grain sizes with critical stress=400 MPa.
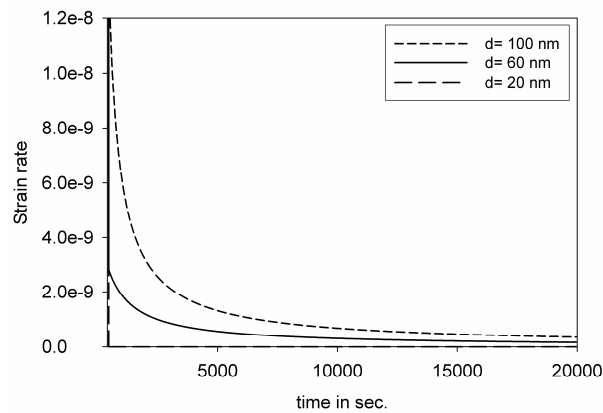
Figure 5.27: Strain rate Vs. time at different grain sizes with imposed stress=400 MPa.

The effects of temperature and stress on the creep behavior of NC materials are

shown in Figure 5.28 and Figure 5.29, respectively. In the case of the temperature

dependence of the creep rate, three temperatures were simulated: 300K, 400K and 500K.

The grain size is equal to 100 nm. An increase in the temperature leads to an increase in

creep rate. However, the order of magnitude of the creep rate remains relatively small, in

the order of 10E-10/s. The same conclusion can be drawn with respect to the effect of the

applied stress on the creep rate, which was simulated with d=100 nm and T=300K (see

Figure 5.29).
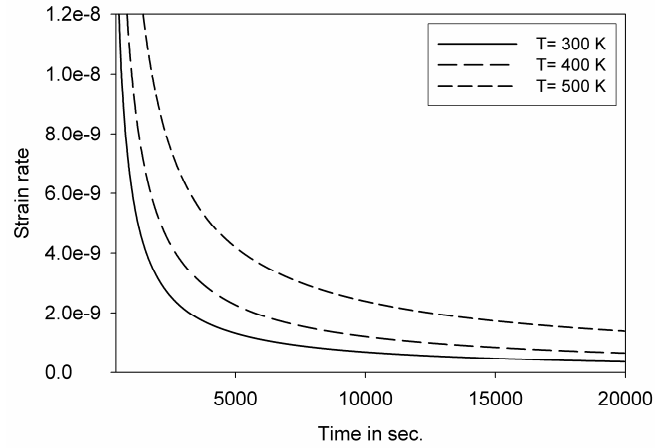
Figure 5.28: Strain rate vs. time at different temperatures, d=100 nm,

stress= 400 MPa.
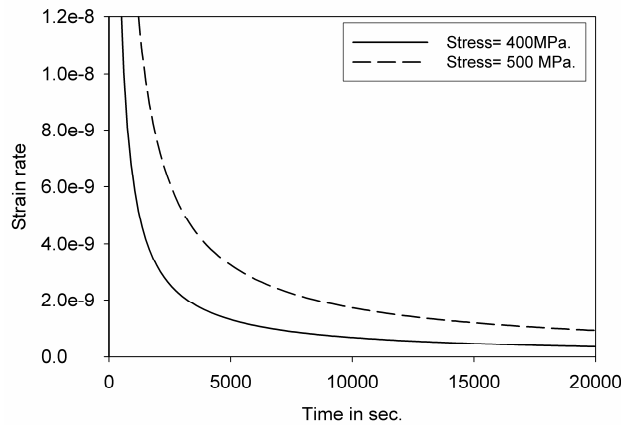
Figure 5.29: Strain rate vs. time at different stresses, d=100 nm T=300K

From these results it can be concluded that the creep behavior of NC materials is similar to that of coarse grained materials. Therefore, even though grain boundaries and triple junctions are favorable paths for vacancy diffusion, the reported steady state creep rates are attributed to dislocation activities. The model is in agreement with several experimental data reporting steady state creep rates which are several order of magnitude lower than predicted by the equation of Coble creep (Sanders et al., 1997; Yin et al., 2001). Even though Cai et al. reported creep rates in the same order of Coble creep (Cai et al., 2000) and grain boundary sliding creep (Cai et al., 2001) on 30 nm grained NC copper, the relevance of these results was strongly argued in Li et al.'s work (Li et al., 2004). Li et al. performed the same tests as Cai et al. on the same material, and reported extremely small steady state creep rates compared to those reported by Cai et al., explaining the discrepancy as a result of material damage in the test samples.

Size effect in the yield stress

Let us now discuss the size effect in the yield stress. From the simulations performed via MD on bicrystal interfaces, it is clear that high stresses are required in grain boundaries for the dislocation emission mechanism to be activated. Also, recall that the activation of grain boundary dislocation emission leads to the penetration of dislocations within the grain boundary opposite to the source which itself engenders a softening in the response of the material. Figure 5.30, presents the evolution of the yield stress, estimated via the 0.5% offset method, with the inverse of the square root of the grain size (e.g., Hall Petch plot). It can clearly be noticed that in the case where stress heterogeneities are not taken into account (K=1) the yield stress increases at all times with a decrease in the grain size. The predicted slope (e.g. Hall-Petch slope) is in very good agreement with experimental measures. However, the breakdown of the Hall Petch law cannot be predicted which results from the fact that grain boundary dislocation emission is not activated in the material.

When stress heterogeneities are accounted for, by setting K equal to 2 for example, one can notice that the model predicts both the increase in the yield stress with a decrease in the grain size, and the breakdown of the Hall Petch law. The critical stress at which the breakdown is predicted is ~25nm. The predicted breakdown of the Hall Petch law results from the activation of the grain boundary dislocation emission and penetration mechanism.
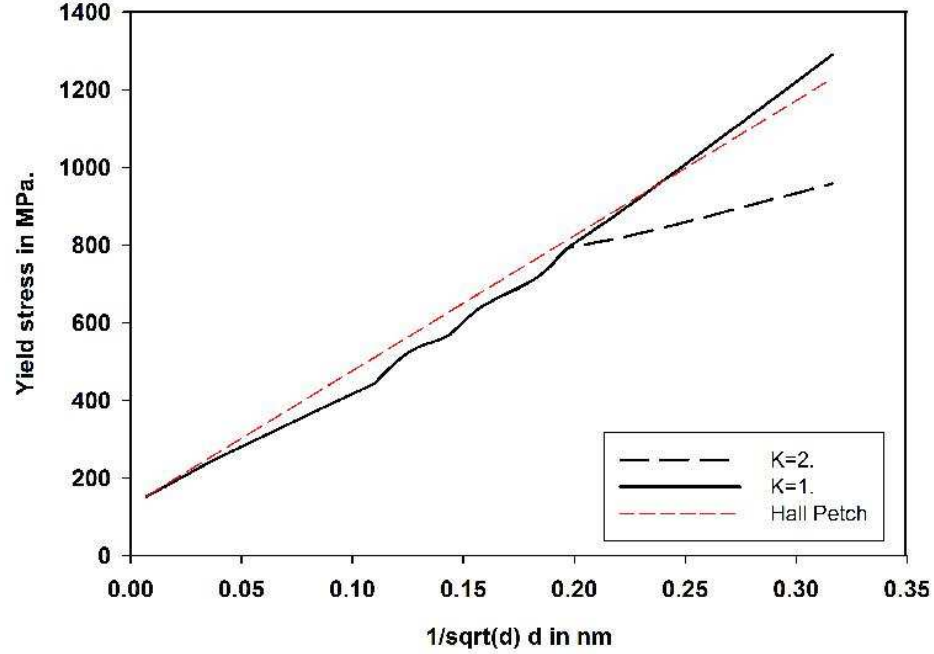
Figure 5.30: Yield stress as a function of the inverse of the square root of the grain size.

In chapter 3, several micromechanical schemes were introduced to perform the scale transition from the microscopic scale to the atomistic scale. It was stated that the 3PVP model shall lead to softer predictions of the macroscopic response of NC materials. Indeed, using the 3PVP model, developed in cooperation with S. Benkassem, with same parameters and keeping the stress heterogeneity factor equal to 1 leads to the grain size yield strength plot presented in Figure 5.31. One can observe that this model predicts an increase in the yield stress with a decrease in the grain size down to a critical grain size in the neighborhood of 25 nm. A decrease in the Hall-Petch slope, in the range of ~20 percent is predicted below the critical grain size. First, let us recall that the 3PVP scheme does not account for elasticity. Hence, the predicted values of the yield stress are much smaller than that presented in Figure 5.30. This shall not penalize the value of the Hall-

Petch slope. Also, let us note that the predicted decrease in the Hall-Petch slope remains less pronounce than in the case where stress heterogeneities are accounted for.

In conclusion, both 2-phase and 3-phase models suggest that grain boundary dislocation emission may indeed be a source of the abnormal size effects observe in NC materials. However, a more local approach, allowing the precise quantification of the effect of stress heterogeneities on the emission of dislocation by grain boundaries is necessary.
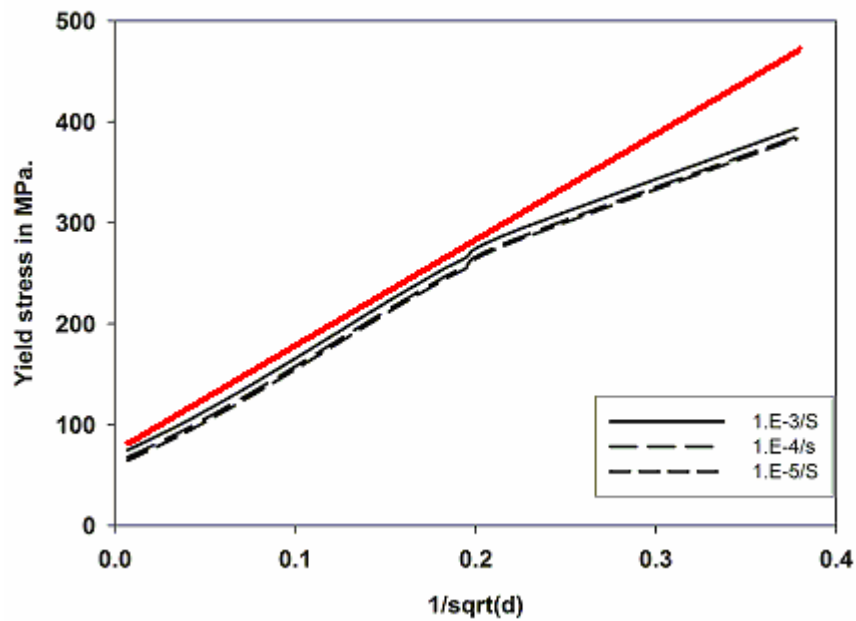
Figure 5.31: Yield stress as a function of the inverse of the square root of the grain size with use of the 3PVP model.

Summary and discussion

In summary, the influence of grain boundary dislocation emission and penetration on the response of polycrystalline materials was investigated via the use of molecular dynamics simulations which were used to inform a novel constitutive law accounting for grain boundary dislocation emission and penetration. The behavior of grain cores was modeled with a modification of typical strain hardening laws and the scale transition was performed via the use of secant-self-consistent micromechanical schemes.

MD simulations at 10 K on a planar and stepped $\Sigma 5$ (210) 53.1^{o} boundary interface allowed the estimation of the critical emission stress and free enthalpy of activation used to described, via statistical mechanics, the probability of emission of a dislocations. These simulations revealed that high stresses, in the order of 2 GPa, must be present in grain boundaries for the emission of dislocation to be activated. Also, it was shown that in the particular case of the $\Sigma 5$ (210) 53.1^{o} boundary interface, grain boundary ledges are more prone to emit dislocation than the planar interface with same misorientation of the two crystalline lattices.

At the continuum level, the emission of dislocation was considered as the triggering mechanism to grain boundary penetration which was modeled as a soft collision resulting in a softening of the plastic response of grain boundaries.

The 2PEVPT self-consistent micromechanical scheme was used to predict the macroscopic response of polycrystalline materials with grain sizes ranging from several microns down to ~10nm. Recall that this scale transition scheme is based on the

assumption that the bonding between inclusions and the matrix is perfect. Hence, grain boundary sliding was neglected. Also, inclusions were taken as spherical which imposes on all fields (e.g. stress and strain field) to be homogeneous within each phase. However, simple finite element simulations revealed that the stress heterogeneity within the matrix phase can be relatively large. These stress heterogeneities were accounted for in the constitutive law of the matrix phase representing grain boundaries and triple junctions.

The model was applied to copper and lead to excellent predictions of the macroscopic response of polycrystalline materials with grain size ranging from several microns down to ~50nm (see Figure 5.23). Also, it was shown that when stress concentrations are accounted for, grain boundary dislocation emission and penetration can lead to a decrease in the Hall Petch slope. Moreover, using the 3PVP scheme confirms that the grain boundary dislocation emission mechanism may contribute to the decrease in the Hall-Petch slope.

However, this model presents some limitations: (1) the MD simulations were performed solely for one particular bicrystal geometry, (2) grain boundary sliding is not accounted for, (3) the constitutive law of grain interiors is still based on typical strain hardening theories which leads to over predictions of the local stresses in the inclusion phase when the grain size is smaller than ~50nm, and (4) the local nature of the stress heterogeneities is lost when it is introduced in the constitutive law of the matrix phase.

These four limitations have motivated the study presented the following section

and in Chapter 6. Indeed, MD simulations (performed by Dr.D.Spearot) are currently

being extended to more grain boundary geometries. A novel micromechanical scheme

(e.g. 2PEVPWI), presented in Chapter 3, was introduced to predict the effect of grain

boundary sliding. The sliding mechanism is described in following section. Finally, a

refined numerical model (currently under implementation) will be presented which will

allow the precise estimation of stress heterogeneities within all phases (Chapter 6).

Grain boundary sliding

In this last section of Chapter 5, the 2PEVPWI micromechanical scheme will be

used to model the joint effect of grain boundary sliding (for which a new stick-slip

inspired law is introduced) and of grain boundary dislocation emission on the response of

pure F.C.C polycrystalline materials. These two mechanisms are obviously expected to

play a dominant role in the NC regime. This scheme was implemented solely in the

viscoplastic case. Hence, elasticity is neglected. While the present author developed the

3PEVPT micromechanical scheme, S. Benkassem implemented the model in the

viscoplastic case. The code is based on the 3PVP code developed by the author. Hence,

the numerical details of this scheme are presented in S. Benkassem Ph.D. thesis.

Methodology

Although the details of the 2PEVPWI scheme were presented Chapter 3, let us

briefly recall its principle. First, the real material, composed of grain interiors, grain

boundaries and triple junctions is represented in an equivalent manner as a coated

inclusion embedded in a matrix phase. The coating phase represents grain boundaries and

triple junctions, the matrix phase represents the effective materials (which properties and response is to be found), and the inclusion phase represents grain interiors.

Then, in order to perform the scale transition this equivalent problem is solved in two steps. In the first step the problem of an inclusion embedded in a matrix is treated. The matrix has the properties of the coating in the original 3-phase topology (e.g., grain boundaries and triple junctions). In this problem the two phases have imperfect bonding. The solution of this first subproblem leads to an estimation of the behavior of the coated inclusion. The second step of the scale transition procedure consists of inserting the homogenized coated inclusion into a matrix phase representative of the effective medium. The bonding between the homogenized coated inclusion and the effective medium is taken as perfect.

In the initial 2-Phase problem, the constitutive law of the inclusion phase is given by the formalism used for the description of grain interiors in previous section (see equation (5.4) to(5.24)). Hence, this formalism is well suited to describe the response of inclusion with sizes ranging from several microns down to approximately ~40-50nm. Indeed, below this grain size the initial dislocation density within the grain interiors is severely reduced and dislocation storage and dislocation annihilation shall not be active. This is one of the limitations of the previously exposed models. In order to assess of the effect of this approximation, dislocation activity can be deactivated in simulations. This will also improve the accuracy of the predictions of the response of the grain interiors in the NC regime. The response of the coating phase is driven by the mechanism of

dislocation emission and dislocation penetration which are described with equations (5.25) to(5.34).

The third mechanism which is taken into account is that of unaccomodated grain boundary sliding. Let us emphasize the fact that this mechanism is taken into account, in the micromechanical scheme, in the solution of the first subproblem; namely the imperfectly bonded inclusion embedded into a matrix representing grain boundaries and triple junctions. Let us now develop the equation describing the unaccomodated grain boundary sliding.

Formalism of the stick-slip mechanism

A model for the unaccomodated grain boundary sliding mechanism, which leads to the relative solid motion of grains, was developed by Wei and Anand (2004). This model is based on the first two laws of thermodynamics and relies on the assumption that the sliding can be considered isotropic in its tangential direction. The interface model developed was introduced in a finite element code and lead to excellent predictions of the effect of grain boundary sliding on the response of NC materials. Indeed, the proposed model is based on a crystal plasticity approach and the geometric modeling is realistic in terms of grain orientation distributions and grain shape. However, the details of the motions of atoms are not described since the model was developed at the continuum scale.

On the contrary, Warner et al. (2006) performed shear test on 11 bicrystal interfaces with large angle grain boundaries. Let us note here that contrary to Spearot et al. (2005), the interfaces are constructed directly from the CSL notation. The evolution of

the shear force vs. shear strain on the bicrystal interfaces are presented in Figure 5.32

(Warner et al. 2006). One can observe a linear increase of the shear stress with respect to

the shear strain up to a critical value at which the shear stress drastically decreases.

Further deformation leads to an almost linear increase in the shear stress prior to a sharp

decrease at a given stress value lower than that of the first decrease in the shear stress. The

authors introduced a constitutive law for the interfaces between two grains, based on work

by Nguyen et al. (2002) and describing the sliding mechanisms as a stick-slip mechanism.
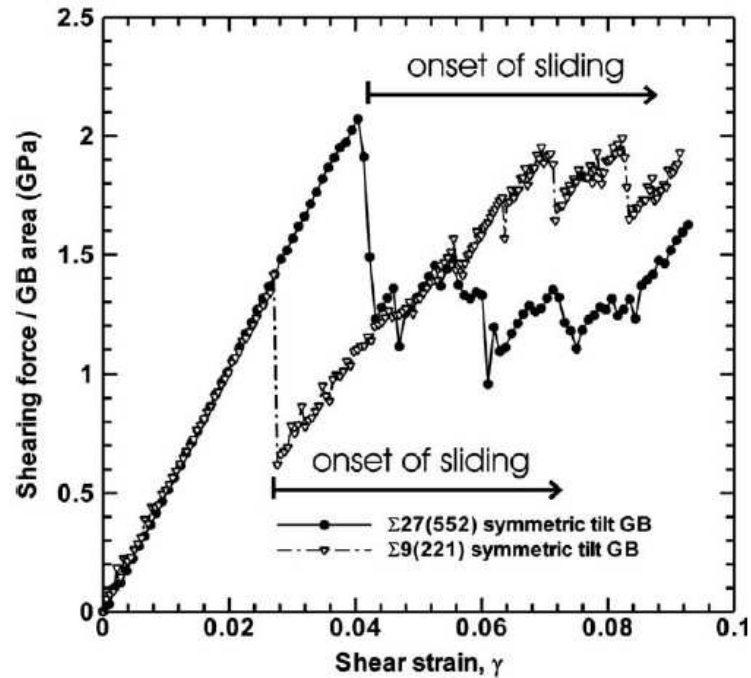
Figure 5.32: Shear stress vs. Shear strain for symmetric tilt grain boundaries simulated by

the quasicontinuum method.

Here, we propose to use the aforementioned stick-slip law, adapted to the two-phase scale-transition model, in order to account for the relative sliding of grains. Recall that in the formalism of the 2PEVPWI model, the jump in the displacement is given by:

$$\Delta u_i \equiv u_i(S^+) - u_i(S^-) = \eta_{ij}\sigma_{jk}n_k \quad , \tag{5.39}$$

Where, η_{ij} represents the compliance of the interface. Hence, from the present law, the jump in the displacement is proportional to the traction vector at the interface. Let us now neglect the effect of void creation which would clearly lead us out of the range of application of the model for slightly weakened interface developed by Qu (1993) and on which the 2PEVPT scheme relies on. Hence, one obtains the following expression of the compliance of the interface:

$$\eta_{ij} = \alpha\left(\delta_{ij} - n_i n_j\right) \tag{5.40}$$

The sliding coefficient α is then given by the following law which corresponds to the converse of the law proposed by Warner et al. (2006):

$$\alpha = \frac{\delta_c}{\sigma_c\left(1 - \dfrac{\sum\limits_i [u_i]}{\delta_c}\right)} \tag{5.41}$$

In equation (5.41), δ_c denotes a critical sliding distance which is approximated as 1nm. σ_c denotes the critical sliding stress. Recall that the coating phase represents both grain boundaries and triple junctions. In order to account for the effect of both the triple junctions and the grain boundaries, a simple rule of mixture is used to estimate the critical stress at which sliding occurs. Hence one obtains:

$$\sigma_c = f_{gb}\sigma_{gb} + f_{tj}\sigma_{tj} \qquad \begin{cases} \sigma_{tj} = 800 Mpa \\ \sigma_{gb} = 2.45 Gpa \end{cases} \qquad (5.42)$$

Here f_{gb} and f_{tj} denote the volume fraction of grain boundaries and triple junctions, respectively. The expressions of the respective volume fractions are given by (2.6). Note that $\sigma_{gb} = 2.45 Gpa$ is chosen based on simulation by Warner et al. (2006) who reported values ranging from 1.61 GPa. to ~3GPa. for symmetric tilt grain boundaries. Since triple junctions exhibit a structure devoid of atomic order the critical stress of triple junctions is chosen as the yield stress of amorphous Cu.

Considering the fact that inclusions are supposed spherical, the sum of the jump in the displacements in all directions in equation (5.41) can be replaced by the sum of the average displacements in all directions. Numerically, the average is obtained simply via use of Gauss integration. The numerical scheme employed is given in S.Benkassem Ph.D. thesis.

The model was applied to the case of pure Cu. The parameters used in this simulation are the same as used in previous section. Figure 5.33, presents the microscopic response of 30 nm grained Cu with 3 different values of the critical distance δ_c .The effect of stress heterogeneities is not accounted for. It can be seen that a change in δ_c from 1nm to 3 nm does not influence the predicted macroscopic response. Also the simulations reveal that grain boundary sliding is already activated. Its effect can be observed in the zoom of the beginning of the plastic response presented in Figure 5.33. Indeed one can see that the activity of the sliding mechanism results in sharp jumps, in the range of 1MPa., in the stress values. These jumps cannot be observed in the case of 1 micron grained Cu.
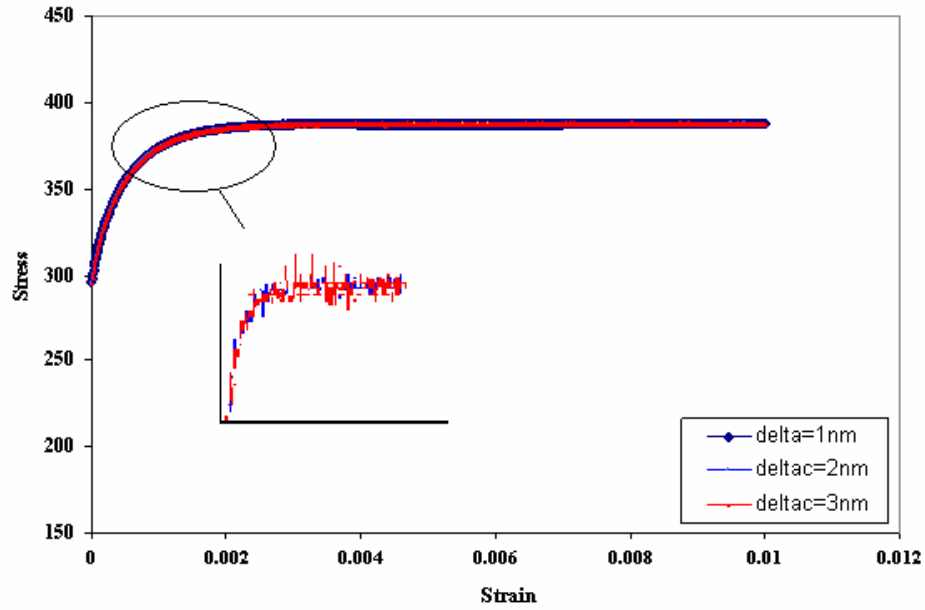
Figure 5.33: Macroscopic stress-strain curves of 30 nm Cu.

In order to predict the combined effect of grain boundary sliding and of the grain boundary dislocation emission and penetration mechanism the model was used with different values of the stress heterogeneity factor. In figure 5.34 one can observe the predicted Hall-Petch plot for three different values of the stress heterogeneity factor K: 1, 1.5 and 2. It can be observed that compared to the 3PVP model (see Figure 5.31), the effect of grain boundary sliding leads to a more pronounced decrease in the Hall-Petch slope. Indeed at a grain size of ~25 nm the deviation from the Hall-Petch law is much larger when grain boundary sliding is accounted for. Let us recall that the localization of

the activity of grain boundary sliding cannot be predicted in this model due to the spherical inclusion assumption and due to limitations inherent from the use of Eshelbian micromechanics. Also, an increase in the stress heterogeneity factor, which physically corresponds to an increase in the activity of the grain boundary dislocation emission and penetration, leads to a more pronounced softening in the Hall-Petch plot. Note that in the limit case where the stress heterogeneity factor is set to 2, a slightly negative Hall-Petch slope is predicted.
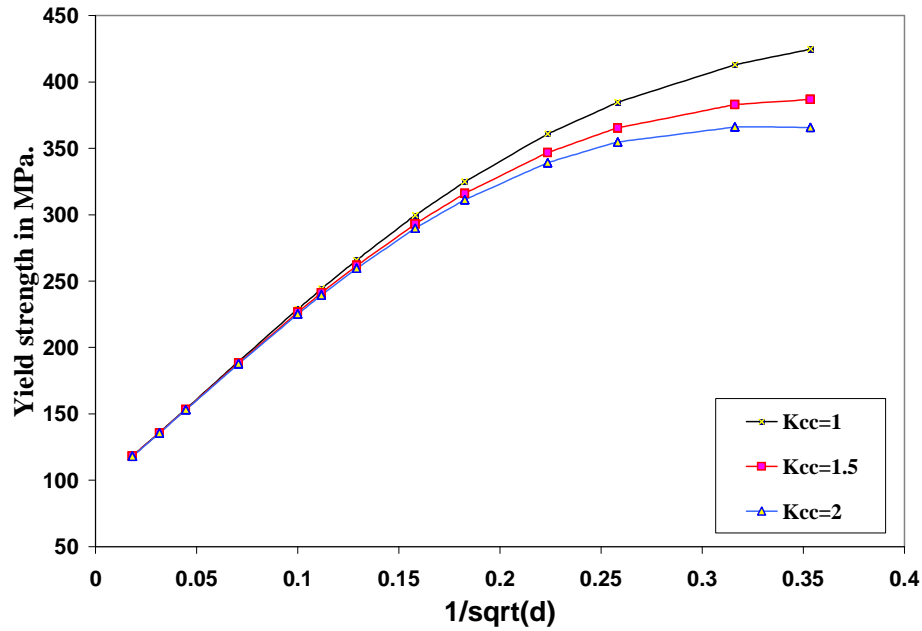
Figure 5.34: Hall-Petch plot for different values of the stress heterogeneities factor.

As mentioned in the discussion of the previous section, dislocation activity is known to be severely reduced in NC materials. However, this effect was not accounted for in previous models. Hence, in Figure 5.35 one can observe two Hall-Petch plots. The pink case corresponds to the black curve in Figure 5.34 (e.g., dislocation activity, dislocation

emission and grain boundary sliding can be active). The blue curve corresponds to the case where dislocation activity (e.g., storage and annihilation) is stopped for grain size smaller than 30 nm. One can observe that stopping the dislocation activity results in a sharp decrease in the Hall-Petch slope. This decrease can be considered as an artifact of the simulation. Indeed, when the dislocation activity is first stopped (d=30nm), plastic deformation in the inclusions (grain interiors) remains non negligeable and the inclusion phase cannot harden. Since, the yield stress is obtained via the 0.2 percent offset rule; it is expected to observe this decrease in the Hall-Petch plot upon stopping the dislocation activity. However, interestingly, one can observe that independently on the dislocation activity, both curves present similar slopes. This let us conclude that while previous model could not predict in a quantitative manner the size effect of the yield stress in NC materials, the results remain valid qualitatively.
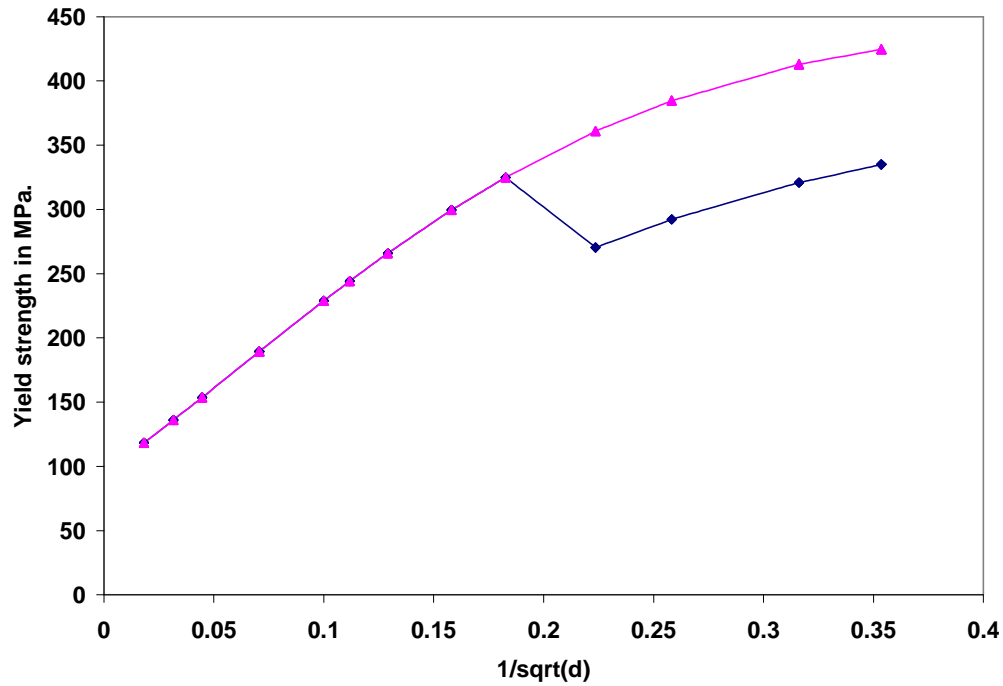
Figure 5.35: Effect of the activity of dislocations on the yield strength of NC Cu. The pink curve corresponds to the case where both dislocation activity, grain boundary sliding and grain boundary dislocation emission are accounted for. The blue curve corresponds to the case where dislocation activity is deactivated when the grain size is smaller than ~30nm.

Discussion

In sections in the above, the effects of grain boundary dislocation emission and penetration and of grain boundary sliding on the response of NC materials were investigated.

First, a hierarchal scale transition based on the input of parameters obtained via MD simulations into a secant-self-consistent scheme was used to simulate the sole effect

of grain boundary dislocation emission. In order to account for stress heterogeneities in the grain boundaries, a parameter, estimated via finite element simulations, was introduced into the constitutive law of the grain boundaries. It was concluded that high stress, in the order of a few GPa., are necessary for dislocations to be emitted from the grain boundaries. Also, MD simulations indicated that grain boundary ledges are source of dislocations. In the case of a $\Sigma5$ {210} grain boundaries containing ledges are more prone to emit dislocation than perfect planar grain boundaries. It was shown that typical work hardening laws describing the behavior of grain interiors were not suited to describe the size effect within crystallites. Therefore, these laws were modified to account for the effect of grain boundaries on the flow stress of crystallites at zero Kelvin. Finally, it was shown that the activity of grain boundary dislocation emission and penetration can result in the so called breakdown of the Hall-Petch law. However, this model can only lead to approximate predictions of the behavior of NC materials. Indeed, the parameters extracted from molecular dynamics simulations and describing the response of grain boundaries were calculated for one particular misorientation angle. Also, the effect of stress heterogeneities, which is obviously a local phenomenon, is not precisely accounted for in the present model. This results from the fact that the present micromechanical scheme can solely predict homogeneous state of stress and strain within each phase. However let us note that Lebensohn et al. (2007) recently solved such problems in the case of non spherical inclusions via the use of fast Fourier transforms. Finally, the decrease in the dislocation activity within the grain cores was not accounted for. This approximation naturally leads to overpredicted responses of the inclusion phase.

Second, the effect of grain boundary sliding was studied. The sliding process was modeled as a stick-slip mechanism. Void creation was not accounted for. It was shown that grain boundary sliding does not require such high stresses as grain boundary dislocation emission in order to be activated. Also, it does results in the observed breakdown of the Hall-Petch law. Moreover, it was shown that the simultaneous activity of grain boundary sliding and grain boundary dislocation emission results in a more pronounced breakdown of the hall-Petch law.

As clearly mentioned in this discussion the proposed models have the merit to allow a qualitative prediction of the effects of grain boundary sliding and grain boundary dislocation emission on the response of NC materials. However, a rigorous quantitative analysis is not permitted with the present approach. Hence, in the following chapter a complementary approach based on a non-conventional finite element method is presented that would allow a local prediction of stress states within all constituents.

References

Bachurin, D.V., Murzaev, R.T. and Nazarov, A.A., (2003). "Atomistic computer and disclination simulation of [001] tilt boundaries in nickel and copper". Fizika Metallov i Metallovedenie 96, 11-17.

Bitzek, E. and P. Gumbsch, (2005). "Dynamic aspects of dislocation motion: atomistic simulations". Materials Science and Engineering A 400-401, 40-44.

Cai, B., Kong, Q.P., Lu, K, Lu, L. (2000). "Low temperature creep of nanocrystalline pure copper". Materials Science and Engineering A 286 (1), 188-192.

Capolungo, L., Cherkaoui, M., Qu, J. (2005). "A self consistent model for the inelastic deformation of nanocrystalline materials". Journal of Engineering Materials and Technology 127: 400-407.

Capolungo, L., Cherkaoui, M., Qu, J. (2007a). " On the elastic-viscoplastic behavior of nanocrystalline materials". International Journal of Plasticity 23:561:591.

Capolungo, L., Cherkaoui, M., McDowell, D.L., Qu, J, Jacob, K.I.. (2007b). " Dislocation nucleation from bicrystal interfaces and grain boundary ledges: Relationship to nanocrystalline deformation". Journal of the Mechanics and Physics of Solids, in press.

Cheng, S., E. Ma, Wang, Y.M., Kecskes, L.J.., Youssef, K.M. Koch, C.C., Trociewitz, U.P., Han, K. (2005). "Tensile properties of in situ consolidated nanocrystalline Cu". Acta Materialia 53, 1521-1533.

Estrin, Y., Mecking, H. (1984). "A unified phenomenological description of work hardening and creep based on one parameter models". Acta Metallurgica 32:57-70.

Kelchner, C.L., Plimpton, S.J. and Hamilton, J.C., (1998). "Dislocation nucleation and defect structure during surface indentation". Physical Review B 58: 11085-11088.

Kim, H. S., Y. Estrin, Bush, M.B. (2000). "Plastic deformation behaviour of fine grained materials". Acta materialia 48, 493-504.

Kocks, U. F. (1976). "Laws for work hardening and low temperature creep". Transactions of the ASME, 76-85.

Kocks, U. F., Argon, A.S., Ashby, M.F. 1975. "Thermodynamics and kinetics of slip". Progress in Materials Science 19, 1-291.

Kocks, U. F., Mecking, H. (2003). "Physics and phenomenology of strain hardening". Progress in Materials Science 48, 171-273.

Lebenshon, R., Bringa, E.M., Caro, E.A. " A viscoplastic micromechanical model for the yield strength of nanocrystalline materials". Acta Materialia 55:261-271.

Li, Y. J., W. Blum, Breutinger, F. 2004. "Does nanocrystalline Cu deform by Coble creep near room temperature". Materials science and engineering A 387-389, 585-589.

Melchionna, S., Ciccotti, G. and Holian, B.L., (1993). "Hoover npt dynamics for systems varying in shape and size". Molecular Physics 78, 533-544.

Meyers, M. A., Ashworth, E. (1982)."Model for the effect of grain size on the yield stress of metals ". Philosophical Magazine A: Physics of Condensed Matter, Defects and Mechanical Properties 46:737-759

Mishin, Y. M. J. Mehl, D. A. Papaconstantopoulos, A. F. Voter,. Kress, J.D. (2001)." Structural stability and lattice defects in copper: Ab initio, tight-binding, and embedded-atom calculations" Physical. Review B 63 224106:1-16

Muller, P., Saul, A. (2004). "Elastic effects on surface physics". Surface Science reports 54: 157-258.

Nes, E. (1997). "Modeling of work hardening and stress saturation in FCC metals". Progress in Materials Science 41:129-193.

Nguyen, O., Ortiz, M. (2002). "Coarse-graining and renormalization of atomistic binding relations and universal macroscopic cohesive behavior". Journal of the Mechanics and Physics of Solids 50:1727–1741.

Qu, J, (1993). "The effect of slightly weakened interfaces on the overall elastic properties of composite materials". Mechanics of Materials 14: 269-281.

Sanders, P. G., J. A. Eastman, Weertman, J.R. (1997). "Elastic and tensile behavior of nanocrystalline copper and palladium". Acta Metallurgica 45: 4019-4025.

Shuttleworth, R. (1950)."The surface tension of solids". Proceedings of the physical society A 63: 444-457.

Spearot, D.E., Jacob, K.I., McDowell, D.L. (2005). "Nucleation of dislocations from [001] bicrystal interfaces in aluminum". Acta Materialia 53, 3579-3589.

Spearot, D.E., Capolungo, L., Qu, J., Cherkaoui, M. (2007). " Elastic Bifurcation during Tensile Deformation of <100> Bicrystal Interfaces in Copper". *submitted to Computational Materials Science.*

Wang, G.-F.,. Feng, X.Q., Shou-Wen, Y. Ce-Wen, N. (2003). "Interface effects on effective elastic moduli of nanocrystalline materials." Materials Science and Engineering A 363: 1-8.

Warner, D.H., Sansoz, F., Molinari, J.F. (2006). "Atomistic based continuum investigation of plastic deformation in nanocrystalline copper". International Journal of Plasticity 22: 754-774.

Wei, Y.J., Anand, L. (2004). "Grain boundary sliding and separation in polycrystalline metals: application to nanocrystalline fcc metals". Journal of the Physics and Mechanics of Solids 52: 2587-2616.

Yin, W.M., Whang, S.H., Mirshams, R., Xiao, C.H. (2001). "Creep behavior of nanocrystalline nickel at 290 and 373 K". Materials Science and Engineering A301: 18-22.

CHAPTER 6

TOWARDS A NUMERICAL MODEL FOR NC MATERIALS

In this chapter, a novel approach is introduced to model the grain boundary dislocation emission and penetration mechanism. Indeed, as shown in previous chapter, a precise quantification of the effect and activity of grain boundaries as dislocation sources and sinks cannot be achieved with the aforementioned hierarchal scale transition. Recalling the discussion dedicated to the limitations and strengths of existing modeling techniques (presented in Chapter 1), the finite element method appears well suited to predict such effects. In particular, the finite element method allows a precise description of the material's geometry which as shown in previous chapters is a key feature in NC materials.

This chapter shall be considered as a work in progress for the long term objective is to simulate the behavior of NC materials in a realistic fashion. Precisely, the tool to be developed shall allow a realistic microstructural description of the materials (e.g., grain shape, grain size distribution, grain boundary misorientations, initial dislocation densities, slip systems, etc…) and shall also account for all mechanisms studied in previous chapters (e.g., grain boundary dislocation emission, penetration and unaccomodated grain boundary sliding). The description of the microstructure via the finite element method has already been treated elsewhere and does not represent the primary challenge of this analysis. For example, Warner et al. (2006), simulated the response of a microstructure

composed of 200 grains with a log-normal distribution of the grain size via the use of Voronoi tessellation and the use of Monte Carlo's procedure. Similarly, owing to the recent development of interface element, grain boundary sliding has already been dealt with. For example, the reader can refer to the work of Wei and Anand (2004), and Warner and Molinari (2006).

Consequently, the major challenge is to develop a finite element method capable of rigorously describing the mechanisms of dislocation emission and dislocation penetration from/ into grain boundaries. Such an approach can be developed solely if the size of elements is smaller than that of the grains and of the characteristic length of grain boundaries. At this scale, all dislocations shall be considered geometrically necessary. Typically finite element approaches accounting for the effect of geometrically dislocation rely on a crystal plasticity formulation and on the use of Nye's (1953) dislocation tensor (Arsenlis et al 1999, Huang et al. 2004; Cheong at al. 2005). These approaches are successful in modeling size effects in the response of materials. In general, the flux of geometrically necessary dislocations is not accounted for. However, Arsenlis et al.(2004) introduced a framework, which necessitates higher order boundary conditions, in order to allow the transfer of dislocations between elements. While this method appears suited to treat the problem of grain boundary dislocation emission and penetration, the authors argued that GND cannot be created within an element. Also, the model was simplified to a two-dimensional single crystal with only one active slip system. Hence, the approach is not suited to describe the activity of grain boundary dislocation emission and penetration. Here, a novel model is introduced to treat such phenomena.

Let us consider the case of a bicrystal interface which geometry is presented in Figure 6.1. In the proposed model, the bicrystal interface is composed of two grains (in blue and yellow) and two half grain boundaries (in green and purple). Both blue and green grain interiors and grain boundaries have similar crystallographic orientation. Similarly, the yellow grain interior and the purple half-grain boundary have the same orientation. Clearly with this approach, it will be ensured that grain boundary dislocation emission occurs on the primary slip systems. However, the response of grain boundaries will require further development in order to account for the possible constraints within the available slip systems.
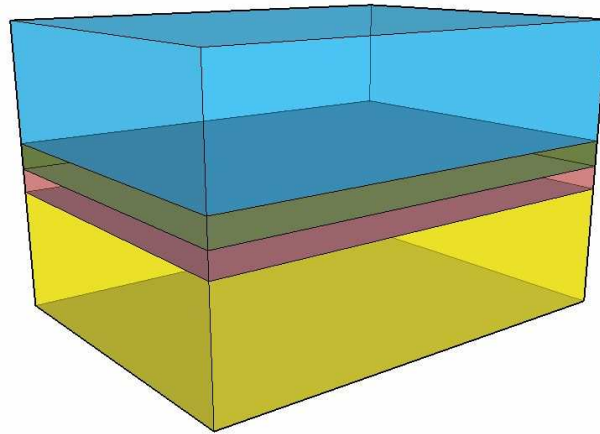

Figure 6.1: Schematic of a bicrystal interface.

Crystal plasticity

As revealed by MD simulations presented in Chapter 5, grain boundaries emit dislocation on the primary slip system. In order to obtain a precise description of the

dislocation activity a crystal plasticity approach shall be used. Indeed, with this approach inhomogeneities in the plastic deformation within grain interiors and grain boundaries could be predicted. Let us briefly recall the formalism of crystal plasticity. First, the deformation gradient can be decomposed as the product of an elastic deformation gradient and a plastic deformation gradient:

$$\mathbf{F} = \mathbf{F}^{e}\mathbf{F}^{P} = \frac{\partial x}{\partial X} \tag{6.1}$$

Here $\mathbf{F}^{e}$ and $\mathbf{F}^{P}$ denote the elastic deformation gradient and the plastic deformation gradient. x and X denote the position vector in the current deformed configuration and in the initial undeformed configuration. Typically the plastic deformation gradient rate is related to the shear strain rate as follows:

$$\dot{\boldsymbol{F}}^{P} = \left\{ \sum_{\alpha} \dot{\gamma}^{\alpha} \boldsymbol{m}^{\alpha} \otimes \boldsymbol{n}^{\alpha} \right\} \boldsymbol{F}^{P} \tag{6.2}$$

Here α denotes the slip system. $\dot{\gamma}^{\alpha}$, $\boldsymbol{m}^{\alpha}$ and $\boldsymbol{n}^{\alpha}$ denote the shear strain rate, the slip direction and the normal to the slip plane, respectively. As described in equation (6.2), we suppose here that plastic deformation occurs on active slip systems. Recall that the effect of grain boundary sliding is to be neglected. Also, this approach is clearly well suited in the case of grain interiors. However, it will clearly require further extension in the case of grain boundaries. For example, constraints between slip systems shall be added. A

formulation could be obtained simple shear tests on bicrystal interfaces performed via MD. The constitutive law is written as follows

$$T = L \cdot E^e \tag{6.3}$$

Where T is the second Piola-Kirchhoff tensor. The Green Lagrange deformation tensor is given by:

$$E^e = \frac{1}{2}\{F^{eT}F^e - 1\} \tag{6.4}$$

Here the superscript T denotes the transpose of a tensor. The Cauchy stress tensor is related to the second Piola-Kirchhoff tensor as follows:

$$T = F^{e^{-1}}\left\{(\det F^e)\sigma F^{e^{-T}}\right\} \tag{6.5}$$

With the framework presented in the above, the effect of dislocation activity (e.g., transport, nucleation and absorption) is described in the shear strain rate for which two equations dependent on the dislocation density are presented in subsequent sections.

Inelastic deformation of grain cores

Recall that as exhibited by TEM observations, grain cores in NC materials are initially devoid of dislocations. As a first approach the occasional presence of twin

boundaries, which is dependent on the fabrication process, will be neglected. Hence, in this model the inelastic slip rate cannot be described via traditional phenomenological models based on the evolution of statistical dislocations via growth and annihilation. Indeed those mechanisms shall not be prominent in NC materials with small grain size which we are interested into in this chapter. Therefore, it can be concluded that the viscoplastic deformation of grain cores results solely from the glide of dislocations on a given slip system. The anelastic strain rate is proportional to the number of dislocations. Hence, Orowan's equation best describes the inelastic strain rate which is written as follows:

$$\dot{\gamma}^\alpha = \rho_M b^\alpha \overline{v}^\alpha \tag{6.6}$$

Here ρ_M describes the mobile dislocation density. Recall that considering the reduced size of the representative element used in these derivations, all dislocations shall be considered as geometrically necessary. Let us note that the mobile dislocation density can be decomposed as the sum of the contribution of edge and screw components. In this case (6.6) takes the form:

$$\dot{\gamma}^\alpha = \rho_M^{ed} b^\alpha \overline{v}_{ed}^\alpha + \rho_M^{sc} b^\alpha \overline{v}_{sc}^\alpha \tag{6.7}$$

In equations (6.6) and (6.7), $\overline{v}^\alpha$ denotes the average velocity of dislocations traveling on slip system α. Typically, the effect of the presence of immobile dislocations is accounted for either under the form of a slip resistance term or of a "yield strength"

299

term. In the present case, dislocation is not affected by immobile dislocations and the dislocation velocity can be taken as a constant. The superscripts and subscripts "ed" and "sc" refer to the edge an screw segments of dislocations, respectively.

The unit cell representing the material has sub-granular dimensions. Moreover, dislocations sources are not present within the crystals. Therefore, dislocations are simply transmitted from a unit cell, smaller than a grain, to a neighboring unit cell and the evolution of the mobile geometrically necessary dislocation density arises from the flux of dislocations which description will be presented later in this chapter.

Inelastic deformation of grain boundaries

Away from triple junctions grain boundaries exhibit a well defined structure typically described with disclinations structural unit models and dislocation unit models (in the limit of the structural units model) . Recall that MD simulations have shown that the emission of a partial Shockley dislocation from grain boundaries can lead to local atomic rearrangement. In the case of grain boundaries containing E structural units, atomic shuffling is known to occur prior to dislocation emission. Also, dislocations (partial and full) emitted from grain boundary were shown to glide on the primary slip systems of the adjacent crystal (Sansoz et al. 2005). Hence, as a first approach, grain boundaries can be considered as composed of two half unit cells which orientations coincide with that of the adjacent grains (see Figure 6.2).
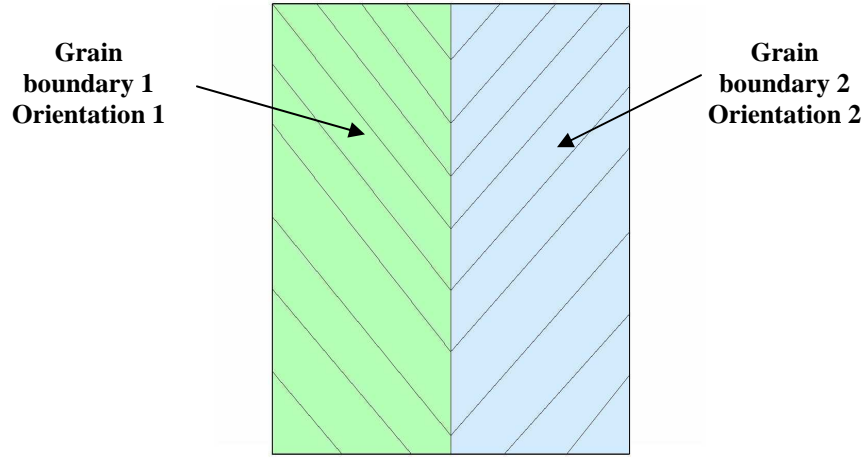
Figure 6.2: Grain boundary representation.

With this description of grain boundaries, the imposed geometric orientation will ensure on dislocations to be emitted on the primary slip systems. The inelastic shear strain rate can be written as:

$$\dot{\gamma}^\alpha = \rho_M^{ed} b^\alpha \overline{v}_{ed}^\alpha + \rho_M^{sc} b^\alpha \overline{v}_{sc}^\alpha \qquad (6.8)$$

As mentioned in the above, the emission process leads to local atomic rearrangement. Conversely, the penetration of an emitted dislocation shall also have similar effects. As a first approach, the microstructural change engendered by dislocation emission and penetration will be neglected. However, imposing constraints on the slip systems will allow the description of the effect of dislocation emission and penetration on grain boundaries. These constraints will be based on molecular dynamics simulations on bicrystal interfaces (tensile and shear tests).

The dimensions of the representative element must be smaller than that of grain boundaries. In this case, the evolution of the dislocation density is driven by two processes: (1) the nucleation of a dislocation and, (2) the inward and outward dislocation flux corresponding to the dislocation penetration process and to the dislocation emission process, respectively.

Dislocation density evolution

From the discussions on the evolution of the dislocation density presented in the previous two sections it can be readily concluded that formalism to be presented here in the case of grain boundaries, where dislocations can be nucleated and transmitted, is a general case compared to that of the grain cores. Hence, in what follows the developments to be presented will treat solely of grain boundaries. In order to retrieve the representation of the dislocation density evolution within grain interiors, all terms related to dislocation nucleation shall be disregarded.

Let us now consider a unit cell representing a portion of a grain boundary depicted in Figure 6.3. On a given slip system dislocations evolve via flux of dislocations which ensure the transmission of dislocations, resulting from the grain boundary dislocation emission and penetration mechanism, and the continuity of the lattice curvature as discussed in work by Arsenlis and Parks (2004). These dislocations have both edge and screw components.
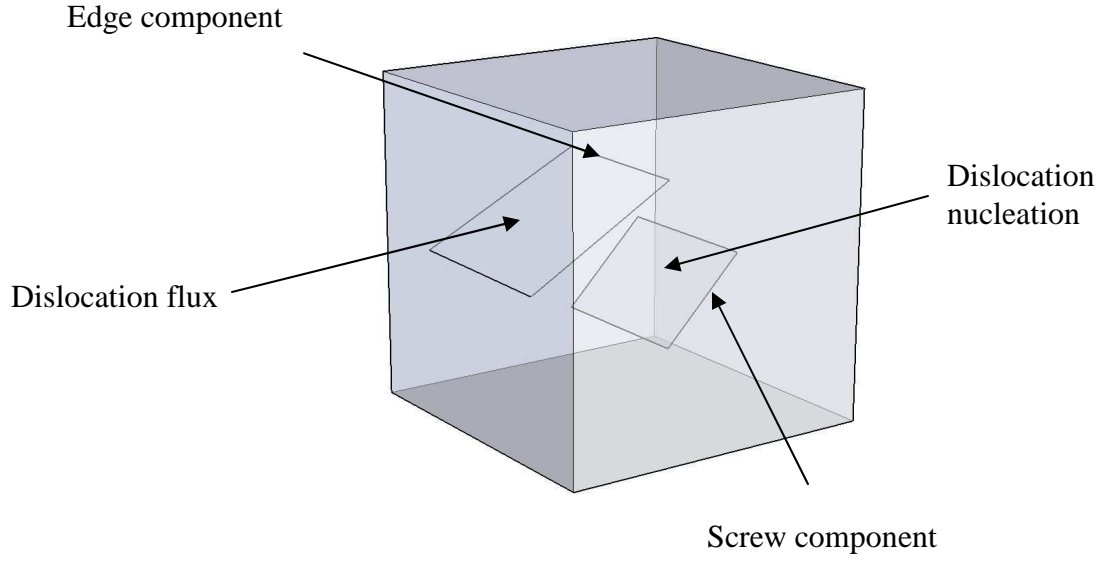
Figure 6.3: schematic of the dislocation evolution process.

Hence in a general case the rate of evolution of the dislocation density is written as follows:

$$\dot{\rho}_M^\alpha = \dot{\rho}_{nucl}^\alpha + \dot{\rho}_{flux}^\alpha \tag{6.9}$$

Here the subscripts flux and nucl refer to the dislocation evolution due to flux and to nucleation. Let us now present the modeling of both the dislocation flux and the dislocation nucleation mechanism. Consider a cylinder with outward unit normal $\boldsymbol{n}$ (see Figure 6.5). The flux of dislocations on slip system α is given by:

$$\dot{\rho}_{flux}^\alpha = \dot{\rho}_{flux,ed}^\alpha + \dot{\rho}_{flux,sc}^\alpha \tag{6.10}$$

303

Let us first consider the case of a edge dislocations which velocity vector is given by $\bar{v} \cdot \boldsymbol{m}^{\alpha}$. Here $\boldsymbol{m}^{\alpha}$ is the direction of the slip direction vector. The dislocation flux is the integral over the surface area to be crossed by the moving dislocation of the product of the dislocation velocity vector and of the edge dislocation density:

$$\dot{\rho}_{flux,ed}^{\alpha} = \int_{dS} \rho_{ed}^{\alpha} \bar{v} \boldsymbol{m}^{\alpha} \cdot \boldsymbol{n} dS \tag{6.11}$$

Recalling the multiplicative decomposition of the deformation gradient, it is important to note that the integral in equation (6.11) refers to the intermediate configuration (see Figure 6.6 extracted from Meissonier et al. 2000). Using the divergence theorem in the reference configuration one obtains:

$$\dot{\rho}_{flux,ed}^{\alpha} = -\frac{\partial \rho_{ed}^{\alpha}}{\partial \boldsymbol{X}} \bar{v} \cdot \boldsymbol{F}^{p^{-1}} \boldsymbol{m}^{\alpha} \tag{6.12}$$

Similarly in the case of screw dislocations one obtains:

$$\dot{\rho}_{flux,sc}^{\alpha} = -\frac{\partial \rho_{sc}^{\alpha}}{\partial \boldsymbol{X}} \bar{v} \cdot \boldsymbol{F}^{p^{-1}} \boldsymbol{t}^{\alpha} \tag{6.13}$$

Note that in the case of the screw component of the flux term, the dislocation velocity lies on the $\boldsymbol{t}^{\alpha}$ direction corresponding to the vector normal to the slip direction and to the normal to the slip plane.
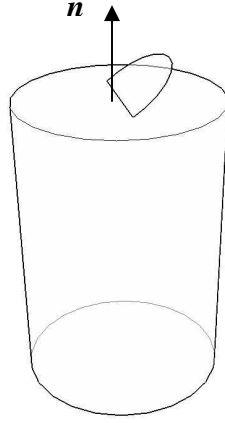
Figure 6.4: Schematic of the description of the dislocation flux.

Also, let us note here that equations (6.12) and (6.13) can be obtained simply by simplifying the expression of the evolution of geometrically necessary dislocation developed by Arsenlis and Parks (2004), via a reasoning based on the strain gradients within the lattice. Indeed, the previously mentioned authors obtain a final expression of the dislocation flux containing a flux term, similar to the present study, and a jog and kink creation term which are not relevant in the study.
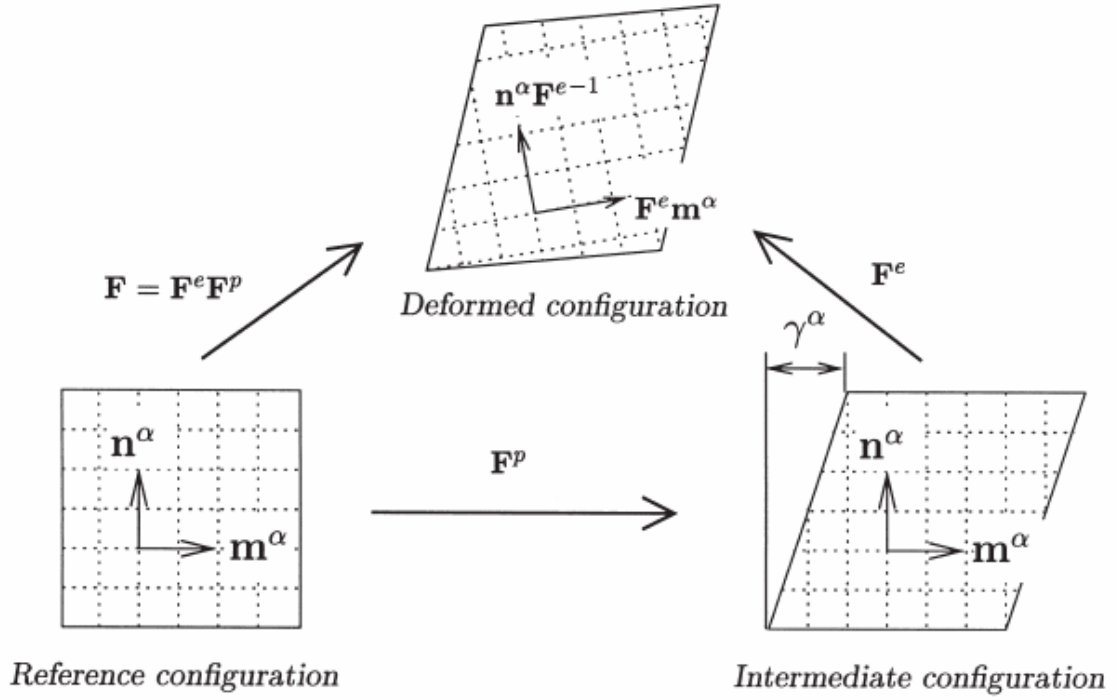
Figure 6.5: Multiplicative decomposition of the deformation gradient.

Dislocation nucleation is thermally activated and occurs solely within the grain boundary phase. As revealed by bicrystal simulation of perfect planar interfaces and stepped interfaces, emitted dislocations have both edge and screw characters:

$$\dot{\rho}_{nucl}^{\alpha} = \dot{\rho}_{nucl,ed}^{\alpha} + \dot{\rho}_{nucl,sc}^{\alpha} \tag{6.14}$$

Supposing Boltzmann distribution for the probability of successful emission, as in previous chapter, the nucleation of both edge and screw dislocations is written as follows:

$$\dot{\rho}^{\alpha}_{nucl,ed} = \varpi l_e \exp\left(\frac{-\Delta G_0}{kT}\left(1-\left(\frac{\tau^{\alpha}}{\tau_{crit}}\right)^p\right)^q\right)$$

(6.15)

and

$$\dot{\rho}^{\alpha}_{nucl,sc} = \varpi l_{sc} \exp\left(\frac{-\Delta G_0}{kT}\left(1-\left(\frac{\tau^{\alpha}}{\tau_{crit}}\right)^p\right)^q\right)$$

(6.16)

Here ϖ, l_{sc}, l_e τ^{α}, τ_{crit}, ΔG_0, k, T, p and q denote the frequency of attempts of nucleation of a dislocation, the length of the screw and edge segments necessary for the nucleation to be successful, , the resolve shear stress on slip system α, the critical shear stress for dislocation nucleation, the free enthalpy of activation, Boltzmann's constant, the temperature and two parameters describing the shape of the dislocation nucleation resistance diagram, respectively. All parameters in the exponential term of equation (6.16) can be obtained via the same procedure presented in Chapter 5. Also, the critical length at which a dislocation nucleation event is a success can be obtained via MD simulations. The frequency of attempt shall be smaller than the atomic frequency (in the order of 10^{13}/s) and smaller the dislocation ground frequency (in the order of 10^{12}/s) (Kocks and Ashby, 1975).

Application via the finite element method

The model presented in the above can be implemented with use of the finite element method on the condition that the dislocation rate balance can be formulation within a framework similar to that of the finite element method (e.g., weak formulation of a principle of virtual power). As discussed in work by Arsenlis and Parks (2004), in order

to ensure the continuity of the lattice curvature and the transfer of emitted dislocations, higher order boundary conditions must be imposed on each element.

Let us present the weak formulation of the problem in the case of edge dislocations and grain boundaries. The case of grain cores is obtained simply by disregarding the dislocation nucleation terms. Combining all terms (e.g., flux and nucleation) describing the rate of change of the dislocation density, the dislocation rate balance is written as:

$$0 = \dot{\rho}_{ed}^{\alpha} + \frac{\partial \rho_{ed}^{\alpha}}{\partial \boldsymbol{X}} \overline{v} \cdot \boldsymbol{F}^{p^{-1}} \boldsymbol{m}^{\alpha} - \varpi l_e \exp\left(\frac{-\Delta G_0}{kT}\left(1 - \left(\frac{\tau^{\alpha}}{\tau_{crit}}\right)^p\right)^q\right) \tag{6.17}$$

Let us multiply the previous dislocation balance equation by a virtual dislocation density, $\tilde{\rho}$, which must respect the real boundary conditions. Hence, one obtains after integration over the volume element:

$$0 = \int_V \tilde{\rho}\dot{\rho}_{ed}^{\alpha} dV + \int_V \tilde{\rho}\frac{\partial \rho_{ed}^{\alpha}}{\partial \boldsymbol{X}} \overline{v} \cdot \boldsymbol{F}^{p^{-1}} \boldsymbol{m}^{\alpha} dV - \int_V \tilde{\rho}\varpi l_e \exp\left(\frac{-\Delta G_0}{kT}\left(1 - \left(\frac{\tau^{\alpha}}{\tau_{crit}}\right)^p\right)^q\right) dV \tag{6.18}$$

As usual when using the finite element method, let us take the weak formulation of equation (6.18):

$$0 = \int_V \tilde{\rho} \dot{\rho}_{ed}^{\alpha} dV - \int_V \frac{\partial \tilde{\rho}}{\partial \boldsymbol{X}} \rho_{ed}^{\alpha} \overline{v} \cdot \boldsymbol{F}^{p^{-1}} \boldsymbol{m}^{\alpha} dV + \int_S \tilde{\rho} \rho_{ed}^{\alpha} \overline{v} \cdot \boldsymbol{F}^{p^{-1}} \boldsymbol{m}^{\alpha} dS - \int_V \tilde{\rho} \varpi l_e \exp\left[\frac{-\Delta G_0}{kT} \left(1 - \left(\frac{\tau^{\alpha}}{\tau_{crit}} \right)^p \right)^q \right] dV$$

$$(6.19)$$

In equation (6.19) the surface integral term is equivalent to the product of the virtual dislocation density by the dislocation flux term given in (6.11). Let us define the dislocation flux term as follows:

$$\boldsymbol{\Psi} = \rho_{ed}^{\alpha} \overline{v} \cdot \boldsymbol{F}^{p^{-1}} \boldsymbol{m}^{\alpha} \cdot n \qquad (6.20)$$

Consequently equation (6.19) can be rewritten in the following form:

$$0 = \int_V \tilde{\rho} \dot{\rho}_{ed}^{\alpha} dV - \int_V \frac{\partial \tilde{\rho}}{\partial \boldsymbol{X}} \rho_{ed}^{\alpha} \overline{v} \cdot \boldsymbol{F}^{p^{-1}} \boldsymbol{m}^{\alpha} dV + \int_S \boldsymbol{\Psi} dS - \int_V \tilde{\rho} \varpi l_e \exp\left[\frac{-\Delta G_0}{kT} \left(1 - \left(\frac{\tau^{\alpha}}{\tau_{crit}} \right)^p \right)^q \right] dV$$

$$(6.21)$$

The above expression can now be implemented via the use of the finite element method which details are provided in the following section. Also, recall that equation (6.21) and its equivalent in terms of screw dislocations must be valid on all slip systems. Hence, the system of non linear equations to be solved consists of 24 equations corresponding to both the edge and the screw components on the 12 active slip systems.

Let us recall here the general methodology used in finite elements. The numerical implementation of the weak formulation of the dislocation evolution equation, given in (6.21), is decomposed into three steps: (1) discretization of the dislocation density, (2) global linearization procedure occurring at the element level within a user element subroutine (in Abaqus) and (3) time discretization procedure at the material's level within a user material subroutine in Abaqus. Let us note here that the set of differential equations presented here must be solved simultaneously with the set of equations resulting from the weak formulation of the principal of virtual power which details are presented in work by Meissonnier et al. (2000). Hence, for clarity of the model, solely the framework of the implementation of the effect of dislocation densities on NC materials will be presented

Discretization

Let us consider the case of a 20-nodes cubic element. The dislocation density, may it be virtual or real, can be interpolated from the 20 nodal values. The discretization can be written as follows:

$$\rho = \sum_{i=1}^{i=20} N^i \overline{\rho}^i = N \overline{\rho} \tag{6.22}$$

Where N^i are the second order interpolation functions given by:

$$N^i\left(\xi,\eta,\zeta\right)=\frac{1}{8}\left(1+\xi^i\xi\right)\left(1+\eta^i\eta\right)\left(1+\zeta^i\zeta\right)\left(\xi^i\xi+\eta^i\eta+\zeta^i\zeta-2\right) \qquad \text{for i=1,...,8,}$$

$$N^i\left(\xi,\eta,\zeta\right)=\frac{1}{4}\left(1-\xi^2\right)\left(1+\eta^i\eta\right)\left(1+\zeta^i\zeta\right) \qquad \text{for i=9,11,17,,19}$$

$$N^i\left(\xi,\eta,\zeta\right)=\frac{1}{4}\left(1-\xi^i\xi\right)\left(1-\eta^2\right)\left(1+\zeta^i\zeta\right) \qquad \text{for i=10,12,18,20}$$

$$N^i\left(\xi,\eta,\zeta\right)=\frac{1}{4}\left(1-\xi^i\xi\right)\left(1-\eta^i\eta\right)\left(1-\zeta^2\right) \qquad \text{for i=13,14,15,16}$$

(6.23)

Also in equation (6.22), the interpolation matrix has dimensions $N=\left[24*480\right]$ and has

interpolation matrix has the following shape:

$$N=\begin{bmatrix} N_1 & 0 & N_2 & 0 & ... & ... & ... & ... & ... & 0 \\ 0 & N_1 & 0 & N_2 & ... & ... & ... & ... & ... & 0 \\ ... & ... & ... & ... & ... & ... & ... & ... & ... & ... \\ ... & ... & ... & ... & ... & ... & ... & ... & ... & ... \\ 0 & ... & ... & ... & ... & N_1 & ... & 0 & N_{20} & 0 \\ 0 & ... & ... & ... & ... & 0 & ... & N_{19} & 0 & N_{20} \end{bmatrix}$$

(6.24)

The discretized dislocation vector is given by:

$$
\tilde{\rho} =
\begin{bmatrix}
\rho_e^{1,1} \\
\rho_s^{1,1} \\
\rho_e^{1,2} \\
\rho_s^{1,2} \\
\vdots \\
\rho_e^{1,20} \\
\rho_s^{1,20} \\
\rho_e^{2,1} \\
\rho_s^{2,1} \\
\vdots \\
\rho_e^{12,20} \\
\rho_s^{12,20}
\end{bmatrix}
\tag{6.25}
$$

Here the first superscript defines the slip system number while the second superscript defines the node number. In equation (6.19) the virtual dislocation density gradient needs to be evaluated, leading to:

$$
\frac{\partial \tilde{\rho}}{\partial \boldsymbol{X}} = \nabla \boldsymbol{N} \, \overline{\boldsymbol{\rho}} = \nabla_{(\xi,\eta,\zeta)} \boldsymbol{N} \left[\sum_{j=1}^{20} X^j \otimes \nabla_{(\xi,\eta,\zeta)} N^j \right] \overline{\boldsymbol{\rho}} = \boldsymbol{G}\overline{\boldsymbol{\rho}}
$$

with

$$
\boldsymbol{G} = \nabla_{(\xi,\eta,\zeta)} \boldsymbol{N} \cdot \boldsymbol{det} \left[\left[\sum_{j=1}^{20} X^j \otimes \nabla_{(\xi,\eta,\zeta)} N^j \right] \right]^{-1}
\tag{6.26}
$$

Here $\boldsymbol{G}$ is a [72*480] matrix. Inserting (6.22) and (6.26) into (6.19) and considering all slip systems and both edge and screw components of the dislocation density, one obtains :

312

$$R(\rho) = F^{in} - F^{bd} = 0 \tag{6.27}$$

With

$$F^{in} = \int_V \left[N^T \dot{\rho} - G^T H \cdot \rho \bar{v} - N^T \Phi \right] dV \tag{6.28}$$

And

$$F^{bd} = - \int_S N^T \Psi dS \tag{6.29}$$

Here the superscripts *"in"* and *"bd",* denote the evolution of the dislocation density within the element and due to transport through the boundaries, respectively. In equation (6.28), **H** is a [72*24] matrix which is given by:

$$H = \begin{bmatrix} H_1 & 0 & 0 & ... & 0 & 0 \\ 0 & H_2 & 0 & ... & 0 & 0 \\ & & \cdot & & & \\ & & & \cdot & & \\ & & & & \cdot & \\ 0 & 0 & 0 & ... & 0 & H_{24} \end{bmatrix} \tag{6.30}$$

In equation (6.30) H_i, i=1,24 is a [3*1] matrix which components are given by:

$$H_i = \begin{cases} F^{p^{-1}} m^i & \text{if i is odd} \\ F^{p^{-1}} t^{i/2} & \text{if i is even} \end{cases} \tag{6.31}$$

Also, in equation (6.28) the term $\boldsymbol{\Phi}$ is a [24*1] matrix which components are given by:

$$\Phi_\iota = \begin{cases} \varpi l_e \exp\left(\dfrac{-\Delta G_0}{kT}\left(1 - \left(\dfrac{\tau^i}{\tau_{crit}} \right)^p \right)^q \right) & \text{if i is odd} \\[3ex] \varpi l_s \exp\left(\dfrac{-\Delta G_0}{kT}\left(1 - \left(\dfrac{\tau^{i/2}}{\tau_{crit}} \right)^p \right)^q \right) & \text{if i is even} \end{cases} \tag{6.32}$$

Finally, one can discretize the dislocation density and the dislocation flux vector $\boldsymbol{\Psi}$ similarly to equation (6.22). Hence, one obtains:

$$R(\bar{\rho}) = \int_V N^T N dV \dot{\bar{\boldsymbol{\rho}}} - \int_V \bar{v} G^T \mathbf{H N} dV \bar{\boldsymbol{\rho}} - \int_V N^T \boldsymbol{\Phi} dV + \int_S N^T \boldsymbol{\Psi} dS \tag{6.33}$$

Equation (6.33) can be written as follows:

$$R(\bar{\rho}) = F_I \dot{\bar{\boldsymbol{\rho}}} - F_{II} \bar{\boldsymbol{\rho}} - F_{III} + F_{IV} \tag{6.34}$$

With:

$$F_I = \int_V N^T N dV$$

$$F_{II} = \int_V \bar{v} G^T \mathbf{H} N dV$$

$$F_{III} = \int_V N^T \Phi dV \qquad (6.35)$$

$$F_{IV} = \int_S N^T \Psi dS$$

Supposing instantaneous motion of dislocations through crystals (grain cores as well as grain boundaries), overall in a unit cell the time rate of dislocation density is constant. Indeed, in the case of grain core, a dislocation entering the representative element is instantaneously transmitted to the adjacent element. Also, in the case of grain boundaries, a nucleated dislocation is instantaneously transmitted to the adjacent element. Hence, equation (6.34) can be simplified into:

$$R(\bar{\rho}) = -F_{II}\bar{\rho} - F_{III} + F_{IV} \qquad (6.36)$$

This algebraic equation is clearly non linear for the matrices F_{II}, F_{III} and F_{IV} are dependent on the dislocation density. The solution procedure is detailed in following section.

Global linearization

During each time step within the calculation, the finite element code must find the zero of the vectorial function R. The Newton Raphson algorithm is used to solve the system of non linear equations. Hence at a given time step, the solution $\bar{\rho}^{final}$ is obtained as follows:

$$R\left(\overline{\rho}^r + \delta\overline{\rho}^r\right) = R\left(\overline{\rho}^r\right) + \frac{\partial R\left(\overline{\rho}^r\right)}{\partial \overline{\rho}^r}\delta\overline{\rho}^r + \mathrm{O}\left(\delta\overline{\rho}^r\right)^2 \qquad (6.37)$$

The previous equation can be written as follows:

$$\overline{\rho}^{r+1} = \overline{\rho}^r - \left[\frac{\partial R\left(\overline{\rho}^r\right)}{\partial \overline{\rho}^r}\right]^{-1} R\left(\overline{\rho}^r\right) \qquad (6.38)$$

From (6.36) the tangent stiffness matrix $\dfrac{\partial R\left(\overline{\rho}^r\right)}{\partial \overline{\rho}^r}$ is readily approximated and given by:

$$\frac{\partial R\left(\overline{\rho}^r\right)}{\partial \overline{\rho}^r} = F_{II} \qquad (6.39)$$

The terms F_{II}, F_{III} and F_{IV} must be calculated in order to define the tangent stiffness matrix and the residual vector $R\left(\overline{\rho}^r\right)$. These terms are calculated at the material level through the user material subroutine in Abaqus.

Time integration procedure.
The system in the above corresponds to 24 algebraic equations which are all given by integral of tensor products depending on the plastic deformation gradient. In order to calculate these integrals, the well known Gauss integration procedure will be used. This

obviously require the knowledge of the deformation gradient and second Piola kirchoff

stress at each time involved in the Newton Raphson procedure presented in the above

(denoted with *r* in (6.38)). As extensively discussed in work by Meissonier et al. (2000).,

the plastic strain gradient at subincrement n+1 can be written as function of the its

equivalent at sub increment n as follows:

$$\boldsymbol{F}^{P} = \left(1 - \sum_{\alpha=1}^{n_{\alpha}} \Delta\gamma^{\alpha}\boldsymbol{P}^{\alpha}\right)^{-1}\boldsymbol{F}_{n}^{P} \tag{6.40}$$

Here the subscript *n* denotes the value of the tensor considered at subincrement *n*. For

simplicity of the notations, the values of the tensors at subincrement n+1 will not have

any subscript (unless necessary for comprehension). Let us note here that the goal of the

time integration procedure is to calculate the term on the right hand side of equation

(6.38). Therefore the subincrements in the time integration procedure shall not be

confused with that of the global linearization. The inverse of the plastic deformation

gradient at subincrement n+1 is given by:

$$\boldsymbol{F}^{P^{-1}} = \boldsymbol{F}_{n}^{P^{-1}}\left(1 - \sum_{\alpha=1}^{n_{\alpha}} \Delta\gamma^{\alpha}\boldsymbol{P}^{\alpha}\right) \tag{6.41}$$

In equations (6.40) and (6.41), the plastic shear strain rate increment, $\Delta\gamma^{\alpha}$, is given by:

$$\Delta\gamma^{\alpha} = \left[(1-\theta)\dot{\gamma}_{n}^{\alpha} + \theta\dot{\gamma}^{\alpha}\right]\Delta t \tag{6.42}$$

Where $\theta = 1$ since we chose to perform an implicit scheme. In this particular case the increment in dislocation densities is provided at the element level since dislocation densities are nodal quantities. Equation (6.42) can be written in the following form:

$$\Delta \gamma^\alpha = \left(\Delta \rho_M^{ed} b^\alpha \overline{v}_{ed}^\alpha + \Delta \rho_M^{sc} b^\alpha \overline{v}_{sc}^\alpha \right) \Delta t$$

Let us now recall the expression of the Green Lagrange strain tensor:

$$E^e = \frac{1}{2} \left[\left(FF^{P^{-1}} \right)^T \left(FF^{P^{-1}} \right) - I \right] \tag{6.43}$$

Introducing (6.40) and (6.41) in the above equation one obtains:

$$E^e = \frac{1}{2} \left[\left(FF_n^{P^{-1}} \left(1 - \sum_{\alpha=1}^{n_\alpha} \Delta \gamma^\alpha P^\alpha \right) \right)^T \left(FF_n^{P^{-1}} \left(1 - \sum_{\alpha=1}^{n_\alpha} \Delta \gamma^\alpha P^\alpha \right) \right) - I \right] \tag{6.44}$$

The above equation can be written as follows:

$$E^e = \frac{1}{2} \left[A - I - \sum_{\alpha=1}^{n_\alpha} \Delta \gamma^\alpha \left(P^{\alpha^T} A + A P^\alpha \right) \right] \tag{6.45}$$

Where A is given by:

$$A = F_n^{P\text{-}T} F^T F F_n^{P\text{-}1}$$

(6.46)

Using the constitutive law one obtains an estimate of the second Piola Kirchhof stress tensors at time n+1:

$$T^* = T^{tr} - \sum_{\alpha=1}^{n_\alpha} \Delta\gamma^\alpha C^\alpha$$

(6.47)

Where

$$T^{tr} = \frac{1}{2}l:(A\text{-}I)$$

(6.48)

And

$$C^\alpha = \frac{1}{2}l:\left(AP^\alpha + P^{\alpha^T}A\right)$$

(6.49)

Hence the set of equations to be solved is the following:

$$\bar{T} = T^* \text{-} \left(T^{tr} - \sum_{\alpha=1}^{n_\alpha} \Delta\gamma^\alpha C^\alpha\right) = 0$$

(6.50)

319

Obviously the set of equation (6.50) is implicit and can be solved with the use of the Newton Raphson procedure which is briefly recalled here. Let us define the following system:

$$R(v) = 0$$

A solution for the system can be found by iteratively computing the following:

$$v^{r+1} = v^r - \left[\frac{\partial R(v^r)}{\partial v} \right]^{-1} R(v^r)$$

Applying (6.52) to the system (6.50) one obtains:

$$\left[T^* \right]^{r+1} = \left[T^* \right]^r - G^{r-1} \left[\bar{T} \right]^r$$

Let us note here that r denote the iteration step and not the time step. The Jacobian matrix is given by:

$$G = \left[I \right]$$

Hence, while the proposed finite element method largely increases the size of the system to be solved at the element level, the Newton Raphson procedure at the material's level is also largely reduced. This is due to the fact that the dislocation densities are nodal quantities. Hence the increment in the dislocation densities is known at each subincrement.

Summary and discussion

In this chapter, a novel non-conventional finite element method was introduced in order to model the activity and effect of grain boundary dislocation emission and penetration. The present conceptualization is based on a dislocation rate balance governed by the nucleation and transport of dislocations in the case of grain boundaries. Nucleation is precluded in grain interiors. The dislocation rate balance is solved via the finite element method by introducing a virtual dislocation density and by taking the weak formulation of the resulting equation. It was shown that this method is equivalent to taking strain gradient approach. Owing to the new set of equations to be solved in terms of dislocation densities and flux, higher order boundary conditions (e.g., dislocation densities and flux) must be introduced. The numerical scheme to be used is summarized in Figure 6.6.
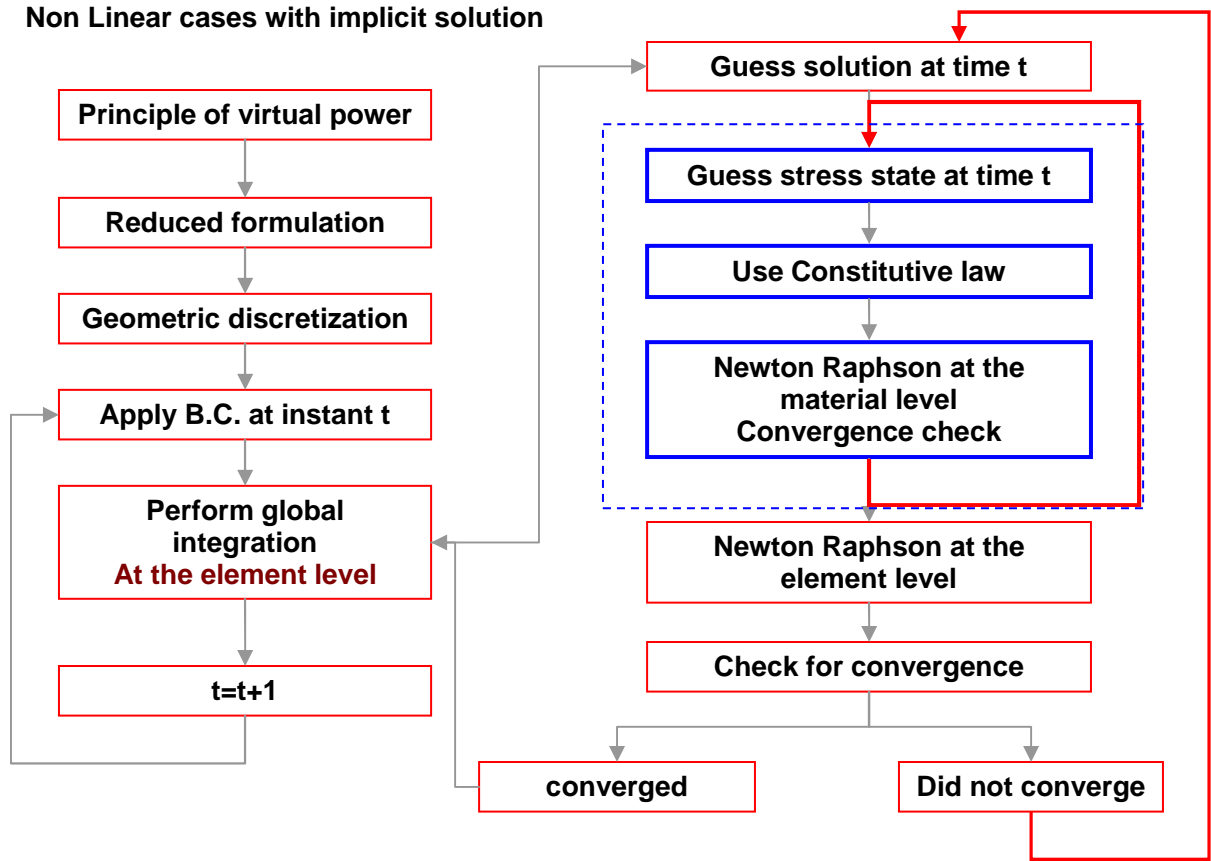
Non Linear cases with implicit solution

Figure 6.6: Numerical scheme of the finite element implementation.

The framework presented in this chapter is currently being implemented in order to study the response of bicrystal interfaces. The code is programmed in Fortran and is based on Dr. Esteban Busso's work on strain gradient crystal plasticity.

The long term objective is to use the presented framework in order to reproduce realistic microstructures (e.g. grain boundary distribution, grain size distribution, grain shapes) in which all known plastic deformation mechanisms are accounted for in the most adapter fashion. These microstructures will then be subjected to various type of

constraints. Finally, through a parametric study, the model will allow the fabrication of

material by design. Hence, the presented framework may be of use to the industry.

References

Arsenlis, A., Parks, D.M. (1999). "Crystallographic aspects of geometrically necessary and statistically stored dislocation density". Acta Materialia 47: 1597-1616.

Arsenlis, A., Parks, D.M.,Becker, R., Bulatov, V.V. (2004). "On the evolution of crystallographic dislocation density in non-homogeneously deforming crystals". Jounrla of the Mechanics and Physics of Solids 52-1213-1246.

Cheong, K.S., Busso, E.P. (2005). "A study of microstructural length scale effects on the behaviour of FCC polycrystals using strain gradient concepts ". International Journal of Plasticity 21:1797-1814.

Huang, Y., Qu, S., Hwang, K.C., Li, M., Gao, H. (2004). "A conventional theory of mechanism-based strain gradient plasticity." International Journal of Plasticity 20:753–782.

Kocks, U. F., U. F. Argon, et al. (1975). Progress in materials science 19: 110-170.

Meissonier, F.T., Busso, E.P., O'Dowd, N.P. (2000). "Finite element implementation of a generalised non-local rate-dependent crystallographic formulation for finite strains". International journal of plasticity 17:601:640.

Nye, J.F. (1953). "Some geometric relations in dislocated crystals". Acta metallurgica 1:153-162.

Sansoz, F, Molinari, J.F. 2005. Mechanical behavior of Sigma tilt grain boundaries in nanoscale Cu and Al: a quasicontinuum study. Acta materialia 53, 1883-1893

Warner, D. H., Sansoz, F.,Molinari, J. F. (2006). "Atomistic based continuum investigation of plastic deformation in nanocrystalline copper". International Journal of Plasticity 4: 764-774.

Wei, Y. J., Anand, L. (2004). "Grain-boundary sliding and separation in polycrystalline metals: application to nanocrystalline fcc metals". Journal of the Mechanics and Physics of Solids 52:2587-2616.

CHAPTER 7

CONCLUSION

The presented research work aimed at investigating the size effect in the elastic-response of pure F.C.C. polycrystalline materials. The domain of grain size covered ranged from several microns down to ~10 nm. The principal objectives of this work were to identify and model the active deformation mechanisms in nanocrystalline materials and to develop new tools allowing rigorous modeling of size effects.

First, the effect of diffusion mechanisms was studied via the used of a secant-self consistent scheme based on a two-phase representation of the material. Precisely, the material was represented by an inclusion phase, representing grain cores, and by a matrix phase, representing grain boundaries and triple junctions. Plastic deformation within the grain cores was driven by dislocation activity (e.g. dislocation storage and annihilation) and by steady state vacancy diffusion along the grain interior grain boundary interface (e.g. Coble creep). As a first approach the elasto-plastic response of grain boundaries was modeled as elastic-perfect-plastic. The model was applied to pure copper. It was shown that, on the condition that vacancy diffusion is indeed active in NC materials, the abnormal response of NC materials, characterized by the breakdown of the Hall Petch law, could result from the activity of Coble creep. While the model lead to acceptable predictions of the yield strength/ grain size relation, the plastic response of polycrystalline aggregates with small grain size (e.g. inferior to ~60nm) was clearly overestimated.

Second, a similar approach was used to estimate the combined effect of vacancy diffusion and unaccomodated grain boundary sliding (e.g. Lifschitz sliding). It was clearly shown that the activity of Lifschitz sliding leads to an overestimated softening in the response of NC materials. Therefore, the simultaneous activity of Coble creep and Lifschitz sliding is not relevant to the case of NC materials.

Third, grain boundary assisted deformation was studied via the use of molecular dynamics and continuum micromechanics. In the case of the sole elastic response of nanocrystalline materials, tensile tests on several symmetric bicrystal interfaces were performed via molecular dynamics simulations at 10K. These simulations revealed the activity of a particular mechanism, corresponding to an energy redistribution from the interface to its surrounding, which enhanced the energy storage capacity of a bicrystal interface. This novel mechanism occurs solely in the case where the bicrystal interface contains C structural units.

In the case of elasto-plasticity, a model was introduced to describe the activity and effect of grain boundary dislocation emission and penetration.
Existing molecular dynamics simulations had revealed the thermally activated nature of the mechanism which was consequently modeled as such. Precisely, the model relies on the assumption that while the triggering mechanism to grain boundary deformation is the nucleation of dislocation, the mechanism engendering plastic deformation is the penetration of dislocations within grain boundaries. A hierarchal scale transition

technique was introduced to model the aforementioned mechanisms. The mechanism of dislocation nucleation was modeled as a thermally activated mechanism. The parameters required in the model were obtained by molecular dynamics simulations at 10K. The penetration of dislocations within grain boundaries was modeled as a soft collision. Also, molecular simulation on a perfect planar interface and on an interface with same misorientation but containing a step revealed that, for this particular geometry, grain boundary ledges may be the primary interphase dislocation sources.

The limitations of typical work hardening laws to describe the size effect within inclusions ranging from conventional sizes down to the ultra-fine regime were shown. Therefore, the effect of grain boundaries on the flow stress of grain interiors at zero Kelvin was accounted for via the introduction of a Hall-Petch term.

Two-dimensional finite element simulations were performed on a representative element in order to estimate the stress heterogeneities within grain boundaries. The simulations revealed a stress heterogeneity factor in the order of 3. Therefore a stress heterogeneity factor was introduced in the constitutive law of grain boundaries

The transition from the microscopic to the macroscopic scale was performed with use of a two-phase secant–self-consistent scheme and of a novel three-phase micromechanical scheme. The latter is valid in the case of viscoplasticity alone and allows a precise description of the effect of the grain boundary/grain core interface. These models were applied to the case of pure copper in tension and in the quasistatic regime.

The model allowed close to perfect prediction of the response of polycrystalline materials with grain sizes ranging from several microns down to ~ 40nm. Note that the size effect in the strain rate sensitivity could not successfully be reproduced. The model showed that relatively high stresses are necessary within grain boundaries for dislocation emission and penetration to be active. However, when the stress heterogeneities are accounted for, the grain boundary dislocation emission and penetration mechanism leads to appropriate predictions of the softening in the plastic response of nanocrystalline materials. Also, creep test simulation shown that in agreement with recent experiments, nanocrystalline materials shall not exhibit creep rates different from that of conventional materials.

The effect of unaccomodated grain boundary sliding was modeled with use of a novel three-phase micromechanical scheme valid in the case of elastoplasticity. The proposed scheme accounts for the effect of slightly weakened interfaces and uses the field translation method. Base on existing quasicontinuum simulations, a viscous sliding law (e.g. stick-slip) was introduced to describe the grain boundary/grain core interface. The mode was applied to the case of pure copper. It was shown that grain boundary sliding does not necessitate high stress level within the grain boundaries to be activated. Hence, this mechanism, may dominate that of grain boundary dislocation emission and penetration. Clearly, this is dependent on the materials microstructure.

The presented research will be used in future research in order to pursue the investigations on NC materials. The desired objective is to allow the fabrication of

nanocrystalline materials by design. Prior to reaching this objective, several studies will be conducted.

First, the implementation of the non-conventional finite element method presented in Chapter 6 will be finalized. This will allow a precise prediction of stress and strain distributions within the microstructure. As mentioned throughout this dissertation, the model requires the estimations of several parameters such as the free enthalpy of activation of the dislocation emission mechanism. Therefore, the collaboration with Dr. Spearot, who performed all molecular simulation used in this research, will be pursued in order provide sufficient data in order to allow the modeling of the geometric dependence of the parameters. Such a study could be performed via the use neural networks.

Second, the two-phase micromechanical scheme accounting for the relative sliding of grains will be implemented in the case of elasto-viscoplasticity. The model will account for grain size distribution, grain boundary misorientation distributions and the constitutive law of grain cores will be modified to account for the reduced dislocation density within grain interiors.

APPENDIX A

SOLUTION TO NAVIER'S EQUATION

In this appendix, the solution to Navier's equation will be derived via the use of Fourier's functions. The same notation defined in Chapter 3 will be used in this appendix. Navier's equation is given by:

$$c_{ijkl}u_{k,lj} - c_{ijkl}\varepsilon_{kl,j}^* = 0 \qquad (A.1)$$

For the sake of simplicity the solution of Navier equation will be brought in two steps. In a first step, the eigenstrain will be supposed to be a known periodical function and, in a second step the same reasoning as presented in step 1 will be applied in the case where the eigenstrain is a random function that will be decomposed in an infinite sum of periodical functions. If the eigenstrain is a periodical function, it can then be written as follows:

$$\varepsilon_{ij}^* = \overline{\varepsilon}_{ij}^*(\xi)\exp(i\xi \cdot x) \qquad (A.2)$$

Here ξ defines the period of the function. The solution of eq (A.1) will be periodical as well with the same period. Hence, the displacement field can be written as follows:

$$u_{ij} = \bar{u}_{ij}(\xi)\exp(i\xi \cdot x) \tag{A.3}$$

Introducing equations (A.2) and (A.3) into equation (A.1), one obtains the following equation:

$$C_{ijkl}\bar{u}_k(\xi)\xi_l\xi_j = -iC_{ijkl}\bar{\varepsilon}_{kl}^*\xi_j \tag{A.4}$$

Let us define **K** as the second order matrix which components are defined as follows:

$$K_{ik} = C_{ijkl}\xi_l\xi_j \tag{A.5}$$

Similarly, one can define the vector $\boldsymbol{\alpha}$ which components are:

$$\alpha_i = -iC_{ijkl}\bar{\varepsilon}_{kl}^*\xi_j \tag{A.6}$$

Thus finding a solution to equation (A.4) is equivalent to finding a solution to the following system:

$$K_{ij}\bar{u}_j = \alpha_i \tag{A.7}$$

In the case where **K** can be inverted, $\boldsymbol{u}$ is given by:

$$\bar{u}_i = \frac{N_{ij}(\xi)}{D(\xi)}\alpha_j \tag{A.8}$$

The invert of K is given by:

$$K_{ij}^{-1} = \frac{N_{ij}(\xi)}{D(\xi)} \tag{A.9}$$

Here **N** and **D** are the cofactors and determinant of K, respectively. Also one has:

$$D(\xi) = e_{mnl}K_{m1}K_{n2}K_{l3} \tag{A.10}$$

And

$$N_{ij}(\xi) = \frac{1}{2}e_{ikl}e_{imn}K_{km}K_{ln} \tag{A.11}$$

Here *e* is the third order permutation tensor. A solution to Navier's equation can be obtained by introducing equation (A.8) into equation (A.2). However, the accuracy of the solution will be very limited since the eigenstrain was initially approximated by a periodical function. Hence, let us proceed to the second step of this development. In order to obtain a precise solution of Navier equation, one must take into account all the frequencies and related terms of Fourier extension of the eigenstrain. If the eigenstrain is developed in its Fourier's sum, it can then be written as follows:

$$\varepsilon_{ij}^* = \int_{-\infty}^{\infty} \bar{\varepsilon}_{ij}^*(\xi)\exp(i\xi \cdot x)d\xi \tag{A.12}$$

The Fourier coefficients are given by:

$$\bar{\varepsilon}_{ij}^*(\xi) = (2\pi)^{-3}\int_{-\infty}^{\infty}\varepsilon_{ij}(x)\exp(-i\xi \cdot x)dx \tag{A.13}$$

Thus, using the first step of this proof, the solution to the integral equation can be written in a general manner in the following form:

$$u_i(x) = -i \int_{-\infty}^{\infty} C_{jlmn} \bar{\varepsilon}_{mn}^*(\xi) \xi_l N_{ij}(\xi) D^{-1}(\xi) \exp(i\xi \cdot x) d\xi \tag{A.14}$$

From the compatibility equation, one obtains:

$$\varepsilon_{ij}(x) = \frac{1}{2} \int_{-\infty}^{\infty} C_{klmn} \bar{\varepsilon}_{mn}^*(\xi) \xi_l \left(\xi_l N_{ik}(\xi) + \xi_i N_{jk}(\xi) \right) D^{-1}(\xi) \exp(i\xi \cdot x) d\xi \tag{A.15}$$

Hooke's law also provides a solution for the local stress:

$$\sigma_{ij}(x) = C_{ijkl} \int_{-\infty}^{\infty} C_{pqmn} \bar{\varepsilon}_{mn}^*(\xi) \xi_q \xi_l N_{kl}(\xi) D^{-1}(\xi) \exp(i\xi \cdot x) d\xi - \varepsilon_{kl}^*(x) \tag{A.16}$$

Introducing equation (A.13) in the above set of equations, one obtains the solution to Navier's equation:

$$u_i(x) = \frac{-i}{(2\pi)^3} \int_{-\infty}^{\infty} \int_{-\infty}^{\infty} C_{jlmn} \varepsilon_{mn}^*(x') \xi_l N_{ij}(\xi) D^{-1}(\xi) \exp(i\xi \cdot (x - x')) d\xi dx$$

$$\varepsilon_{ij}(x) = (2\pi)^{-3} \int_{-\infty}^{\infty} \int_{-\infty}^{\infty} \frac{1}{2} C_{klmn} \varepsilon_{mn}^*(x') \xi_l \left(\xi_l N_{ik}(\xi) + \xi_i N_{jk}(\xi) \right) D^{-1}(\xi) \exp(i\xi \cdot (x - x')) d\xi dx$$

$$\sigma_{ij}(x) = C_{ijkl} (2\pi)^{-3} \int_{-\infty}^{\infty} \int_{-\infty}^{\infty} C_{pqmn} \varepsilon_{mn}^*(x') \xi_q \xi_l N_{kl}(\xi) D^{-1}(\xi) \exp(i\xi \cdot (x - x')) d\xi dx' - \varepsilon_{kl}^*(x)$$

$$\tag{A.17}$$

Finally, all equations in the above can be written in a simpler form by introducing

Green's operator defined as follows:

$$G_{ij}(x-x') = (2\pi)^{-3} \int_{-\infty}^{\infty} N_{ij}(\xi) D^{-1}(\xi) \exp(i(x-x')) d\xi \qquad (A.18)$$

Proceeding by identification one obtains:

$$u_i(x) = -\int_{-\infty}^{\infty} C_{jlmn} \varepsilon_{mn}^*(x') G_{ij,l}(x-x') dx'$$

$$\varepsilon_{ij}(x) = -\frac{1}{2} \int_{-\infty}^{\infty} C_{klmn} \varepsilon_{mn}^*(x') G_{kp,ql}(x-x') dx'$$

$$\sigma_{ij}(x) = -C_{ijkl} \int_{-\infty}^{\infty} C_{pqmn} G_{kp,ql}(x-x') dx' + \varepsilon_{kl}^*(x)$$

$$(A.19)$$

APPENDIX B

DERIVATION OF NAVIER'S EQUATION FOR A TWO PHASE

ELASTIC MATERIAL

In this appendix the integral equation, is derived via the use of Kunin's projection operator presented in Chapter 3. The same convention as defined in Chapter will be used. Recall that Navier's equation is written as follows:

$$\boldsymbol{\varepsilon}(r) = \boldsymbol{E} - \boldsymbol{\Gamma}^{C} \otimes \delta \mathbf{C} : \boldsymbol{\varepsilon} \tag{B.1}$$

Where the projection operator is defined as follows:

$$\boldsymbol{\Pi}^{\mathbf{C}} = \boldsymbol{\Gamma}^{\mathbf{C}} : \mathbf{C} \tag{B.2}$$

Here **C** is the spatial average of the elastic tensor which was results from the decomposition of the local elastic tensor as the sum of a spatially invariant term and a fluctuation term. $\boldsymbol{\Gamma}^{\mathbf{C}}$ denotes Green's modified operator. The equivalent properties proposed by Kunin are the following:

$$div(\boldsymbol{\sigma}) = 0 \Leftrightarrow \boldsymbol{\Pi}^{C} \otimes \mathbf{S} : \boldsymbol{\sigma} = 0 \tag{B.3}$$

$$\boldsymbol{\varepsilon} = \nabla^{s} u \Leftrightarrow \boldsymbol{\Pi}^{C} \otimes \boldsymbol{\varepsilon} = \boldsymbol{\varepsilon} - \mathbf{E} \tag{B.4}$$

Let us now establish equation (B.1) with the use of the projection operators. The decomposition of the compliance tensor in the sum of an average value over the space and of the elastic fluctuation in the neighborhood of **S** gives the following result:

$$S : \sigma = S : c : \varepsilon = (s - \delta S) : c : \varepsilon = \varepsilon - \delta S : c : \varepsilon \qquad (B.5)$$

Introducing equation (B.5) into equation (B.3) one obtains:

$$\Pi^C \otimes S : \sigma = \Pi^C \otimes \varepsilon - \Pi^C \otimes \delta S : c : \varepsilon = 0$$

Using equation (B.4), one obtains:

$$\varepsilon(r) = E - \Gamma^C \otimes \delta C : \varepsilon \qquad (B.6)$$

APPENDIX C

DERIVATION OF THE LOCALIZATION TENSORS AND

EFFECTIVE PROPERTIES

In this appendix the localization tensors in the cases of purely elastic and purely viscoplastic two-phase composite isotropic materials are derived. First let us provide some mathematical background. Let I denote the identity tensor, and K and J be two fourth order tensors extracting the deviatoric and spherical part of a two order tensors. These tensors can be written as functions of the Kronecker's symbol δ_{ij} as follows

:

$$I = I_{ijkl} = \frac{1}{2}\left(\delta_{ik}\delta_{jl} + \delta_{il}\delta_{jk}\right) \qquad \text{(C.1)}$$

$$J = J_{ijmn} = \frac{1}{3}\delta_{ij}\delta_{mn} \qquad \text{(C.2)}$$

$$K = I - J \qquad \text{(C.3)}$$

These tensors are typically used to expand fourth order isotropic tensors as the sum of a spherical and deviatoric term. Also, the product the combinations of the products of the above mentioned tensors give the following:

$$J_{ijkl}J_{klmn} = \frac{1}{9}\delta_{ij}\delta_{kl}\delta_{kl}\delta_{mn} = \frac{1}{3}\delta_{ij}\delta_{mn} = J_{ijmn} \qquad \text{(C.4)}$$

$$I_{ijkl}J_{klmn} = \frac{1}{2}\left(\delta_{ik}\delta_{jl} + \delta_{il}\delta_{jk}\right)\frac{1}{3}\left(\delta_{kl}\delta_{mn}\right)$$

$$= \frac{1}{6}\left(\delta_{ik}\delta_{jl}\delta_{kl}\delta_{mn} + \delta_{il}\delta_{jk}\delta_{kl}\delta_{mn}\right)$$

$$= \frac{1}{6}\left(\delta_{ij}\delta_{mn} + \delta_{ij}\delta_{mn}\right) \tag{C.5}$$

$$= J_{ijmn}$$

$$I_{ijkl}I_{klmn} = \frac{1}{2}(\delta_{ik}\delta_{jl} + \delta_{il}\delta_{jk}) \cdot \frac{1}{2}(\delta_{km}\delta_{ln} + \delta_{kn}\delta_{lm})$$

$$= \frac{1}{4}\left(\delta_{ik}\delta_{jl}\delta_{km}\delta_{ln} + \delta_{ik}\delta_{jl}\delta_{km}\delta_{ln} + \delta_{il}\delta_{jk}\delta_{km}\delta_{ln} + \delta_{kn}\delta_{lm}\right)$$

$$= \frac{1}{4}\left(2\delta_{im}\delta_{jn} + 2\delta_{in}\delta_{jm}\right) \tag{C.6}$$

$$= I_{ijmn}$$

And

$$K_{ijkl}J_{klmn} = (I_{ijkl} - J_{ijkl})J_{klmn} = J_{ijmn} - J_{ijmn} = 0 \tag{C.7}$$

With the above relations, the expressions of the localization tensors in the case of a simply viscoplastic and a simply linear elastic response can be found. Recall that the localization tensors in the case of elasticity and viscoplasticity are given by, respectively:

$$A^{Ce} = \left[I + S^E : C^e : (c - C^e)\right]^{-1} \tag{C.8}$$

$$A^{Be} = \left[I + S^E : B^e : (b - B^e)\right]^{-1} \tag{C.9}$$

Since the study is limited to the case of isotropic response the localization tensors within each phase (denoted with superscript *=I,M) can be decomposed with use of the fourth order tensors **K** and **J**:

$$A_{ijkl}^{Ce*} = N^{C*} K_{ijkl} + M^{C*} J_{ijkl} \tag{C.10}$$

And

$$A_{ijkl}^{Be*} = N^{B*} K_{ijkl} + M^{B*} J_{ijkl} \tag{C.11}$$

The following proofs will be derived solely for the case of elasticity. The solution in the case of viscoplasticity can be found by identification. In the case of linear elastic inclusions spherical inclusions with isotropic response, Eshelby's tensor is constant and can be written as follows:

$$S_{ijkl}^{E} = \alpha J_{ijkl} + \beta K_{ijkl} \text{ with } \alpha = \frac{1}{3}\frac{1+\nu}{1-\nu} \text{ and } \beta = \frac{2}{15}\frac{4-5\nu}{1-\nu} \tag{C.12}$$

Then, the inverse of the localization tensors can be calculated relatively simply as follows:

$$(A^{Ce})^{-1} = I + S^{E} : (C^{e})^{-1} : (c - C^{e}) = K + J + (\alpha J + \beta K) : (\frac{1}{2\mu^{e}} K + \frac{1}{3k^{e}}) : (c - C^{e})$$

$$\tag{C.13}$$

Using the expression of the elastic tensor moduli (both local and global), the equation in the above can be written as follows:

$$(A^{Ce})^{-1} = \frac{(\mu - \mu^e)\beta + \mu^e}{\mu^e}K + \frac{(k - k^e)\alpha + k^e}{k^e}J \qquad (C.14)$$

Here μ and k define the shear and bulk moduli, respectively. The decomposition of the inverse of the localization tensor as a sum of two products of a scalar by one of the two basic fourth order tensor K and J, allows us to determine the concentration tensors by simply inverting the two scalars. The effective properties of the materials can be obtained with use of the closed forms of the localization tensors. Since the material (globally as well as locally) behaves isotropically, the effective elastic tensor can be written as follows:

$$C^e = 3k^e J + 2\mu^e K \qquad (C.15)$$

Let us recall that the effective elastic tensor is also defined as follows:

$$C^e = \overline{cA^{Ce}} = fc^I A^{CeI} + (1 - f)c^M A^{CeM} \qquad (C.16)$$

Since, $\overline{A^{Ce}} = 1 = f\overline{A^{CeI}} + (1 - f)\overline{A^{CeM}}$, the effective elastic tensor can be written as follows:

$$C^e = c^M + f(c^I - c^M)A^{CeI} = 3k^M J + \mu^M K + 2fN^{CI}(\mu^I - \mu^M)K + 3fM^{CI}(k^I - k^M)J)$$

Finally, the effective properties are found by identification, leading to the following:

339

$$\mu^e = \mu^M + f(\mu^I - \mu^M)\frac{\mu^e}{\mu^e + \beta(\mu^I - \mu^e)} \qquad (C.17)$$

And

$$k^e = k^M + f(k^I - k^M)\frac{k^e}{k^e + \alpha(k^I - k^e)} \qquad (C.18)$$

APPENDIX D

DERIVATION OF THE HARDENING RATE

In this appendix, the hardening rate, $\theta = \dfrac{d\sigma}{d\varepsilon_{eq}^{I,vp}}$, is derived in the particular case of a

constant strain rate. The flow stress at zero Kelvin accounts for the effect of the presence of

stored dislocations and the long range effect of grain boundaries:

$$\sigma_f = \alpha MGb\sqrt{\rho} + \frac{\beta}{\sqrt{d}} \tag{D.1}$$

The evolution of the dislocation density is given by:

$$\frac{d\rho}{d\varepsilon_{eq}^{I,vp}} = M\left(\frac{k}{d} + k_1\sqrt{\rho} - k_2\rho\right) \tag{D.2}$$

The viscoplastic strain rate is related to the equivalent stress by the following power law relation:

$$\dot{\varepsilon}_{eq}^{I,vp} = \dot{\varepsilon}_0 \left(\frac{\sigma_{eq}^I}{\sigma_f}\right)^m \tag{D.3}$$

In the simple one dimensional case, the differential of equation (C.3) leads to:

$$d\sigma = \frac{\partial \sigma}{\partial \ln \dot{\varepsilon}_{eq}^{I,vp}} d \ln \dot{\varepsilon}_{eq}^{I,vp} + \frac{\partial \sigma}{\partial \sigma_f} d\sigma_f \qquad (D.4)$$

Using the constant strain rate hypothesis, the hardening rate is given by:

$$\theta = \frac{d\sigma}{d\varepsilon_{eq}^{I,vp}} = \frac{\partial \sigma}{\partial \sigma_f} \frac{d\sigma_f}{d\varepsilon_{eq}^{I,vp}} \qquad (D.5)$$

Using equation (D.2) and (D.3), equation (D.5) becomes:

$$\theta = \left(\frac{\dot{\varepsilon}_{eq}^{I,vp}}{\dot{\varepsilon}_0} \right)^{1/m} \frac{\alpha M^2 Gb}{2\sqrt{\rho}} \cdot \left(\frac{k}{d} + k_1 \sqrt{\rho} - k_2 \rho \right) \qquad (D.6)$$

From equation (D.1) and (D.3) the square root of the dislocation density is given by:

$$\sqrt{\rho} = \frac{1}{\alpha MGb} \left(\sigma \left(\frac{\dot{\varepsilon}_{eq}^{I,vp}}{\dot{\varepsilon}_0} \right)^{-1/m} - \frac{\beta}{\sqrt{d}} \right) \qquad (D.7)$$

Introducing (D.7) into (D.6) and grouping the terms leads to:

$$\theta = \left(\frac{\dot{\varepsilon}_{eq}^{I,vp}}{\dot{\varepsilon}_0}\right)^{1/m} \frac{\alpha^2 M^3 G^2 b^2}{2\left(\sigma\left(\frac{\dot{\varepsilon}_{eq}^{I,vp}}{\dot{\varepsilon}_0}\right)^{-1/m} - \frac{\beta}{\sqrt{d}}\right)} \cdot$$

$$\left(\begin{array}{l} \dfrac{k}{d} - \dfrac{k_1\beta}{\alpha MGb\sqrt{d}} - \dfrac{k_2\beta^2}{d\cdot(\alpha MGb)^2} + \\[4mm] \sigma\left(\dfrac{k_1}{\alpha MGb}\left(\dfrac{\dot{\varepsilon}_{eq}^{I,vp}}{\dot{\varepsilon}_0}\right)^{-1/m} + \dfrac{2k_2\beta}{\sqrt{d}\cdot(\alpha MGb)^2}\left(\dfrac{\dot{\varepsilon}_{eq}^{I,vp}}{\dot{\varepsilon}_0}\right)^{-1/m}\right) \\[4mm] - \dfrac{k_2\sigma^2}{(\alpha MGb)^2}\left(\dfrac{\dot{\varepsilon}_{eq}^{I,vp}}{\dot{\varepsilon}_0}\right)^{-2/m} \end{array}\right)$$

(D.8)

Introducing $Z = \dfrac{2\beta k_2}{\alpha MG k_1 b\sqrt{d}}$ into equation (D.8) leads to:

$$\theta = \frac{Mk_2}{2\left(\sigma\left(\frac{\dot{\varepsilon}_{eq}^{I,vp}}{\dot{\varepsilon}_0}\right)^{-1/m} - \frac{\beta}{\sqrt{d}}\right)} \cdot \left(\frac{\dot{\varepsilon}_{eq}^{I,vp}}{\dot{\varepsilon}_0}\right)^{-1/m}$$

$$\left(\begin{array}{l} \left(\dfrac{k}{k_2 d} - \dfrac{Z}{2}\left(\dfrac{k_1}{k_2}\right) - \dfrac{Z^2(k_1)^2}{4(k_2)^2}\right)(\alpha MGb)^2\left(\dfrac{\dot{\varepsilon}_{eq}^{I,vp}}{\dot{\varepsilon}_0}\right)^{2/m} + \sigma\cdot\alpha MGb\dfrac{k_1}{k_2}(1+Z)\left(\dfrac{\dot{\varepsilon}_{eq}^{I,vp}}{\dot{\varepsilon}_0}\right)^{1/m} \\[4mm] -\sigma^2 \end{array}\right)$$

(D.9)

Let us now write equation (D.9) as follows:

$$\theta = \frac{Mk_2(\sigma_s)^2}{2\left(\sigma\left(\frac{\dot{\varepsilon}_{eq}^{I,vp}}{\dot{\varepsilon}_0}\right)^{-1/m} - \frac{\beta}{\sqrt{d}}\right)} \cdot \left(\frac{\dot{\varepsilon}_{eq}^{I,vp}}{\dot{\varepsilon}_0}\right)^{-1/m}\left(1 - \left(\frac{\sigma}{\sigma_s}\right)^2 - 2\left(1-\left(\frac{\sigma}{\sigma_s}\right)\right)L\right)$$

(D.10)

Identifying the terms of equation (D.10) with those of equation (D.9) leads to:

$$\sigma_s = \frac{\alpha MGbk_1}{2k_2} \cdot \left(\frac{\dot{\varepsilon}_{eq}^{I,vp}}{\dot{\varepsilon}_0}\right)^{1/m} \left(1 + Z + \left(1 + \frac{4kk_2}{d(k_1)^2}\right)^{1/2}\right)$$ (D.11)

And

$$L = \frac{\alpha MGbk_1}{2k_2\sigma_s} \cdot (1 + Z)\left(\frac{\dot{\varepsilon}_{eq}^{I,vp}}{\dot{\varepsilon}_0}\right)^{1/m}$$ (D.12)

With equation (D.11) and (D.12), equation (D.9) can be written as follows:

$$\theta = \frac{Mk_2(\sigma_s)^2}{2\left(\sigma\left(\dfrac{\dot{\varepsilon}_{eq}^{I,vp}}{\dot{\varepsilon}_0}\right)^{-1/m} - \dfrac{\beta}{\sqrt{d}}\right)} \cdot \left(\frac{\dot{\varepsilon}_{eq}^{I,vp}}{\dot{\varepsilon}_0}\right)^{-1/m} \cdot$$

$$\left(1 - \left(\frac{\sigma}{\sigma_s}\right)^2 - 2\left(1 - \left(\frac{\sigma}{\sigma_s}\right)\right)\right)(1+Z)\left(1 + Z + \left(1 + \frac{4kk_2}{d(k_1)^2}\right)^{1/2}\right)^{-1}\right)$$ (D.13)